2010-01-01

Phase Change Materials for Thermal Regulation of Building Integrated Photovoltaics

Ahmad Hassan
Technological University Dublin

1-1-2010

Phase Change Materials for Thermal Regulation of Building Integrated Photovoltaics

Ahman Hassan (Thesis)
Dublin Institute of Technology

Phase Change Materials for Thermal Regulation of Building Integrated Photovoltaics

Ahmad Hasan BSc, MSc

Dublin Energy Lab.

Dublin Institute of Technology

Thesis submitted for PhD

July, 2010.

Supervised by

Professor Brian Norton

Dr. Sarah McCormack

Dr. Ming Jun Huang

Abstract

In outdoor deployed photovoltaics (PV), standard test conditions (STC) of 25 °C PV temperature, 1000 Wm^{-2} solar radiation intensity and 1.5 air-mass rarely prevail. PV temperature can rise 40-100 °C above STC inducing a power drop in crystalline silicon PV with a coefficient of -0.4 to -0.65 %/K above STC. Increased operating temperature also results in accelerated PV degradation due to cell delamination allowing moisture ingress.

Conventional building integrated photovoltaics (BIPV) cooling techniques using passive or active heat removal by air or water flow are limited by (i) very low heat transfer or (ii) large capital as well as maintenance costs respectively. A PV cooling technique employing phase change materials (PCM) exploits latent heat absorption during solid-liquid phase change in a very narrow range of PCM transition temperature was investigated.

The current research aims to investigate suitable PCM materials through experimental characterization in terms of melting point, heat of fusion, thermal conductivity, density and specific heat capacity to determine the suitability of different PCMs for PV cooling in different climatic conditions indoors and outdoors employed at small scale cell size PV systems as well as larger PV panel size system through extensive experimental work supported by the reasonable numerical modeling to determine the associated power improvement of PV through cooling produced by PCM.

Indoor experiments were conducted at small scale cell size PV at 500 Wm^{-2}, 750 Wm^{-2} and 1000 Wm^{-2} insolation representative PV operating condition that would require PV cooling in most cases. The effect of (i) thermal mass of PCM (ii) melting point of PCM and (iii) thermal conductivities of PCM and PV-PCM system on temperature regulation performance of PCM was observed. Two out of five PCM, a salt hydrate ($CaCl_2.6H_2O$) and a eutectic mixture of capric -palmitic acid (CP), , an aluminium alloy based PV-PCM systems were found optimum for PV temperature regulation at most of the solar radiation intensities. To extend experiments on PV panel size systems, A larger scale PV-PCM system with dimensions 700 cm x 600 cm with metallic fins was fabricated. PCM $CaCl_2.6H_2O$ and CP found optimum through cell size experiments were characterized at 500 Wm^{-2}, 750 Wm^{-2} and 1000 Wm^{-2} insolation contained in the large scale PV-PCM system. The experiments on large scale PV-PCM systems showed promise for PV cooling provided by PCM and associated power gain. PV-PCM systems were then characterized outdoors in Dublin, Ireland (53.33 N, 6.25 W) and Vehari, Pakistan (30.03 N, 72.25 E) to observe their performance in real time outdoor condition in different climates. Higher PV cooling and associated power savings were observed in climate of Vehari than that of Dublin. Out of the two PCMs, $CaCl_2.6H_2O$ achieved higher PV cooling and power saving than CP. In the best case, peak PV cooling of 21.5 °C with associated measured peak power saving of 13 % and predicted peak power saving of 14 % were recorded in Vehari on 30-10-2009. The results show that PCM are an effective way to cool PV and maintain higher power outputs in higher insolation climates.

Declaration

I certify that this thesis which I now submit for examination for the award of PhD is entirely my own work and has not been taken from the work of others, save and to the extent that such work has been cited and acknowledged within the text of my work. This thesis was prepared according to the regulations for postgraduate study by research of the Dublin Institute of Technology and has not been submitted in whole or in part for another award in any Institute. The work reported on in this thesis conforms to the principles and requirements of the Institute's guidelines for ethics in research.

The Institute has permission to keep, lend or copy this thesis in whole or in part, on condition that any such use of the material of the thesis be duly acknowledged.

Signature _____ Date _____

Acknowledgements

This thesis would not have been possible without the excellent guidance and support I have received from my supervisors Dr. Sarah McCormack, Dr. Ming Jun Huang and Prof. Brian Norton. I am very grateful to them for all their dedication. It has been a pleasure working with them on this project and I look forward to future collaborations together.

I would like to express my appreciation to all my colleagues, Jawad, Haq, Mahmood, Manus and Kevin for their continued support and encouragement over the last number of years. I would extend my thanks to Peter O' Farrel and Cecil Potterman for their help in fabrication of the PV-PCM systems. I can not forget inputs from Nari, Juanka and Daniel for their hand in installing the system outdoors on Focas roof and monitoring. I am thankful to Professor Nadeem A. Mufti for allowing me collaborate with UET Lahore for outdoor experiments in Pakistan. I would like to acknowledge all the assistance received from Ulster University for use of their solar simulator facility. I would also acknowledge the technical and financial assistance provided by COST through action TU0802: Next generation cost effective phase change materials for increased energy efficiency in renewable energy systems in buildings. I am very grateful to everyone in the FOCAS institute who provided me with invaluable advice and technical instruction.

Thanks to my late father, mother and brothers, who never gave up on me throughout my career. All thanks and appreciation to my wife and little daughter Sarah for their patience and prayers while bearing with my work. Thanks to Almighty providing me courage and spirit to bear and come out from typical PhD low times.

Abbreviations

BIPV	Building integrated photovoltaics
$CaCl_2$	$CaCl_2.6H_2O$
CL	Capric acid-lauric acid
CP	Capric acid-palmitic acid
DSC	Differential scanning calorimetry
DTA	Differential thermal analysis
EVA	Ethyl vinyl acetate
GaAs	Gallium arsenide
GaSb	Gallium antimonide
HTF	Heat transfer fluid
PCM	Phase change material
PV	Photovoltaic
PV-PCM_1	PV module containing integrated PCM, CP
PV-PCM_2	PV module containing integrated PCM, $CaCl_2.6H_2O$
PV-T	Photovoltaic thermal systems
RET	Renewable energy technologies
STC	Standard test conditions
THM	Temperature history method
TMS	Thin metal sheets
W_p	Watt peak

Nomenclature

A	Surface area	[m^2]
A_c	Convective heat transfer area of the tube	[m^2]
A_1	Integral of time-temperature curve during liquid phase $= \int_0^{t_1} ((T - T_{\infty,a})\, dt$	[˚Cs]
A_2	Integral of time-temperature curve during phase change $= \int_{t_1}^{t_2} ((T - T_{\infty,a})\, dt$	[˚Cs]
A_3	Integral of time-temperature curve of solid PCM till thermal equilibrium with ambient $= \int_{t_2}^{t_3} ((T - T_{\infty,a})\, dt$	[˚Cs]
A_{PV}	Area of the PV exposed to solar radiations	[m^2]
Bi	Biot number	[−]
$C_{P,\,l}$	Specific heat capacity of liquid PCM	[$kJkg^{-1}K^{-1}$]
$C_{P,\,s}$	Specific heat capacity of solid PCM	[$kJkg^{-1}K^{-1}$]
$C_{p,\,t}$	Specific heat capacity of glass tube	[$kJkg^{-1}K^{-1}$]
$C_{p,\,w}$	Specific heat capacity of water	[$kJkg^{-1}K^{-1}$]
E	East	[-]
FF	Fill factor	[−]
FF_{st}	FF neglecting temperature influence	[−]
FF_T	FF calculated considering temperatures influence	[−]
G	Solar radiation	[Wm^{-2}]
Gr	Grashof number	[-]

H	Latent heat of fusion	[kJkg^{-1}]
h	Sensible enthalpy	[kJkg^{-1}]
h_c	Convective heat loss coefficient	[Wm^{-2}K^{-1}]
h_{ca}	Combined convective and radiative heat loss coefficient	[Wm^{-2}K^{-1}]
I	Current	[A]
I_{sc}	Short circuit current	[A]
J_{sc}	Short circuit current density	[Am^{-2}]
l	Length scale	[m]
L	Liquid fraction	[-]
m	Mass	[kg]
m_p	Mass of PCM	[kg]
m_t	Mass of glass tube	[kg]
m_w	Mass of distilled water	[kg]
N	North	[-]
Nu	Nusselt number	[-]
NOCT	Normal operating cell temperature	[˚C]
P	Electrical power	[W]
Pe	Peclet number	[-]
p	Pressure	[Nm^{-2}]
p'_s	Boundary pressure	[Nm^{-2}]
P_m	Maximum power point	[W]
Pr	Prandtl number	[-]

P_s	Power saving	[W]
P_T	Power produced by PV at a temperature T	[W]
Q_A	Heat lost from PV available to PV-T	[J]
Q_s	Heat storage capacity	[kJK^{-1}]
q'''	Volumetric heat source	[-]
q_r	Radiation flux	[Wm^{-2}]
q	Unit charge	[C]
R	Radius of the glass tube	[m]
Ra	Raleigh number	[-]
Re	Reynolds number	[-]
R_s	Series resistance	[Ω]
R_{sh}	Shunt resistance	[Ω]
S_b, S_y, S_z	Source terms in momentum equation	[-]
S_h	Source term in energy equation	[-]
St	Stanton number	[-]
Ste	Stefan number	[-]
T_{amb}	Ambient temperature	[°C]
T_c	Temperature coefficient of power drop	[°C]
T_{cell}	Temperature of PV cell	[°C]
T_{FF}	Temperature coefficient of fill factor	[-]
T_i	Interface temperature	[°C]
T_m	Equilibrium temperature of melting/freezing	[°C]
T_p	Temperature coefficient of power	[$\%/C^{-1}$]

T_{PV}	Temperature of the reference PV	[°C]
T_{PVPCM}	Temperature of PV-PCM	[°C]
T_r	Reference PV temperature	[°C]
T_s	Surface temperature	[°C]
T_{sun}	Temperature of sun	[°C]
T_s	Surface temperature	[°C]
u_1	Actual fluid velocity	[ms^{-1}]
U_{PV}	Overall heat loss coefficient	[$Wm^{-2}K^{-1}$]
V	Output voltage	[V]
v	Superficial velocities in y direction	[ms^{-1}]
V_{oc}	Open circuit voltage	[V]
v_w	Wind speed	[ms^{-1}]
W	West	[-]
w	Superficial velocities in z direction	[ms^{-1}]
w_i	Interface velocity	[ms^{-1}]
x	Position of the interface	[m]
α	Thermal diffusivity	[m^2s^{-1}]
α_{pv}	Absorptance of PV	[−]
β	Thermal expansion coefficient	[K^{-1}]
Γ	Thermal regulation enhancement	[°C-min]
ΔT	Change in temperature	[°C]
γ	Heat flow into the solid phase	[Js^{-1}]
η	Efficiency	[%]

θ	Coefficient of solar irradiance	[-]
η_e	Energy efficiency of PV system	[%]
η_r	Reference PV module efficiency	[%]
κ	Thermal conductivity	[$Wm^{-1}K^{-1}$]
κ_s	Thermal conductivity solid phase	[$Wm^{-1}K^{-1}$]
κ_l	Thermal conductivity liquid phase	[$Wm^{-1}K^{-1}$]
λ	Porosity	[-]
μ	Superficial fluid velocity	[ms^{-1}]
μ_1	Superficial fluid velocity	[ms^{-1}]
μ_k	Kinetic mobility	[-]
ν	Kinematic viscosity	[m^2s^{-1}]
ξ	Half mushy zone	[-]
ρ	Density	[gcm^{-3}]
σ	Stefan Boltzmann's constant	[$Wm^{-2}K^{-4}$]
τ	Transmittance of PV	[-]

Definitions of Dimensionless numbers

Gr = Grashof number- is the ratio of buoyancy forces to viscous forces acting on a fluid. It determines the transition from laminar flow to turbulent flow for natural convection heat transfer in fluids. The natural convection is laminar at lower *Gr* while it is turbulent at higher *Gr* values, the transition to turbulent flow occurs at $10^7 < Gr < 10^8$. For vertical

heated wall, similar to the PV wall heated by incoming solar radiation in current work, the Gr_l is:

$$Gr_l = \frac{g\beta(T_s - T_\infty)l^3}{\upsilon^2}$$

Where g is the gravitational constant, β is the coefficient of thermal expansion of PCM, T_s is the surface temperature, T_∞ is the bulk temperature, v is the kinematic viscosity of PCM, κ= is the thermal conductivity of the PCM, ρ is the density of the PCM, c_p is the specific heat capacity of the PCM and l is the distance from the front surface.

$\boldsymbol{Nu_l}$ **= Nusselt number**- is the ratio of convective to conductive heat transfer normal to a boundary. A Nu_l number close to unity shows that the convection and conduction are of similar magnitude and that the flow is laminar. A larger value of Nu_l shows the presence of strong convection and the transition of fluid flow from laminar to turbulent, the turbulent flow happens at Nu_l values in the range of 100-1000.

$$Nu_l = \frac{h_c l}{\kappa}$$

Where h_c is the convective heat transfer coefficient.

$\boldsymbol{Pe_l}$ **= Peclet number-** is the ratio of rate of advection of a physical quantity by flow to the rate of diffusion of the same quantity driven by appropriate gradient. It describes the

transport phenomena in a fluid flow, in context of the heat transport it is the product of the Reynolds number and Prandtl number.

$$Pe_l = Re_l . Pr_l = \frac{lv}{\frac{\kappa}{\rho c_p}}$$

Where *v* is the velocity of the fluid.

***Pr* = Prandtl number** - is the ratio of momentum diffusivity to thermal diffusivity. It can be observed that the *Pr* depends only on the fluid and its physical state and does not include any length scale variable. Low *Pr* values (i.e., 0.015 for Mercury) indicate that conduction is effective with thermal diffusivity dominant while high values (100 – 40000 for engine oils) show that convection is effective with momentum diffusivity dominant.

$$P_r = \frac{c_p \mu}{\kappa}$$

Whew μ is the dynamic viscosity of the fluid.

***Ra* = *Raleigh Number* -** is the product of the Grashof number (Gr_x) and Prandtl number (*Pr*). The *Ra* mostly occurs at 10^6-10^8 for most of the engineering problems. The lower *Ra* values show stronger conduction heat transfer while the higher values shows strong convection heat transfer in the fluids.

$$Ra = Gr_x . Pr = \frac{g\beta}{\nu\alpha}(T_s - T_\infty)x^3$$

Where α is the thermal diffusivity.

Reynolds Number *(Re)*-is the ratio of internal forces to viscous forces. The *Re* describes whether the fluid flow is laminar or turbulent. The *Re* value showing transition from laminar to turbulent flow depends on the geometry of the system in which fluid is flowing (i.e., in a pipe with a fully developed flow, the laminar flow occurs at Re < 2300 and the turbulent flow occurs at Re > 4000).

$$Re = \frac{\rho v l}{\mu}$$

Stanton number *(St)*- is the ratio of the heat transferred into the fluid to the thermal capacity of the fluid. It is used to measures the heat transfer in the forced convection flows. It can also be written in terms of Nusselt, Reynolds and Prandtl numbers.

$$St = \frac{Nu}{Re.Pr} = \frac{h_c}{c_p \rho v}$$

Stefan number *(Ste)* is the ratio of sensible heat to the latent heat.

$$Ste = \frac{c_p \Delta T}{H}$$

Where ΔT is the temperature difference between phases and *H* is the latent heat.

Table of Contents

List of Figures

List of Tables

1 INTRODUCTION

1.1 World Energy Outlook

World primary energy demand is projected to increase by 40 % by 2030 compared to reference scenario in 2007 (IEA, 2009 a). This increase will be met by 77 % share of fossil fuels and 23 % share of the renewable energy sources (IEA, 2009 a). The CO_2 emissions will increase from 28.8 *Gt* CO_2 equivalent in 2007 to 40.2 *Gt* CO_2 equivalent in 2030. With a 25 % probability that the global temperature does not rise above 2 °C, the CO_2 emitted needs to be below 1 trillion tonnes over the period 2000-2049, of which 313 billion tonnes have already been emitted from 2000-2009 (IEA, 2009 a). If the present trend continues, global temperature will rise by 6 °C toward the end of this century (IEA, 2009 b).

All proven global oil and natural gas reserves are predicted to be economically usable and exploitable until 2048 (Goswami, 2007) and 2065 (Breeze, 2005) respectively if the current trend in consumption growth continues with the little hope for them being cost competitive in future with the current trend in price hike. Nuclear power as an immediate alternative to fossil fuels is also unlikely to provide a significant proportion of energy need in near future in due to political issues, unavailability of technology to most of the world nations, finite resources of nuclear fuels (currently uranium) and risk of nuclear accidents (Kreith and Goswami, 2007). Due to the finite fossil fuel and nuclear reserves, renewable energy technologies (RETs) must provide an increasing

proportion of future energy if the world's population are to expect a secure and sustainable developed society.

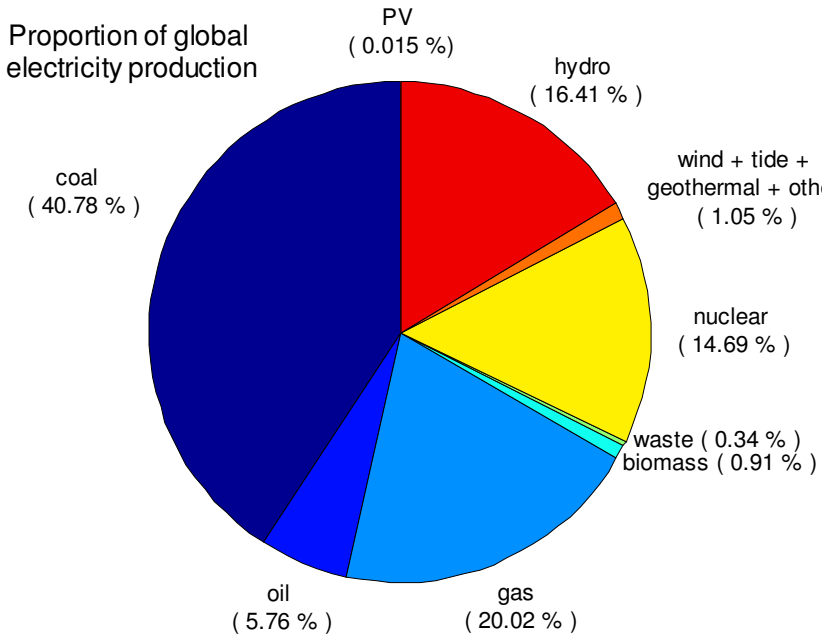

Figure 1.1 Supply of global electricity production by fuel type in 2006 (IEA, 2009 a).

Electricity generation currently accounts for over 30% of global primary energy demand (Kreith and Goswami, 2007). In 2006, RETs provided 18% of electricity supply while photovoltaics (PV) supplied 0.015 % when PV production was only 1603 MW_p as shown in Figure 1.1 (IEA, (2009 a). From 2006 to 2009 PV production has increase to 6,802 MW_p and is expected to reach 22,325 MW_p at the end of 2013 (EPIA, 2010), 14 times more than it was in 2006. PV converts solar energy, whose potential is such that one hour of solar energy falling on earth could meet the current global annual primary energy demand (Morton, 2006). The immense potential of solar

energy along with rapidly increasing share of PV in energy supply clearly shows PV has an important role in long-term future energy supply.

1.2 Introduction to Photovoltaic Devices

Photovoltaics (PV) are renewable energy systems which convert sunlight directly into electricity. Incoming solar radiation (*G*) is absorbed by a semiconductor absorbing material that generates electron-hole pair mobile charge carriers responsible for an electric current (Würfel, 2005). PV devices are classified according to the type of light absorbing materials, thickness of the absorbing material and application of the PV.

1.2.1 Quantum Efficiency of Photovoltaic Cells

Not all solar radiation (*G*) falling on the PV surface is involved in the electrical conversion process. Only *G* with energy equal to or above the band gap of the cell material takes part in conversion process. Incoming *G* is either (i) reflected back from the surface of the cell, (ii) transmitted through or (iii) absorbed by the PV cell material. The ratio of absorbed *G* to incoming *G* is called the "external quantum efficiency" of the PV cell (Yang, *et al*., 2008). Absorbed *G* generates electron-hole pairs which travel to their corresponding electrodes. Electrons that reach the electrodes successfully to travel through an external circuit to combine with the holes from the other side of the junction are responsible for the photo-generated current available from the cell. Electrons that recombine with the holes in the bulk material before reaching electrodes do not contribute to the electrical current from the PV cell

and constitute "recombination losses" (Gangadhar and Bhattacharyya, 1968; Lu, 1996). The ratio of electrical current produced from the cell to the absorbed *G* is called "internal quantum efficiency" (Yang, *et al.*, 2008).

1.2.2 Maximum Power Point

PV can operate over a wide range of voltage (*V*) and current (*I*) depending on the resistive load applied in the external electrical circuit. Applying a very low resistance results in a negligibly small *V* and maximum *I* termed as "short circuit current". By increasing the load, *I* decreases and *V* increases, at a very high resistive load *I* is negligibly small and *V* is very high which is "open circuit voltage". Since the power is product of *V* and *I*, no power is produced at either open circuit or short circuit conditions as either *I* or *V* becomes zero. The load for which PV yields optimum *V* and *I* producing maximum electrical power (*P*) is called the "maximum power point" P_m. P_m varies with *G* and PV temperature.

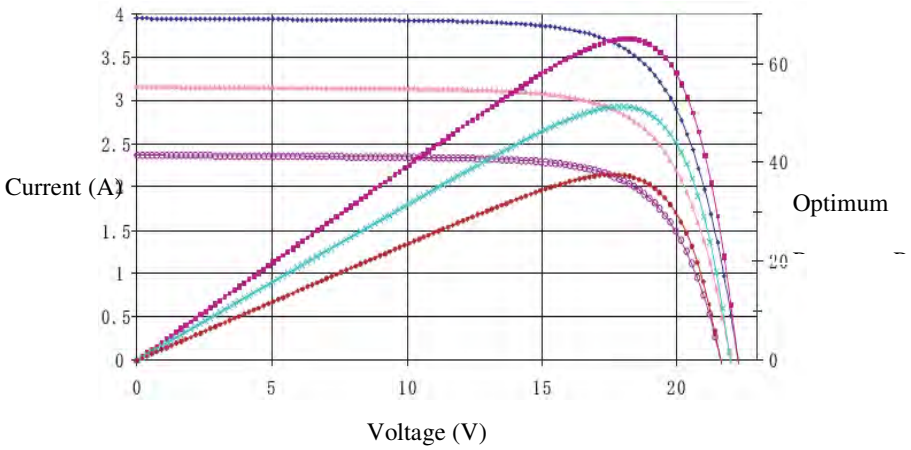

Figure 1.2 I-V characteristic curve of a PV showing the maximum power point (Suntechnic, 2006)

1.2.3 Electrical Conversion Efficiency

A solar cell's rated electrical conversion efficiency, η is the ratio of G converted to electricity at P_m to the total G falling on the PV surface area (A) when a solar cell is connected to an electrical circuit at standard test conditions (STC). STC are 1000 Wm^{-2} solar radiation intensity (ASTM G 173-03, 2003), 25 ºC PV temperature and 1.5 air mass solar spectrum (NREL, 2007)

$$\eta = \frac{P_m}{G \times A} \tag{1.1}$$

The highest reported efficiencies are summarised in Figure 1.2 (Kazmerski, 2008)

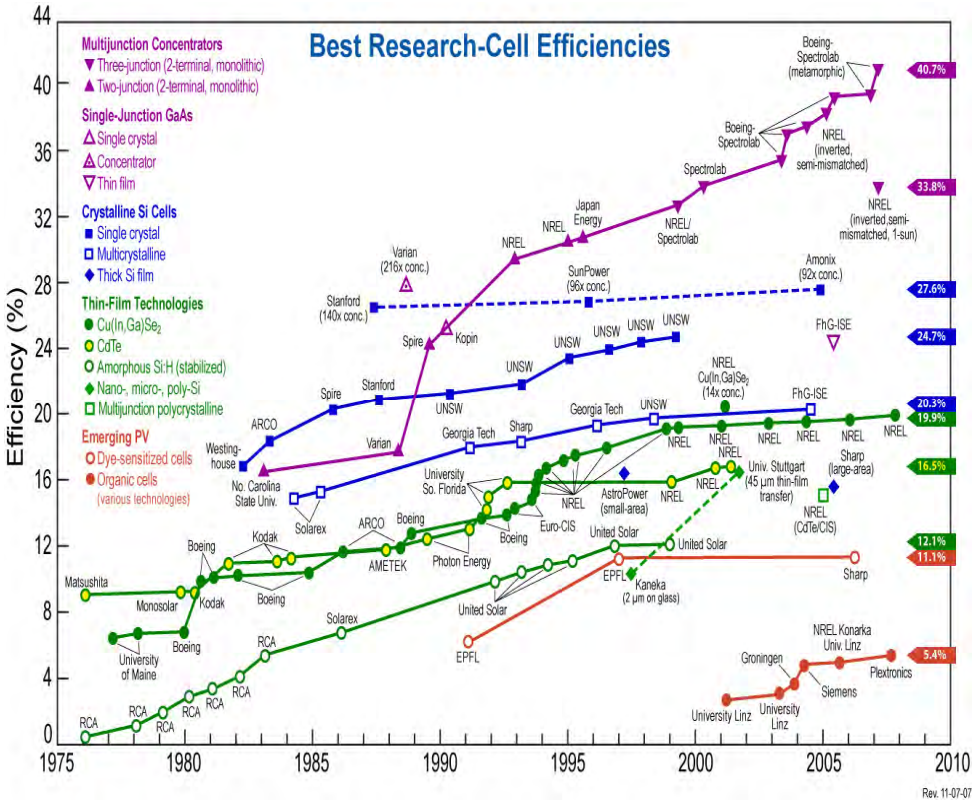

Figure 1.3 Electrical energy conversion efficiencies of different types of PV cells (Kazmerski, 2008)

1.2.4 Fill Factor

The "Fill factor" (*FF*) is defined as a ratio of P_m to the product of open circuit voltage (V_{oc}) and short circuit current (I_{sc}) that determines actual performance of the solar cell given by equation 1.1.

$$FF = \frac{P_m}{V_{OC} I_{SC}} \tag{1.1}$$

FF decreases with increasing series resistance. Series resistance depends strongly on temperature, *T* and weakly on *G* so indirectly *FF* is a weak function of *G* and strong function of *T* (Nelson, 2003).

1.3 Effect of Temperature on Photovoltaic Power

Effect of temperature on power output and long term stability of PV cells and modules have been widely studied both indoors and outdoors (Radziemska and Klugmann, 2002). The normal operating cell temperature (NOCT) for different cells is very important parameters for the service life of the PV cells and required for design qualification for universally acceptability of the PV and its structural stability to operate in different operating temperature. The NOCT is supplied by the PV manufacturers which normally lies in the range of -40 °C to +85 °C (Suntech, 2007) for crystalline PV cells. Depending on PV cell and encapsulation materials, different responses of PV cells and modules to temperature increase beyond characterization and NOCT have been reported as are described in the following sections.

1.3.1 Crystalline Silicon Photovoltaic Cells

For crystalline silicon PV the influence of temperature and wavelength on electrical parameters of crystalline silicon solar cells and modules are illustrated in figure 1.4. PV voltage decreases while current increases with increasing temperature however the increase in current is much less than the decrease in voltage (Radziemska and Klugmann, 2002).

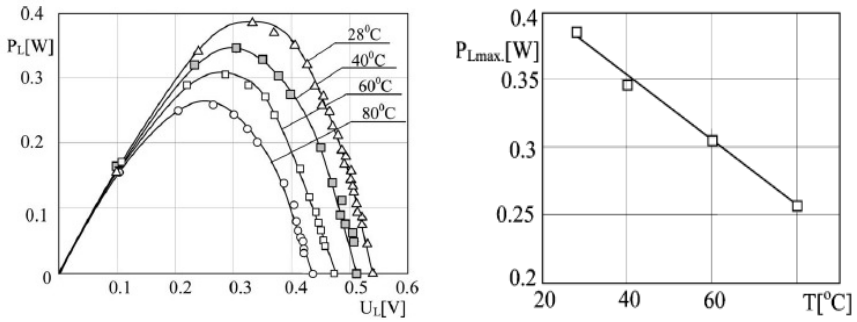

(a) (b)

Figure 1.4 Effect of temperature on power output of the crystalline PV (a) output power against voltage (b) temperature dependence of the maximum output power

Figure 1.4 shows power output for a polycrystalline silicon solar cell with voltage where temperatures range from 28 ºC- 80 ºC. From the figure 1.4 b it is clear that temperature elevation reduces PV power output (Radziemska and Klugmann, 2002). At elevated PV module temperatures reduced power output has been reported for crystalline silicon solar cells with a temperature induced power drop coefficient of -0.5 % $°C^{-1}$ to -0.65 % $°C^{-1}$ (Radziemska, 2003; Breteque, 2009).

1.3.2 Amorphous Silicon Solar Cells

Temperature has a very different effect on the performance of amorphous silicon solar cells. Initially they show decreased power output with increasing temperature (Hoheisel *et al*., 1991) but after prolonged exposure the power output stabilizes due to temperature-induced recovery of the light induced degradation and the efficiency of the cells is stabilized at higher temperatures. (Yoshihiro, and Shingo, 1994; Gottschalg, *et al*., 2005; Shima, *et al*., 2005). The performance of amorphous PV modules with insulated and uninsulated back was monitored for 2 years; the insulated back PV being at 4.2 °C higher temperature than uninsulated back PV produced 7.3 % higher power output for the duration of the experiment (Yamawaki, *et al*., 1997). It has also been demonstrated that for prolonged exposure, performance of amorphous silicon solar cells takes into account of temperature and illumination history of the cells. The cells may respond differently to same temperature and illumination during different seasons of the year as shown in the figure 1.5 (Fukushige *et al*., 2009).

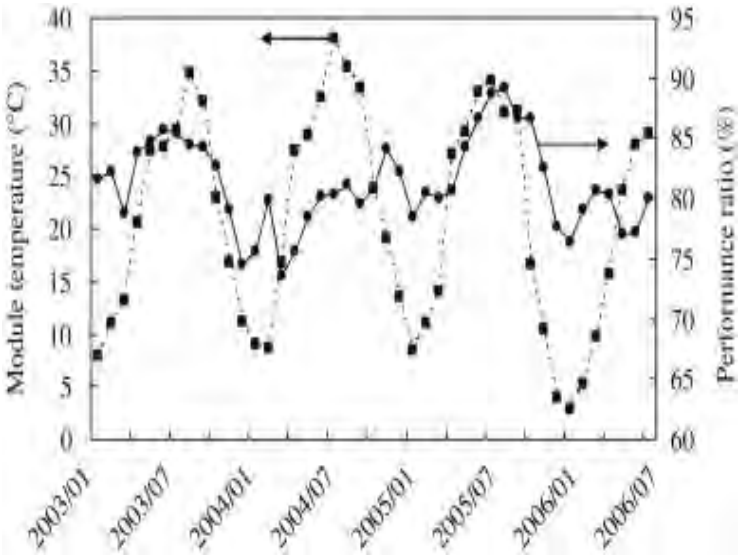

Figure 1.5 Long time performance monitoring of amorphous silicon solar cells showing that the amorphous PV produces different output power during different seasons at same PV temperatures.

1.3.3 GaSb and GaAs Cells

The effect of temperature on electrical output of GaAs and GaSb have been studied between temperature range of 0 °C to 120 °C which showed a power reduction of -0.28 % $°C^{-1}$ and -0.84 % $°C^{-1}$ respectively (Siefer, *et al.*, 2005) due primarily to decreased V_{oc}. A GaAs PV cell produced 80 % of its nominal power at 90 °C (Ferguson and Fraas, 1995).

1.3.4 Dye-Sensitized Solar Cells

Dye sensitized solar cells have been studied at temperatures 5-55 °C. They have shown an increase in power output from lower temperatures up to maximum 40 °C. At temperatures higher than 40 °C, decreased power output with increasing temperature have been observed as shown in figure 1.6 (Berginc *et al*., 2007) . At lower temperatures the current is limited by low diffusion of charge carrier (i.e.tri-iodide) and temperature needs to increase to get higher current. At higher temperatures above 40 °C the recombination losses dominate over diffusion current and the current starts decreasing resulting in decreased power output. The optimum current is achieved at intermediate temperatures which depends on the concentration of the charge carrier (Berginc *et al*., 2008)

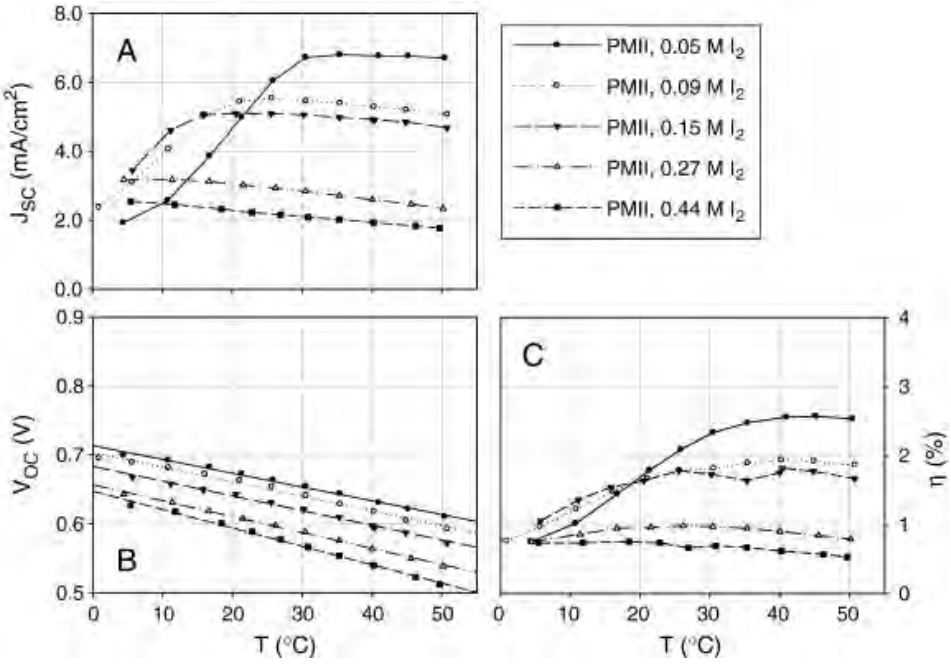

Figure 1.6 Dependence of the V_{oc} and I_{sc} (J_{sc}) on the temperature of dye sensitized cells.

1.3.5 Organic Solar Cells

In polymer-fullerene organic PV cells increasing temperature results in increased current and decreased voltage, however the increase in current is higher than the decrease in voltage resulting in a net increase in power with increasing temperature. Temperature induced increase in power is followed by a saturation limit, primarily due to saturation current normally occurring in the range of 47 °C - 60 °C (Katz, *et al*., 2001; Kumar *et al*., 2007).

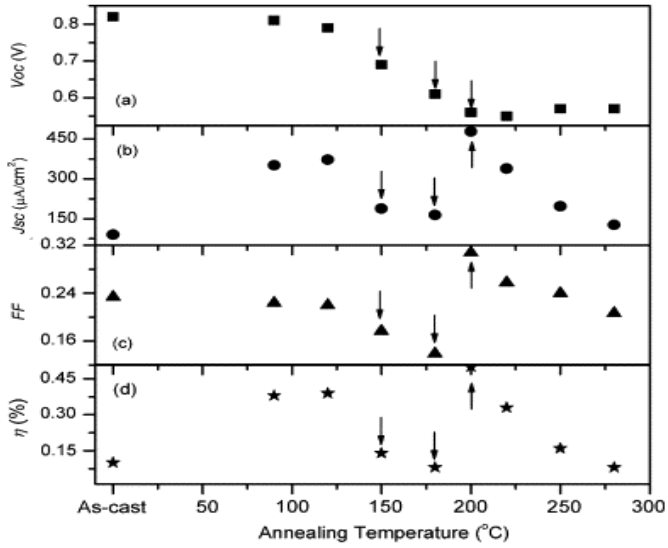

Figure 1.7 Temperature dependence of organic PV cells showing an increase in efficiency (power output) with increasing temperature from 0 °C-120 C, a decrease in efficiency from 120 °C-200 °C, a peak in efficiency at 200 °C and then continued decrease in efficiency from 200 °C -300 °C.

1.3.6 Temperature Induced Structural Damage in Photovoltaic Panels

Crystalline silicon PV exposure to high outdoor temperatures above 85 °C have been reported to induce structural damage in PV panels resulting in moisture ingress, in 17 months (Igari *et al*., 1994). Damage of PV after five years has been reported primarily due to delamination of encapsulating material ethylene-vinyl-acetate (EVA) along with semiconductor degradation resulting in PV power drop of 1 % annually (Berman, *et al*., 1995). In another study a performance degradation of 4.8 % for single crystalline and 2 % for polycrystalline silicon PV has also been reported after five years of outdoor exposure (Machida *et al*., 1997). Moisture ingress results in a reduced active area, corrosion in the metallic contacts, reduced photon absorption leading to reduced charge carrier generation and reduced current resulting in up to a net 14 % drop in power output (Machida, *et al*., 1997; Saly *et al*., 2001; Gxasheka *et al*., 2005).

1.3.7 Outdoor Temperatures Recorded at Photovoltaic Devices

The PV operating temperature depends on the site where they are deployed (Bücher, 1997). The operating temperature of crystalline silicon PV cell considering ambient temperature and solar radiation and module temperature (Mattei, *et al*., 2006) may be calculated from equation 1.2.

$$T_{cell} = \frac{U_{PV} T_{amb} + G[(\alpha_{pv}\tau) - \eta_r - T_c \eta_r T_r]}{U_{PV} - \theta G} \tag{1.2}$$

Where η_r is reference module efficiency, T_r is the PV cell reference temperature

(typically 25 °C), G is the solar irradiance on the module (typically 1000 W m^{-2}), θ is the solar irradiance coefficient of PV power which describes the effect of solar radiation intensity on the PV power, T_c is the temperature coefficient of the PV power which describes the effect of PV temperature on power output of PV module, T_{cell} is PV cell temperature which depends on environmental conditions, U_{PV} is overall heat loss coefficient of PV which considers only convective heat loss ignoring radiative heat loss from the PV panel, α_{pv} is absorptance of PV and τ is transmittance of PV encapsulation. This model assumed that the PV cell and cover have the same temperature while the temperature is uniformly distributed over the PV surface.

Mathematical correlations have shown that the PV operating temperature and associated power drop largely depends on climate where the PV panels are deployed (Skoplaki, and Palyvos, 2009). In Germany 50 % of the solar radiation incident on a PV panel is above 600 Wm^{-2} while in Sudan this value reaches 80 % resulting in different operating temperatures and associated power drop (Bücher, 1997; Emmanuel, 2009). A maximum PV operating temperature of 125 °C has been reported in southern Libya (27.6 N and 14.2 E) resulting in a 69 % reduction in the nominal power (Nassar, *et al.* 2007). The advisable operating temperature limit for PV ranges from -40 °C to 85 °C (Suntechics, 2008), however in hot and arid climates, PV temperature frequently rises above this temperature range (Nassar *et al*. 2007), which results in temperature-induced power failure as well as PV cell delamination and rapid degradation (Saly *et al*., 2001) urging a strong need for PV temperature regulation to maximise both panel lifetime and power output.

1.3.8 Effect of Photovoltaic Building Integration on Photovoltaic Temperature

Integration of the PV into building façades thermally insulates back of PV panel when compared to free standing PV. In a study this thermal insulation has resulted in 20.7 °C increase in PV temperature leading to a 9.3 % decrease in electrical yield of PV façade due solely to its building integration which produces thermal insulation at PV back (Krauter *et al*., 1999). A similar result has been reported by (Tripanagnostopoulos *et al*., 2002) who compared free-back-PV with an insulated-back PV and reported that temperature increased from 43 °C in free back PV to 55 °C in insulated back PV (representing BIPV) resulting in a 9 % decrease in PV efficiency in Greece. In a computational study conducted for weather conditions of Macau, China, a 260 m^2 BIPV wall was modelled and a temperature of 85 °C was predicted on such BIPV system in July (Chow *et al*., 2003). In a separate study, integration of a PV into a building in Mâcon, France was reported to reduce PV annual conversion efficiency by 2.6 %, resulting in PV power drop of 28 % due to increased PV temperature caused by building integration of PV (Fraisse *et al*., 2007)

1.4 Cooling of Photovoltaic Devices

Different passive and active heat removal techniques have been used to maintain PV at low temperatures. Passive heat removal in free standing PV relies on the buoyancy driven air flow in a duct behind the PV. Active cooling of PV relies on air or water flow on the front or back of the PV surface.

1.4.1 Passive Cooling by Arranging a Duct Behind Photovoltaics

This passive technique is the most conventional for PV cooling and employs a duct with length L behind the PV installed at an angle θ to the horizontal as shown in figure 1.8. The incident thermal energy q is removed by the buoyant circulation of air moving with velocity u acting as heat transfer fluid to regulate PV temperature., effect of which has been studied and a temperature decrease of 20 °C has been reported by heat removal due to buoyancy driven air flow (Brinkworth *et al*., 1997). A design parameters study of the duct found that cooling of PV is enhanced significantly due to wind which increases the heat loss from the PV front surface and increases the air flow into the duct (Brinkworth, 2000). Optimisations of cooling ducts have found that the ratio of duct length to the hydraulic depth of 20 gives the optimal cooling of the PV (Brinkworth and Sandberg, 2006) with the ratio not being affected significantly by the slope of the PV array.

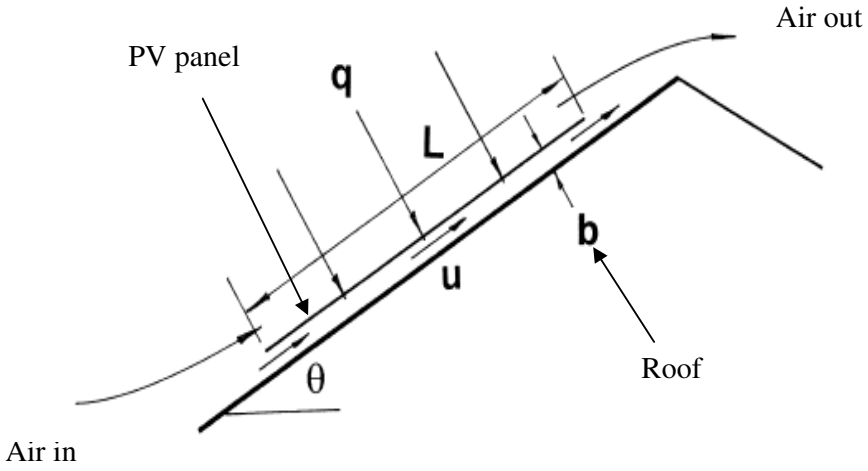

Figure 1.8 Schematic diagram of a duct behind PV (Brinkworth, B. J. and Sandberg, M., 2006)

1.4.2 Air Gap Ventilation of Building Integrated Photovoltaics

Passive heat removal in building integrated photovoltaics (BIPV) relies on buoyant circulation of air in an open air channel behind the PV (Sandberg and Moshfegh, 1998; Gan, and Riffat, 2004; Lee, *et al*., 2009). A theoretical analysis of buoyancy driven air flow in such a design showed a maximum 5 °C temperature reduction in averaged monthly temperature resulting in a net 2.5 % increase in yearly electrical output of the PV (Yun *et al*., 2007).

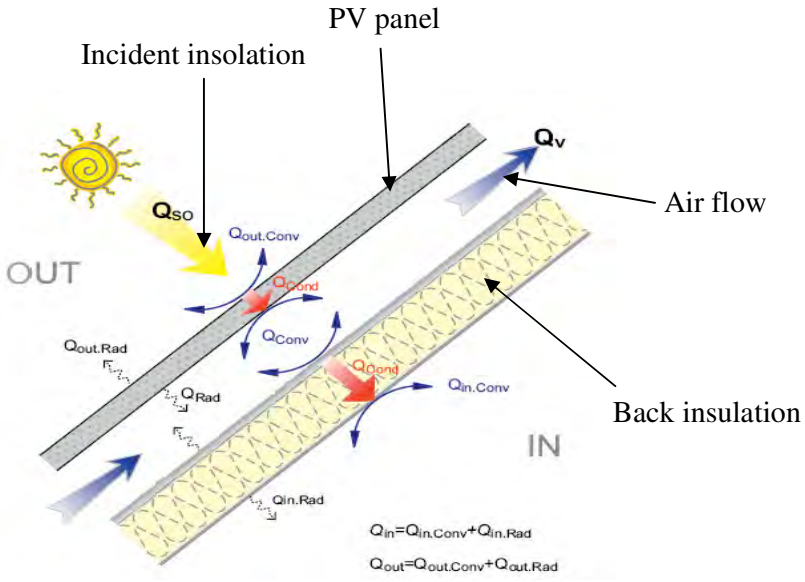

Figure 1.9 Schematic diagram of a ventilated roof (Lee *et al*., 2009)

Effect of air flow at (i) different inlet velocities (ii) front and (iii) back air gaps in PV was modelled and a maximum 34.2 °C front surface temperature decrease was predicted at air inlet velocity of 1 ms^{-1} at front and back air gap of 20 mm (Mallick *et al*., 2007). Though the temperature reduction and the associated prevention of power

drop is very low in such PV systems, improvements can be made in the air channel by (i) suspending metal sheets (ii) inserting fins and (iii) optimising distance between the walls (Fossa *et al*., 2008). A ventilated façade has been recently reported by numerical simulations to achieve a maximum of 40 % net electrical and thermal energy savings in summer times due to PV cooling (Patania *et al*., 2010).

1.4.3 Hybrid Photovoltaic Thermal Systems

A hybrid PV-T façade element combined with active water cooling has achieved a temperature decrease of 20 °C and an electrical power improvement of 9 % (Krauter *et al*., 1999). The temperature of the PV applying PV-T with air and water has been reported to drop from 55 °C to 41 °C and 38 °C respectively yielding an 11 % and 13.3 % increase in efficiency respectively (Tripanagnostopoulos *et al*., 2002).

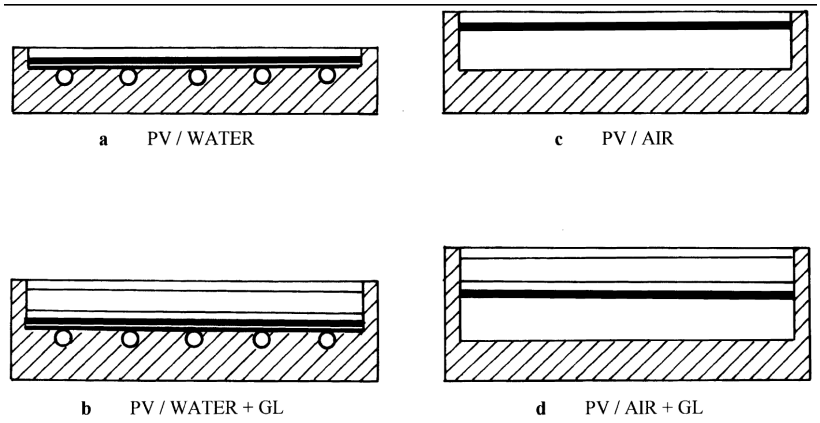

Figure 1.10 Schematic diagrams of a typical PV-T commonly used, (a) unglazed PV-T with water as coolant (b) glazed PV-T with water as coolant (c) unglazed PV-T with air as coolant (d) glazed PV-T with air as coolant.

Although PV-T achieved higher temperature reduction and power output than PV alone, in summer when there is no heating demand, heat insulation effect on the back of PV results in increased PV temperatures above 100 °C. At this higher temperatures PV shows structural damage as the EVA in the PV modules can not withstand this temperature for prolonged exposure (Fraisse *et al*., 2007) which finally reduced the PV life. Low cost improvement have been suggested in air cooled PV-T by inserting fins and thin metal sheets (TMS) in the air channel to avoid over heating in summer as shown in Figure 1.11 (Tonui and Tripanagnostopoulos, 2007). A review of PV/T systems have been made which describes the types of PV-T systems based on their design and heat transfer fluid, their different design parametric studies, their effectiveness in different operating conditions through experimental and modelling work (Charalambous *et. al,* 2007)

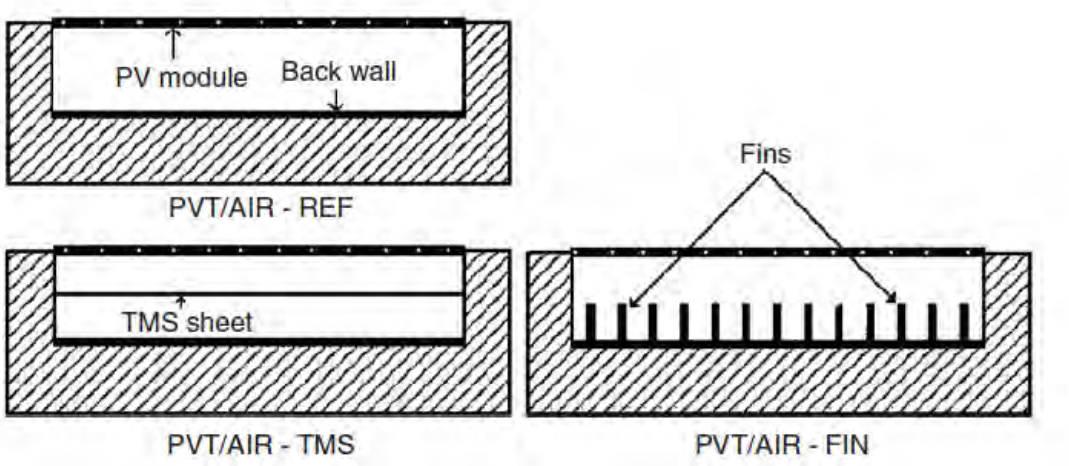

Figure 1.11 Cross section view of air cooled PV-T collector showing reference PV-T, PV-T with thin metal sheets (TMS) and PV-T with fins arrangement.

1.4.4 Hydraulic Cooling of Photovoltaics

Hydraulic water flow over the front surface of the PV can decrease the cell temperature by up to 22 °C and can improve electrical output by 10 % after subtracting the power consumed by pump; however the initial and maintenance costs for the pump were ignored (Krauter, 2004).

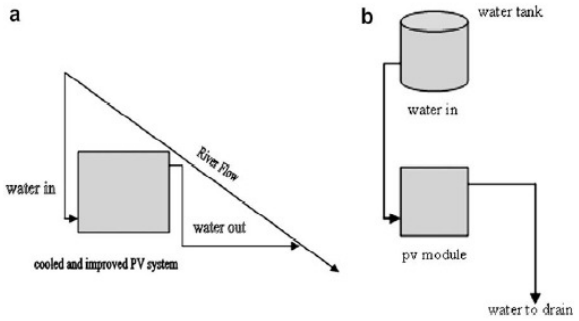

Diagram 1. A. Proposed cooling system. B. Simulated system.

Figure 1.12 Schematic of a gravity fed water cooling technique (Wilson, 2009)

A gravity fed water cooling technique has also been devised which has theoretically reduced PV cell temperature by 28 °C due to water cooling from initial 62 °C (Wilson, 2009). Although such systems are cost effective and simple, at higher temperature regions a very high water flow rate is needed which increases the pumping power and capital investment.

1.5 Research Aims and Proposed Methodology

Part of the energy carried in solar radiations falling on the PV surface is reflected back from the PV surface while most of it is absorbed in the PV. A certain part of the absorbed energy corresponding to the PV conversion efficiency is converted into electricity while the rest transformed to thermal energy. The absorbed thermal energy increases the PV temperature which has a strong negative impact on the electrical output of the PV as well as on their long-term operation reliability which urges the need of PV temperature regulation. Previous research on temperature regulation of PV to prevent temperature dependent power drop have applied different active and passive cooling techniques however almost each of the techniques is restricted by one or the other factors like (i) high initial costs, (ii) operation and maintenance costs, (iii) low heat removal rate and (iv) inability to produce cooling in higher temperature summer environments.

A novel PV cooling technique using solid-liquid phase change materials (PCM) to overcome the above stated limitations was employed by (Huang *et al*., 2004, 2006a, 2006b). The solid liquid PCM can absorb large amount of latent heat while melting at a constant temperature and regulate PV temperature close to their characterization temperature.

The detailed energy flows in such a PV-PCM systems are shown in Figure 1.13. The technique can combine the benefits of high heat transfer rates achievable in active heat dissipation systems and low operating and capital costs achievable in passive systems. Incorporating PCM with PV to form a PV-PCM system may enable PV to achieve energy conversion efficiencies closer to those at the standard cell

characterisation condition of 25°C. Additionally the large amount of heat stored as latent heat in PCM can potentially be used for further applications of water or space heating converging to a new type of PV-T system.

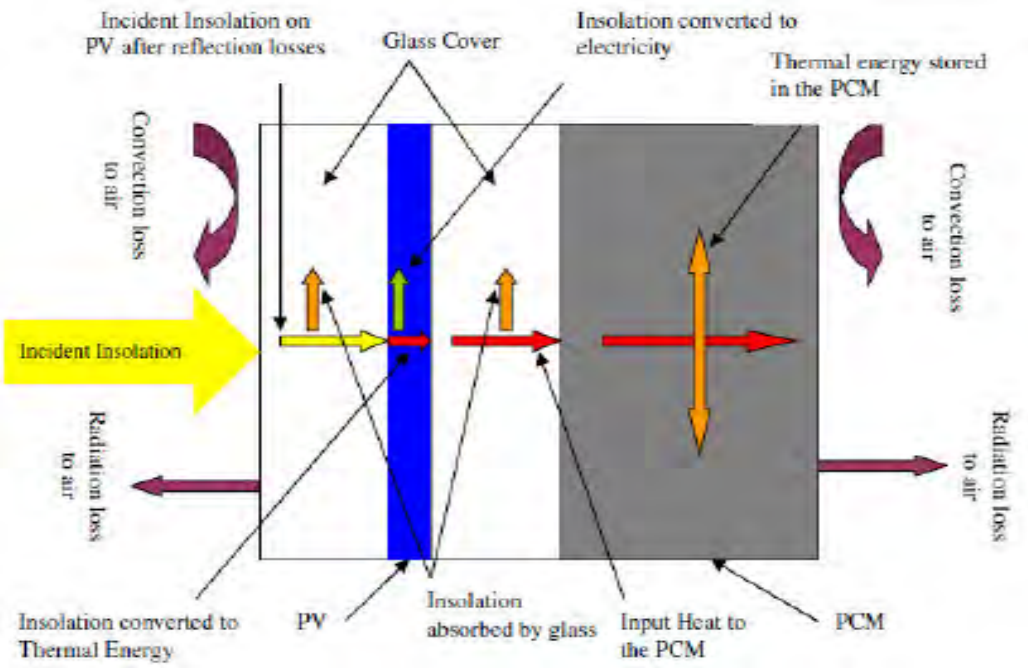

Figure 1.13 The schematic diagram of the energy flow in the PV-PCM system under investigation

In previous research a rectangular container of dimensions 30 cm x 13.2 cm x 4 cm fitted with aluminium fins with front side selectively coated containing PCM was studied (Huang *et al.*, 2004). The fabricated PV-PCM system was evaluated numerically with a 2D finite volume heat transfer model that was validated experimentally with paraffin wax RT25 as PCM located behind a PV (Huang *et al.*, 2006a). For 3D heat transfer analysis, a small scale 3D model was developed and validated with the experimentally-validated 2D model (Huang *et al.*, 2006b).

Aim of the current research is to experimentally investigate the PV cooling technique introduced by Huang *et al.* extending its use to (i) identify and thermophysically characterize new PCMs for their suitability for PV cooling applications (ii) experimentally evaluate the new PCMs indoors with different PV-PCM system configurations at various solar radiation intensities to adopt PV-PCM systems for different weather conditions in order to identify suitable PCM and PV-PCM system (iii) Integrate the optimum PCM into large scale PV panel size system with optimum PV-PCM configurations, measure PV temperature regulation achieved by PCM and quantify the increased electrical output brought about by PV cooling indoors (iv) Evaluate the PV cooling and increased electrical output through use of the novel PV-PCM system outdoors by extensive experimentation in different climates i.e. (i) high latitude cooler climate and (ii) low latitude hotter climate.

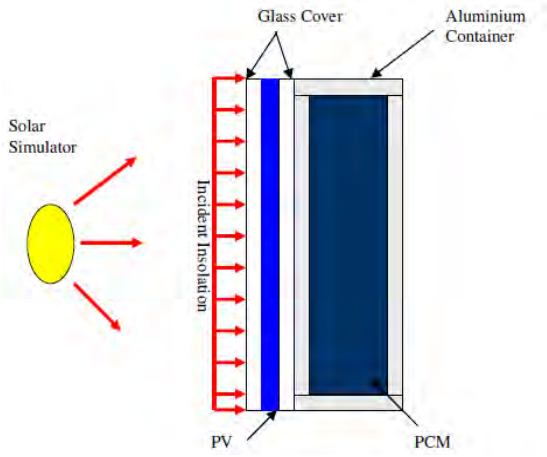

Figure 1.14 Schematic diagram of the experimental setup consisting of a PV cell attached at the front surface of an aluminium container filled with PCM.

In the present work instead of coated aluminium plate, actual PV cells were attached to the front surface of small cell size (10 cm x 10 cm x 5cm) PV-PCM systems shown in Figure 1.14 (Hasan *et al*., 2010).

Five different PCMs, paraffin wax RT20 (Rubitherm, 2009), salt hydrate $CaCl_2.6H_2O$ (Sigmaaldrich, 2009 a), mixture of salt hydrate and paraffin wax SP22 (Rubitherm, 2009), eutectic mixture of fatty acids, capric acid-lauric acid (CL) (Sigmaaldrich, 2009 b), and eutectic mixture of fatty acids, capric acid-palmitic acid (CP) (Sigmaaldrich, 2009 c), were studied in four different cell size PV-PCM systems. Extensive indoor experiments were conducted to determine thermal regulation of PV indoors at 500 Wm^{-2}, 750 Wm^{-2} and 1000 Wm^{-2} solar radiation intensities to optimise the PV-PCM system. The best PV-PCM system (system A detailed in chapter 4) and the best PCM (CP and $CaCl_2.6H_2O$ detailed in chapter 4) were identified small scale cell size indoor experiments.

The best PV-PCM system (A) was fabricated at a larger PV panel scale (70 cm x 60 cm x 5 cm) consisting of PV panel, PCM container fitted with straight back to back aluminium fins and two PCM contained in the PV-PCM system. These PV-PCM systems were evaluated indoors with a large scale solar simulator at solar radiation intensities of 500 $W^{-}m^{2}$, 750 Wm^{-2} and 1000 Wm^{-2}. Temperatures and electrical parameters of PV were measured to quantify thermal regulation of PCM and the associated improvement in power output.

The PV-PCM systems were then installed outdoors in high latitude cooler climatic conditions of Dublin, (53.33 N, 6.24 W) Ireland from 28-08-2009 to 15-09-2009 and in low latitude warmer climates of Vehari, (30.03 N, 72.25 E) Pakistan from 25-10-2009- 13-11-2009. Temperature and electrical parameters were measured at both

locations applying the same experimental setup and measurement procedures. It was found that such systems achieved higher temperature regulations and greater associated power increase in a warmer climate. In the best case a 21.5 °C peak temperature reduction was recorded with a predicted peak PV power saving of 14 % in Vehari, Pakistan

1.6 References

ASTM G 173-03 (2003). "Standard Tables for Reference Solar Spectral Irradiances, Direct Normal and Hemispherical on 37° Tilted Surface." ASTM International, http://rredc.nrel.gov/solar/spectra/am1.5/ last visited 03.06.2010

Berginc, M., Krasovec, U.O., Jankovec, M. and Topic, M. (2007). "The effect of temperature on the performance of dye-sensitized solar cells based on a propyl-methyl-imidazolium iodide electrolyte." Solar Energy Materials and Solar Cells 91(9): 821-828.

Berginc, M., Krasovec, U.O., Hocevar, M. and Topic, M. (2008). "Performance of dye-sensitized solar cells based on Ionic liquids: Effect of temperature and iodine concentration." Thin Solid Films 516(20): 7155-7159.

Berman, D., Biryukov, S. and Faiman, D. (1995). "EVA laminate browning after 5 years in a grid-connected, mirror-assisted, photovoltaic system in the Negev desert: effect on module efficiency." Solar Energy Materials and Solar Cells 36(4): 421-432.

Breeze, P. (2005). Power generation technologies. Burlington, USA, Newnes/Elsiver.

Brinkworth, B, J., Cross, B, M., Marshall, R, H. and Yang, H (1997). "Thermal regulation of photovoltaic cladding". Solar Energy 61 (3): 169-178

Brinkworth, B. J. (2000). "A procedure for the routine calculation of laminar free and mixed convection in inclined ducts." International Journal of Heat and Fluid Flow 21(4): 456-462.

Brinkworth, B. J. and Sandberg, M. (2006). "Design procedure for cooling ducts to minimise efficiency loss due to temperature rise in PV arrays." Solar Energy 80(1): 89-103.

Bücher, K. (1997). "Site dependence of the energy collection of PV modules." Solar Energy Materials and Solar Cells 47(1): 85-94.

Charalambous, P.G, Maidment, G.G, Kalogirou, S.A and Yiakoumetti, K. (2007). "Photovoltaic thermal (PV/T) collectors: A review." Applied Thermal Engineering 27 (2-3): 275–286.

Chow, T. T., Hand, J. W. and Strachan, P. A. (2003). "Building-integrated photovoltaic and thermal applications in a subtropical hotel building." Applied Thermal Engineering 23(16): 2035-2049.

Breteque, E A.de.la. (2009). "Thermal aspects of c-Si photovoltaic module energy rating." Solar Energy 83(9): 1425-1433.

Ferguson, L. G. and Fraas, L. M. (1995). "Theoretical study of GaSb PV cells efficiency as a function of temperature." Solar Energy Materials and Solar Cells 39(1): 11-18.

Fossa, M., Ménézo, C. and Leonardi, E. (2008). "Experimental natural convection on vertical surfaces for building integrated photovoltaic (BIPV) applications." Experimental Thermal and Fluid Science 32(4): 980-990.

Fraisse, G., Ménézo, C. and Johannes, K. (2007). "Energy performance of water hybrid PV/T collectors applied to combisystems of Direct Solar Floor type." Solar Energy 81(11): 1426-1438.

Fukushige, S., Ichida, K., Minemoto, T. and Takakura, H . (2009). "Analysis of the temperature history of amorphous silicon photovoltaic module outdoors." Solar Energy Materials and Solar Cells 93(6-7): 926-931.

Gan, Guohui and Riffat, Saffa B. (2004). "CFD modelling of air flow and thermal performance of an atrium integrated with photovoltaics." Building and Environment 39(7): 735-748.

Gangadhar, R. B. and Bhattacharyya, A. B. (1968). "Drift-field photovoltaic cell performance with bulk and surface recombinations" International Journal of Electronics 25(1): 17 - 26.

Goswami, D.Y. (2007). Energy: "The Burning Issue". Refocus 8 (1): 22-25..

Gottschalg, R., Betts, T. R., Infield, D. G. and Kearney, M. J. (2005). "The effect of spectral variations on the performance parameters of single and double junction amorphous silicon solar cells." Solar Energy Materials and Solar Cells 85(3): 415-428.

Gxasheka, A. R., van Dyk, E. E. and Meyer, E. L. (2005). "Evaluation of performance parameters of PV modules deployed outdoors." Renewable Energy 30(4): 611-620.

Hasan, A., McCormack, S.J., Huang, M.J. and Norton, B. (2010). "Evaluation of phase change materials for thermal regulation enhancement of building integrated photovoltaics." Solar Energy doi:10.1016/j.solener.2010.06.010.

Hoheisel, M., Reichle, E., Harms, H. and Kotschy, J. (1991). "Temperature dependence of the photocurrent in pin and nip solar cell structures made from a-Si:H." Journal of Non-Crystalline Solids 137-138(2): 1181-1184.

Huang, M. J., Eames, P. C. and Norton, B. (2004). "Thermal regulation of building-integrated photovoltaics using phase change materials." International Journal of Heat and Mass Transfer 47(12-13): 2715-2733.

Huang, M. J., Eames, P. C. and Norton, B. (2006). "Comparison of a small-scale 3D PCM thermal control model with a validated 2D PCM thermal control model." Solar Energy Materials and Solar Cells 90(13): 1961-1972.

Huang, M. J., Eames, P. C. and Norton, B. (2006). "Phase change materials for limiting temperature rise in building integrated photovoltaics." Solar Energy 80(9): 1121-1130.

IEA. (2009 a). "Key World Energy Statistics 2009". www.iea.org/Textbase/stats/." Retrieved 03/06/2010.

IEA. (2009 b). "CO2 emissions from Fuel Combustion 2009". www.iea.org/Textbase/stats/." Retrieved 03/06/2010.

Igari, S., Nose, J., Hiruma, T., Nagamine, F. and Fujisawa, K. (1994). "Accelerated degradation test method for a-Si PV modules." Solar Energy Materials and Solar Cells 34(1-4): 473-483.

Katz, E. A., Faiman, D., Tuladhar, S. M., Kroon, J. M., Wienk, M. M., Fromherz, T., Padinger, F., Brabec, C. J. and Sariciftci, N. S. (2001). "Temperature dependence for the photovoltaic device parameters of polymer-fullerene solar cells under operating conditions." Journal of Applied Physics 90(10): 5343-5350.

Krauter, S, Arau´jo, R.G., Schroer, S, Hanitsch, R., Salhi, M.J, Triebel, C. and Lemoine, R. (1999). “Combined photovoltaic and solar thermal systems for facade integration and building insulation" Solar Energy 67 (4-6): 239-248.

Krauter, S. (2004). "Increased electrical yield via water flow over the front of photovoltaic panels." Solar Energy Materials and Solar Cells 82(1-2): 131-137.

Kreith, F. and Goswami, D.Y. (2007). Handbook of energy efficiency and renewable energy. Taylor & Francis Group, CRC Press, USA..

Kumar, P., Jain, S. C., Kumar, V., Misra, A., Chand, S. and Kamalasanan, M. N. (2007). "Current-voltage characteristics of an organic diode: Revisited." Synthetic Metals 157(22-23): 905-909.

Lee, S., Park, S. H., Yeo, M. S. and Kim, K. W. (2009). "An experimental study on airflow in the cavity of a ventilated roof." Building and Environment 44(7): 1431-1439.

Lorenzo, E. (1994). "Solar Electricity: Engineering of Photovoltaic Systems." Universidad Politecnica Madrid, Progensa, Spain.., ISBN: 8486505550 ISBN-13: 9788486505554.

Lu, F.H. (1996). "Loss minimization through recombination centre identification in solar cells." Physica status solidi. B. Basic research 194(1): 91-100.

Luque, A and Hegedus, S. (2003). "Handbook of Photovoltaic Science and Engineering." John Wiley and Sons. ISBN 0471491969

Machida, K., Yamazaki, T. and Hirasawa, T. (1997). "Secular degradation of crystalline photovoltaic modules." Solar Energy Materials and Solar Cells 47(1-4): 149-153.

Mallick, T. K., Eames, P. C. and Norton, B. (2007). "Using air flow to alleviate temperature elevation in solar cells within asymmetric compound parabolic concentrators." Solar Energy 81(2): 173-184.

Mattei, M., Notton, G., Cristofari, C., Muselli, M. and Poggi, P. (2006). "Calculation of the polycrystalline PV module temperature using a simple method of energy balance." Renewable Energy 31(4): 553-567.

Morton, O. (2006). "Solar energy: A new day dawning? Silicon Valley sunrise." Nature 443: 19-22.

Nassar, Yasser Fathi and Salem, Abubaker Awidat (2007). "The reliability of the photovoltaic utilization in southern cities of Libya." Desalination 209(1-3): 86-90.

Nelson, J. (2003). "The Physics of Solar Cells." Imperial College Press. ISBN 978-1-86094-340-9.

NREL (2007). "Solar Spectral Irradiance: Air Mass 1.5". National Renewable Energy Laboratory." http://rredc.nrel.gov/solar/spectra/am1.5/ Last visited 03.06.2010.

Kazmerski, L. (2008). "Highest reported PV cell Efficiencies" NREL. http://en.wikipedia.org/wiki/File:PVeff(rev100414).png#filelinks. Last visited 18.07.2010.

Patania, F., Gagliano, A., Nocera, F., Ferlito, A. and Galesi, A. (2010). "Thermofluid-dynamic analysis of ventilated facades." Energy and Buildings 42 (7): 1148-1155.

Radziemska, E. (2003). "The effect of temperature on the power drop in crystalline silicon solar cells." Renewable Energy 28(1): 1-12.

Radziemska, E. and Klugmann, E. (2002). "Thermally affected parameters of the current-voltage characteristics of silicon photocell." Energy Conversion and Management 43(14): 1889-1900.

Saly, V., Ruzinsky, M. and Redi, P. (2001). "Indoor study and ageing tests of solar cells and encapsulations of experimental modules" . 24th International Spring Seminar on Electronics Technology, May 5-9, Calimanesti-Caciulata, Romania: 59-62.

Sandberg, M. and Moshfegh.B (1998). "Ventilated-solar roof air flow and heat transfer investigation." Renewable Energy 15(1): 287-292 Shima, M., Isomura, M., Wakisaka, K., Murata, K. and Tanaka, M. (2005). "The influence of operation temperature on the output properties of amorphous silicon-related solar cells." Solar Energy Materials and Solar Cells 85(2): 167-175.

Siefer, G., Abbott, P., Baur, C., Schlegl, T. and Bett, A.W. (2005). "Determination of the temperature coefficients of various III-V solar cells." Proceedings of 20th European Photovoltaic Solar Energy Conference: Barcelona, 6-10 June: 495-498

Skoplaki, E. and Palyvos, J. A. (2009). "Operating temperature of photovoltaic modules: A survey of pertinent correlations." Renewable Energy 34(1): 23-29.

Suntechics (2008). Product Mannual, Suntechnich STP065-12/Sb PV Panel

Tripanagnostopoulos, Y., Nousia, T., Souliotis, M. and Yianoulis, P. (2002). "Hybrid photovoltaic/thermal solar systems." Solar Energy 72(3): 217-234.

Wilson, E. (2009). "Theoretical and operational thermal performance of a wet crystalline silicon PV module under Jamaican conditions." Renewable Energy 34(6): 1655-1660.

Würfel, P. (2005). "Physics of solar cells, from basic principles to advanced concepts." Wiley-VCH, Weinheim: ISBN 3-527-40428-7.

Yamawaki, T., Mizukami, S., Yamazaki, A. and Takahashi, H. (1997). "Thermal recovery effect on light-induced degradation of amorphous silicon solar module under the sunlight." Solar Energy Materials and Solar Cells 47(1-4): 125-134.

Yang, W. J., Ma, Z. Q., Tang, X., Feng, C. B., Zhao, W. G. and Shi, P. P. (2008). "Internal quantum efficiency for solar cells." Solar Energy 82(2): 106-110.

Yoshihiro, H. and Shingo, O. (1994). "Dependence of the I-V characteristics of amorphous silicon solar cells on illumination intensity and temperature." Solar Energy Materials and Solar Cells 33(2): 157-168.

Yun, G. Y., McEvoy, M. and Steemers, K. (2007). "Design and overall energy performance of a ventilated photovoltaic façade." Solar Energy 81(3): 383-394.

2 INTRODUCTION TO PHASE CHANGE MATERIALS

Different types of phase change materials (PCM) are summarised along with their advantages and disadvantages. An overview is provided of research on the thermophysical properties of PCM. The fundamentals of modelling solid-liquid phase changes are reported together with major applications of PCMs.

2.1 Phase Change Mechanism

On application of heat, the internal energy of a solid is increased to a specific melting point at which it becomes a liquid. In pure materials liquefaction/solidification occurs at the distinct temperature T_m, which is known as equilibrium temperature of melting/freezing. This temperature depends solely on pressure and is constant if melting/solidification proceeds at a slow rate. In this case no curvature of the solid-liquid interface is present and no significant difference in specific heats between phases exists. For phase transformation occurring at the equilibrium temperature, the latent heat of melting corresponds to difference of the products of solid and liquid phase densities and specific enthalpies at the temperature T_m (Banaszek *et al*., 2005). Phase change materials (PCM) absorb or releases large amount of heat at constant phase transition temperature when they undergo phase change as shown in Figure 2.1.

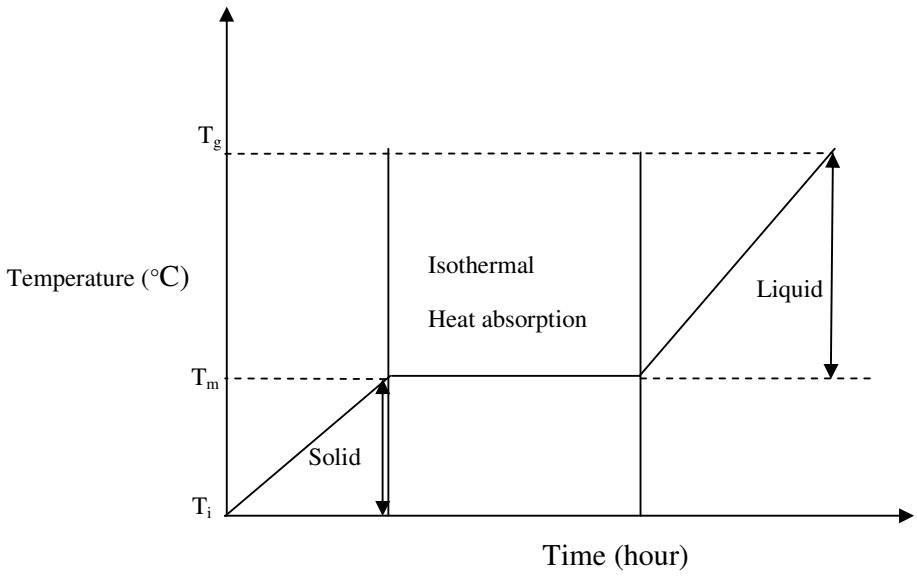

Figure 2.1 Theoretical phase change diagram of solid-liquid phase change materials.

PCM exhibit solid-liquid, liquid-gas phase change and vice versa. Although liquid-to gas phase change also involves heat absorption, yet they show large volume changes during phase change. Thus to exploit the heat from liquid-gas phase change, very large containment volumes are required. Solid-liquid PCM are particularly promising as they show very little volume change during phase change which enables heat to be stored in a smaller volume.

Absorption of a large amount of heat at constant temperature during phase change is one of the main advantages of PCM. The isothermal nature of heat absorption and release shown in figure 2.1 renders PCM a suitable candidate for thermal energy storage and temperature control applications.

2.2 Classification of Phase Change Materials

PCM are classified as organic, inorganic and eutectic mixtures. Organic PCM consist of paraffin wax and fatty acids, inorganic PCM consist of salt hydrates and eutectic PCM consist of both organic and inorganic materials. The advantages and disadvantages of each of the PCM class are summarised in table 2.1.

	Organic	Inorganic	Eutectics
Advantages	• Availability in a large temperature range • Freeze without much super cooling • Ability to melt congruently • Self nucleating properties • Compatibility with conventional material of construction • No segregation • Chemically stable • High heat of fusion • Safe and non-reactive • Recyclable	• High volumetric latent heat storage capacity • Low cost and easy availability • Sharp melting point • High thermal conductivity • High heat of fusion • Low volume change • Non-flammable	• Eutectics have sharp melting point similar to pure substance • Volumetric storage density is slightly above organic compounds
Disadvantages	• Low thermal conductivity in their solid state. High heat transfer rates required during the freezing cycle • Volumetric latent heat storage capacity is low • Flammable. This can be easily alleviated by a proper container • Due to the cost consideration only technical grade paraffins may be used which are essentially paraffin mixture and are completely refined of oil	• Change of volume is very high • Super cooling is major problem in solid-liquid transition • Nucleating agents are needed and they often become imperative after repeated cycling • Corrosion causes damage to containment materials and reduces the life of containers • Severe dehydration during thermal cycling yields mass loss, increase in melting point and decrease in latent heat.	• Only limited data is available on thermo-physical properties as the use of this materials are very new to thermal storage application

Table 2.1 Summary of advantages and disadvantages of different types of phase change materials (Sharma *et al*, 2004; Sharma, 2005, Sharma *et al*. 2009)

2.3 Thermophysical Properties of Phase Change Materials

Fatty acids, myristic acid, palmitic acid and stearic acid having melting temperature ranges of 50 °C-70 °C have been investigated for thermal energy storage (Hasan and Sayigh, 1994). Their densities and dilation volumes were measured using dilatometry techniques and thermal cycling properties were measured using differential scanning calorimetry. It was found that fatty acids were stable to thermal cycling showing little change in melting points and heat of fusion. Thermal properties of binary and ternary mixtures of palmitic acid, stearic acid and oleic acid have also been measured. It has been reported that a reversible solid-solid phase change in oleic acid occurs before melting and a liquid-liquid phase change before solidification (Cedeño *et al.*, 2001) . The thermal properties of capric acid, lauric acid and pentadecane mixtures have been measured and their use was evaluated for cooling applications (Dimaano and Watanabe, 2002). An improvement in the melting characteristics of capric-lauric acid mixture was observed by addition of 10 % pentadecane to the mixture (Dimaano and Watanabe, 2002).

The total melting and solidification time and the effect of Reynolds and Stefan number on the phase transition behaviour of encapsulated eutectic mixtures of lauric and stearic acids have been described (Sari and Kaygusuz, 2002). Corrosion and thermal stability of stearic, palmitic, myristic and lauric acid were investigated for metallic containment while subjecting them to thermal cycling (Sari and Kaygusuz, 2003; Sari *et al.*, 2004). It was concluded that palmitic and myristic acid may be suited for long-term thermal energy storage with respect to thermal cycling. Stainless steel with chromium oxide (Cr_2O_3) and aluminium with aluminium oxide (Al_2O_3) were found compatible with fatty acids with respect to corrosion. Thermal conductivity of PCM may be enhanced using expanded graphite and carbon fibre. A

linear increase in thermal conductivity of PCM with increasing mass fraction of expanded graphite and carbon fibre has been reported (Karaipekli *et al.*, 2007).

Paraffin wax has been used in a spiral thermal energy storage unit and its melting characteristics were monitored (Banaszek *et al.*, 1999). It was concluded that paraffin melts and solidifies over a range of temperatures and it is difficult to separate sensible and latent heat effects which lead to time changes in melting and solidification. The heat transfer characteristics of paraffin wax in granules of 1-3 mm diameter have been described (Nagano *et al.*, 2004) and the temperature variations in the melting PCM measured. When preparation of stabilized composites of paraffin with high density polythene and expanded graphite was investigated (Sari, 2004), it was found that the thermal conductivity of the composite can be increased by 14%-24% by addition of 3 % expanded graphite. Thermal conductivity improvement of paraffin waxes using graphite matrix has also been reported (Mills *et al.*, 2006). Heating and cooling time of aluminium foam filled with PCM were reported to increase as a function of surface area density of the aluminium foam (Hong and Herling, 2006; Sarier and Onder, 2007).

2.4 Modelling of Phase Change Materials

Modelling of phase change phenomena is one of the most important contemporary research activities. The phase change mechanism occurs in number of natural and industrial processes which have significant environmental and financial impact. As the variety of process involving phase change is increasing, so is the scope and complexity of modelling. The natural process involving solid-liquid phase change comprises but not limited to melting of ice on the glaciers due to varying weather conditions which is becoming increasingly important area of research to observe the

effects of green house gas emissions. The accurate modelling of the phenomena may bring understanding about the future aspects of the issue and may guide humanity to take appropriate measures to avoid future disasters. In industrial processes the processing of materials in foundry and semiconductor industry is taking much importance in the present day sciences. Certain measurement constraints involved in studying the behaviour of materials during solidification in high temperature regimes have increased the importance of precise prediction of such phenomena through modelling. Very careful modelling of phase change can predict the behaviour of materials during cooling and solidification which can other wise be either impossible to measure or is very costly and time consuming thus bringing a huge saving of time and cost. Having obtained precise understanding of the solidification phenomena through predictive modelling tools such materials can be manipulated to obtain desired material properties and purity grades. The recent modelling activities in the area of PCM for energy storage and temperature regulation applications are reviewed below:

Control volume two-dimensional numerical models based on local energy balances and an enthalpy based approach has been developed. Heat transfer and solid liquid phase transition phenomena were studied in a PCM–air spiral thermal energy storage system (Banaszek *et al.*, 2000). The effects of fluid motion, turbulence of air, curvature of air passage and free convection in melting wax were accounted for by boosting heat transfer coefficients. The melting behaviour of PCM by free convection in concentric annuli of different shapes has been numerically described by a finite element computational model (Khillarkar *et al.*, 2000). A finite element semi-analytical model was developed to investigate PCM potential for air conditioning applications (Vakilaltojjar and Saman, 2001). An effective specific heat capacity

approach was used (Roy and Avanic, 2001a, 2001b) to study heat transfer in phase change suspensions in a circular duct. The effect of tube length and bulk Stefan number on laminar and turbulent flow with constant heat flux were described.

An effective specific heat capacity model was developed to enhance forced convective heat transfer in microencapsulated phase change slurries (Hu and Zhang, 2002). It was observed that the conventional Nusselt number correlations used to describe heat transfer in single phase fluids were not suitable to accurately describe the heat transfer in the microencapsulated PCM and a modification in the correlations was necessary to study heat transfer. A numerical model for transient natural convection heat transfer with coupled phase change using fixed solution was used (Scanlon and Stickland, 2004) to investigate the melting of lauric acid adopting a non-Boussinesq approach, where the density inversion effects were considered. A fully implicit two dimensional control volume numerical model based on the enthalpy formulation was used (Trp, 2005) to describe transient forced convection heat transfer between the moderate prandtl number heat transfer fluid (HTF) and the tube wall in shell and tube latent heat thermal energy storage. Banaszek *et al.,* 2005 studied the physical phenomena of solidification such as formation of mushy zone, variation of microstructure during solidification and role of convection in growth of solid phase. Mathematical models for dendrites growth, interface tracking method and interface non tracking methods, macroscopic modelling of mushy zone and macroscopic computer simulation methods were used along with experimental techniques to validate the solidification modelling.

Thermal conductivity and charging/discharging of an inorganic PCM containing carbon fibre were studied using a Crank Nicolson numerical computational model based on enthalpy formulation (Frusteri *et al.*, 2006). It was reported that the thermal

conductivity of the PCM increases linearly with an increase of carbon fibre loading. A transient finite volume numerical model based on a generalized enthalpy formulation developed was used (Nayak *et al.*, 2006) to discover the significant effect of a thermal conductivity enhancer on PCM performance. A simulation model was developed (Cheralathan *et al.*, 2006) to describe the effect of porosity, Stanton number, Stefan number, and Peclet number on the thermal energy storage employing a spherical container containing encapsulated PCM integrated with a chiller .

2.5 Model Development for the PV-PCM system

Solar energy incident on the surface of PV is reflected and absorbed by PV module. Part of the absorbed light generates electricity and greater proportion converts into heat. Converted heat raises the temperature of the PV and is also transferred from the back of the PV to PCM. Heat loss takes place in the system by conduction, convection and radiation (Huang *et al.,* 2006c, 2006b). Heat transfer mechanism in PV-PCM systems described previously in figure 1.13 is modelled using a detailed finite element heat transfer simulation model in FLUENT 6.1.2.2.

2.5.1 Conduction

One dimensional heat diffusion equation is solved for simulating heat transfer in the solid PCM region. The general form of the equation is (Mills, 1999)

$$\frac{\partial^2 T}{\partial^2 x} = \frac{\rho c}{k}\frac{\partial T}{\partial t} = \frac{1}{\alpha}\frac{\partial T}{\partial t} \qquad (2.1)$$

Here α is thermal diffusivity which is a measure of how quickly a material can carry heat away from heat source. A material does just not transmit heat and is also warmed

so α involves both the conductivity κ and the volumetric heat capacity ρc. In solid regions, the energy transport equation used by FLUENT has the form:

$$\frac{\partial}{\partial t}\rho h = \frac{\partial}{\partial x_i}\left(k\frac{\partial T}{\partial x_i}\right) + \dot{q}''' \tag{2.2}$$

Where

ρ = density

h = sensible enthalpy = $\int_{T_{ref}}^{T} c_p dT$

T = temperature

$\dot{q}'''$ = volumetric heat source

The terms on the right-hand side of eq. 2.2 are the heat flux due to conduction and volumetric heat sources within the solid, respectively.

2.5.2 Radiation

Radiation can be viewed either in terms of electromagnetic waves or in terms of transport of photons. Materials can exhibit different radiative behaviour at different wavelengths. An important consideration in radiative heat transfer is the emissivity. The P1 (Fluent, 2005a) radiation model used in FLUENT incorporates radiation loss in the model by using the emissivity of the medium. Emissivity is the ratio of the radiation emitted by the surface at a given temperature to the radiation emitted by a blackbody at the same temperature. The simple model in Fluent takes less computation time as compared to other models. The transport equation for radiation is (Fluent, 2005a):

$$-\Delta q_r = \alpha_{pv} G - 4\alpha_{pv}\sigma T^4 \tag{2.3}$$

Where q_r = radiation flux, G = incident radiations, σ = Stefan-Boltzmann constant

α_{pv} = Absorption coefficient and T =Temperature. The expression for $-\Delta q_r$ is directly substituted into the energy equation to account for heat sources (or sinks) due to radiation.

2.5.3 Convection

Convection is the mode of energy transfer between a solid surface and the adjacent liquid or gas that is in motion. It involves the combined effects of conduction and fluid motion (Mills, 1999). There are two types of convection i.e. forced convection and natural convection. When fluid is forced to flow over the surface by external mean such as a fan then it is called forced convection. In contrast, natural convection occurs if the fluid motion is caused by buoyancy forces induced by density difference due to the variation of temperature within the fluid. In present model only natural convection is considered as the only heat transfer due to convection that ensues. The Boussinesq approximation model is used as this achieves faster solution convergence in the numerical analysis of many natural convection problems. The Boussinesq approach treats density as a constant value in all solved equations except for the buoyancy term in the momentum equation (Huang, *et al*. 2006, Fluent, 2005b)

$$(\rho - \rho_o) g \cong -\rho_o \beta (T - T_o) g \tag{2.4}$$

Where ρ_o is constant density of the flow, T_o is operating temperature, β is thermal expansion coefficient. The eq. 2.4 is obtained by using Boussinesq approximation given in equation 2.5:

$$\rho = \rho_o \left(1 - \beta \Delta T\right) \tag{2.5}$$

Boundary pressure for Boussinesq approximation is redefined as given by equation 2.6 (Fluent, 2005b)

$$P_s^{'} = \rho_o g x + P_s \tag{2.6}$$

Here p_s is atmospheric pressure, ρ_o is the operating density of air, g is the gravitational acceleration and x is the height of inlet.

2.5.4 Heat Transfer in PCM

An enthalpy formulation based fixed grid methodology is used in FLUENT for the numerical solution of convection-diffusion controlled mushy region phase-change problem (Fluent, 2005c). In pure materials, phase change takes place at a distinct temperature. However in metallurgical alloys, phase change takes place over a temperature range (Voller and Prakash, 1987).

$$\xi \le T \le -\xi \tag{2.7}$$

Here ξ is half mushy range, that is, the evolution of latent heat has a functional relationship with temperature e.g. $\Delta H = f\left(T\right)$. The enthalpy of the material (the total heat content) can be expressed as $H = h + \Delta H$ i.e. the sum of sensible heat, $h = cT$ and latent heat ΔH which is specified as a function of temperature. As latent heat is

associated with the liquid fraction in the mushy zone, a general form $f(T)$ can be written:

$$f(T)=\begin{cases} L, & T \geq T_1 \\ L(1-F_s) & T_1 > T \geq T_s \\ 0, & T < T_s \end{cases} \tag{2.8}$$

Where L is the fully liquid fluid, $F_s(T)$ is the local solid fraction, T_1 the liquid temperature at which solid formation commences and T_s is the temperature at which full solidification is achieved.

2.5.5 The Governing Equations

The forms of governing equations are similar to the equations for an isothermal phase change in a cavity Voller *et al.* 1985, Voller *at al.,* 1986 and Voller *et al.,* 1987. In FLUENT, the entire cavity is regarded as porous medium, where the porosity is the ratio of volume of void spaces to the total volume of a medium)

λ takes the value $\lambda=0$ in the solid phase and in the liquid phase, and $0<\lambda<1$ in the mushy zone. The governing equations can then be written in terms of velocity defined as:

$$u = \lambda u_1 \tag{2.9}$$

Where u_1 is the actual fluid velocity. On recognizing that the porosity $\lambda = 1 - F_s$, the above relationship can be expanded to give

$$u=\begin{cases} u_1 & \text{in the liquid phase} \\ (1-F_s)u_1 & \text{in the mushy zone} \\ 0 & \text{in the solid phase} \end{cases}$$

Using this definition along with the assumption of Newtonian, incompressible, laminar flow the governing equations are as follows (Patankar, 1980)

Conservation of Mass

$$\frac{\partial v}{\partial y}+\frac{\partial w}{\partial z}=0 \tag{2.10}$$

Where w and v are the superficial velocities in the z- and y-directions, respectively.

Conservation of Momentum

$$\frac{\partial(\rho v)}{\partial t}+div(\rho \mathbf{u} v)=div(\mu\, grad\ v)-\frac{\partial P}{\partial y}+S_y \tag{2.11a}$$

$$\frac{\partial(\rho w)}{\partial t}+div(\rho \mathbf{u} w)=div(\mu\, grad\ w)-\frac{\partial P}{\partial z}+S_z+S_b \tag{2.11b}$$

Where P is pressure, ρ is density, μ is the liquid viscosity, **u** = (v, w), and S_y, S_z and S_b are the source terms.

Conservation of Energy

The heat equation is given as below:

$$\frac{\partial \rho h}{\partial t}+div(\rho \mathbf{u} h)=div(\alpha\ grad\ h)-S_h=0 \tag{2.12}$$

2.5.6 Discretized Form of the Equations

To numerically solve the governing equations along with the associated source terms a finite domain method is used (Voller and Prakash, 1987). The finite domain discretization, following the notation in (Patankar, 1980) and referring to figure 2.2 given below:

$$a_p T_p = a_E T_E + a_W T_W + a_N T_N + a_S T_S + a_p^o T_p^o + b \qquad (2.13)$$

Where the subscripts indicate the appropriate nodal values, the $a's$ are coefficients which depend on the diffusion and convective fluxes into the p_{th} control volume, $a_p^o = \rho \delta z \delta y / \delta t$ and $()^o$ represent evaluation at the previous time step. The parameter b incorporates a discretized form of the source term S_h.

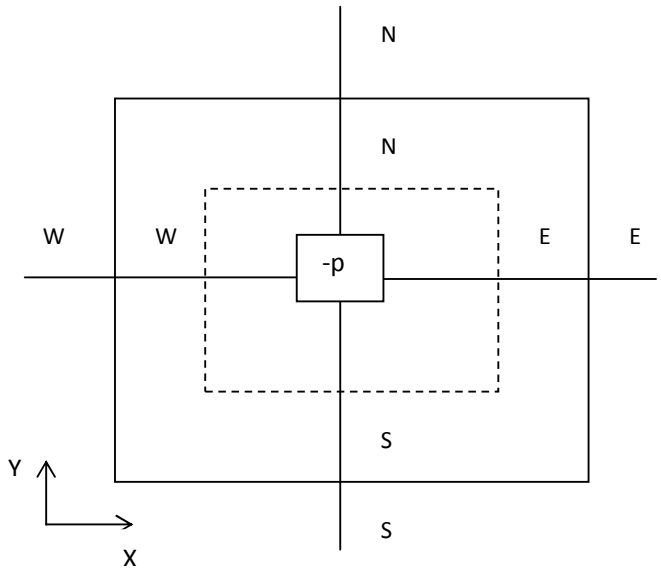

Figure 2.2: The numerical control volume

The momentum equation (velocity *v* in y-direction)

$$a_p v_p = a_E v_E + a_W v_W + a_N v_N + a_S v_S + a_p^o + b \qquad (2.14)$$

Where

$$a_E = \frac{k_e \Delta y}{(\delta x)_e} \quad , \; a_W = \frac{k_w \Delta y}{(\delta x)_w} \quad , \; a_N = \frac{k_n \Delta x}{(\delta x)_n} \quad , \; a_S = \frac{k_s \Delta y}{(\delta y)_s} \quad , \; a_p^o = \frac{\rho c \Delta x \Delta y}{\Delta t}$$

The important difference between equation 2.13 and 2.14 is that the grids used are 'staggered' over the enthalpy grid in momentum equation. (See the dashed control volume in figure 2.2. The reason for this is so that pressure, which is driving force for the velocities, can be correctly accounted (Patankar, 1980, Voller and Prakash 1987). The finite domain equations are solved by employing the PHOENICS code.

2.5.7 Geometry of the Model

The geometry of the model is developed in Gambit 2.1.6 and exported to FLUENT in filename.msh format. Two models are developed for analysis. First one is PV cell without integrated PCM and second one is PV/PCM system. The geometry is given below in figure 2.3 for both models.

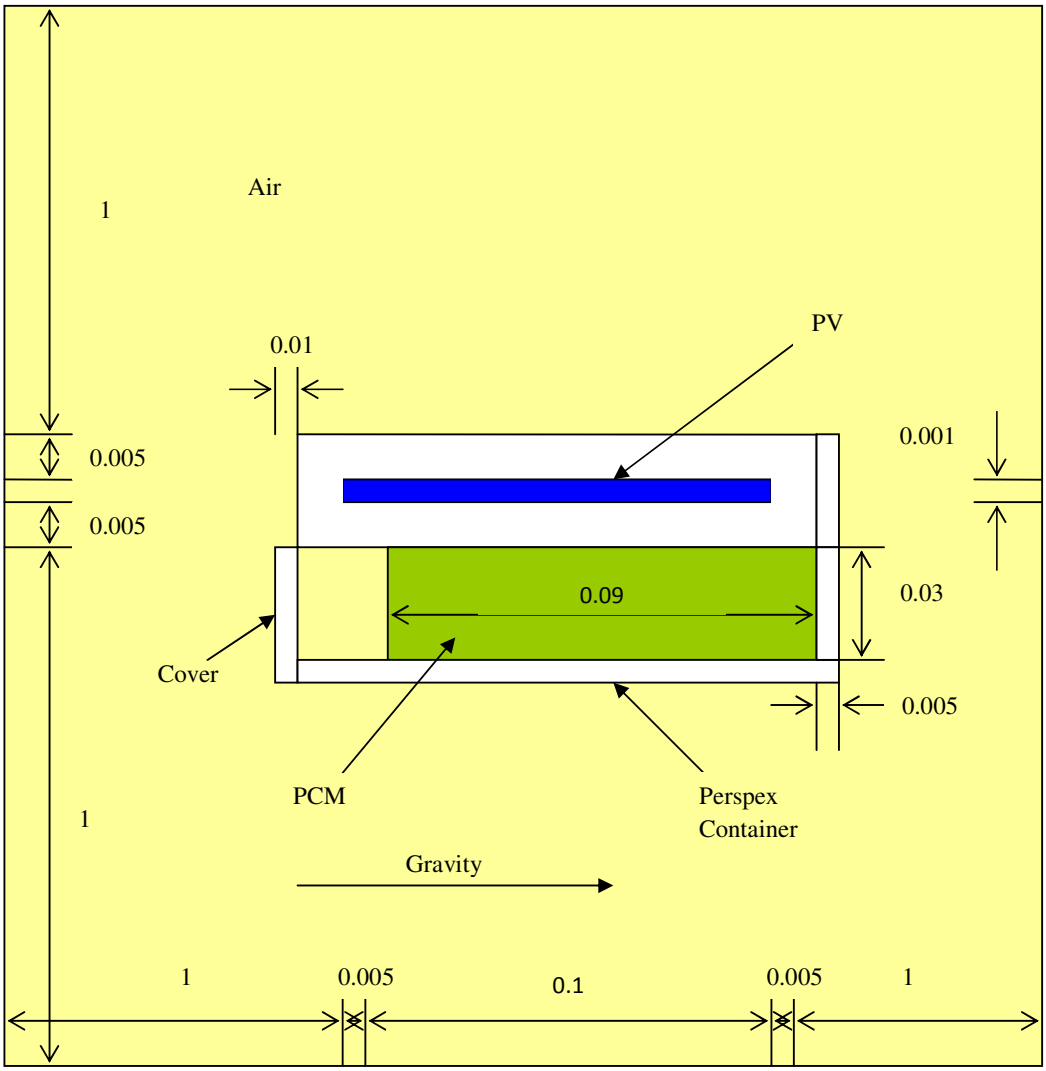

Figure 2.3: Geometry of PV/PCM System*

2.5.8 Meshing of the Model

Gambit 2.1.6 is used for the meshing of the model. The PV cell is meshed into 100 x 4 divisions i.e. aspect ratio of 4 which is well within permissible limit and the mesh is

* Not drawn on scale and all dimensions are in metres.

shape regular (Braess, 2001). The cover system is meshed into 240 x 16 divisions. PCM is meshed into 180 x 120 divisions. Entrapped air in container is meshed into 40 x 120 divisions and atmospheric air is meshed into 100 divisions with increasing ratio of 1.2 i.e. each length of next cell is 1.2 times the length of previous cell so cell size increases as it goes away from PV-PCM System. A refined mesh takes more computation time when compared to a coarse mesh so meshing of air is done in such a way that the mesh is refined near to PV-PCM System and takes active part in convection while as it moves away from the system, heat transfer is less so the mesh gets coarse as it moves away from the PV-PCM system. Detail of the Grid used in Model of PV and PV-PCM system is shown in table 2.2 below:

		Cells	**Faces**	**Nodes**
Model	PV	90720	182548	91821
	PV-PCM	152240	306718	154467

Table 2.2: Detail of the Grid used in Model of PV cell and PV-PCM system

2.5.9 Boundary Conditions

For fluid flow, zero velocity in the solid phase is attained by employing high viscosity. No explicit pressure boundary condition is given. The boundary conditions for energy equations are: (i) Energy influx due to solar input and (ii) Energy loss due to convection and radiation to ambient. For buoyancy-driven flows, pressure inlet and outlet boundary conditions are used by FLUENT and as there is no externally imposed pressure gradient so

atmospheric pressure is applied but for buoyancy-driven flows, redefined pressure is used which is calculated from the following equation (Fluent, 2005d).

$$p_s' = \rho_o g x + p_s \tag{2.15}$$

Wall boundary conditions are used to bound fluid and solid regions in FLUENT. Thermal along with radiation boundary conditions are applied to calculate heat transfer between solid to solid (Cover System to PV cell) and solid to fluid (Cover to air, Back of PV to PCM and Back of container to air). Different boundary conditions at the wall are as follows: Heat influx boundary condition Wm^{-2} is applied at the top of PV cell. Adiabatic boundary condition is applied on the sides of cover system and of the container as mentioned in (Huang *et al.,* 2006) in a similar problem. As the P1 radiation model is used to simulate radiation losses so emissivity of all media are given and values can be found in the Appendix. Initial temperature on the surface of the PV and container walls are given as calculated experimentally. As the Boussinesq approximation is used to simulate natural convection losses to air, so operating density of air is given along with operating temperature and gravitational acceleration. Solidification and melting model is activated for simulating phase change phenomenon and density as a function of temperature, heat capacity, thermal conductivity, viscosity as a function of temperature, absorption coefficient, melting heat, liquidus temperature and solidus temperature are given as input to model. Velocity suppression is achieved by giving a high value of viscosity at and beyond solidus temperature so that zero velocity at solid phase can be simulated. Three types of continuums are defined in the model i.e. solid, fluid and PCM. Inputs for solids are heat capacity, thermal conductivity and density. Inputs for fluid are density, heat capacity, thermal conductivity, viscosity and thermal expansion coefficient. PCM is

categorized as fluid in Gambit but as solidification-melting model is activated, it is changed to solid-fluid and the properties given as input are described in table 3.2 Flow, Energy and P1 equations (i.e. equations 2.1- 2.15) are activated in solution control tab along with PRESTO, pressure discretization scheme because of buoyancy driven flow. Discretization of pressure-velocity coupling, momentum and energy are kept to default values as well as relaxation factors. The solution is initialized at the upper surface of the PV cell with 2D double precision, segregated and unsteady solver with absolute velocity based formulation and cell based gradient option. The results obtained from the model will be described in chapter 4.

2.6 Applications of Phase Change Materials

The major research areas of PCM have been their use as a temperature regulator for high power dissipation electronic packaging, mobiles phones and space vehicles in space vehicles (Pal and Joshi, 1995; Gurrum *et al.*, 2002), thermal energy storage (Sharma *et al.*, 2009; Agyenim *et al.,* 2010), food and biological preservation (Wyatt, 1991; Mcdermott, 1997; Drage, 2009), electricity demand peak shifting or lowering (Fath, 1995, 1998; Enibe, 2003; Halford and Boehm, 2007), medical therapies (Saly, I.O. (1996; Junghanss, 2009), textile fabrics for human comfort (Mondal , 2008 ; Sánchez, *et al. 2010)* building fabrics that provide passive cooling of buildings (Zalba *et al.*, 2004; Huang *et al.*, 2006a) and thermal management of motors, actuators and power converters in electric vehicles (Jackson III *et al.*, 2002). The areas in which PCM are currently applied are listed in table 2.2.

		References
Applications	Thermal energy storage systems for solar energy storage and harnessing	Pillai and Brinkworth, 1976; Fath, 1998; Zalba *et al.*, 2003; Kenisarin and Mahkamov, 2007; Regin *et al.*, 2008; Sharma *et al.*, 2009; Agyenim *et al.*, 2010
	Thermal protection of electronic devices computer chips, space vehicles, power electronics and packaging	Tan and Tso, 2004; Wang *et al.*, 2007; Kandasamy *et al.*, 2008; Wang *et al.*, 2008; Fok *et al.*, 2010
	Thermal regulation of building integrated photovoltaics	Huang *et al.*, 2004, 2006b
	Passive cooling of building by heat storage in building fabrics to main human comfort temperature and electrical appliances in buildings	Hariri and Ward, 1988; Zalba *et al.*, 2004; Huang *et al.*, 2006a; Pasupathy *et al.*, 2008; Zhou *et al.*, 2009; Zhu *et al.*, 2009; Kenisarin, 2010
	Cooling during off-peak loads to reduce installed power by peak shaving. Heating sanitary hot water, using off-peak loads.	Fath, 1995, 1998; Enibe, 2003; Halford and Boehm, 2007
	Solar energy storage at high temperatures in solar tower power plants	Hoshi *et al.*, 2005; Michels and Pitz, 2007; Gil *et al.*, 2010; Kenisarin, 2010
	Thermal protection, preservation and transport of food items.	Wyatt, 1991; Mcdermott, 1997; Drage, 2009
	Encapsulation in textile fabric to maintain human comfort temperature	Mondal , 2008 ; Sánchez, *et al. 2010*
	Medical applications in transport of blood at controlled temperature, operating tables, hot-cold therapies	Saly, I.O. (1996; Junghanss, 2009
	Engine cooling (electric and combustion) Thermal comfort in vehicles	Jackson III *et al.*, 2002.

Table 2.3 Summary of applications of phase change materials.

2.7 References

Agyenim, F., Hewitt, N., Eames, P. and Smyth, M. (2010). "A review of materials, heat transfer and phase change problem formulation for latent heat thermal energy storage systems (LHTESS)." Renewable and Sustainable Energy Reviews 14(2): 615-628.

Aziz, M. (1996). "Interface attachment kinetics in alloy solidification." Metallurgical and Materials Transactions A 27(3): 671-686.

Banaszek, J., Domañski, R., Rebow, M. and El-Sagier, F. (1999). "Experimental study of solid-liquid phase change in a spiral thermal energy storage unit." Applied Thermal Engineering 19(12): 1253-1277.

Banaszek, J., Domañski, R., Rebow, M. and El-Sagier, F. (2000). "Numerical analysis of the paraffin wax-air spiral thermal energy storage unit." Applied Thermal Engineering 20(4): 323-354.

Banaszek, J., Furmanski, P. and Rebow, M. (2005). "Modelling of Transport Phenomena in Cooled and Solidifying Single Component and Binary Media." Oficyna Wydawnicaz Politechniki Warszawskiej.

Cedeño, F. O., Prieto, M. M., Espina, A. and García, J. R. (2001). "Measurements of temperature and melting heat of some pure fatty acids and their binary and ternary mixtures by differential scanning calorimetry." Thermochimica Acta 369(1-2): 39-50.

Cheralathan, M., Velraj, R. and Renganarayanan, S. (2006). "Heat transfer and parametric studies of an encapsulated phase change material based cool thermal energy storage system" Journal of Zhejiang University Science A 7 (11): 1886-1895.

D. Braess, Finite Elements Theory fast solver and Application in solid mechanics, Cambridge University Press. 2001

Dimaano, M. N. R. and Watanabe, T. (2002). "The capric-lauric acid and pentadecane combination as phase change material for cooling applications." Applied Thermal Engineering 22(4): 365-377.

Enibe, S. O. (2003). "Thermal analysis of a natural circulation solar air heater with phase change material energy storage." Renewable Energy 28(14): 2269-2299.

Fath, H. E. S. (1995). "Transient analysis of thermosyphon solar air heater with built-in latent heat thermal energy storage system." Renewable Energy 6(2): 119-124.

Fath, H. E. S. (1998). "Technical assessment of solar thermal energy storage technologies." Renewable Energy 14(1-4): 35-40.

Fluent Instruction Manual, Theory of the Energy Equation, 2005a

Fluent Instruction Manual, Theory of the P1 Radiation Model, 2005b

Fluent Instruction Manual, Phase Change Problem Theory, 2005c

Fluent Instruction Manual, Input for Buoyancy-driven flows, 2005d

Fok, S. C., Shen, W. and Tan, F. L. (2010). "Cooling of portable hand-held electronic devices using phase change materials in finned heat sinks." International Journal of Thermal Sciences 49(1): 109-117.

Frusteri, F., Leonardi, V. and Maggio, G. (2006). "Numerical approach to describe the phase change of an inorganic PCM containing carbon fibres." Applied Thermal Engineering 26(16): 1883-1892.

Gau, C. and Viskanta, R. (1984). "Melting and solidification of a metal system in a rectangular cavity." International Journal of Heat and Mass Transfer 27(1): 113-123.

Gil, A. , Medrano, M. , Martorell, I. , Lázaro, A. , Dolado, P. , Zalba, B. and Cabeza, L. F. (2010). "State of the art on high temperature thermal energy storage for power generation. Part 1--Concepts, materials and modellization." Renewable and Sustainable Energy Reviews 14(1): 31-55.

Drage, G. (2009). "Phase Change Material Used in Temperature Controlled Packaging & Transport". Environmental services industry community.Web page

Gurrum, S. P., Joshi, Y. K. and Kim, J. (2002). "Thermal Management of High Temperature Pulsed Electronics Using Metallics Phase Change Materials " Numerical Heat Transfer, Part A: Applications: An International Journal of Computation and Methodology 42(8): 777 - 790.

Halford, C. K. and Boehm, R. F. (2007). "Modeling of phase change material peak load shifting." Energy and Buildings 39(3): 298-305.

Hariri, A. S. and Ward, I. C. (1988). "A review of thermal storage systems used in building applications." Building and Environment 23(1): 1-10.

Hasan, A. and Sayigh, A. A. (1994). Some fatty acids as phase-change thermal energy storage materials. Oxford, Royaume-Uni, Elsevier.

Hong, S.T. and Herling, D. R. (2006). "Open-cell aluminum foams filled with phase change materials as compact heat sinks." Scripta Materialia 55(10): 887-890.

Hoshi, A., Mills, D. R., Bittar, A. and Saitoh, T. S. (2005). "Screening of high melting point phase change materials (PCM) in solar thermal concentrating technology based on CLFR." Solar Energy 79(3): 332-339.

Hu, X. and Zhang, Y. (2002). "Novel insight and numerical analysis of convective heat transfer enhancement with microencapsulated phase change material slurries: laminar flow in a circular tube with constant heat flux." International Journal of Heat and Mass Transfer 45(15): 3163-3172.

Huang, M. J., Eames, P. C. and Hewitt, N. J. (2006a). "The application of a validated numerical model to predict the energy conservation potential of using phase change materials in the fabric of a building." Solar Energy Materials and Solar Cells 90(13): 1951-1960.

Huang, M. J., Eames, P. C. and Norton, B. (2004). "Thermal regulation of building-integrated photovoltaics using phase change materials." International Journal of Heat and Mass Transfer 47(12-13): 2715-2733.

Huang, M. J., Eames, P. C. and Norton, B. (2006b). "Phase change materials for limiting temperature rise in building integrated photovoltaics." Solar Energy 80(9): 1121-1130.

Jackson III, W.B. , Gould, R.D. and Mulligan, J.C. (2002). "Performance of an octacosane based micro PCM fluid for cooling EV electronics " 8th AIAA/ASME Joint Thermophysics and Heat Transfer Conference24-26 June 2002, St. Louis, Missouri.

Junghanss, T., Boock, A.U., Vogel, M., Schuette, D., Weinlaeder, H. and Pluschke, G. (2009) "Phase Change Material for Thermotherapy of Buruli Ulcer: A Prospective Observational Single Centre Proof-of-Principle Trial". PLoS Negl Trop Dis. 3(2): e380

Kandasamy, R., Wang, X. Q. and Mujumdar, A. S. (2008). "Transient cooling of electronics using phase change material (PCM)-based heat sinks." Applied Thermal Engineering 28(8-9): 1047-1057.

Karaipekli, A., SarI, A. and Kaygusuz, K. (2007). "Thermal conductivity improvement of stearic acid using expanded graphite and carbon fiber for energy storage applications." Renewable Energy 32(13): 2201-2210.

Kenisarin, M. and Mahkamov, K. (2007). "Solar energy storage using phase change materials." Renewable and Sustainable Energy Reviews 11(9): 1913-1965.

Kenisarin, M. M. (2010). "High-temperature phase change materials for thermal energy storage." Renewable and Sustainable Energy Reviews 14(3): 955-970.

Khillarkar, D. B., Gong, Z. X. and Mujumdar, A. S. (2000). "Melting of a phase change material in concentric horizontal annuli of arbitrary cross-section." Applied Thermal Engineering 20(10): 893-912.

Ludwig, A. (1991). Limit of absolute stability for crystal growth into undercooled alloy melts. Tarrytown, NY, ETATS-UNIS, Pergamon Press.

Mcdermott, M. B. (1997). "Heat retentive food service base device" . United States Patent 5611328

Michels, H. and Pitz, R. P. (2007). "Cascaded latent heat storage for parabolic trough solar power plants." Solar Energy 81(6): 829-837.

Mills, A.F., Heat Transfer, 2nd edition, Prentice –Hall Inc. 1999

Mills, A., Farid, M., Selman, J. R. and Al-Hallaj, S. (2006). "Thermal conductivity enhancement of phase change materials using a graphite matrix." Applied Thermal Engineering 26(14-15): 1652-1661.

Mondal, S. (2008). "Phase change materials for smart textiles - An overview" Applied Thermal Engineering. 28 (11-12). 1536-1550

Nagano, K., Takeda, S., Mochida, T. and Shimakura, K. (2004). "Thermal characteristics of a direct heat exchange system between granules with phase change material and air." Applied Thermal Engineering 24(14-15): 2131-2144.

Nayak, K. C., Saha, S. K., Srinivasan, K. and Dutta, P. (2006). "A numerical model for heat sinks with phase change materials and thermal conductivity enhancers." International Journal of Heat and Mass Transfer 49(11-12): 1833-1844.

Pal, D. and Joshi, Y. (1995). "Application of Phase Change materials for Passive Thermal Control of Plastic Quad Flat Packages (PQFP): A Computational Study." Eleventh IEEE SEMI-THERMTM Symposium: 65-71

Pasupathy, A., Athanasius, L., Velraj, R. and Seeniraj, R. V. (2008). "Experimental investigation and numerical simulation analysis on the thermal performance of a building roof incorporating phase change material (PCM) for thermal management." Applied Thermal Engineering 28(5-6): 556-565.

Patankar, S.V., Numerical Heat Transfer and Fluid Flow. Hemisphere, Washington DC (1980)

Pillai, K. K. and Brinkworth, B. J. (1976). "The storage of low grade thermal energy using phase change materials." Applied Energy 2(3): 205-216.

Regin, A. F., Solanki, S. C. and Saini, J. S. (2008). "Heat transfer characteristics of thermal energy storage system using PCM capsules: A review." Renewable and Sustainable Energy Reviews 12(9): 2438-2458.

Roy, S. K. and Avanic, B. L. (2001a). "Laminar forced convection heat transfer with phase change material suspensions." International Communications in Heat and Mass Transfer 28(7): 895-904.

Roy, S. K. and Avanic, B. L. (2001b). "Turbulent heat transfer with phase change material suspensions." International Journal of Heat and Mass Transfer 44(12): 2277-2285.

Sánchez, P., Fernandez, S. M. V., Romero, A. Rodríguez, J. F. and Silva, L. S (2010). "Development of thermo-regulating textiles using paraffin wax microcapsules." Thermochimica Acta 498 (1-2): 16-21

Salyer, I.O. (1996). "Thermoplastic, moldable, non-exuding phase change materials". United States Patent 5565132

Sari, A. (2004). "Form-stable paraffin/high density polyethylene composites as solid-liquid phase change material for thermal energy storage: preparation and thermal properties." Energy Conversion and Management 45(13-14): 2033-2042.

Sari, A. and Kaygusuz, K. (2002). "Thermal performance of a eutectic mixture of lauric and stearic acids as PCM encapsulated in the annulus of two concentric pipes." Solar Energy 72(6): 493-504.

Sari, A. and Kaygusuz, K. (2003). "Some fatty acids used for latent heat storage: thermal stability and corrosion of metals with respect to thermal cycling." Renewable Energy 28(6): 939-948.

SarI, A., SarI, H. and Önal, A. (2004). "Thermal properties and thermal reliability of eutectic mixtures of some fatty acids as latent heat storage materials." Energy Conversion and Management 45(3): 365-376.

Sarier, N. and Onder, E. (2007). "Thermal characteristics of polyurethane foams incorporated with phase change materials." Thermochimica Acta 454(2): 90-98.

Scanlon, T. J. and Stickland, M. T. (2004). "A numerical analysis of buoyancy-driven melting and freezing." International Journal of Heat and Mass Transfer 47(3): 429-436.

Schrage, D. S. (1999). A simplified model of dendritic growth in the presence of natural convection. Amsterdam, PAYS-BAS, Elsevier.

Sharma, S.D., Kitano, K and Sagara, K (2004). "Phase Change Materials for Low Temperature Solar Thermal Applications": Res. Rep. Fac. Eng. Mie Univ., Vol. 29, pp. 31-64.

Sharma, S.D.(2005) "Latent Heat Storage Materials and Systems: A Review". International Journal of Green Energy, 2: 1–56.

Sharma, A., Tyagi, V. V., Chen, C. R. and Buddhi, D. (2009). "Review on thermal energy storage with phase change materials and applications." Renewable and Sustainable Energy Reviews 13(2): 318-345.

Tan, F. L. and Tso, C. P. (2004). "Cooling of mobile electronic devices using phase change materials." Applied Thermal Engineering 24(2-3): 159-169.

Trp, A. (2005). "An experimental and numerical investigation of heat transfer during technical grade paraffin melting and solidification in a shell-and-tube latent thermal energy storage unit." Solar Energy 79(6): 648-660.

Vakilaltojjar, S. M. and Saman, W. (2001). "Analysis and modelling of a phase change storage system for air conditioning applications." Applied Thermal Engineering 21(3): 249-263.

Voller, V. R. and Prakash, C. (1987). "A fixed grid numerical modelling methodology for convection-diffusion mushy region phase-change problems." International Journal of Heat and Mass Transfer 30(8): 1709-1719.

Wang, G.X., Yao, C. and Chung, B. T. F. (2003). "Thermal analysis on planar interface stability in solidification of semitransparent materials ". Journal of Applied Physics and Heat Transfer17(2) 153-160.

Wang, X. Q., Yap, C. and Mujumdar, A. S. (2008). "A parametric study of phase change material (PCM)-based heat sinks." International Journal of Thermal Sciences 47(8): 1055-1068.

Wang, X.Q., Mujumdar, A. S. and Yap, C. (2007). "Effect of orientation for phase change material (PCM)-based heat sinks for transient thermal management of electric components." International Communications in Heat and Mass Transfer 34(7): 801-808.

Worster, M.G. (1992). "Instabilities of the liquid and mushy regions during solidification of alloys." Journal of Fluid Mechanics 237: 649-669.

Wyatt, B. W. (1991). "Heat retentive server with phase change core".United States Patent 4982722.

Yao, Chengcai, Chung, B. T. F. and Wang, G. X. (2002). "Mushy zone equilibrium solidification of a semitransparent layer subject to radiative and convective cooling." International Journal of Heat and Mass Transfer 45(11): 2397-2405.

Zalba, B. , Marín, J. M., Cabeza, L. F. and Mehling, H. (2003). "Review on thermal energy storage with phase change: materials, heat transfer analysis and applications." Applied Thermal Engineering 23(3): 251-283.

Zalba, B., Marín, J. M., Cabeza, L. F. and Mehling, H. (2004). "Free-cooling of buildings with phase change materials." International Journal of Refrigeration 27(8): 839-849.

Zhou, G., Yang, Y., Wang, X. and Zhou, S. (2009). "Numerical analysis of effect of shape-stabilized phase change material plates in a building combined with night ventilation." Applied Energy 86(1): 52-59.

Zhu, N., Ma, Z. and Wang, S. (2009). "Dynamic characteristics and energy performance of buildings using phase change materials: A review." Energy Conversion and Management 50(12): 3169-3181.

3 CHARACTERIZATION OF PHASE CHANGE MATERIALS

3.1 Selection of Phase Change Materials

The properties of phase change materials (PCM) will predominantly determine the performance of PCM-based thermal-regulation devices. For an integrated novel PV-PCM device, the required PCM properties include:

- Fixed melting point close to device desired operating temperature
- Larger latent heat of fusion for a given mass of PCM; as the latent heat of fusion increases so will be the duration of both heat absorption and attained temperature regulation.
- Good thermal conductivity; this encourages efficient heat transfer into solid PCM through the melting-front, enabling uniform temperature distribution via reduced thermal gradient in the PCM
- Phase congruence; this encourages uniform thermophysical behaviour
- Good solidification properties with no, or low, supercooling; in the current work solid PCM absorbs heat and melts during daytime to regulate PV temperature. The absorbed heat is released nocturnally by ambient and radiative cooling bringing back to solid phase. A PCM with higher supercooling needs to be cooled below freezing point to initiate solidification. In sunny warm climates where the need for daytime PV temperature regulation is critical, the night time ambient temperatures are also higher. Such higher night time temperatures do not support PCM cooling

below freezing points (about 25 °C in this application) hampering PCM solidification process rendering PCM with supercooling unsuitable in such climates. It should be noted that though the night time air temperatures can remain warm, clear skies can provide a heat sink for radiative cooling.

- Chemical stability; this ensures (i) longer life of PCM itself (ii) no or less change in melting point and (iii) no or less change in the heat of fusion
- No toxicity; this assures (i) safe disposal of materials to the environment and (ii) renders possible their use in buildings by being compatible with most building codes and regulations.
- No combustibility; this assures (i) fire safety when included in a building integrated façade and (ii) less risk in device manufacture.
- No or low corrosion of the containment materials; this enhances the container life
- Low cost; this will (i) aid the achievement of economic viability and (ii) reduce initial cost thereby enabling a greater penetration of cost sensitive application contexts.

The properties desired for a suitable PCM are classified and summarized in Table 3.1. A systematic choice is difficult as a particular PCM may only have some of the desired characteristics, but may not possess the others. Very little literature compares performance of different PCM types for thermal regulation. Its high latent heat of fusion, cheap and abundant availability and no-toxicity makes water an ideal PCM; however its solid–liquid phase change temperature at atmospheric pressure is 0 °C

which makes it an unsuitable PCM for any application where ambient temperatures are generally above 0 °C.

		Requirement	Reason for requirement
Properties	Thermal	High latent heat High heat capacity Good thermal conductivity Reversible phase change Fixed melting point	Maximum heat absorption Minimum sensible heating Efficient heat removal Diurnal response Consistent behaviour
	Physical	Congruent melting Low volume expansion High density	Minimum thermal gradient, No overdesign Low containment requirement
	Kinetic	No supercooling, Good crystallisation rate	Easy to freeze Faster solidification
	Chemical	Chemical stability, Non-corrosive, Non-flammable, Non explosive, Non-toxic	Long life Long container life Comply building safety codes Environment friendly
	Economic	Abundant, Available, Cheap and Cost effective	Market competitiveness Economic viability and market penetration
	Environmental	Recyclable/Reusable Odour free	Ease to dispose of Comfortable to apply in dwellings environment

Table 3.1 Properties of a PCM desired for Photovoltaic thermal regulation

In order to simplify the selection of a suitable PCM, an extensive literature review was conducted of all known PCM classes, i.e. paraffin, salt hydrates, fatty acids and mixtures of salt hydrate and paraffins to identify a PCM that had a melting point

between 21 °C- 29 °C i.e. 25 ± 4 °C with latent heat of fusion >130 J g^{-1}. The range of melting points from 21 °C - 29 °C were chosen because:

(i) a PCM that melts and absorbs latent heat below 25 °C (e.g. at 21 °C in this case) has the advantage of stabilizing PV temperature close to the PV characterization temperature of 25 °C due to PCM melting below this desired PV temperature. Nevertheless when ambient temperatures are higher than PCM melting point (in this case an ambient temperature of 25 °C will be higher than PCM melting point which is below 21 °C) melting ensues due to ambient heat gain in addition to incoming solar radiations. This may lead to a shorter melt time, shorter period of heat absorption and subsequently a shorter duration of PV temperature regulation. (ii) A PCM with melting points above 25 °C (e.g. 29 °C) may have advantage of not melting at most ambient temperatures and being melted solely by incident solar radiations. Consequently they may continue melting and absorbing heat for a longer period providing a longer duration of PV temperature regulation. However the disadvantage of melting commencing and absorbing heat above a temperature of 25 °C is higher temperatures at the PV surface. Table 3.2 lists the PCMs identified from the literature possessing the desired properties.

				PCM				
				RT20	SP224A	$CaCl_2.6H_2O$	CL	CP
Thermophysical Properties of PCMs	Melting point, (˚C)		experimental	22	21.6	29.6	20.6	22.4
			literature	21[a]	23[a]	29.8[b]	18.5[c]	22.5[c]
	Heat of fusion, ($kJkg^{-1}$)		Experimental DSC	139	125	212	188	195
			Experimental THM	143	135	210	179	190
			literature	134[a]	150[a]	191[b]	168[c]	173[c]
	Thermal Conductivity ($Wm^{-1}{}^{\circ}C^{-1}$)	Solid		0.2[a]	0.6[a]	1.08 [f]	0.143[d]	0.143[d]
		liquid		0.18[e]	0.4[f]	0.56[f]	0.139[d]	0.139 [d]
	Specific heat capacity ($KJkg^{-1}K^{-1}$)	Solid	Experimental (THM)	1.5	1.7	1.77	1.8	2.2
			Experimental (DSC)	1.3	1.6	1.6	1.9	1.9
			Literature	1.4[e]	1.4[b]	1.4[b]	1.97[g]	2[g]
		Liquid	experimental THM	1.6	1.8	2.2	2.12	2.4
			Experimental (DSC)	1.8	1.7	1.9	2.3	2.2
			literature	1.7[e]	1.95[b]	2.1[b]	2.24[g]	2.3[g]
	Corrosion to metallic containers			No[a]	Yes[a]	Yes[h]	Yes[h]	Yes[h]
	Thermal cyclic stability			Yes	N.A	Yes[b], No[i]	Yes[j]	Yes[j]
	Chemical Classification			Paraffin wax	Mixture of paraffin wax and salt hydrate	Salt hydrate	Eutectic mixture of fatty acids	Eutectic mixture of fatty acids
	Density (kgm^{-3})	Solid		0.88[a]	1.49[a]	1.71 [b]	0.89[c]	0.87[c]
		Liquid		0.75[a]	1.44[a]	1.56[f]	0.77[c]	0.79[c]
	Kinematic viscosity ($m^2.sec^{-1}$) $x10^{-3}$			6.25[e]	1.23[a]	1.84[e]	0.0022[g]	0.0023[c]
	Coefficient of thermal expansion (K^{-1})			0.001[e]	0.0008[a]	0.0005[f]	0.00067[g]	0.00078[c]
	Material source			Rubith-erm (2010)	Rubith-erm (2010)	Sigma Aldrich (2010)	Sigma Aldrich (2010)	Sigma Aldrich (2010)

Table 3.2 Thermophysical characteristics identified from literature and experiments of suitable PCMs for temperature regulation of Photovoltaics at close to their characterization temperature.

(a-Rubitherm, 2009 a), (b- Tyagi and Buddhi, 2008), (c- Sari and Karaipekli, 2008), (d-Sharma and Sagara, 2005), (e- Huang *et al.,* 2006 a), (f- Zelba,2003), (g- Sari, A and Kayazug, K., 2002), (Cabeza *et al.,* 2002), (i- El-Sebaii *et al.*, 2009), (j-Sedat *et al.*, 2005)

3.2 Characterization of Phase Change Materials.

SP22, RT20 and $CaCl_2.6H_2O$ were sourced as ready-to-use from commercial manufacturers CL (eutectic mixtures capric acid (45%) and lauric acid (55%) by weight) and CP (eutectic mixture of capric acid (75.2%) and palmitic acid (24.8%) by weight) were prepared in the laboratory from individual chemicals in the form of capric acid, lauric acid and palmitic acids. The fatty acids were mixed as solids in the eutectic combinations given in Table 3.2 to get a net mixture of 25 g. Each solid mixture was melted at 60 °C for three hours to obtain a homogenous solution that then cooled to solidify as eutectic solids. Prepared PCMs were characterized using (i) differential scanning calorimetry (DSC) and (ii) temperature history method (THM) to determine their thermophysical properties. Each was compared with data available in the literature. DSC is a standard instrument to determine thermophysical properties of materials while THM is custom-built method to determine those properties of PCM that are function of PCM mass (and are not determined easily by DSC) such as subcooling and supercooling etc.

3.2.1 Differential Scanning Calorimetry

Differential scanning calorimetry (DSC) is a thermodynamic technique to determine thermophysical materials properties including melting point, heat of fusion, specific heat capacity, melting onset, melting peak transition range. The temperature over which a given sample of a material completely melts is a function of sample mass and the heating rate (Dötsch and Fink 1987; Marini *et al.* 1988). The energy input is measured to establish a nearly zero temperature difference between an empty reference metallic pan and an identical metallic pan containing the sample material, both subjected to identical temperature regimes in heating and/or cooling mode at a controlled rate of temperature rise. DSC setup includes a nitrogen tank for purging at a fixed pressure, a cooling media (liquid nitrogen) to perform cooling, the calorimeter itself and a data acquisition system. DSC systems in common use are classified as either a power-compensation DSC or a heat-flux DSC (Ekeren *et al.* 1997; Bailey and Hay 1999; Danley 2002).

The sample and the reference temperatures are controlled independently using identical separate crucibles. Identical sample and reference temperatures are maintained by varying the power inputs to the two crucibles. The difference in the energy required to maintain these identical temperatures is a measure of the enthalpy (or heat capacity change) in the sample compared to the reference (Sichina, 2000)

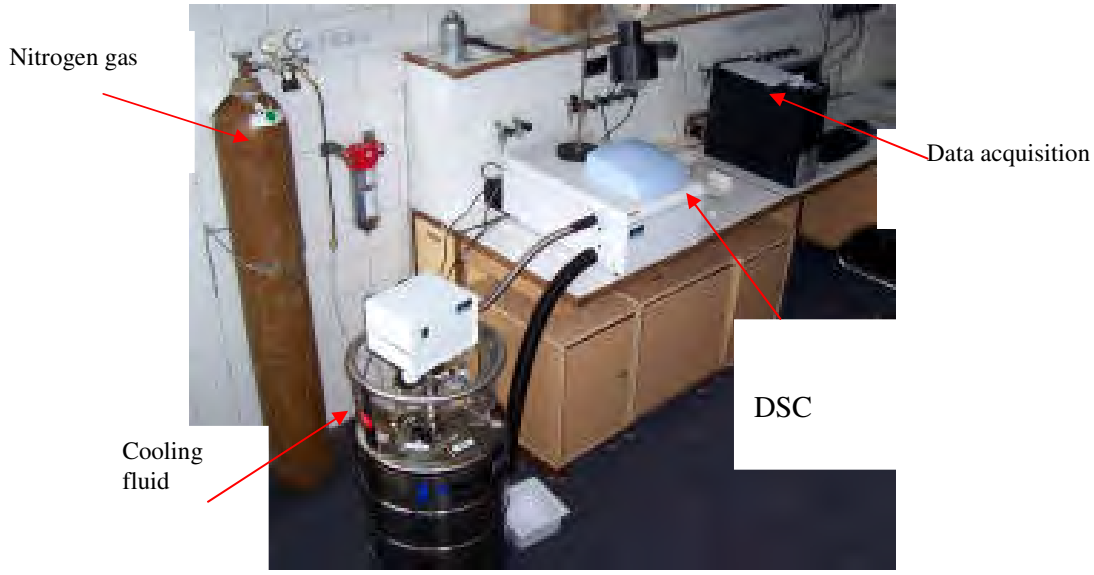

Figure 3.1 Experimental setup for a PerkinElmer 8000 N5340511 power compensation differential scanning calorimeter (DSC)

In a heat-flux DSC, the sample and the reference are connected by a low-resistance heat-flow path (a metal disc). The whole assembly is enclosed in a single crucible shown in figure 3.2. Enthalpy or heat capacity changes in the sample caused a difference in its temperature relative to the reference. The temperature difference was recorded and related to enthalpy change in the sample compared with the reference (Danley, 2002). The resulting heat flow was small compared with that in differential thermal analysis (DTA) because the sample and reference were in good thermal contact.

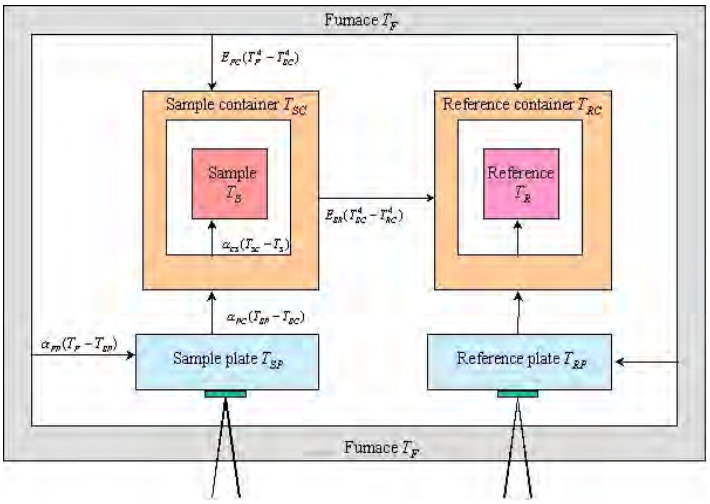

Figure 3.2 : Schematic diagram of a heat flux differential scanning calorimetry

3.2.1.1 Experiments

In this study a heat-flux DSC was used, this provided quick, accurate and detailed measurements from only a very small, 3 to 10 mg sample. Paraffin wax RT20, salt hydrate $CaCl_2.6H_2O$, a mixture of salt hydrate and paraffin wax SP22, a eutectic mixture of capric acid-lauric acid and a eutectic mixture of capric acid-palmitic acid were characterized sing 5 mg sample of each PCM. During the experiment the crucibles were purged with a constant supply of nitrogen gas whilst each sample was heated from 10 °C to 60 °C at a heating rate of 5 °C min^{-1}. At the end of each heating run, the crucibles were cooled to 10 °C with liquid nitrogen in preparation for the next run. Three runs were performed for each PCM with the same experimental conditions to ensure repeatability. The variation of less than 1 % was observed in measured values that represents the accuracy of the device.

Thermal properties of the samples were analysed in the form of energy-time relationships termed thermograms for predetermined operating temperature ranges during the heating (i.e., melting) cycles. The difference in heat input between the reference pan and the pan containing sample for a unit temperature rise formed the DSC output that was plotted against temperature rise. Evaluation of DSC thermograms determined the PCM phase transition temperature, specific heat and latent heat of fusion.

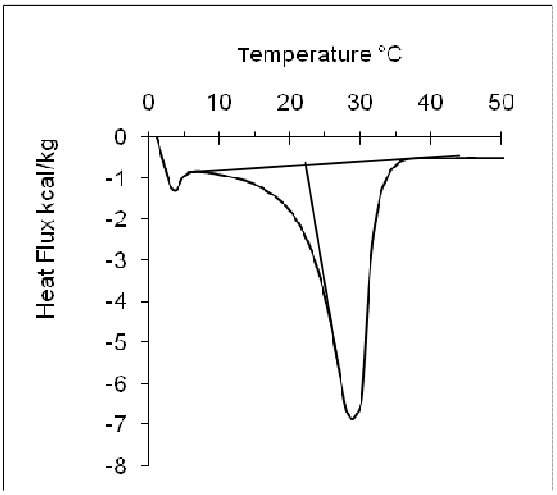

Figure 3.3 : DSC results for RT20 PCM

Paraffin wax RT20 was studied to compare these current results with those obtained from previous work that also used paraffin wax RT25 PCM for temperature regulation of building integrated photovoltaics (Huang *et al.* 2006a; Huang *et al.* 2006b)

Figure 3.3 presents the DSC thermograph obtained with paraffin wax RT20 showing the PCM started latent heat of absorption at 18.7 °C with a peak at 24 °C and

completed heat absorption at 31.4 °C. The melting range was 22 °C to 25 ˚C with a latent heat of fusion of 139 Jg^{-1} respectively are in good agreement with the manufacturer corresponding data of melting point of 21 °C and heat of fusion of 134 Jg^{-1} (Rubitherm, 2009). This very large heat absorption from 18.7 °C to 31.4 °C can be attributed to (i) heat transfer mechanisms in the sample crucible, (ii) low thermal conductivity of RT20 and (iii) a too small sample size. The melting point is taken as the point where the slope of the thermograph is maximum so as to ensure the latent heat is taken at close to isothermal conditions. RT20 thus is a potential candidate PCM for PV temperature regulation due to its higher heat of fusion appropriate lower melting point well below a desired PV temperature of 25 °C. However RT20 also has certain drawbacks of which the most important are (i) its low density of 0.88 gcm^{-3} in solid phase and 0.75 gcm^{-3} in liquid phase which means that mass required would occupy comparatively large volume, thus making a PV-PCM unit less readily integrated into typical building facades, (ii) low thermal conductivity of 0.2 $Wm^{-1}K^{-1}$ and (iii) its large volume expansion of 14 % from solid to liquid phase change (Rubitherm, 2009) may cause containment design problems. The wide range heat absorption in Figure 3.3 (18.7 °C to 31.4 °C) of paraffin RT20 may seem unsuitable for temperature control close to 25 °C. However predicted device design manipulations such as inserting thermal conductive fins in PCM container to enhance heat transfer rate can cause the PCM to melt in a relatively narrow temperature range (Huang *et al.* 2004). Combustibility of RT20 with flash point of 154 ˚C (Rubitherm, 2009) can also be a potential problem restricting its use in building integrated

applications as it would not comply with building safety and/or design codes in various legislations.

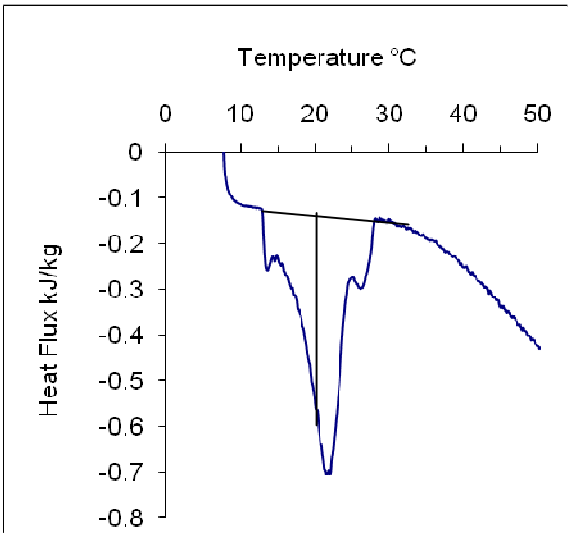

Figure 3.4 :DSC results for the SP22 PCM

Figure 3.4 presents DSC thermographs of a mixture of paraffin wax and salt hydrate, SP22 showing that the PCM has a moderate melting range of 15 °C to 26.8 °C with a peak at 23 °C. The melting range was 21.6 °C to 24 ˚C with the latent heat of fusion of 125 J-g^{-1}. While the melting point and heat storage capacity indicated in the manufacture's catalogue were 23 °C and 150 kJ kg^{-1} respectively in the temperature range of 13°C-28 °C (Rubitherm, 2009). The difference between these values can be attributed to (i) the range of melting, (ii) method of measurement and (iii) too small mass of the sample. Further characterization was conducted with larger sample masses described in section 3.2.2.

PCM SP224A (referred to as SP22 onwards) shows promise for an integrated PV-PCM application due to (i) high heat of fusion (ii) high thermal conductivity of 0.6 W $m^{-1}K^{-1}$ (iii) high density of 1.49 g-cm^{-3} and (iv) low volume expansion of 4.03 % while changing phase from solid to liquid. The large heat absorption range (15 °C-26.8 °C) and beyond evident from the curve suggests that SP22 4A can be a suitable material for thermal energy storage applications as it can store energy as a sensible and latent heat however it may not be suitable for PV temperature control applications where the need is to melt just above typical ambient temperatures (i.e., 25 °C). Furthermore SP22 PCM being a mixture of paraffin wax and a salt hydrate (Rubitherm, 2009) may lead to incongruent melting due to different melting behaviour and thermophysical properties of the constituent PCMs. For effective temperature regulation a PCM should have little or no phase incongruence.

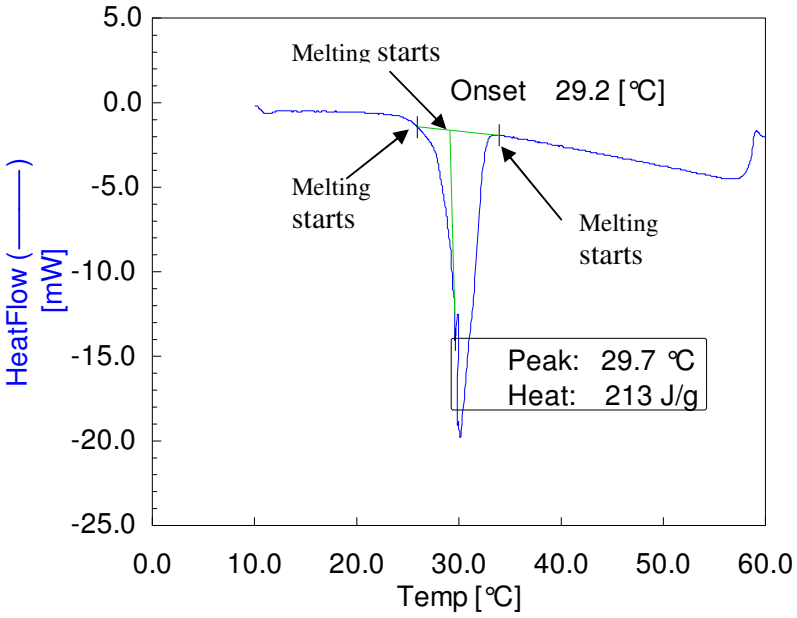

Figure 3.5: DSC results for the $CaCl_2.6H_2O$ PCM

Figure 3.5 presents the DSC thermograph of pure salt hydrate $CaCl_2.6H_2O$ and shows that heat absorption began at 25.9 °C and completed at 33.9 °C with a peak at 29.7 °C. The melting range was 29.6 °C and 30.4 ˚C with a latent heat of fusion of 213.2 Jg^{-1} which are in agreement with the reported melting point of 29.8 °C and heat of fusion of 191 Jg^{-1} (Tyagi and Buddhi, 2008). $CaCl_2.6H_2O$ PCM thus has the lowest temperature range of heat absorption (25.9 °C -33.9 °C) of the PCMs measured. The variation observed in heat of fusion was due to (i) grade and purity of the PCM, (i.e., the PCM used in current experiments and those used in the reference literature were different) and (ii) the thermal cycles and dehydration the PCM had undergone before performing the experiment. $CaCl_2.6H_2O$ PCM shows (i) a good range of melting, (ii) relatively high heat of fusion, (iii) high thermal conductivity of 1.09 $Wm^{-1}K^{-1}$ and (iv) high density of 1.71 g cm^{-3} and (v) very good thermal cycling properties if carefully melted in hermetically sealed containers (Tyagi and Buddhi, 2008). However the melting occurs at a higher temperature than the desired temperature of 25 °C, this PCM also has a higher corrosion rate in metallic containers materials (Cabeza *et al.,* 2002; Farrell *et al,.* 2006) compared to the other PCMs and a tendency to dehydrate during melting when exposed to air (El-Sebaii *et al.*, 2009).

The DSC results for a eutectic mixture of capric-lauric acid in figure 3.6 show that the heat absorption commenced at 18 °C and completed at 27 °C with the peak at 24.6 °C. The lower and upper melting points were 19.6 and 22.5 ˚C with latent heat of fusion 188 J g^{-1} that are in good agreement with previously reported values of 18.5 °C and 168 J- g^{-1} respectively (Sari and Karaipekli 2008).

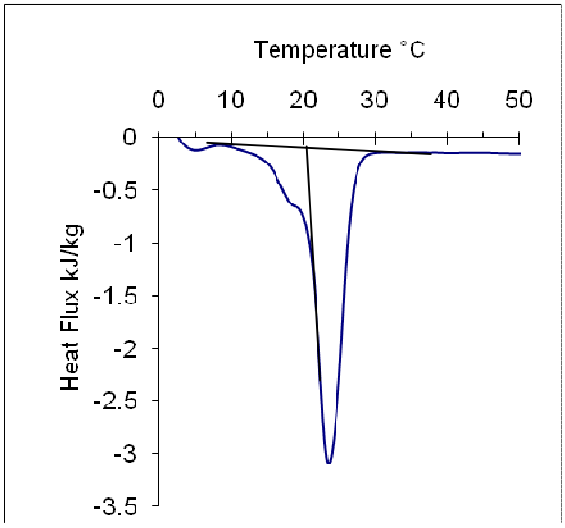

Figure 3.6 : DSC results for the capric-lauric acid PCM

This PCM has (i) a suitable melting point (ii) a relatively high heat of fusion (iii) moderate volume expansion and (iv) good thermal cyclic stability when subjected to several solid to liquid phase change cycles (Sedat *et al.*, 2005; Shilei *et al.*, 2006; Sari and Karaipekli, 2008). However this PCM has also (i) a wide heat absorption temperature range (18 °C - 27 °C) may be attributed to (i) its very low thermal conductivity of 0.14 W $m^{-1}K^{-1}$ and (ii) relatively low density of 0.89 g-cm^{-3} in solid phase (Sharma and Sagara, 2005).

Figure 3.7 shows DSC thermographs for eutectic mixture of capric-palmitic acid. Heat absorption commenced at 19 °C and had completed at 31.4 °C with a peak at 26.4 °C. The melting range was found be 22.4 °C to 25 ˚C with latent heat of fusion of 195 Jg^{-1} while comparable values in literature were 22.5 °C and 173.6 Jg^{-1} respectively (Karaipekli and Sari, 2007; Sari and Karaipekli, 2008).

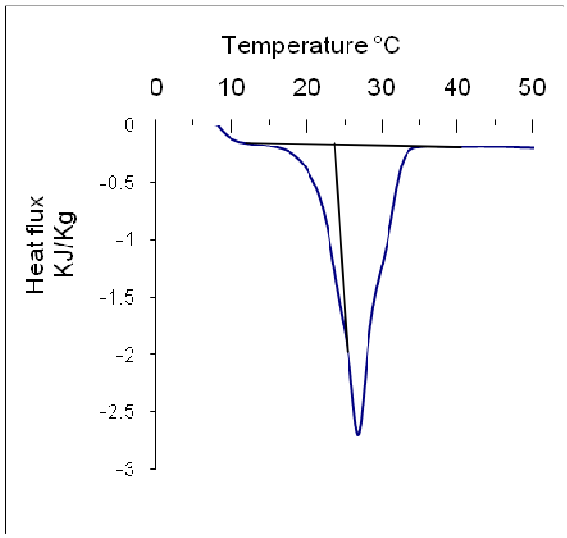

Figure 3.7 : DSC results for the capric-palmitic acid PCM

This PCM also shows promise for a PV cooling application due to (i) its high heat of fusion (ii) suitable melting point, (iii) melting peak in close proximity to the desired PV temperature and (iv) a moderate volume expansion of 8-10 % during phase change from solid to liquid. However, this PCM shows (i) an undesired wide range of heat absorption of 19 °C – 31.4 °C) caused by its very low thermal conductivity of 0.14 W $m^{-1}K^{-1}$ and (ii) also possesses a relatively low density of 0.87 kg dm^{-3} in solid phase (Schuette and Vogel, 1939; Sharma and Sagara, 2005). DSC characterizations results are summarized and compared with those found in literature in table 3.3.

As can be seen in table 3.2 none of the PCM possesses all of the desired properties. While changing phase from solid-liquid during measurement, each sample is far from

thermal equilibrium. A significant temperature gradient arises within the sample due to the PCM's relatively low thermal conductivity. This can lead to a deviation of several degrees Celsius from the indicated heat storage capacity with respect to temperature depending on sample size, heating rate and heat storage capacity of the sample. In order to study PCM behaviour more precisely further experiments were conducted using the temperature history method.

3.2.2 Temperature History Method (THM)

The limitations of DSC in accurately determining the thermophysical properties of PCM is that the sample mass is found to be optimum at 5 mg which is not representative of the masses in the range of kilograms used in practical applications. Supercooling-subcooling and nature of melting that depend on the quantity of PCM may vary substantially with a change of PCM sample mass from mg to kilogram. Therefore although the properties measured from DSC may serve as a reference, they do not give reliable information about the bulk PCM behaviour for practical large-scale applications. In order to determine properties for a reasonable PCM sample mass, Yinping *et al.* (1999) introduced the temperature history method (THM) based on recording the temperature of a PCM while it cools from a higher temperature liquid state to a lower temperature solid state through solidification. The cooling curve thus obtained can be used to determine the (i) start and end of solidification, (ii) specific heat capacity, (iii) amount of sub cooling/super cooling, (iv) latent heat released during solidification, and (v) temperature dependent enthalpy. The original method introduced by Yinping *et al* (1999) assumed that degree of super cooling

represented the end of melting and assumed no sensible heat due to incongruence, the latter occurring in real melting/solidification contribute to errors in determining thermophysical properties. The method was improved by Hong et al. (2004) by (i) considering the end of melting to be when the derivative of the temperature time graph on the cooling curve becomes minimum and (ii) including sensible heating in the calculation of heat capacity and enthalpy (Hong *et al.* 2004). Although the original THM was improved by the inclusion of considering sensible heating, the method derived by Hong et al. (2004) did not determine the temperature dependence of heat capacity and enthalpy of PCM. The THM was further extended by Marin et al. (2003) to determine temperature dependent properties such as specific heat capacity and enthalpy of the PCM and produced enthalpy temperature curves for PCMs (Marín *et al.,* 2003).

3.2.2.1 Experiments

To characterize PCM by THM, 25 g samples of each of the five PCMs was placed in 15 cm long glass test tubes with 1cm internal diameter and 0.8 mm wall thickness. These dimensions were selected to ensure that the Biot number, Bi = hR/2k was < 0.1 where *h* is the convective heat transfer coefficient, *R i*s radius of the tube and *k* is the thermal conductivity of the tube material. Satisfying these conditions enables heat transfer to occur solely in one-dimension along the length of the tube containing PCM so the tube can be considered a lumped system in front of heating or cooling source and the lumped capacitance method can be applied. The PCM and the reference (distilled water with known specific heat capacity) contained in the tube were heated

with the temperature raised to above 40 °C, then maintained at this temperature for 2 hours to get a homogenous solution of PCM and finally exposed to cool ambient. Temperatures of the PCM and the reference were recorded while cooling until the PCM solidified and temperature-time graphs were plotted for both the reference and the PCM. The governing equations to calculate specific heat capacity, heat of fusion and heat transfer coefficient are obtained by simple energy balance (Yinping *et al* 1999) as follows:

$$(m_t c_{p,t} + m_p c_{p,l})(T_0 - T_s) = h_c A_c A_1 \qquad (3.1)$$

Where m_p and m_t are the masses of the tube and PCM respectively, $c_{p,\,l}$ and $c_{p,\,t}$ are the mean specific heat capacities of the liquid PCM and the tube material respectively, h_c is the convective heat transfer coefficient respectively, A_c is the convective heat transfer area of a tube and $A_1 = \int_0^{t_1} ((T - T_{\infty,c})\,dt$ The heat loss by the cooling PCM is due to natural convection given by equation 3.2

$$m_p H_m = h_c A_c A_2 \qquad (3.2)$$

Where H_m is the heat of fusion of the PCM and $A_2 = \int_{t_1}^{t_2} ((T - T_{\infty,c})\,dt$ and $(t_1 \rightarrow t_2)$ is the time in which the phase change occurs and:

$$(m_t c_{p,t} + m_p c_{p,s})(T_s - T_r) = h_c A_c A_3 \qquad (3.3)$$

Where $c_{p,s}$ is the mean specific heat capacity of the solid PCM, $A_3 = \int_{t_2}^{t_3} ((T - T_{\infty,a})\, dt$ T_r is the reference temperature. If a tube containing pure water is suddenly exposed to the same ambient as of the PCM, it also cools and releases heat following the curve shown in figure 3.8. Considering the $B_i < 0.1$ similarly we have:

$$(m_t c_{p,t} + m_w c_{p,w})(T_0 - T_s) = h_c A_c A'_1 \qquad (3.4)$$

$$(m_t c_{p,t} + m_w c_{p,w})(T_s - T_r) = h_c A_c A'_2 \qquad (3.5)$$

Where m_w and $c_{p,w}$ are the mass and mean specific heat capacity of water, respectively,

$A'_1 = \int_0^{t'_1} ((T - T_{\infty,a})\, dt$ and $A'_2 = \int_{t_2}^{t'_2} ((T - T_{\infty,a})\, dt$

Using equation 3.4, the natural convective heat transfer coefficient (h_c) of air outside the tube is calculated which is 4.5 $Wm^{-1}K^{-1}$. Rearranging the equations described above, the specific heat capacity and the latent heat of fusion of the PCM can be calculated using the equations 3.6-3.8.

$$c_{p,s} = \frac{m_w c_{p,w} + m_t c_{p,t}}{m_p} \frac{A_2}{A'_2} - \frac{m_t}{m_p} c_{p,t} \qquad (3.6)$$

$$c_{p,l} = \frac{m_w c_{p,w} + m_t c_{p,t}}{m_p} \frac{A_2}{A'_2} - \frac{m_t}{m_p} c_{p,t} \qquad (3.7)$$

$$H_m = \frac{m_w c_{p,w} + m_t c_{p,t}}{m_p} \frac{A_2}{A'_1} (T_0 - T_s) \qquad (3.8)$$

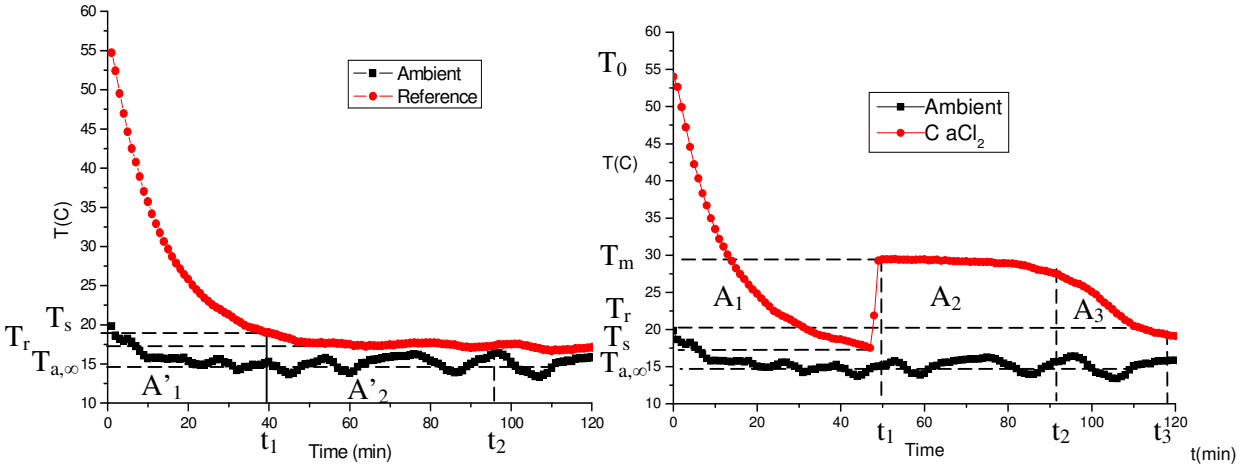

Figure 3.8: Temperature history curves for the distilled water taken as reference (left) and the sample PCM, $CaCl_2.6H_2O$ (right) when cooling from a higher temperature in the same ambient.

Using the equations 3.6-3.8, the specific heat capacity of each of the PCMs in solid and liquid phases is calculated. The $c_{p,\ s}$ and $c_{p,\ l}$ and H_m are calculated and are summarised in table 3.2. The calculated values from THM are closer to the values calculated from DSC analysis and the literature values are within maximum 5 % deviation from measured DSC and 10 % from literature values. The deviation can be attributed to the fact that this method relies on overly simplified custom made set up which are not precisely calibrated like conventional compared to DSC. Most of the reported values in literature are determined using DSC which also shows variation between values of the same material due to different measurement modes, operating conditions and instruments used. Considering these factors, the values obtained from

THM are reasonably accurate and can be compared with measured or literature values. Although THM allows calculating temperature dependent properties however this needs highly calibrated THM, where as the set up used in these experiments is very simple and can not be applied with confidence for temperature dependent properties. The temperature-time curve obtained for RT20 using THM is presented in figure 3.8. The PCM cooled from 40 °C to well below the solidification point until all the PCM had melted. It can be observed from the slope of figure 3.9 that the heat

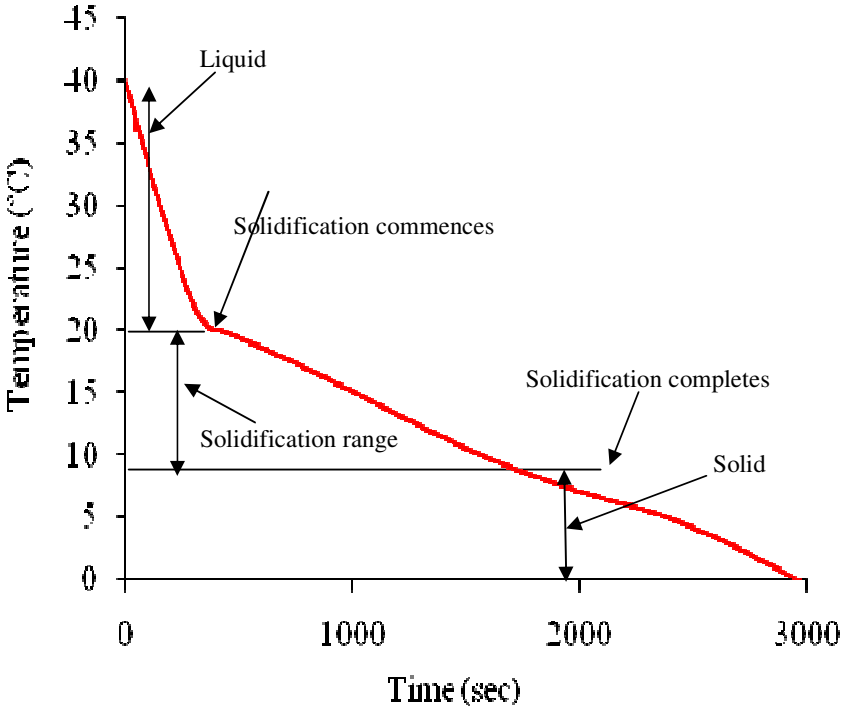

Figure 3.9 : Time- temperature curve for paraffins wax RT 20 using THM

release occurs in three different regimes. The sensible cooling starts from initial temperature of 40 °C down to the start of solidification at 21 °C. From start of

solidification at 21 °C to the end of solidification at 6 °C the heat release occurs as sensible as well as latent heat. After completing solidification, sensible heat is released below 6 °C. The graph shows that RT 20 has a wide range of solidification heat release from 21 °C - 6 °C in contrast to the isothermal heat release desired for this application.

Figure 3.10 shows the THM cooling curve for salt hydrate $CaCl_2.6H_2O$ when cooling from 55 °C to below its solidification point. It is observed that the PCM undergoes 11°C of subcooling before it starts solidification at 29 °C.

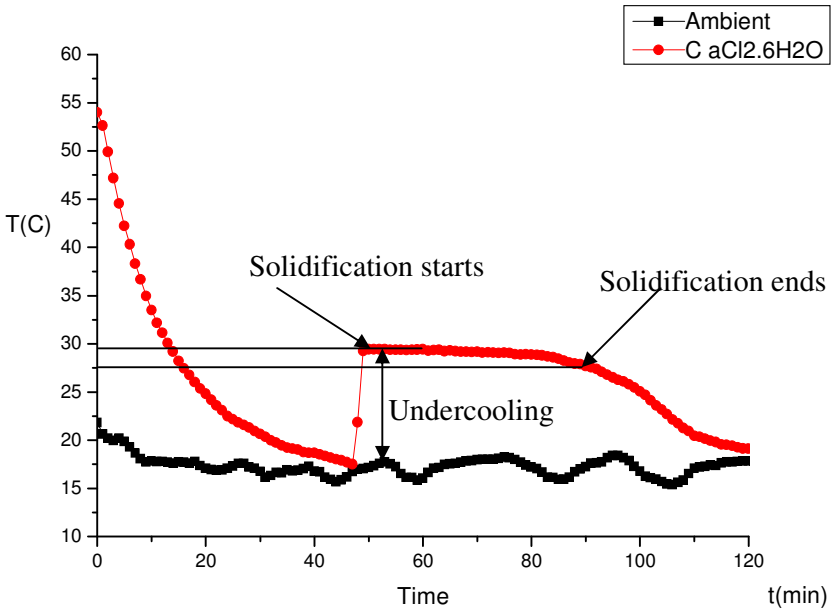

Figure 3.10 Temperature-time curve for salt hydrate CaCl2.6H_2O using THM

The heat release during solidification occurs between 29 °C-27 °C temperature range that is very close to the isothermal condition due to high thermal conductivity (1.09 W $m^{-1}K^{-1}$) of $CaCl_2.6H_2O$ compared to 0.2 W $m^{-1}K^{-1}$ of RT20. Heat release in a narrow

temperature range is a strongly desired property for this application. Subcooling is expected in salt hydrates as the salt needs to be cooled below melting point to start nucleation (Günther *et al.,* 2007b). $CaCl_2.6H_2O$ starts nucleation at a relatively lower temperature of 18 °C, below enough to typical ambient temperature of 25 °C, indicating that subcooling can be a major problem during heat removal from $CaCl_2.6H_2O$.

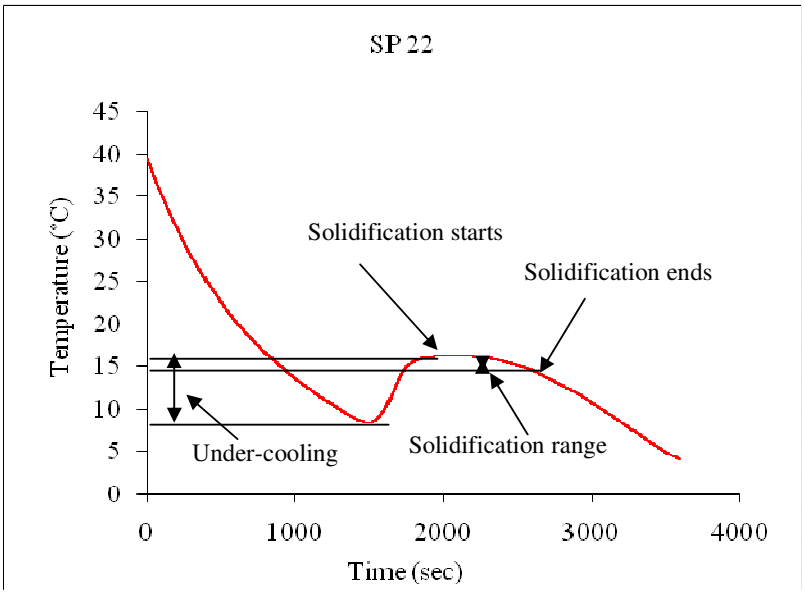

Figure 3.11 : THM Temperature-time curve for SP22 4A, a mixture of salt hydrate and paraffin wax

Figure 3.11 shows the THM curve of a blend of salt hydrate and paraffin wax, SP22 which undergoes 8 °C of subcooling before it starts solidification at 16 °C. The heat release during solidification occurs between 16 °C-15 °C temperature range that is very close to the isothermal due to high, thermal conductivity (0.6 $Wm^{-1}K^{-1}$) of SP22

compared to 0.2 $Wm^{-1}K^{-1}$ thermal conductivity of RT20. Heat release in a narrow temperature range is a strongly desired property for this application. Though subcooling is expected in a salt hydrate such as SP22 (Günther *et al.*, 2007a), the particularly lower subcooling than in $CaCl_2.6H_2O$ observed here is due the salt hydrate being blended with paraffin wax however the disadvantage is it melts over a wider range. This subcooling may be problematic as the salt needs to be cooled to 16 ˚C to start nucleation (Günther *et al.*, 2007b). In warm climates extra cooling may therefore be needed when heat is to be removed from such a PCM.

Figure 3.12 shows the THM time-temperature diagram obtained for eutectic mixture of capric acid-lauric acid cooling from melted state at 40 °C until complete solidification.

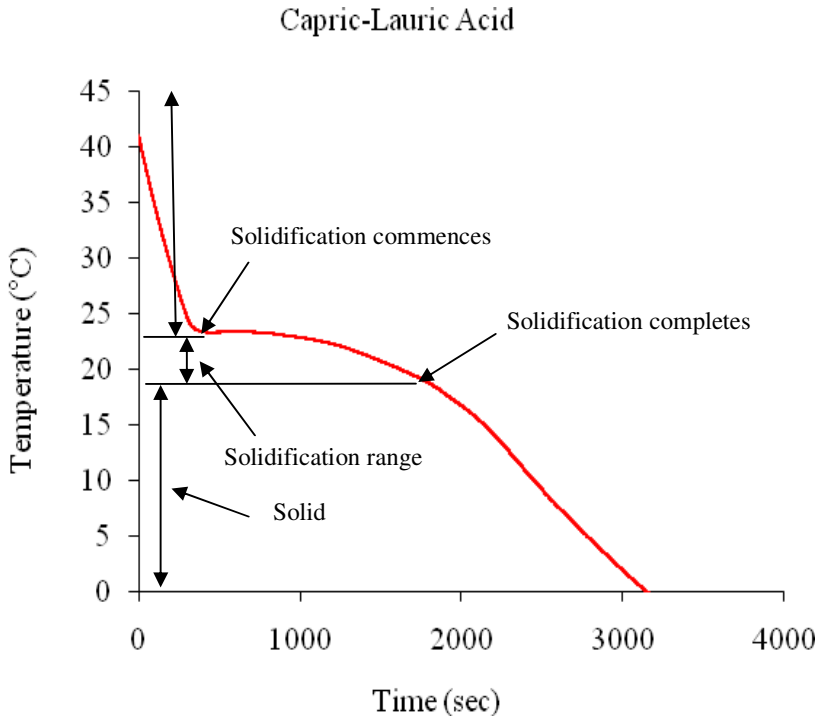

Figure 3.12 : THM Temperature-time curve for eutectic mixture of capric acid-lauric acid.

The graph shows that the fatty acid commences solidification at 24 °C without exhibiting any subcooling and completes solidification at 19 °C showing only 5 °C deviation from the isothermal heat release at solidification. The deviation from isothermal heat release during melting can be attributed to the low thermal conductivity, 0.14 W $m^{-1}K^{-1}$ of the PCM.

Figure 3.13 shows the THM results obtained for eutectic mixture of capric acid-palmitic acid while cooling from 40 °C to the complete solidification.

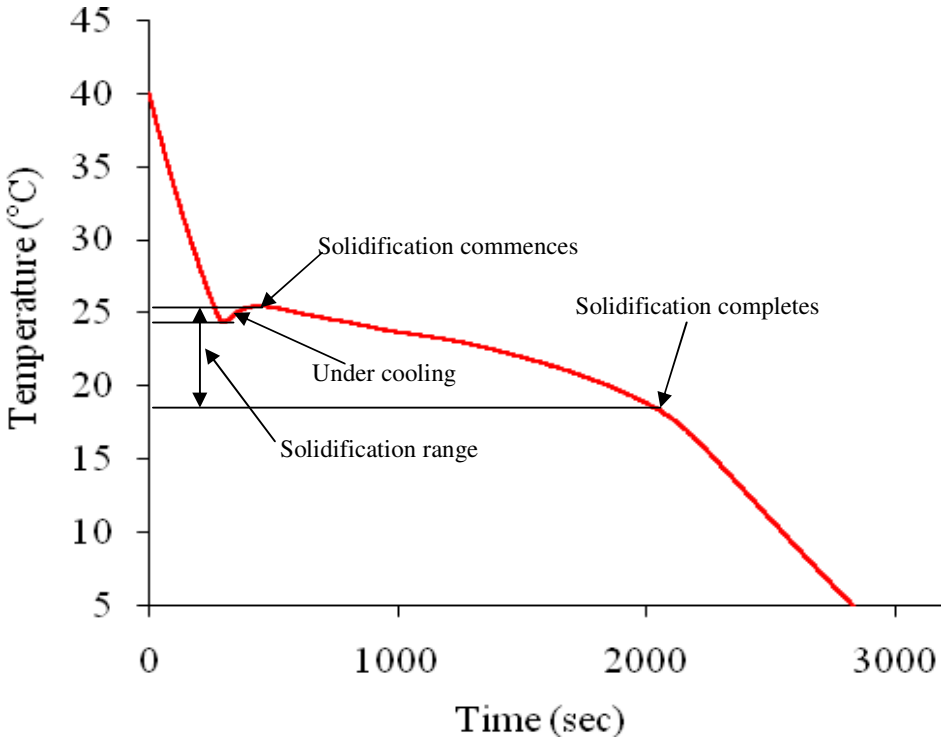

Figure 3.13 THM Temperature-time curve for eutectic mixture of capric acid-palmitic acid fatty acids

Results show that the PCM starts solidification at 25.5 °C with negligible sub-cooling of 1 °C and completes solidification at 18 °C. Heat release during solidification occurs in the temperature range of 7.5 °C which is a little higher than temperature for capric-lauric acid although their thermal conductivities are similar at 0.14 $Wm^{-1}K^{-1.}$ However, the solidification of capric-palmitic acid commences at a temperature 1.5 °C higher than the solidification temperature of capric-lauric acid. Solidification commencing at a higher a higher temperature with very little subcooling are the properties desired for this application.

3.3 Conclusions

Thermophysical characterization of all the PCM with DSC and THM showed good agreement with literature and within measured values. Salt hydrate $CaCl_2.6H_2O$ possessed the highest heat of fusion and narrow transition range which renders it suitable for PV thermal regulation however it starts melting at 29.6 ˚C slightly above desired temperature of 25 ˚C. $CaCl_2.6H_2O$ solidifies at a higher temperature which renders solidification possible at higher nocturnal ambient temperatures. The drawback of $CaCl_2.6H_2O$ is the highest undercooling of 11 ˚C down to 18 ˚C which makes solidification difficult at higher ambient temperatures. Mixture of salt hydrate and paraffin wax, SP22 also shows subcooling of 8 ˚C below its freezing temperature down to 16 ˚C and a wide range of melting/solidification which may impede its solidification. However both $CaCl_2.6H_2O$ and SP22 have higher thermal conductivities which make them suitable for efficient heat removal. Paraffin wax

RT20 melts and solidifies over a wide temperature range along with higher volumetric expansion which makes it unsuitable for the temperature control applications.

Both the fatty acids examined commenced solidification close to 25 °C and were fully solidified at close to 19 °C over a short temperature range with a very clear phase transition boundaries. Although they have very low thermal conductivities, the nature of melting and the start and end of solidification renders them suitable for an application requiring temperature control at around 25 °C. Based on these results it can be seen that a systematic choice of the PCM is however difficult and needs further indoor characterization on real PV systems to compare the potential of each PCM for PV thermal regulation.

3.4 References

Bailey, N. and Hay, J. (1999). "The Application of Modulated Temperature Power Compensation DSC to the Characterisation of Polymer Blends" Journal of Thermal Analysis and Calorimetry 56(3): 1011-1016.

Cabeza, L. F., Roca, J., Nogués, M., Mehling, H. and Hiebler, S. (2002). "Immersion corrosion tests on metal-salt hydrate pairs used for latent heat storage in the 48 to 58°C temperature range" Materials and Corrosion 53(12): 902-907.

Danley, R. L. (2002). "New heat flux DSC measurement technique" Thermochimica Acta 395(1-2): 201-208.

Dötsch, H. and Fink, H. (1987). "Calibration and application of a "heat flux DSC" in the study of heterogeneous catalyzed reactions" Thermochimica Acta 112(1): 51-56.

Ekeren, V.P. J., Holl, C. M. and Witteveen, A. J. (1997). "A comparative test of differential scanning calorimeters" Journal of Thermal Analysis and Calorimetry 49(2): 1105-1114.

El-Sebaii, A. A., Al-Amir, S., Al-Marzouki, F. M., Faidah, A. S., Al-Ghamdi, A. A. and Al-Heniti, S. (2009). "Fast thermal cycling of acetanilide and magnesium chloride hexahydrate for indoor solar cooking" Energy Conversion and Management 50(12): 3104-3111.

Farrell, A. J., Norton, B. and Kennedy, D. M. (2006). "Corrosive effects of salt hydrate phase change materials used with aluminium and copper" Journal of Materials Processing Technology 175(1-3): 198-205.

Günther, E., Mehling, H. and Hiebler, S. (2007a). "Modelling of subcooling and solidification of phase change materials" Modelling and Simulation in Materials Science and Engineering 15(8): 879-893.

Günther, E., Mehling, H. and Werner, M. (2007b). "Melting and nucleation temperatures of three salt hydrate phase change materials under static pressures up to 800 MPa" Journal of Physics D: Applied Physics 40(15): 4636-4642.

Hong, H., Kim, S.K. and Kim, Y.S. (2004). "Accuracy improvement of T-history method for measuring heat of fusion of various materials" International Journal of Refrigeration 27(4): 360-366.

Huang, M. J., Eames, P. C. and Norton, B. (2004). "Thermal regulation of building-integrated photovoltaics using phase change materials" International Journal of Heat and Mass Transfer 47(12-13): 2715-2733.

Huang, M. J., Eames, P. C. and Norton, B. (2006a). "Comparison of a small-scale 3D PCM thermal control model with a validated 2D PCM thermal control model" Solar Energy Materials and Solar Cells 90(13): 1961-1972.

Huang, M. J., Eames, P. C. and Norton, B. (2006b). "Phase change materials for limiting temperature rise in building integrated photovoltaics" Solar Energy 80(9): 1121-1130.

Karaipekli, A. and Sari, A. (2007). "Capric acid and palmitic acid eutectic mixture applied in building wallboard for latent heat thermal energy storage" Journal of Scientific and Industrial Research (JSIR) 66(06) 470-476.

Marín, J.M., Zalba, B., Cabeza, L.F. and Mehling, H. (2003). "Determination of enthalpy-temperature curves of phase change materials with the temperature-history method: improvement to temperature dependent properties" Measurement Science and Technology 14(2): 184-189.

Marini, A., Berbenni, V., Massarotti, V. and Flor, G. (1988). "On the quantitative reliability of heat flux DSC" Journal of Thermal Analysis and Calorimetry 33(1): 337-342.

Rubitherm, Technologies (2009). "Innovative PCM's and Thermal Technology ". Product Mannual RUBITHERM® SP22A17.

Sari, A. and Karaipekli, A. (2008). "Preparation and thermal properties of capric acid/palmitic acid eutectic mixture as a phase change energy storage material" Materials Letters 62(6-7): 903-906.

Schuette, H. and Vogel, H. (1939). "Solidification point curves of binary acid mixtures I. Capric, lauric, myristic, palmitic" Journal of the American Oil Chemists' Society 16(11): 209-212.

Sedat, K, Kamil, K. and Ahmet, S. (2005). "Lauric and myristic acids eutectic mixture as phase change material for low-temperature heating applications" International Journal of Energy Research 29(9): 857-870.

Sharma, S. D. and Sagara, Kazunobu (2005). "Latent Heat Storage Materials and Systems: A Review" International Journal of Green Energy 2(1): 1 - 56.

Shilei, L.V., Neng, Z. and Guohui, F. (2006). "Eutectic mixtures of capric acid and lauric acid applied in building wallboards for heat energy storage" Energy and Buildings 38(6): 708-711.

Sichina, W.J. (2000). "Better Heat Capacity Data with the Power Compensated DSC". PerkinElmers Instruments, Thermal analysis application note 2000

Tyagi, V. V. and Buddhi, D. (2008). "Thermal cycle testing of calcium chloride hexahydrate as a possible PCM for latent heat storage" Solar Energy Materials and Solar Cells 92(8): 891-899.

Yinping, Z., Yi, J. and J, Yi. (1999). "A simple method, the T-history method, of determining the heat of fusion, specific heat and thermal conductivity of phase-change materials" Measurement Science and Technology 10(3): 201-205.

4 INDOOR CHARACTERIZATION OF SMALL SCALE PHOTOVOLTAIC PHASE CHANGE MATERIALS SYSTEMS

4.1 Aim of the Experiments

Five different PCMs were characterized using two different thermophysical techniques i.e. DSC and THM as described in chapter 3. The results described the thermophysical properties of PCMs however they were unable to predict the temperature regulation behavior of PCM when integrated into the PV systems. In order to study the behavior of the PCM indoors when integrated into the PV systems indoor experiments were conducted at constant ambient temperature and with no air flow condition with following variables:

- Thermal mass of PCM
- Thermal conductivity of PCM and PCM container
- Melting point of the PCM
- Solar radiation intensity

4.2 Methodology

- Five different PCMs were evaluated experimentally indoors to determine the temperature regulation effect of each of the PCMs on cell-sized PV-PCM systems.

- Four different cell-size PV-PCM systems with different container material and dimensions detailed in table 4.1 were used to contain PCM behind the PV. The influence of solar radiation intensity, thermal conductivity of the PV-PCM systems and thermal mass of the PCM on thermal regulation of the PV was determined.
- Experiments were conducted at three solar radiation intensities of 500 Wm^{-2}, 750 Wm^{-2} and 1000 Wm^{-2} for each of the PCMs contained in the four different PV-PCM systems.
- Temperatures at front surfaces, back surfaces and side walls of the reference PV and the PV-PCM systems were measured.
- Temperature difference from the reference PV of each PV-PCM system was determined to quantify the temperature regulation achieved by each PCM contained in PV-PCM systems.

This methodology provided temperature reduction data achieved by each PCM, the effect of thermal mass of PCM on PV temperature reduction and the effect of PV-PCM container material on performance of the contained PCM.

4.3 Experimental Set up

Polycrystalline silicon PV cells with dimensions of 10 cm x 10 cm x 0.05 cm were encapsulated between two sheets of 3 mm thick transparent perspex to simulate a cell size section of a PV module. Perspex thickness of 3 mm was selected corresponding to generally applied thickness of PV encapsulation to obtain enough mechanical strength to bear external pressures and wind speed. Perspex was used as encapsulation

material because it was easily accessible, possesses similar optical thermal and mechanical properties to most of the PV encapsulation materials i.e. glass and polymers. Four rectangular containers, as described in table 4.1 were fabricated and a PV cell was attached to the front of each container as illustrated in Figure 4.1 Different container materials and container dimensions were chosen to compare thermal performance of (i) Heat conductive (A & C) compared with heat insolating (B & D) containers (ii) PCM having different thermal masses on PV thermal regulation at different insolations (iii) Thermal performance of corrosive metallic PCM container compared to the non corrosive polymeric PCM containers. The dimensions of 3cm and 5cm were calculated by making thermal balances on a PV-PCM system at 500 Wm^{-2} and 1000 Wm^{-2} to accommodate enough thermal mass of paraffin wax PCM to regulate PV-PCM temperature until fully melted in 8 hours from previous work by authors (Huang *et al*., 2004). The paraffin wax RT25 used in the previous research had similar thermophysical properties to paraffin wax RT20 used in the current research.

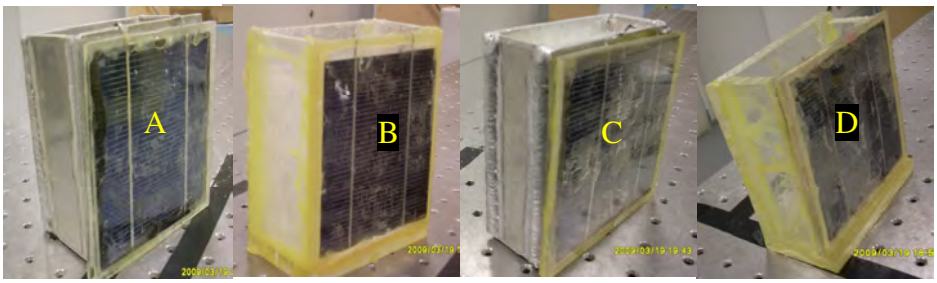

Figure 4.1 Photographs of PV-PCM systems A, B, C and D as described in table 4.1

	PV-PCM systems			
	A	B	C	D
Container material	Aluminium	Perspex	Aluminium	Perspex
Thermal conductivity of material ($Wm^{-1}K^{-1)}$	237	0.19	237	0.19
Container width internal (cm)	5	5	3	3

Table 4.1 PV-PCM systems A, B, C and D fabricated from aluminium (A & C) and perspex (B & D)

Systems A & C were fabricated from 5 mm thickness high thermal conductivity, 237 $Wm^{-1}K^{-1}$ aluminium alloy 1050A from Aalco (Aalco, 2007), which enabled increased heat removal rate from PV into PCM leading to a decreased time of melting of the PCM (Shina and Inagaki, 2005; Sharma *et al.*, 2006). However systems A & C being highly heat conductive had less heat retention due to heat loss to ambient through their conductive surfaces (Martin *et al.* 1990). The high conductivity aluminium side walls and back surface of the PV-PCM systems A and C were kept heat un-insulated to allow maximum heat dissipation through container walls to the ambient to provide maximum cooling of PV cells. Systems B & D were fabricated on all the five sides (front, back, two side and a top and a bottom wall) from a 10 mm thick perspex, "MARCRYL CLEAR" from Vink Plastics that had very low thermal conductivity, 0.19 $Wm^{-1}K^{-1}$ (Vink, 2007). This lower thermal conductivity enabled higher heat retention due to less heat loss to ambient because of thermally insulating

side and back perspex walls however it had a low heat removal rate from PV into PCM (Chen *et al.* 2008) .

Although aluminium has higher thermal conductivity which enables efficient heat transfer from PV surface to PCM, it corrodes with most of the PCM which may result in reduced PCM container life. The advantage of using perspex instead of aluminium is its less corrosion to most of the PCM which yields longer PCM container life however it results in less efficient heat removal which may result in higher temperatures at PV surface.

4.4 Experimental Procedure

The reference experiments were conducted by irradiating the PV section with a Griven GR262 solar simulator at insolations of 500 Wm^{-2}, 750 Wm^{-2} and 1000 Wm^{-2} with ambient temperature at 20 ±1 °C (Appendix A). The spectrum of the solar simulator was measured and compared with the standard solar spectrum to calibrate the solar simulator. The solar radiation intensity was measured at the PV front surface at a fixed position of the solar simulator from the PV cell, the positions were marked and fixed for repeatability to produce desired insolations (i.e., 500 Wm^{-2}, 750 Wm^{-2} and 1000 Wm^{-2}) in particular experiment which were kept constant for the whole duration of the experiment. Although the common design criteria for design qualification of PV is to test them at lower irradiations of 200 Wm^{-2}, however in context of the current research this low irradiation ends up in low temperatures at PV surface which would need little or no cooling rendering use of PCM irrelevant for temperature regulation of PV. Higher solar radiation intensities however are likely to

achieve sufficiently higher temperatures at PV surface that would cause PV power failure and require temperature regulation to maintain rated power output. The insolations of 500 Wm^{-2} to 1000 Wm^{-2} were selected to achieve higher temperature at PV surface representative of high insolation ambient where PV has higher thermal load and can justify use of PCM for PV thermal management. Temperatures at the PV front and back surfaces were measured with calibrated T-type copper-constantan thermocouples with the maximum measured deviation of ±0.2 ˚C. Thermocouples were installed with 2 cm displacement from sides, top and bottom of PV and 3 cm distance from each of the adjacent thermocouple locations at front surface of the PV and are illustrated in figure 4.2.

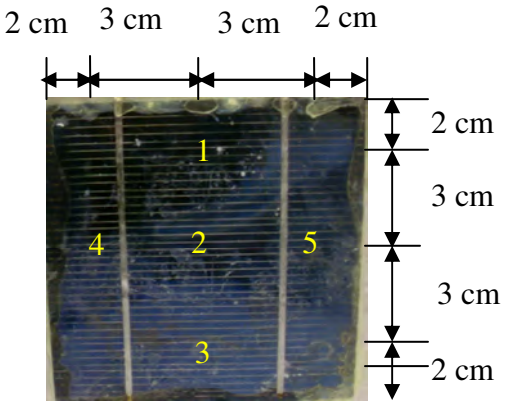

Figure 4.2: Position of thermocouples on front surface of the PV section

The insolation was measured with a Kipp and Zonen CM6B pyranometer with a maximum measured spatial intensity variation of ±2 % over the PV front surface described in appendix B. (Kipp and Zonnen 2003). The data were recorded in ΔT data logger described in Appendix C. Experiments were conducted with each of the selected PCM contained in systems A, B, C & D under the same test conditions (i.e.,

500 Wm^{-2}, 750 Wm^{-2} and 1000 Wm^{-2} at ambient temperature of 20 ±1 °C) with the experimental setup as shown in the Figure 4.3. Each experiment was conducted twice to confirm their repeatability. The error in two corresponding measurements for the same experiments remained always in the range of 1-3 % which can be attributed to the error range of the instruments used.

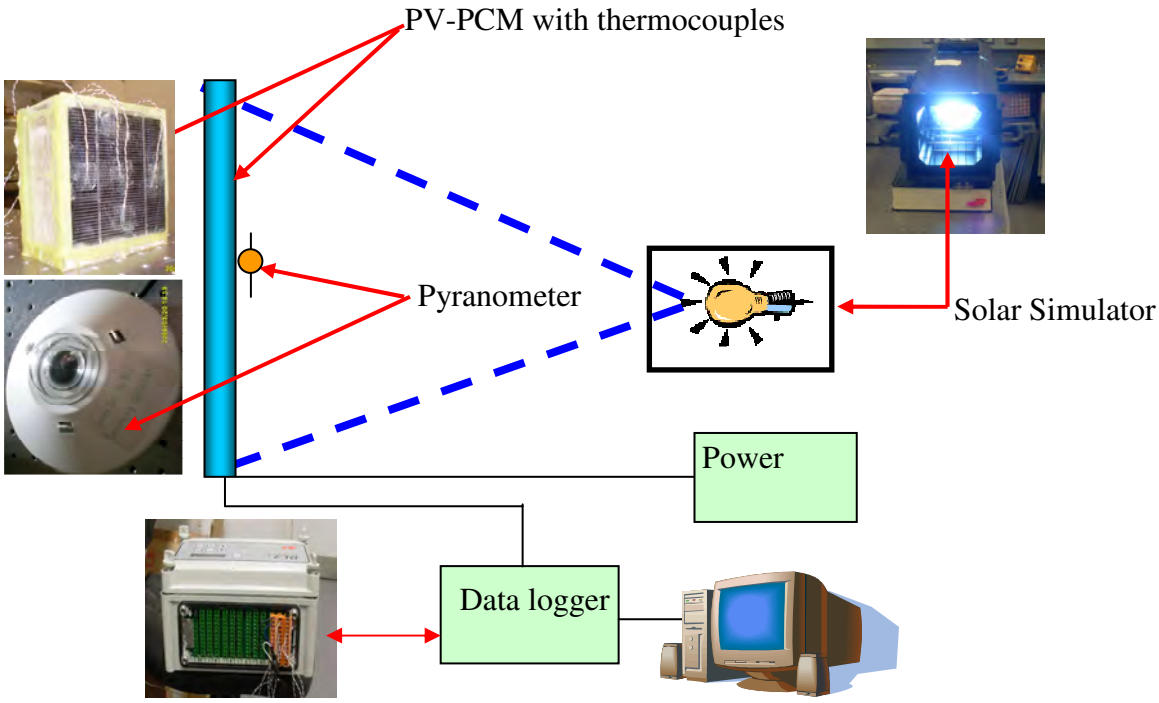

Figure 4.3 Schematic of the experimental setup showing a cell size PV irradiated with a Griven GR262 solar simulator, temperature and irradiation measured with a Kipp and Zonen CM6B pyranometer and T-type thermocouples respectively via a Delta-T 2e data logger.

4.5 Results and Discussion

4.5.1. Validation of PV cell's temperatures

For each experiment the temperature at PV front surface increased rapidly to reach a steady state when heat input to PV due to irradiation equalled the heat lost by the PV to ambient primarily due to natural convection. Reference steady-state temperatures, their corresponding insolations and the time elapsed to reach these steady state temperatures were, 45 °C at 500 Wm^{-2} in 80 minutes, 51 °C at 750 Wm^{-2} in 40 minutes and 57 °C at 1000 Wm^{-2} in 34 minutes. Each of the experiments described in following sections was conducted twice for repeatability and generally good agreement between corresponding measured temperatures was observed with deviation ranging from 1-3 %. In following sections average temperatures at the front surface of PV-PCM systems for each experiment will be compared with the average PV cell temperature without PCM at various insolations, PCMs and PV-PCM systems at fixed ambient temperatures.

Initial simulations were undertaken using the model described in section 2.5 for PV cell without integrated PCM to calculate temperature evolution at the front surface un-cooled PV cell. Model results provide a reference temperature levels obtained at PV front surface which are validated with the measured experimental temperature data shown in figure 30, 31 and 32 at 1000 Wm^{-2}, 750 Wm^{-2} and 500 Wm^{-2} insolation, respectively. In case of 1000 Wm^{-2} insolation the temperature rises to 55 ^{o}C in half an hour while in the same duration, temperature rise was 49^{o}C and 41^{o}C at 750 Wm^{-2} and 500 Wm^{-2} respectively. The initial gradient of temperature is same in both simulated

and experimental results but after 30 minutes the temperature rise is less in simulation as compared to experimental results. This is due to the difference of atmospheric condition between experiment and simulation. In the simulation model air heating adjacent to the heat source, i.e. solar simulator is not considered and the heat transfer is considered only between the PV surface and the adjacent air. In real operating conditions the solar simulator surface also gets heated and transfers heat to the ambient air enclosed between solar simulator and the PV cell reducing temperature difference and the heat transfer between the PV surface and the ambient air resulting in higer PV temperature. However the difference is only ~1-2 Kelvin and will not have a large effect on the solar to electrical conversion efficiency of PV cell. It can be improved by considering air heating near solar simulator and by mesh refinement at the cost of increased computation time.

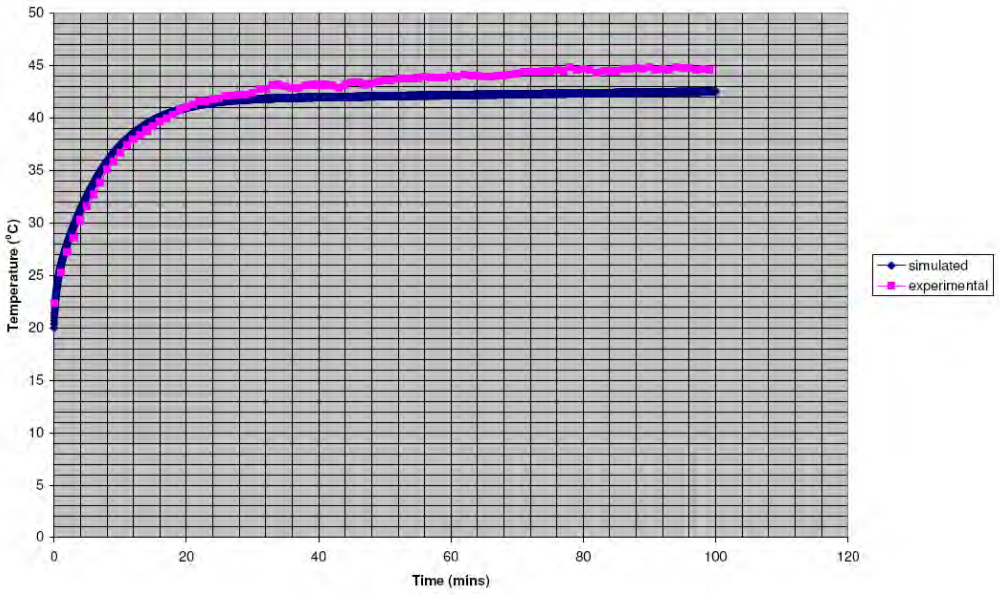

Figure 4.4: Temperature evolution on PV cell at 500 Wm^{-2} insolation and 20 ±1 ˚C ambient temperature.

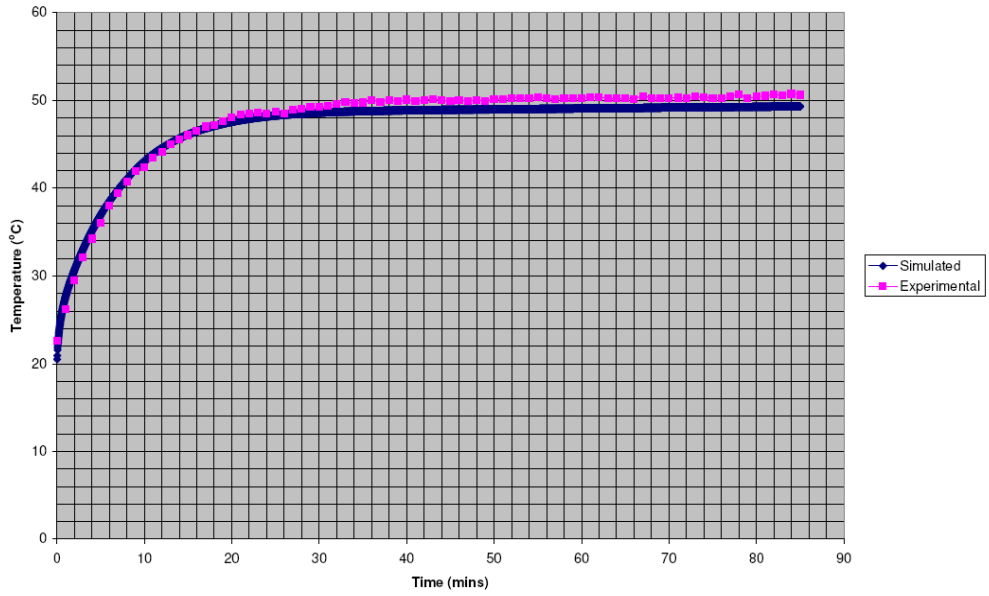

Figure 4.5: Temperature evolution on PV Cell at 750 Wm^{-2} insolation and 20 ±1 ˚C ambient temperature.

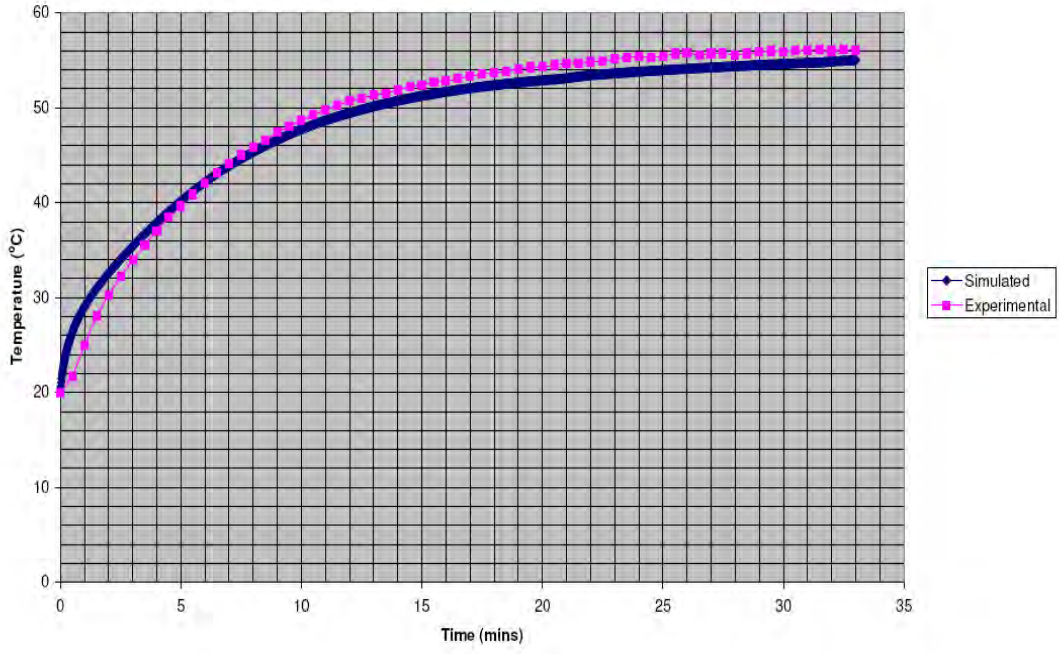

Figure 4.6: Temperature evolution on PV Cell at 1000 Wm^{-2} insolation and 20 ±1 ˚C ambient temperature.

4.5.2. Validation of PV-PCM System

Figure 4.7 shows both experimental and simulated results of the temperature evolution on PV-PCM System at insolation level 1000 Wm^{-2} using PCM RT20. The insolation of 1000 Wm^{-2} was selected as is the insolation at which the PV are rated while the PCM RT20 was selected because its thermophysical properties input to this model were already verified through an earlier modelling work by Huang *et al.,* 2006a using similar thermophysical properties as in the current model. Initial gradient of temperature rise as well as the final temperature rise is the same for both experimental and simulated results. After half hour of exposure to solar radiations at 750 Wm^{-2} the temperature in PV-PCM system rose to 43.5 ^{o}C in simulated result and 45 ^{o}C in experimental results compared to 51 ˚C in PV without PCM. This shows temperature regulation effect of 7.5 ˚C in modelled results and 6 ˚C in experimental results which indicates that the model has over predicted temperature regulation in the start. In the middle part i.e. between 45 minutes to 150 minutes, the model has predicted less temperature regulation than the experimental results as can be seen from figure 4.7. The prime reason for this difference between simulated and experimental result is starting point for phase change process and the variation of density with temperature. In the modelled temperature curve, the gradient of temperature rise starts to decrease earlier than that in experimental curve which indicates an earlier start to melting process and latent heat absorption.

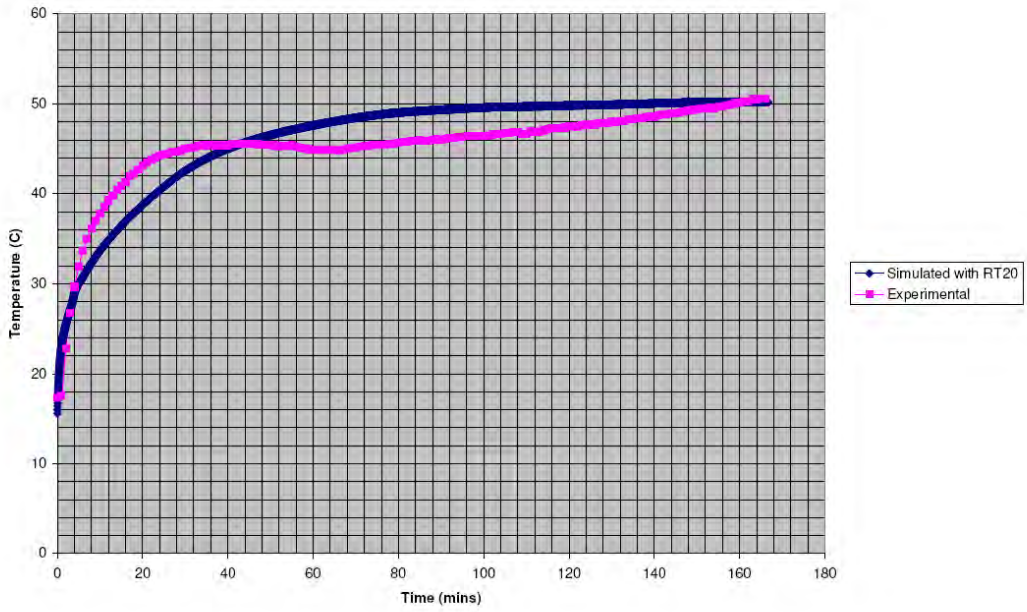

Figure 4.7 : Comparison of temperature evolution on PV Cell with and without integrated PCM RT20 at 1000 Wm^{-2} insolation and 20 ±1 ˚C ambient temperature.

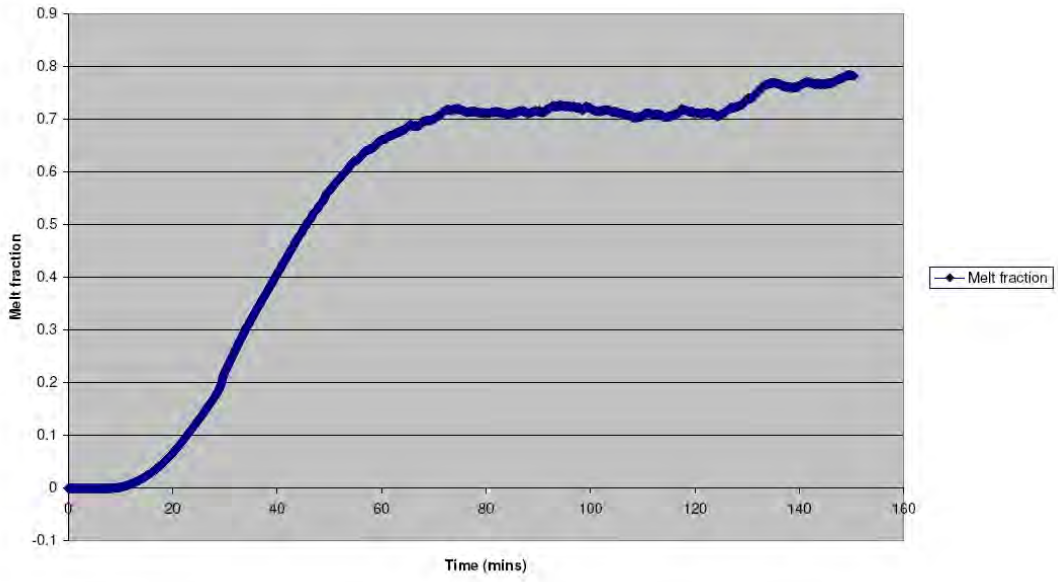

Figure 4.8: Melt fraction of PCM RT20 at 1000 Wm^{-2} insolation and 20 ±1 ˚C ambient temperature

From figure 4.8, it can be seen that the melting started after 10 minutes represented by sharp increase in melt fraction. Due to earlier start of phase change, temperature regulation starts earlier in simulation model which results in over predicted temperature regulation in first half an hour. Later variation in the middle part of both modelled and experimental temperature curves may be, in author's point of view, due to density variation of actual and modelled PCM. The input density in the model is piecewise linear with only two points given as input i.e. density in solid phase and density in liquid phase assuming a linear relationship between these two points while in reality, density variation is highly non-linear behaviour (Huang *et al.,* 2006) In actual conditions, density changes very quickly initially due to heat transfer by conduction between solid PCM and PV Cell while as the melting front move towards the back of the container, density variation reduces due heat to transfer by convection rather than conduction caused in part by lower thermal conductivity of PCM i.e. 0.2 $Wm^{-1}°C^{-1}$.

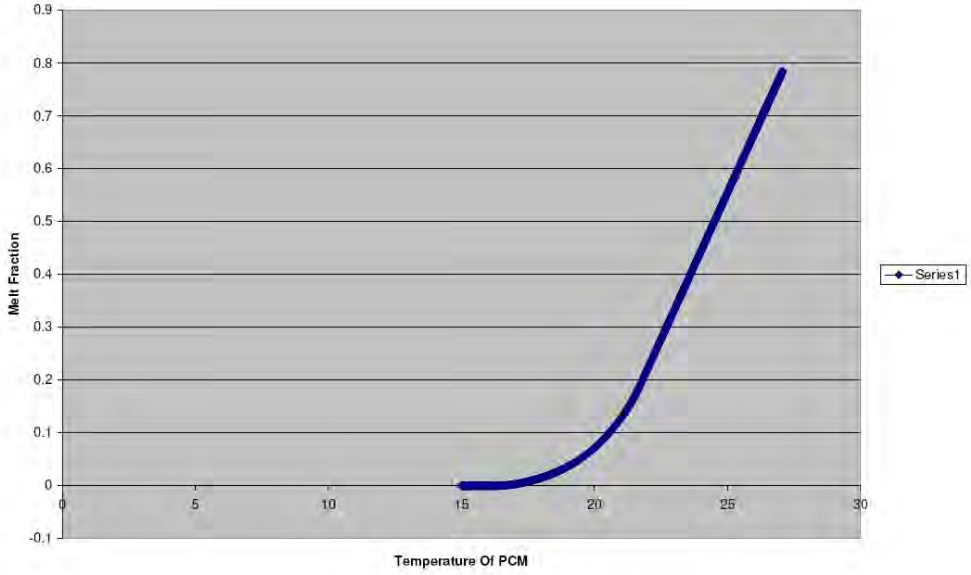

Figure 4.9: Melt fraction against temperature of PCM RT20 at 1000 Wm^{-2} insolation and 20 ±1 ˚C ambient temperature

.

In simulations the density variation is linear so the melt fraction also follows a linear curve with respect to temperature as the melting front moves away as shown in figure 4.9. Figure 4.10 shows distribution of melt fraction during the experiments. Compared to real PV-PCM system the top, bottom, left and right surfaces shown in figure 4.10 are the front, back, top and bottom of the real PV-PCM system.

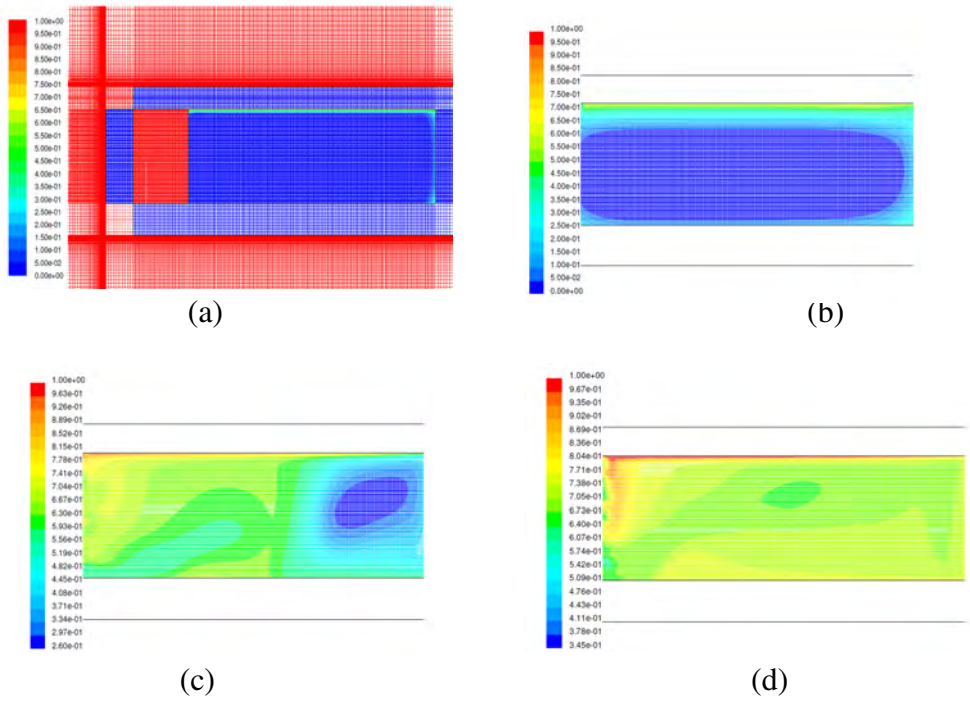

Figure 4.10 : Melt fraction of RT20 at 1000Wm^{-2} insolation and 20±1 ambient temperature (a) after 20 minutes, (b) after 50 minutes, (c) after 100 minutes and (d) after 160 minutes.

It shows that the melting front is planar at the start of the experiment (figure 4.10 a) when heat transfer is due to pure conduction however after 50 minutes, it starts to form curvature (figure 4.10 b) when sufficient PCM melt has developed. After 100

minutes (figure 4.10 c) it can be observed that the lighter PCM with higher melt fraction in the mushy zone moves upward due to buoyancy driven natural convection caused by density difference and heavier PCM with lower melt fraction in the mushy region moves downward in the direction of gravity with solid PCM accumulated at the bottom of the PV-PCM system. After 160 minutes no pure solid is present and the a stronger distribution of melt fraction in the mushy region is observed due to stronger buoyancy driven natural convection with clear distinction of fully melted PCM at top and near the heated surface and heavier less-melted PCM layers moving all the way downwards to the bottom due to gravity. This shows how natural convection in the melt changes the shape of the initially plane melting front.

4.5.3. Heat Transfer Mechanism in the PV-PCM System

In the PV-PCM system, the continuous heat input from incoming solar radiations raised PV and consequently PCM temperature. At start temperature rise in PV-PCM system was rapid up to 25-30 °C due to sensible heating of PV which transferred heat to the solid PCM at the back due to conduction showing very little deviation from the reference system temperature. Above 30 ˚C PV front surface temperature, the PCM contained in PV-PCM system in direct contact with the PV back surface started melting and absorbing PV thermal energy as latent heat. As a result of PCM melting at fixed melting point the rate of temperature rise at PV front surface started to decrease and deviate from the reference system temperature. A thin layer of melted PCM developed between the heated PV back surface and the solid PCM. The melted PCM layer started sensible heating with a rise in temperature while the solid PCM

further away still continued to melt and absorb latent heat. The melted layer had a lower thermal conductivity than the initially solid PCM decreasing heat transfer rate to solid PCM and induced a temperature difference between the melted and solid PCM. As the melt fraction increased, temperature difference in melted PCM induced a density difference in the melt with lighter and heated fluid moving upward to the container top due to buoyant natural convective heat transfer. The natural convection resulted in different rate of melting at top and bottom PCM layers that introduced a curvature in the initial planar melting front that caused the melting front to breakdown. Higher density solid PCM started falling to the bottom of the PCM container while lower density liquid PCM moved upward due to buoyancy to the top of the PCM further increasing the temperature difference between top and bottom of the PCM. As the heat absorption continued, the melt fraction continued to grow rendering increasing convection in the melted PCM compared to conduction in the solid PCM thus a larger deviation from isothermal heat absorption ensued. The melting rate thus decreased the temperature rising slowly controlled by natural convection until whole the PCM had melted. After the PCM had melted fully as the latent heat is fully used a sharp increase in the PV temperature was observed which reached the reference PV temperature in shorter time. In order to describe the heat transfer mechanism in the PCM indicative Raleigh numbers *(Ra)* are calculated using (Huang *et al.,* 2006):

$$Ra = \frac{g\beta(T_s - T_\infty)x^3}{\nu\frac{k}{\rho c_p}} \qquad (4.1)$$

Where g is the gravitational constant, β is the coefficient of thermal expansion of PCM, T_s is the surface temperature, T_∞ is the bulk temperature, v is the kinematic viscosity of PCM, κ= is thermal conductivity of the PCM, ρ is density of the PCM, c_p is the specific heat capacity of the PCM and x is the distance from the front surface.

with the following assumptions (i) The melting front location is taken at the centre of the PCM, i.e. at 2.5 cm from the heated front PV surface after half of the time of turning the solar simulator on (ii) The bulk PCM temperature is taken as average temperature between the front and back surface temperature of PV-PCM system after half of the PCM had melted. (iii) Constant phase and temperature independent values of thermal conductivity, specific heat capacity, density, viscosity and volumetric expansion coefficient of PCM are considered. The thermal mass and *Ra* number were calculated for each PCM and are given in table 4.2. Table 4.2 shows that $CaCl_2.6H_2O$ has the highest thermal mass (2.65 kJK^{-1}) while RT20 has the lowest thermal mass (1.03 kJK^{-1}) while the fatty acids fall in between which indicates that the $CaCl_2.6H_2O$ would result least temperature rise while RT20 would result in the highest temperatures rise with same amount of heat input.

Table 4.2 shows also that the *Ra* number varies from 3.8 $x10^3$ to 1.4 x 10^7 which confirms the presence of natural convection and laminar fluid flow in PV-PCM system. It also shows that the salt hydrates $CaCl_2.6H_2O$ has the lowest *Ra* number (10^3) indicating less convective heat transfer compared to fatty acids having the highest *Ra* (10^7) number showing the strongest convection within all the PCMs. It also shows that in each PCM the *Ra* number increases with increasing solar radiation intensity due primarily to increased temperature difference.

		Thermal mass (kJK^{-1})	Raleigh number
RT20	500	1.03	1.8×10^4
	750	1.03	2.6×10^4
	1000	1.03	3.5×10^4
SP22	500	2.09	8×10^3
	750	2.09	1×10^4
	1000	2.09	1.4×10^4
$CaCl_2.6H_2O$	500	2.65	3.8×10^3
	750	2.65	5.8×10^3
	1000	2.65	7.6×10^3
CL	500	1.39	5.8×10^6
	750	1.39	8.6×10^6
	1000	1.39	1.2×10^7
CP	500	1.47	6.8×10^6
	750	1.47	1.1×10^7
	1000	1.47	1.4×10^7

Table 4.2; Calculated thermal mass and indicative Raleigh numbers from the thermophysical properties of the PCMs described in table 3.2.

4.5.4. Thermal Regulation at 500 Wm^{-2} Insolation

Each experiment was conducted until all the PCM had melted and solar simulator was stopped after PV-PCM temperature equalled reference temperature because if the solar simulator was kept running after the PCM afterwards, the increased thermal mass of PV-PCM system due to PCM would continue absorbing heat and act as heat insulator compared to free back PV thus overheating the PV. In outdoor experiments however it is not possible to stop heat input due to uncontrolled nature of solar radiation, it becomes extremely necessary to remove heat from melted PCM effectively by flowing cooling fluid (water or air) into the PCM at complete PCM

melting. This heat extraction mechanism needs to be optimized for different climates and ambient condition to avoid overheating of the PV-PCM system due to thermal insulation provided by integrated PCM.

Figure 4.11 presents the temperatures on the PV front surface for all PCMs in system A compared with the reference system at 500 Wm^{-2} insolation and 20 ±1 °C ambient temperature.

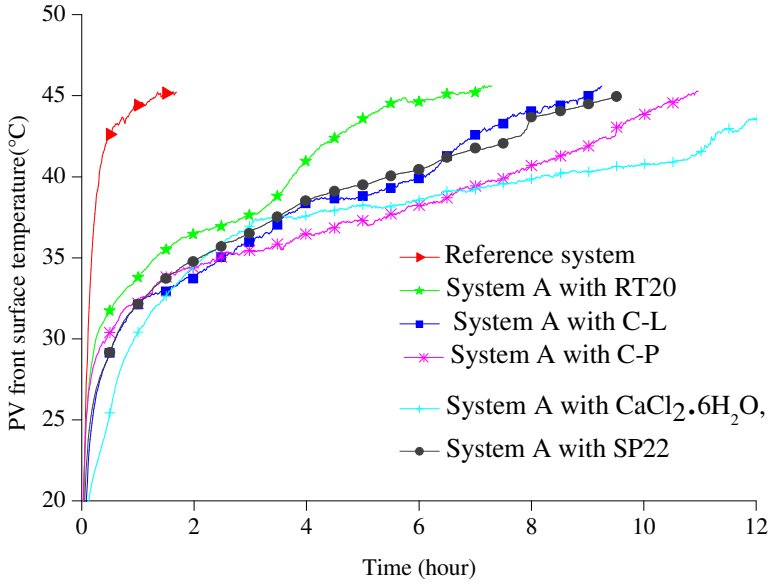

Figure 4.11 Temperature evolution on the front surface of the reference PV system and PV-PCM system A containing each PCM type at an insolation of 500 Wm^{-2} and ambient temperature of 20 ±1 °C

The temperature at the reference system without PCM increased rapidly due to continuous heat input from the solar radiation falling on the PV and reached steady state at 45 °C in 1 hour. The magnitude and duration of deviation of PCM temperature in system A from the reference PV system quantifies the thermal regulation enhancement of PV achieved using PCM. The duration of the deviation is given by

the time in which the temperature in system A containing PCM equalled the temperature in the reference system which is 6.5 hours for RT20, 9 hours for CL, 9.5 hours for SP22, 11 hours for CP and 13 hours for $CaCl_2.6H_2O$. RT20 showed the shortest time of temperature deviation that is expected result due to its lowest thermal mass while $CaCl_2.6H_2O$ showed the longest duration of melting owing to its highest thermal mass compared to other PCMs which fell in between. Observing temperature difference from reference, after 4 hours the temperatures in system A were below the reference temperature by 4.6 °C with RT20, 6.5 °C with SP22, 7 °C with CL, 7.5 °C with $CaCl_2.6H_2O$ and 8 °C with CP respectively. It was observed that RT20 showed the smallest temperature deviation from reference of 4.6 °C and shortest duration of the deviation of 6.5 hours primarily due to lower thermal mass and heat of fusion compared to salt hydrate and fatty acids. CP showed the largest temperature deviation from the reference of 8 °C due to its lower melting point compared to $CaCl_2.6H_2O$ while $CaCl_2.6H_2O$ showed the longest duration of the temperature deviation of 13 hours due to its highest thermal mass and heat of fusion compared to other PCMs.

Results obtained when using PCMs contained in systems B, C and D under the same conditions of 500 Wm^{-2} and 20 ± 1 °C are shown in Figures 4.12 – 4.14. Similar trends in temperature evolution can be observed in all three PV-PCM systems however each PV-PCM system, B, C and D achieved less temperature difference from the reference system for shorter time durations than PV-PCM system A.

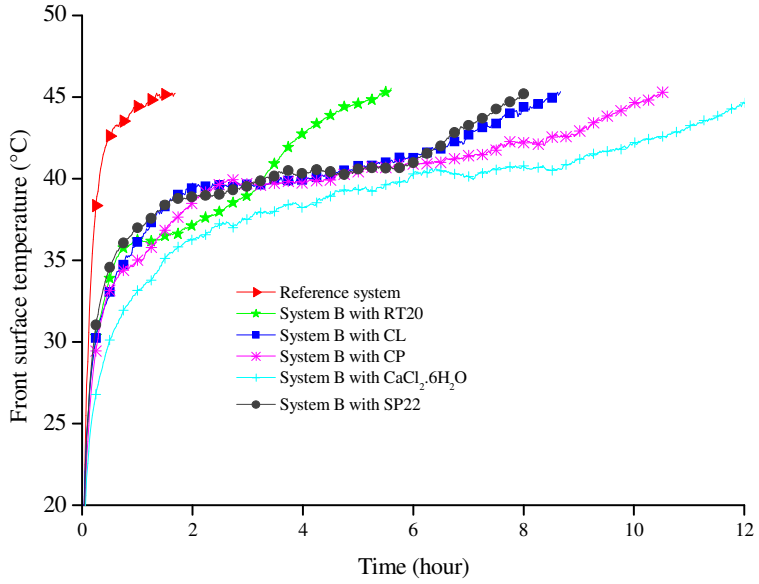

Figure 4.12 Temperature evolution at front surface of the reference PV system and the PV-PCM system B at an insolation of 500 Wm^{-2} and ambient temperature of 20 ±1 °C.

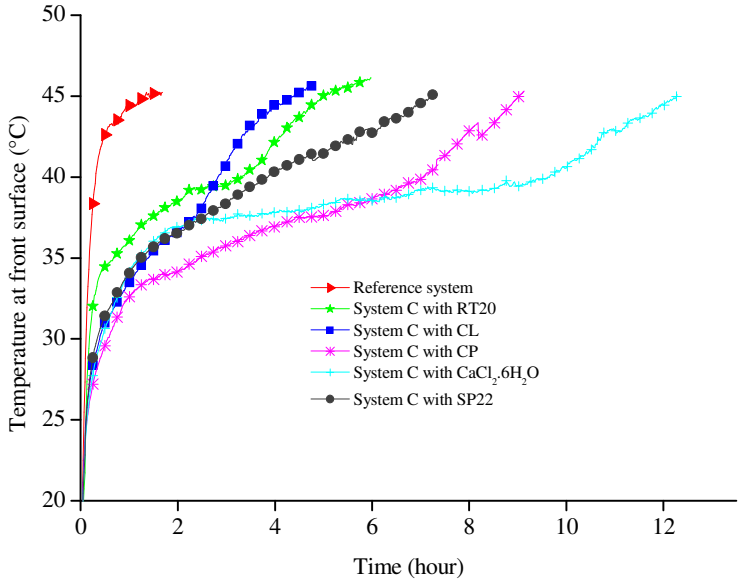

Figure 4.13 Temperature evolution at front surface of the reference PV system and the PV-PCM system C at an insolation of 500 Wm^{-2} and ambient temperature of 20 ±1°C

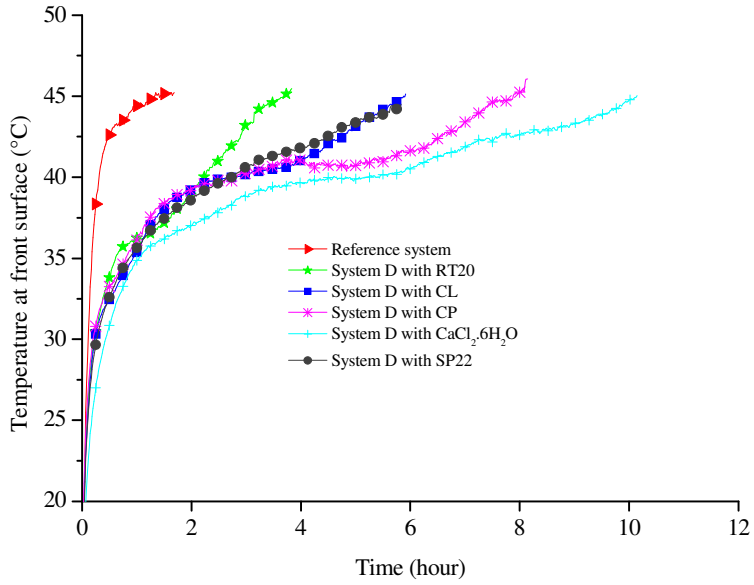

Figure 4.14 Temperature evolution at front surface of the reference PV system and the PV-PCM system C at an insolation of 500 Wm^{-2} and ambient temperature of 20 ±1°C

In order to compare the performance of different PCMs in system A, B, C and D, the duration for which PCM in each of these systems maintained their temperature 10 °C below the reference system temperature is illustrated in Figure 4.15. It can be seen that all PCM types when used in system A maintained a 10 °C temperature reduction for the longest duration compared to system B, C and D. Although system A & B have the same dimensions (accommodating the same PCM thermal mass with same PCM thermophysical properties of melting point, heat of fusion and thermal conductivity) system A been fabricated from aluminium alloy has a higher thermal conductivity than system B which have been fabricated from polymer perspex.

Since system A and B only differ in thermal conductivity of container, it indicates that thermal conductivity of the container helps improve efficient heat transfer in system A

compared to system B yielding lower temperatures at PV front surface for longer durations of time. Similarly PCM in system C maintained a temperature reduction for a longer duration than system D, although both have the same dimensions (accommodating the same PCM thermal mass with same PCM thermophysical properties of melting point, heat of fusion and thermal conductivity) however system C has higher thermal conductivity than system D. It also indicates that the thermal conductivity of the container material helps to achieve lower temperature for longer duration of time. From observation mentioned above it can be concluded that at low insolation all PCM types performed better in high thermal conductivity systems A & C compared with the same sized lower thermal conductivity systems B & D.

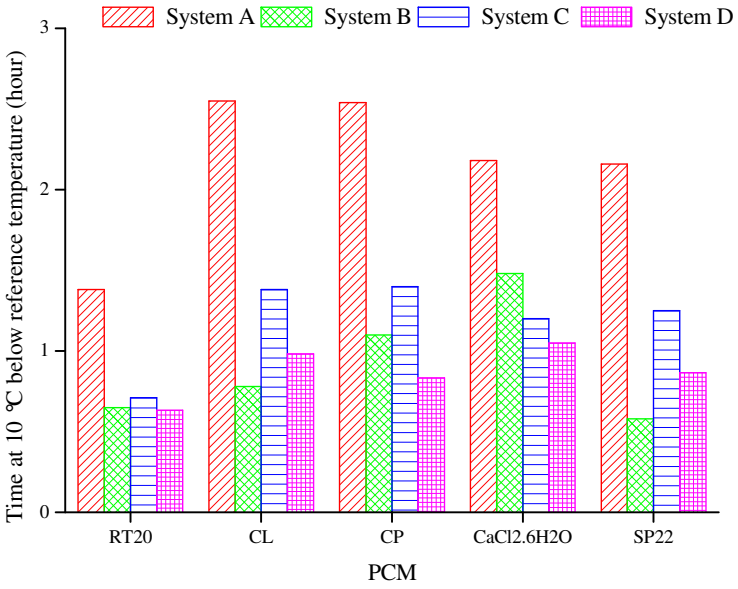

Figure 4.15 Duration for which PCM maintained PV front surface temperature 10 °C below the reference temperature in systems A, B, C and D at an insolation of 500 W m^{-2} and ambient temperature of 20 ±1 °C.

Comparing PCM types, fatty acids CL and CP maintained temperature deviation of 10 °C from the reference for the longest duration of 2.5 hours followed by salt hydrates

SP22 and $CaCl_2.6H_2O$ at 2.25 hours and paraffin wax RT20 at 1.5 hours. Fatty acids CL and CP have a low thermal conductivity of 0.14 $Wm^{-1}K^{-1}$ (Sharma and Sagara 2005) compared to paraffin RT20 having 0.2 $Wm^{-1}K^{-1}$ (Rubitherm 2009 -a), SP22 having 0.6 $Wm^{-1}K^{-1}$ with similar melting points (Rubitherm 2009 -b). It indicates that the lower thermal conductivity PCM types performed better than higher thermal conductivity PCM at lower insolations.

Lower thermal conductivity PCM types performed better than higher thermal conductivity PCM however higher thermal conductivity PV-PCM systems performed better than the lower thermal conductivity PV-PCM systems. This leads to the conclusion that at low insolation the thermal conductivity of the PV-PCM system is more important than the thermal conductivity of the PCM itself to maintain higher thermal regulation.

4.5.5. Thermal Regulation at 750 Wm^{-2} Insolation

Figure 4.16 shows temperatures at the front surface of system A containing each of the five PCMs compared with the temperature at front surface of the reference PV system irradiated at 750 Wm^{-2} and 20 ±1 °C ambient temperature. It can be observed that the temperature rise at front surface of the reference systems and system A is similar for all PCM types up to 30 °C. Above this temperature the temperature rise in the reference continued with the similar gradient however the gradient of temperature rise in system A with different PCMs started to decrease. This indicates onset of latent heat absorption by the melting PCM contained in systems A at the back of PV. Temperature in system A remained lower than the temperature in the reference system

due to continued latent heat absorption. After 4 hours, temperature in system A was below the reference temperature by 4 °C with RT20, 7.5 °C with SP22, 8 °C with CL, 9 °C with CP 10 °C and with $CaCl_2.6H_2O$ respectively.

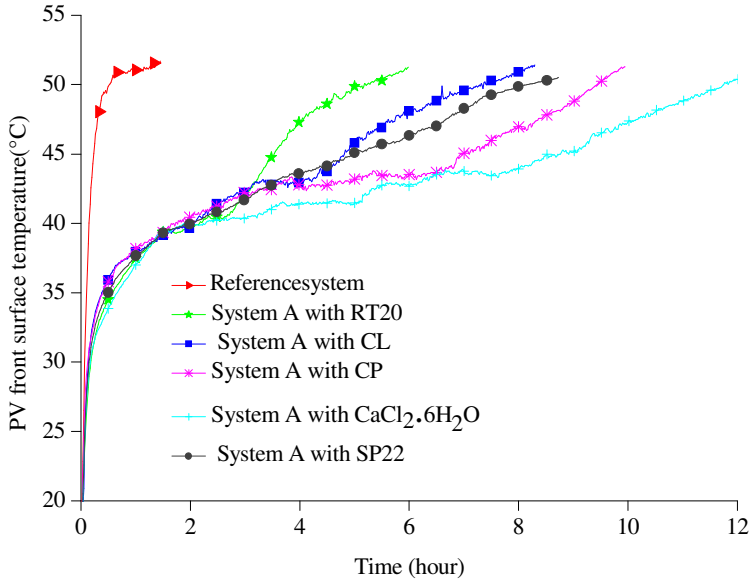

Figure 4.16 Temperature evolution on front surface of PV in system A at an insolation of 750 Wm^{-2} and ambient temperature of 20 ±1 °C

Again PCM RT20 achieved the lowest temperature regulation for the same reasons described in the previous section, however at 750 Wm^{-2} $CaCl_2.6H_2O$ achieved higher temperature regulation than CP in contrast to what was observed at 500 Wm^{-2}. CP has lower melting point while $CaCl_2.6H_2O$ has higher thermal mass and thermal conductivity which shows that at 750 Wm^{-2} the thermal mass and thermal conductivity has relatively stronger effect than the melting point in stabilising lower PV temperatures. After complete melting of the PCM, the temperature in system A started to rise with a higher gradient and eventually equalled the temperature in the reference system. The time for which the temperature in system A remained below the temperature in reference system indicates the potential of each PCM contained in

system A to regulate PV temperature. The duration to reach temperature equilibrium was 6 hours for RT20, 8 hours for CL, 9 hours for SP22, 10 hours for CP and 12 hours for $CaCl_2.6H_2O$. RT20 achieved the smallest temperature difference from the reference and the shortest time to achieve equilibrium for the same reasons explained in previous section. $CaCl_2.6H_2O$ showed the largest temperature difference from the reference system and also achieved the longest duration of the temperature difference primarily because of highest thermal mass, thermal conductivity and heat of fusion of the PCM compared to all other PCMs.

Results obtained when using PCM with system B, C and D under same conditions of 750 Wm^{-2} insolation and 20 ± 1 °C ambient temperature are shown in Figures 4.17 – 4.19. Similar trends as in Figure 4.10 can be observed for the temperature evolution in all the three figures with each of the PV-PCM systems, B, C and D showed a lesser temperature difference from reference than system A.

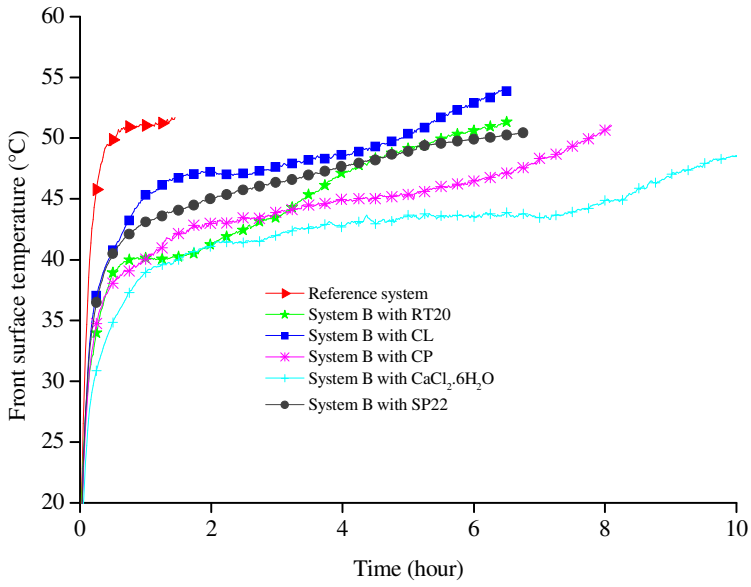

Figure 4.17 Temperature evolution on front surface of PV in system B at an insolation of 750 Wm^{-2} and ambient temperature of 20 ±1 °C.

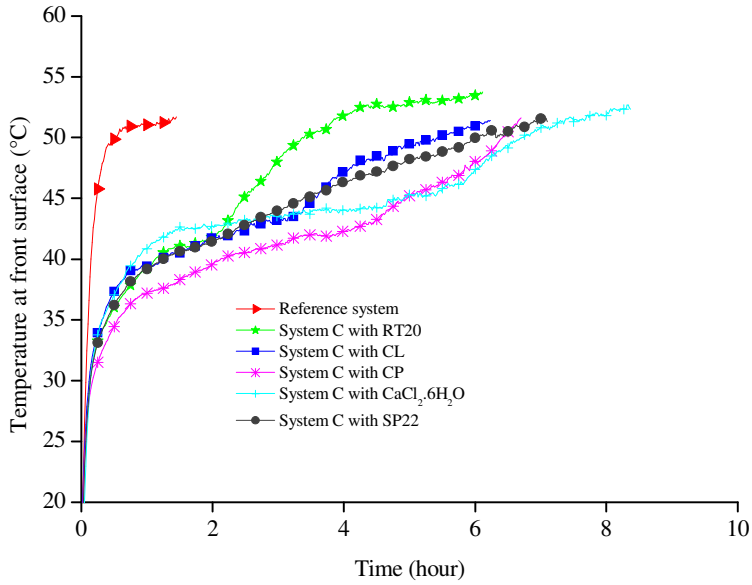

Figure 4.18 Temperature evolution on front surface of PV in system C at an insolation of 750 Wm^{-2} and ambient temperature of 20 ±1 °C.

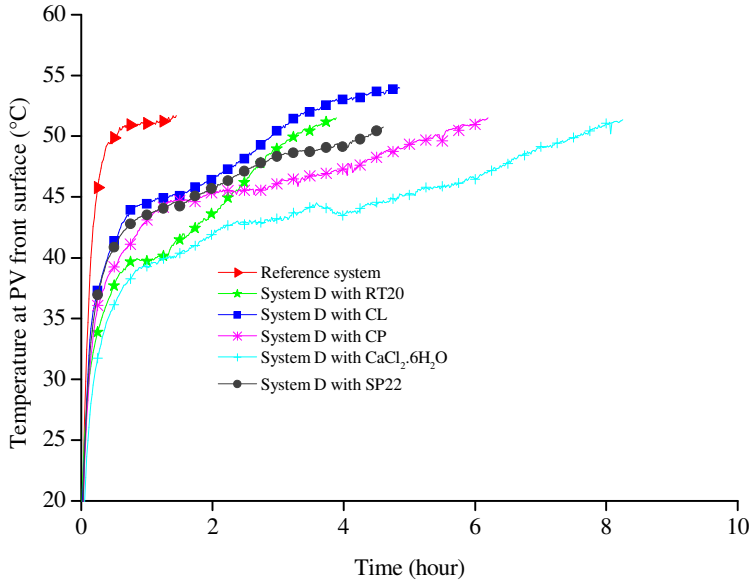

Figure 4.19 Temperature evolution on front surface of PV in system D at an insolation of 750 Wm^{-2} and ambient temperature of 20 ±1 °C.

The duration for which each PCM maintained PV temperature 10 °C below the reference temperature were compared and are illustrated in Figure 4.20.

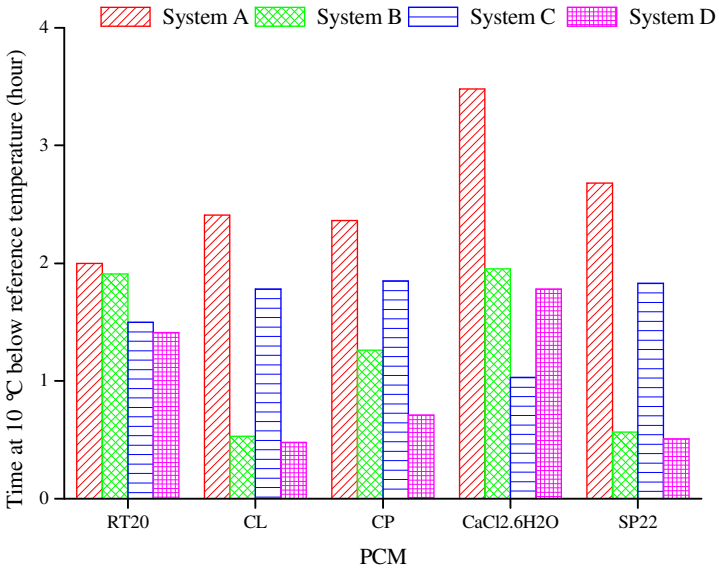

Figure 4.20 Duration for which PCM maintained PV front surface temperature 10 °C below the reference temperature in systems A, B, C and D at insolation of 750 Wm^{-2} and ambient temperature of 20 ±1 °C.

Comparing systems A, B, C and D, the temperature reduction for the longest duration was achieved with system A for all PCMs. Similarly comparing different PCMs, $CaCl_2.6H_2O$ maintained the temperature reduction of 10 °C for the longest duration of 3.5 hours followed by SP22 at 2.7 hours CP and CL at 2.5 hours and RT20 at 2 hours. At 750 Wm^{-2} high thermal conductivity and thermal mass of PCMs, $CaCl_2.6H_2O$ and SP22 performed better than lower thermal conductivity and thermal mass PCMs, CP, CL and RT20 opposite to what was observed at 500 Wm^{-2} insolation where CL and CP performed better than RT20, SP22 and $CaCl_2.6H_2O$. It can be concluded that at intermediate insolation the optimum performance was achieved with

the combination of high thermal conductivity and higher thermal mass PCM $CaCl_2.6H_2O$ with high thermal conductivity PV-PCM sytems A.

4.5.6. Thermal Regulation at 1000 Wm^{-2} Insolation

Figure 4.21 shows temperatures at front surface of system A for all PCMs compared with the reference at 1000 Wm^{-2} insolation and 20 ±1 °C ambient temperature. Similar to the trend observed at 500 Wm^{-2} and 750 Wm^{-2} insolation, the use of the PCM in system A maintained lower temperatures than the reference system.

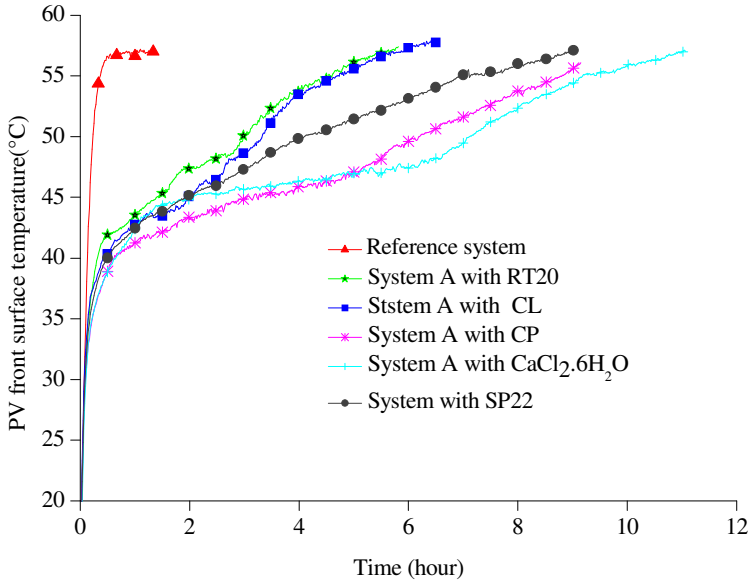

Figure 4.21 Temperature evolution on PV front surface in system A at an insolation of 1000 Wm^{-2} and ambient temperature of 20 ±1 °C.

At start of the experiments the temperature in the reference system and the system A was similar until it reached 35 °C. As soon as the PCM at the back of PV in system A started melting and absorbing latent heat the gradient of temperature rise in systems A

started decreasing and the difference of temperatures between the reference and the system A started to increase. After 4 hours, the temperature in system A was maintained below the reference temperature; 3.5 °C with RT20, 4 °C with CL, 7.5 °C with SP22, 11 °C with $CaCl_2.6H_2O$ and 12 °C with CP.

Each melting PCM in system A continued to absorb latent heat and maintained lower temperature in PV until the whole PCM had melted. At this point gradient of temperature rise in system A started increasing sharply and eventually system A reached temperature equilibrium with reference system. The temperature reduction and time length for such reduction varied for each PCM. The duration in which the PCM in system A equalled the temperature in the reference system is 5.5 hours for RT20, 6 hours for CL, 9 hours for SP22, 9.5 hours for CP and 11 hours for $CaCl_2.6H_2O$ respectively. It is observed that RT20 showed the smallest temperature difference with shortest duration to reach the equilibrium with the reference system due to lower thermal conductivity, thermal mass and heat of fusion compared to $CaCl_2.6H_2O$. C-P showed the largest temperature difference due primarily to lower melting point and higher heat of fusion and $CaCl_2.6H_2O$ showed the longest duration to reach equilibrium with the reference system due to higher thermal mass and heat of fusion. Results obtained when using PCM with system B, C and D under same condition of 1000 Wm^{-2} and 20 ± 1 °C are shown in Figures 4.22 – 4.24. Similar trends can be observed for temperature evolution in all the three figures however each of the PV-PCM systems, B, C and D showed a lesser temperature difference from reference than system A.

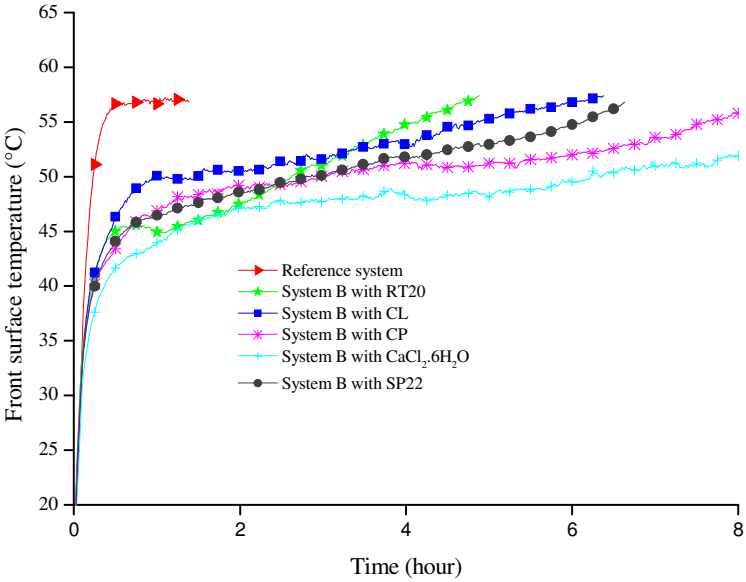

Figure 4.22 Temperature evolution on PV front surface in system B at an insolation of 1000 Wm^{-2} and ambient temperature of 20 ±1 °C.

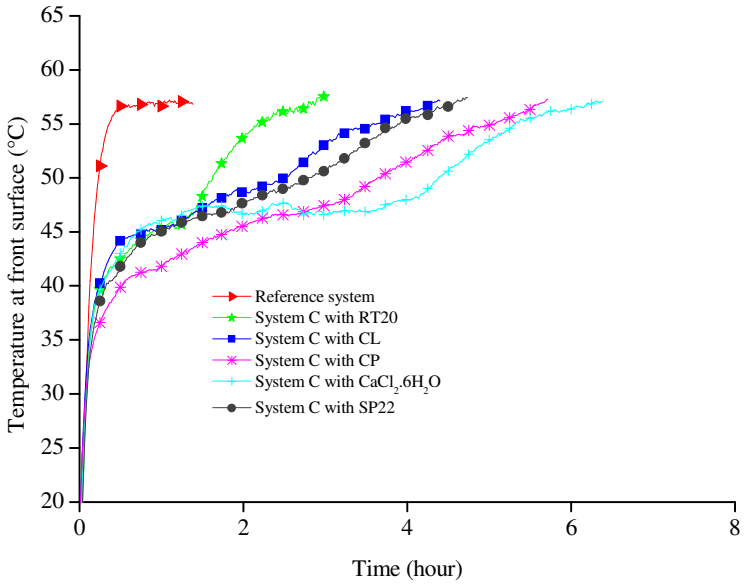

Figure 4.23 Temperature evolution on PV front surface in system C at an insolation of 1000 Wm^{-2} and ambient temperature of 20 ±1 °C.

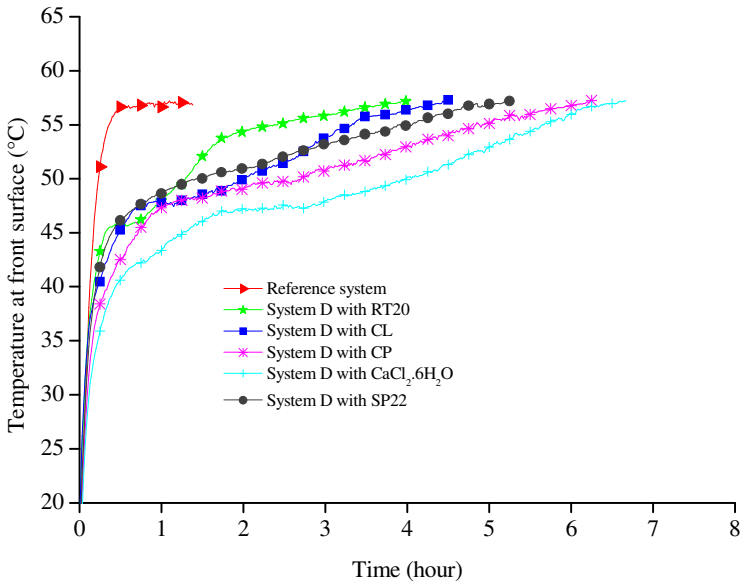

Figure 4.24 Temperature evolution on PV front surface in system D at an insolation of 1000 Wm^{-2} and ambient temperature of 20 ±1 °C.

The duration for which each PCM maintained PV front surface temperature 10 °C below reference temperature are illustrated in Figure 4.25. Comparing containers A, B, C and D, container A achieved the longest duration of the 10 °C temperature reduction for all PCM. Comparing different PCM types, $CaCl_2.6H_2O$ achieved the longest duration of the temperature reduction of 5 hours followed by CP at 4.2 hours, CL and SP22 at 3 hours and RT20 at 2.6 hours in system A. largest amount of temperature difference was obtained with CP in system A while largest duration of temperature difference was achieved with $CaCl_2.6H_2O$ in system A. It illustrates that at high insolation, the combination of low thermal conductivity, lower melting point and comparable heat of fusion PCM, CP in combination with higher thermal conductivity system A achieved the largest temperature reduction. Also the combination of high thermal conductivity, high thermal mass and high heat of fusion

PCM $CaCl_2.6H_2O$ in combination with high thermal conductivity system A achieved the longest duration of temperature difference.

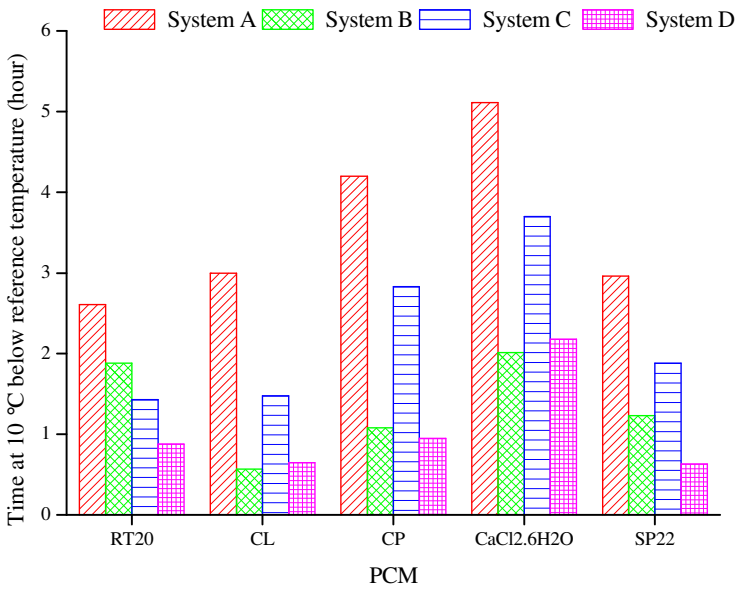

Figure 4.25 : Duration for which PCM maintained PV front surface temperature 10 °C below the reference temperature in systems A, B, C and D at an insolation of 1000 Wm^{-2} and ambient temperature of 20 ±1 °C.

4.5.7. Effect of Thermal Conductivity of Container Material of PV-PCM System on PCM Performance

To determine the best container type two PCMs with different thermal conductivities, thermal mass and heat of fusions, CP and $CaCl_2.6H_2O$ were characterized in same sized systems A & B having different thermal conductivities at 1000 Wm^{-2} insolation and 20 ±1 °C ambient temperature. Temperatures were recorded at the front surface of system A and B using CP and $CaCl_2.6H_2O$ and are illustrated in Figure 4.26 (a) and Figure 4.26 (b) respectively.

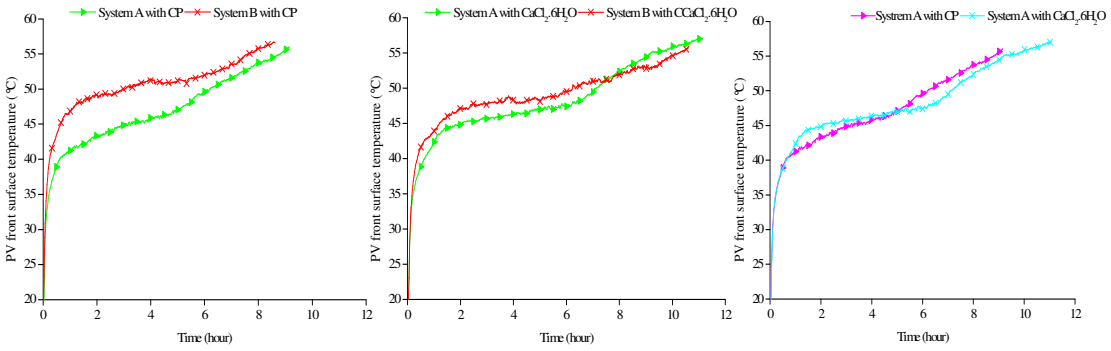

(a) (b) (c)

Figure 4.26 Temperature at PV front surface using (a) C-P in system A and B (b) $CaCl_2.6H_2O$ in system A and B and (c) CP and $CaCl_2.6H_2O$ in system A at an insolation of 1000 Wm^{-2} and ambient temperature of 20 ±1 °C.

System A maintained lower temperatures at the PV front surface than system B for CP as shown in Figure 4.26 (a) with a maximum temperature difference of 5 °C. In Figure 4.26 (b) again system A maintained lower temperature than system B using $CaCl_2.6H_2O$ however the maximum temperature difference was 1 °C. Since for CP the temperature difference in A and B was higher (5 °C) than for $CaCl_2.6H_2O$ (1°C) it suggests that CP having lower thermal conductivity and lower melting point improves more when placed in higher thermal conductivity container than higher thermal conductivity and higher melting point PCM, $CaCl_2.6H_2O$. This is very encouraging behaviour showing that the lower thermal conductivity of PCM can be compensated for by higher thermal conductivity of PV-PCM container if the lower melting point PCM is selected for temperature regulation compared to higher melting point PCM.

To compare CP and $CaCl_2.6H_2O$ in same system A, temperatures at PV front surface are presented in Figure 4.25(c) at 1000 Wm^{-2} insolation and 20 ±1 °C ambient temperature. CP maintained lower PV temperature than $CaCl_2.6H_2O$ for the initial 5

hours in low PV temperature range. After which $CaCl_2.6H_2O$ maintained a lower temperature for rest of experiment at the higher PV temperature range. Since CP has lower thermal conductivity as well as lower melting point than $CaCl_2.6H_2O$,it can be concluded that the lower thermal conductivity PCM with a lower melting point performs better at lower PV operating temperatures. However higher conductivity PCM ($CaCl_2.6H_2O$) with higher melting point performs better at higher PV operating temperature. However PCM with high thermal conductivity, thermal mass and heat of fusion ($CaCl_2.6H_2O$) is highly corrosive to the metallic containers while low thermal conductivity and lower melting point PCM, CP with comparable heat of fusion is less corrosive to the PCM container which brings the possibility that lower thermal conductivity and lower thermal mass PCM, CP to compete with higher thermal conductivity and higher thermal mass PCM at higher PV operating temperature not in terms of producing higher temperature regulation but in terms of longer PCM container life due to reduced corrosion.

4.5.8. Determination of Thermal Regulation Enhancement (Γ) for Different PCM types

PCM can remove thermal energy available at the PV and maintain lower temperatures during melting. Heat removed by PCM is the sum of the sensible heat absorbed when its temperature rises from ambient to its melting point, the latent heat absorbed during melting and the sensible heat from the end of melting until it reaches thermal equilibrium with the reference system. This can be represented by equation 4.2.

$$Q = mC_{p_s}(T_m - T_i) + mL + mC_{p_l}(T_f - T_m) \tag{4.2}$$

Where Q is the heat removed by PCM, $C_{p,\,s}$ and $C_{p,\,l}$ are specific heat capacities of PCM in solid and liquid phase respectively, T_i, T_m and T_f are initial, melting and final temperatures of PCM respectively, m is the mass of PCM and L is the latent heat of fusion of the PCM. The difference between temperature evolution of a reference PV system and PV system with PCM are plotted in figure 4.27.

$$\Gamma = \int_{t=t_o}^{t=t_n} T_{PV}\, dt - \int_{t=t_o}^{t=t_n} T_{PVPCM}\, dt \qquad (4.3)$$

Where T_{PV} and T_{PVPCM} are the PV and PV-PCM temperature, t_o and t_n are the start and end time of the experiment.

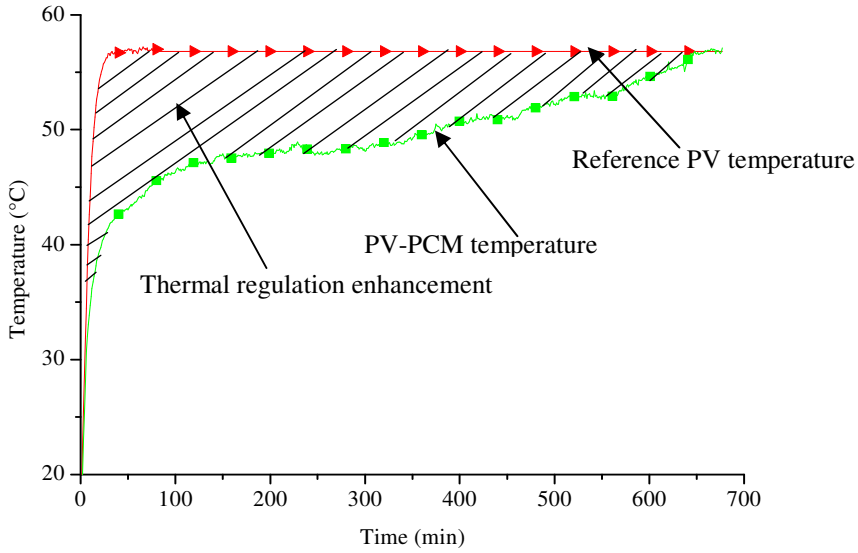

Figure 4.27 Temperature difference between the reference and the PV-PCM systems represented by the shaded area.

Figure 4.27 is a indicative of the total thermal regulation enhancement, Γ provided using PCM. Mathematically Γ for a particular PCM at constant insolation and ambient temperature is obtained by subtracting the integral of PV temperature evolution over time with PCM from the integral of reference PV temperature

evolution over time as shown in equation 4.3. When the test conditions are identical for both the PV and the PV-PCM systems, the equation 4.4 is obtained:

$$\Gamma = \int_{t=t_o}^{t=t_n} (T_{PV} - T_{PVPCM}) \, dt \tag{4.4}$$

While for n discrete measurements of T_{PV} and T_{PVPCM} under identical conditions, the thermal enhancement becomes

$$\Gamma = \sum_{t=0}^{t=n} (T_{PV,t} - T_{PVPCM,t}) \tag{4.5}$$

As described equation 4.5 Γ is a function of deviation of PV temperature with PCM (T_{PVPCM}) from the reference temperature (T_{PV}) and the duration of the deviation.

Figure 4.28 shows that initially there was no deviation between T_{PVPCM} and $T_{PV;}$ however, as the PCM commenced melting, this deviation started and continued increasing to a maximum (14 - 18 °C in 50 minutes) where it stabilized for up to 30 minutes. After which the combination of latent and sensible heating of PCM raised the temperature in the PCM at back of PV yielding higher temperature at PV front surface. The increase of temperature in PV-PCM system resulted in a decrease in the temperature difference from reference (10 - 14 °C in 100 minutes). As the melt fraction of PCM continued to increase, the temperature difference between reference PV and the PV-PCM systems continued to decrease. After the PCM had completed melting the temperature of PCM started increasing with a larger gradient and the

temperature deviation between reference and PV-PCM system started decreasing with larger gradient until T_{PVPCM} equalled T_{PV} and the deviation became zero in 11 hours. $CaCl_2.6H_2O$ and CP achieved the largest temperature deviation of 18 °C followed by SP22 and CL at 16.5 °C and RT20 at 14 °C. $CaCl_2.6H_2O$ maintained the temperature deviation for the longest duration of 11 hours followed by CP at 9.5 hours, SP22 at 9 hours, CL at 6 hours and RT20 at 4.5 hours. A similar trend was observed with PCM in systems B, C and D.

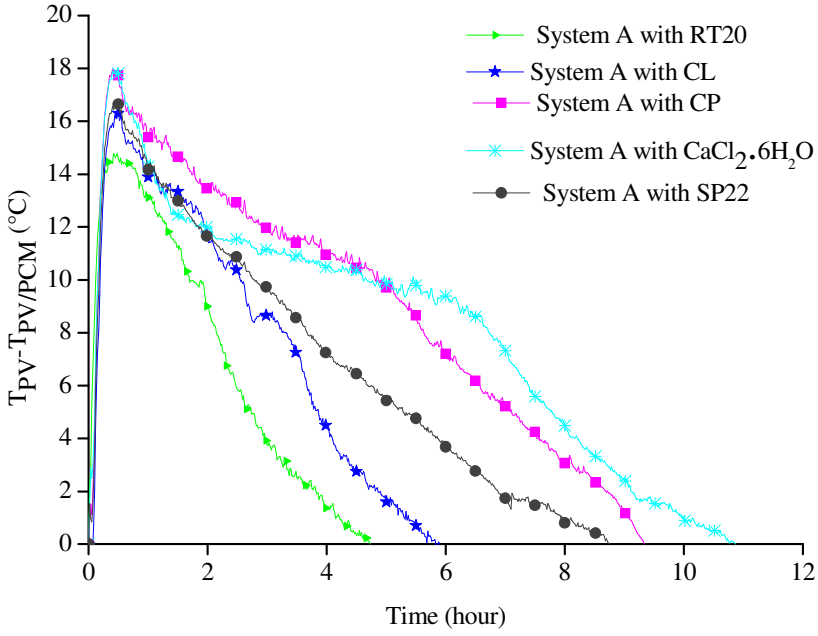

Figure 4.28 Temperature difference from reference for RT20, CL, C-P, $CaCl_2.6H_2O$ and SP22 at an insolation of 1000 Wm^{-2} and ambient temperature of 20 ± 1 °C for system

To quantify the thermal regulation enhancement, Γ for all PCM in PV-PCM systems, integrals of the temperature deviation were determined at 500 Wm^{-2}, 750 Wm^{-2} and 1000 Wm^{-2} insolation and 20 ± 1 °C ambient temperature and are presented in figure 4.29.

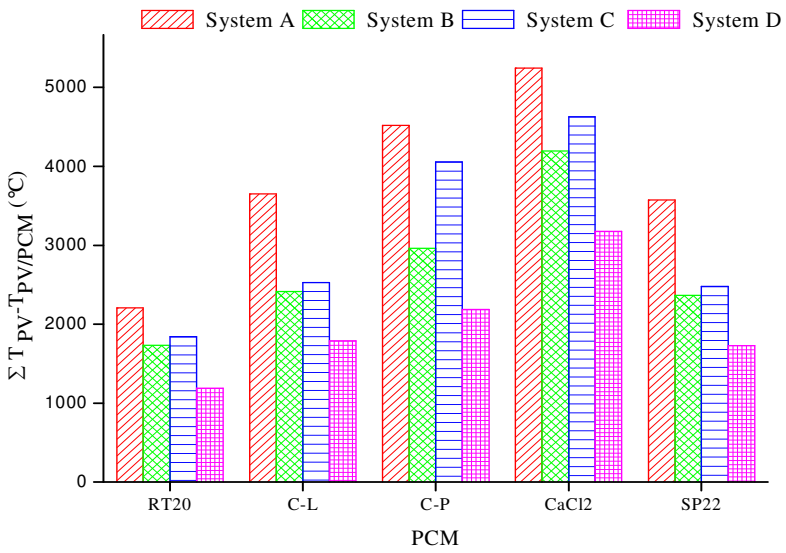

Figure 4.29 Thermal regulation potential for all PCM at 500 Wm^{-2} in systems A, B, C and D.

Figure 4.29 illustrates that at 500 Wm^{-2}, system A achieved the maximum Γ value of all PCM followed by systems C, B and D with systems C & B achieving similar Γ values. Since the high conductivity system C contains 3/5 PCM mass compared to the low conductivity system B, yet achieved the same Γ suggests that 2/5 mass of PCM can be saved by using high thermal conductivity system at low insolation. Comparing PCMs, $CaCl_2.6H_2O$ achieved the highest value for Γ followed by CP, SP22, CL and RT20 respectively which shows that highest thermal conductivity, higher thermal mass PCM $CaCl_2.6H_2O$ in combination with highest thermal conductivity system A achieved the highest Γ.

Figure 4.30 illustrates that system A achieved the highest Γ at 750 Wm^{-2} as well followed by B, C and D. CP and CL gave a marginally higher Γ in container C than B while $CaCl_2.6H_2O$, SP22 and RT20 gave higher Γ in container B than C. Since

container C has higher thermal conductivity than container B, it suggests that it is more appropriate for use with low thermal conductivity PCM (i.e., CP and CL which perform better in C and B) than for higher thermal conductivity PCMs (i.e., $CaCl_2.6H_2O$, SP22 and RT20). Comparing PCMs, $CaCl_2.6H_2O$ achieved the highest Γ followed by CP, CL, SP22 and RT20 the same trend as was observed in the previous section.

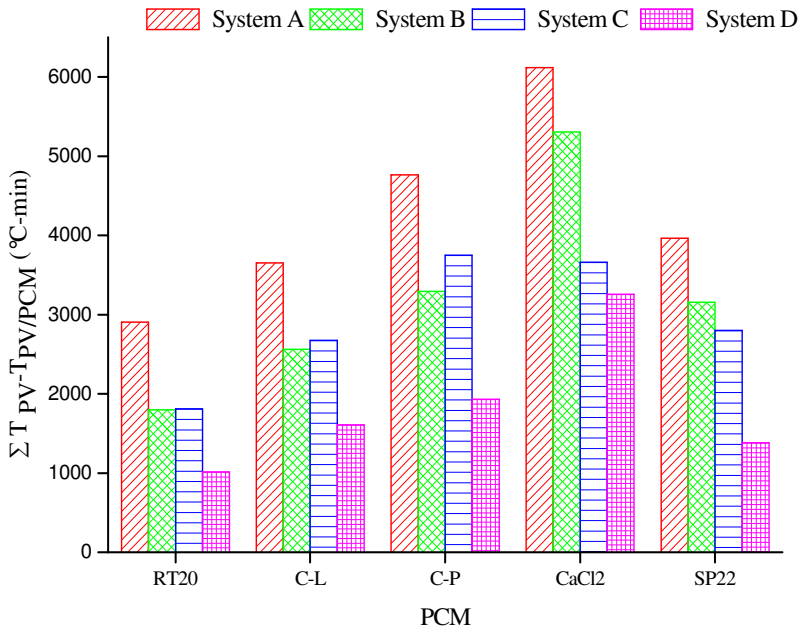

Figure 4.30 Thermal regulation potential for all PCMs at 750 Wm^{-2} in systems A, B, C and D.

Figure 4.31 illustrates that system A achieved the highest Γ followed by, B, C and D respectively at 1000 Wm^{-2}. Comparing B and C, all PCMs showed higher Γ in container B than in container C. This was opposite to the trend observed at 500 Wm^{-2} where all PCMs had higher Γ in container C than in container B. It can be concluded that although the increased PV-PCM thermal conductivity improved Γ for all PCMs

at high insolation, however the improvement at 1000 Wm^{-2} was less than that observed at 500 Wm^{-2} where 2/5 PCM mass saving was achieved due to increased thermal conductivity of the PV-PCM system.

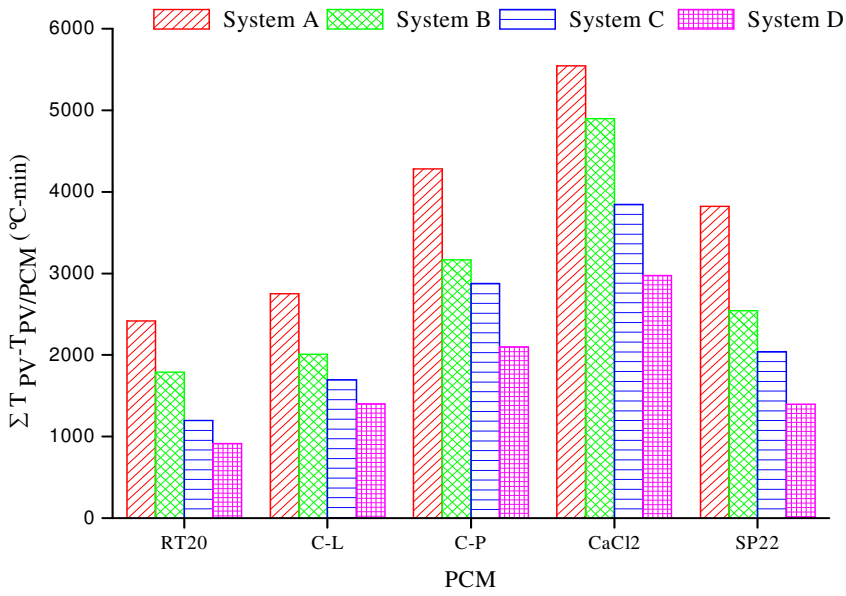

Figure 4.31 Thermal regulation potential for all PCM at 1000 Wm^{-2} in systems A, B, C and D.

The results obtained from all indoor experiments for temperature regulation, end of melting time and thermal regulation enhancement of PV using PCM for all five PCMs, four PV-PCM systems, and three solar radiation intensities are summarized in table 4.3

			PCM				
			RT20	CL	CP	$CaCl_2.6H_2O$	SP22
Time for 10 ˚C temperature regulation (hours)	PVPCM at 500 Wm^{-2}	A	1.4	2.6	2.5	2.2	2.2
		B	0.6	0.8	1.1	1.5	0.6
		C	0.7	1.4	1.4	1.2	1.3
		D	0.6	1	0.8	1	0.9
	PVPCM at 750 Wm^{-2}	A	2	2.4	2.4	3.5	2.7
		B	1.9	0.5	1.3	2	0.6
		C	1.5	1.8	1.9	1	1.8
		D	1.4	0.5	0.7	1.8	0.5
	PVPCM at 1000 Wm^{-2}	A	2.6	3	4.2	5.1	3
		B	1.9	0.6	1.1	2	1.2
		C	1.4	1.5	2.8	3.7	1.9
		D	0.9	0.7	1	2.2	0.6
Time to reach steady state i.e. complete PCM melting (hours)	At PVPCM 500 Wm^{-2}	A	6.5	9	11	13	9.5
		B	5.4	8.6	10.4	12.4	8
		C	5	4.8	9.1	12.3	7.3
		D	3.8	5.9	7.8	10.1	5.8
	PVPCM at 750 Wm^{-2}	A	6	8	10	12	9
		B	6.4	5.3	8.1	11.4	6.8
		C	3.8	6	6.6	7	6.9
		D	3.7	3.2	6	8.1	4.8
	PVPCM at 1000 Wm^{-2}	A	5.6	5.9	9.5	11.1	9
		B	4.76	6.2	8.8	11	6.7
		C	2.8	4.3	5.7	6.3	4.6
		D	3.9	4.4	6.2	6.6	5.2
Thermal regulation enhancement (°C-min)	PVPCM at 500 Wm^{-2}	A	2208	3649	4519	5244	3573
		B	1732	2416	2959	4192	2362
		C	1839	2527	4054	4629	2476
		D	1187	1788	2184	3173	1729
	PVPCM at 750 Wm^{-2}	A	2907	3653	4763	6116	3964
		B	1801	2564	3294	5303	3156
		C	1812	2676	3751	3662	2803
		D	1014	1611	1932	3254	1383
	PVPCM at 1000 Wm^{-2}	A	2420	2755	4280	5545	3823
		B	1793	2012	3170	4899	2545
		C	1199	1698	2877	3846	2041
		D	916	1404	2100	2973	1401

Table 4.3 : Summary of results obtained from indoor experiments at three different solar radiation intensities, four PV-PCM systems and five PCMs at 20±1 ˚C ambient temperature.

4.6 Conclusions

Five PCMs evaluated at three different insolations showed that thermal regulation performance of a PCM depends on the thermal conductivity, thermal mass, heat of fusion and melting point of PCM and over all thermal conductivity of PV-PCM systems. A simple heat transfer simulation model was developed and initial validation of the experimental results was carried out. It was observed that the heat transfer does not happen as pure conduction and natural convection is present which can not be ignored. Comparing PCMs, the highest temperature reduction was achieved (i) at 500 Wm^{-2} by eutectic mixture fatty acids CP (ii) at 750 Wm^{-2} by salt hydrate $CaCl_2.6H_2O$ and (iii) at 1000 Wm^{-2} again by $CaCl_2.6H_2O$. In the best case, CP and $CaCl_2.6H_2O$ maintained a maximum of 18 °C temperature reduction at PV front surface for 30 minutes, while $CaCl_2.6H_2O$ maintained a 10 °C temperature reduction for 5 hours at 1000 Wm^{-2} insolation in system A.

Although time to maintain 10 °C temperature difference is a good figure of merit to evaluate the temperature regulation because in most of the cases PV temperature curve using PCM was flatter at this temperature difference from the reference which means maximum latent heat absorption occurred in this regime. However it does not inform for how long the PCM will maintain temperature difference at a lower temperature than 10 °C. For example some PCMs may maintain 10 °C temperature difference for shorter time duration but may maintain lower temperature difference (say 5 °C) for longer duration which means they still can compete with those producing 10 °C for longer time duration. In order to better understand PCM performance for longer time duration integral of temperature difference over time was

taken. The preferred figure of merit would be Γ as it shows the over all behaviour of PCMs in all temperature difference regimes. Comparing PV-PCM systems, system A yielded the highest temperature reduction and Γ with all PCM types. Finally the thermal conductivity of the PV-PCM system had stronger impact on performance enhancement of lower thermal conductivity and lower melting point eutectics of fatty acids, CL and CP than on higher thermal conductivity salt hydrates SP22 and $CaCl_2.6H_2O$.

It is observed that CP performs best of all PCMs at low insolation (500 Wm^{-2}) while CaCl2.6H2O performs better at intermediate (750 Wm^{-2}) and higher (1000 Wm^{-2}). The reason being probably at low insolation the temperature at PV surface is lower enough that the low melting point PCMs (CP with melting point 22.5 °C) fully melts and absorbs more heat resulting lower temperature at PV than high melting PCMs ($CaCl_2.6H_2O$ with melting point 29.8 °C) which melts partially and absorbs less amount of heat resulting in higher PV temperature. At high temperature the melting point may not be very crucial and the thermal conductivity and heat of fusion (both are higher for $CaCl_2.6H_2O$ than for CP) plays dominant role due to increased need of efficient and maximum heat removal from PV to yield lower temperatures.

Aluminium container always produced the best results with all the PCMs, although it is corrosive with most of the PCMs however this problem can be resolved with further research applying corrosion protective coatings. The effectiveness and cost incurred to such improvements in the container is still an open issue and needs extensive research.

4.7 References

Aalco (2007). "Product Data Sheet Aluminium Alloy 1050A, 2007".

Chen, C. R., Sharma, A., Tyagi, S. K. and Buddhi, D. (2008). "Numerical heat transfer studies of PCMs used in a box-type solar cooker" Renewable Energy 33(5): 1121-1129.

Kipp and Zonnen (2003). "Product Information - CM6B 2003, Kipp and Zonnen Gebrauchsanleitung".

Martin, A. D., Lovingood, R. P., Long, D. D. and Schnep, M. I. (1990). "Cooking System Interactions: Compatibility of Energy Source and Container Material" Family and Consumer Sciences Research Journal 19(2): 159-169.

Rubitherm (2009 -a). "Innovative PCM's and Thermal Technology". Product Information for RT20 RUBITHERM® RT, Rubitherm Technologies.

Rubitherm, Technologies (2009 -b). "Innovative PCM's and Thermal Technology". Product Manual RUBITHERM® SP22A17.

Sharma, A., Sharma, S.D, Buddhi, D and Won, L.D. (2006). "Effect of thermo physical properties of heat exchanger material on the performance of latent heat storage system using an enthalpy method" International Journal of Energy Research 30(3): 191-201.

Sharma, S, D. and Sagara, K. (2005). "Latent heat storage materials and systems: A review". Taylor & Francis. Philadelphia, PA, USA,.

Shiina, Y. and Inagaki, T. (2005). "Study on the efficiency of effective thermal conductivities on melting characteristics of latent heat storage capsules" International Journal of Heat and Mass Transfer 48(2): 373-383.

Tyagi, V. V. and Buddhi, D. (2008). "Thermal cycle testing of calcium chloride hexahydrate as a possible PCM for latent heat storage" Solar Energy Materials and Solar Cells 92(8): 891-899.

Vink, Plastics (2007). "Product Catalogue MARKALY CLEAR, 2007 ".

5 INDOOR LARGE SCALE EXPERIMENTS ON PV-PCM MODULAR SYSTEMS WITH $CaCl_2.6H_2O$ AND EUTECTIC MIXTURE OF CAPRIC PALMITIC ACID.

5.1 Aim of the Experiments

Five different PCMs were characterized indoors with different PCM masses, containment materials and solar radiation intensities on small scale cell size PV-PCM systems discussed in chapter 4. It was observed that the eutectic mixture of capric-palmitic acid (CP) and the salt hydrate ($CaCl_2.6H_2O$) performed better than the other materials, paraffin wax (RT20), eutectic mixture of capric-lauric acid (CL) and the mixture of salt hydrate and the paraffin wax (SP22) in indoor experiments. It was also observed that the system A (i.e., PV integrated into the aluminium container with volume to surface area ration of 5 cm^3cm^{-2}) performed better than all the other systems at all characterization solar radiation intensities (500, 750 and 1000 Wm^{-2}), using all PCMs.

The aim of these experiments is to study the behavior of the two PCMs (CP and $CaCl_2.6H_2O$ that performed better in small scale indoor experiments) on large scale panel size (600 mm x 700 mm) systems. These two PCMs were integrated into large scale PV modules referred to as PV-PCM_1 (i.e., PV module containing integrated CP) and PV-PCM_2 (i.e., PV module containing $CaCl_2.6H_2O$). Indoor experiments were conducted with reference PV module and the two PV-PCM systems using a larger solar simulator housed at the Centre for Sustainable Technologies, Ulster University, Jordanstown, N-Ireland.

5.2 Methodology

- Experiments were conducted at solar radiation intensities of 500 Wm^{-2}, 750 Wm^{-2} and 1000 Wm^{-2} for the reference PV, PV-PCM_1 and PV-PCM_2

- Temperature evolution was recorded at the reference PV system and both the PV-PCM systems and the difference in the temperatures was determined and compared.

- Open circuit voltage (V_{oc}) and the short circuit currents (I_{sc}) were measured for the reference and the two PV-PCM systems. Temperature induced change in I_{sc} being very low has marginal effect on PV power while temperature induced change in V_{oc} is significant that is mainly responsible for the temperature induced change in PV power. Therefore only difference of the V_{oc} between the reference system and the two PV-PCM systems will be analyzed.

- Fill factor (*FF*) was determined from the reference PV power and *I-V* curves provided by the manufacturer at standard test conditions (STC) and were extrapolated to determined *FF* at operating conditions (i.e., solar radiation intensities and temperatures) of reference PV, PV-PCM_1 and PV-PCM_2

- The calculated *FF* was used with measured V_{oc} and I_{sc} to determine measured power output (*P*) for the reference PV and the two PV-PCM systems

- Finally the percentage difference between measured *P* from the reference system and the measured *P* from the two PV-PCM systems were compared to

calculate prevention of temperature dependent power drop, so called power saving (P_s) obtained by PV cooling.

- Temperature reduction achieved by the two PCMs multiplied by temperature coefficient of power drop (T_c), provided by the PV manufacturer's catalogue, to obtain predicted P_s obtained by reduced PV operating temperature.

- Finally the measured and predicted P_s values were compared to validate the experimental results with manufacturer's data.

5.3 Experimental Setup

Three 65 W Suntechnics polycrystalline silicon PV panels (Suntechnics, 2006) were installed and characterized outdoors at Focas Institute, Dublin, (53.33 N, 6.24 W) to observe any inconsistencies in their V_{oc} and $I_{sc.}$ Data measured confirmed the consistency of performance in all the three PV with respect to the V_{oc} and I_{sc} with the highest deviation of ± 1 %.

Two rectangular PCM containers with internal dimensions of 600 mm x 700 mm x 50 mm were fabricated from a 5 mm thick aluminium alloy to contain the PCM. Seven straight fins of dimensions 700 mm x 50 mm x 5 mm with inter fin spacing of 75 mm fabricated from the same alloy were vertically fitted back to back between internal walls of the container to enhance the thermal conductivity of the PCM container. Such finned systems have been reported (Huang *et al.,* 2004; Huang *et al.,* 2006) to achieve increased heat transfer into the PCM matrix. This results in increased PCM melting leading to decreased melting time and reduced PV temperature closer to the desired

PV temperature. The fabricated containers were attached to back of the PV panels with epoxy resin and were fixed to the PV under pressure for 48 hours to allow glue to uniformly settle and yield strong bond between PV and the container.

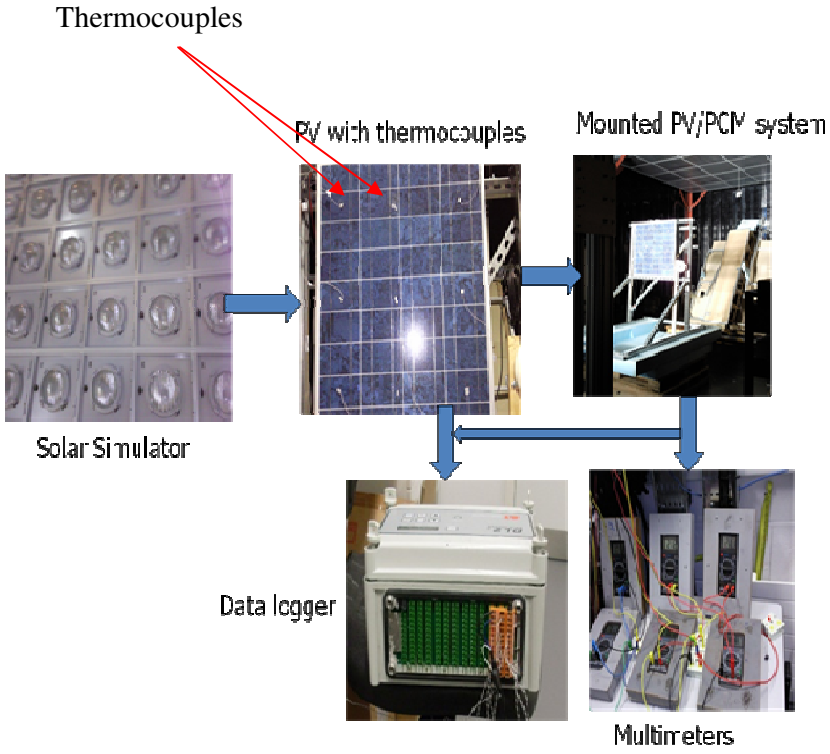

Figure 5.1 Indoor experimental setup consisting of a large scale solar simulator to produce desired insolation, PV with thermocouples, multimeters and data logger.

Figure 5.1 shows the experimental set up where the reference PV and PV-PCM were connected to multimeters to measure their V_{oc} and I_{sc}. The calibrated t-type copper-constantan thermocouples with measurement error of ±0.2 °C were installed on the reference PV and the two PV-PCM systems at locations shown in figure 5.1 (b) to measure temperature. A Kipp and Zonen CM6B pyranometer with an accuracy of ± 0.2 % was installed to measure the solar radiation intensity (Kipp and Zonnen 2003).

A large solar simulator consisting of a 7 x 5 array of 575 W metal halide lamps was used to produce the desired insolation. The solar simulator was capable of producing 1200 Wm^{-2} on a 2 m x 2.2 m target surface area at a variable distance of 1.8 m to 2.2 m with 95 % measured uniform intensity distribution (Zacharopoulus *et al.,* 2009). A delta-T 2e data logger with an accuracy of ± 0.1 % was used to record temperatures and solar radiation intensities described in Appendix F (Delta-T, 2010).

5.4 Experimental Procedure

The PCMs, CP was prepared by mixing 75.2 % by weight of capric acid (≥ 96 % pure from Sigma Aldrich) with 24.8 % by weight of palmitic acid (≥ 98 % pure from Sigma Aldrich). The mixture was heated until all the PCM had melted and stirred for 12 hours to obtain a uniform mixture. The salt hydrate $CaCl_2.6H_2O$ was also melted and stirred for 12 hours to obtain a uniform solution. The melted PCM were filled in their respective PV-PCM systems up to 650 mm of container height leaving a 50 mm empty top space to accommodate PCM expansion during phase change. The PV-PCM systems were kept indoors at 16 °C for 48 hours until both PCM had fully solidified and were ready to be exposed to the solar simulator to start the experiment. Reference experiments were conducted on a vertically installed PV panel without PCM irradiated by the solar simulator at insolations of 500 Wm^{-2}, 750 Wm^{-2} and 1000 Wm^{-2} with an ambient temperature of 20±1 °C. Temperatures at the front and back PV surfaces, V_{oc} and I_{sc} were measured for the reference PV exposed to the solar simulator.

PV-PCM_1 containing fully solidified CP was installed vertically and exposed to solar simulator for 6 hours at 500 Wm^{-2} and temperatures, V_{oc} and I_{sc} were also recorded. The temperatures on front surface of PV and PV-PCM_1, the V_{oc} and I_{sc} were compared to quantify cooling of PV produced by melting CP and the concomitant effect of this cooling on PV electrical output.

After the heating cycle was over, the solar simulator was switched off to allow PCM in the PV-PCM system to cool down for at least 16 hours simulating night time conditions to get it ready for the next run of the experiment. Similarly the experiments were conducted at 750 Wm^{-2} and 1000 Wm^{-2} with the same ambient temperature of 20 ± 1 ˚C. After the experiments were finished with CP, the same experiments under same conditions were conducted using $CaCl_2.6H_2O$ in PV-PCM_2 for the same length of time and again temperatures, V_{oc} and I_{sc} were recorded.

5.5 Results and Interpretations

5.5.1. Thermal Regulation at Low Insolation

Figure 5.2 shows the temperature rise at front surface of the reference PV, PV-PCM_1 and PV-PCM_2 when all three were exposed to a solar radiation intensity of 500 Wm^{-2} and 20 ±1 C ° ambient temperature. It is observed that the reference temperature provided by the PV without PCM stabilized at 40 °C at 500 Wm^{-2} solar radiation intensity. Temperatures in the two PV-PCM systems also followed a similar trend in temperature rise however maintained a lower temperature than the reference temperature.

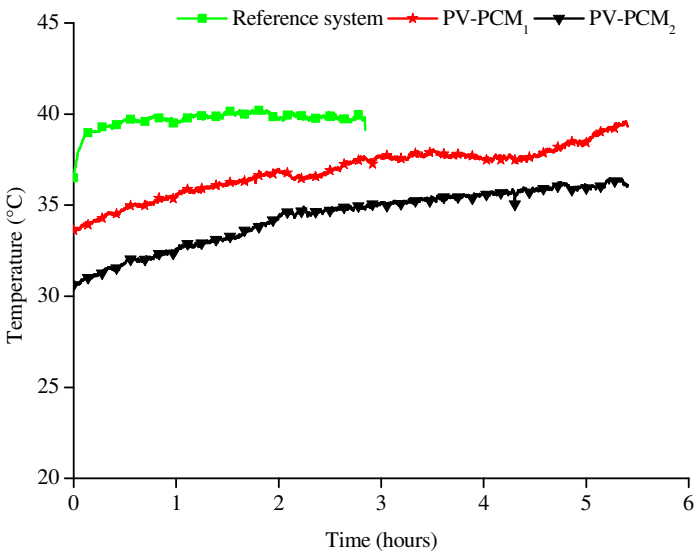

Figure 5.2 Temperature evolution in the indoor experiment at solar radiation intensity of 500 Wm^{-2} and ambient temperature of 20 ±1 °C measured on the front surface of reference PV, PV-PCM_1 and PV-PCM_2

The lower temperature was achieved due to heat (produced by incident radiations at the PV surface) being absorbed by the melting PCM as latent heat of fusion at the back of each PV-PCM system. It is observed that PV-PCM_2 maintained lower temperatures than PV-PCM_1 for the length of the experiments. Temperature difference between the reference PV and the two PV-PCM systems at 500 Wm^{-2} is presented in Figure 5.3. A higher temperature difference was observed in the start of the experiments for 25 minutes with 5 °C for PV-PCM_1 and 8 °C for PV-PCM_2, which continued to decrease as the experiment proceeded. The higher temperature difference occurred at the start of the experiments due to maximum heat absorption by PCMs due to dominant latent heat absorption by PCM close to their melting points.

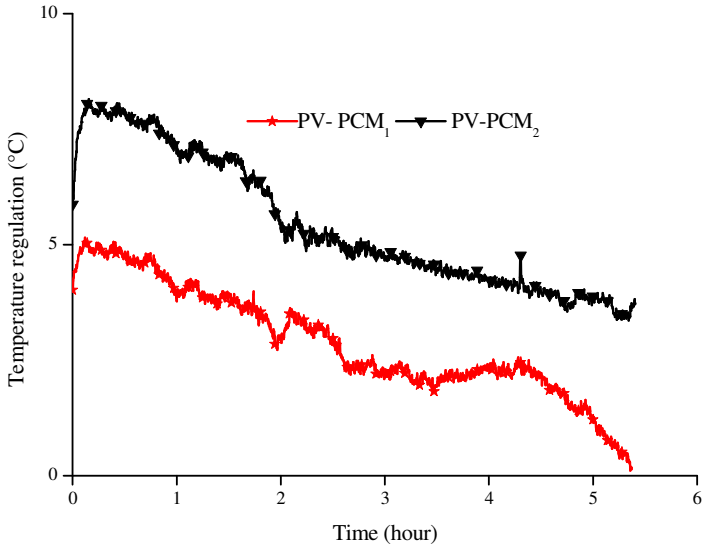

Figure 5.3 Temperature regulation in large scale indoor experiments for the reference PV, PV-PCM_1 and PV-PCM_2 at solar radiation intensity of 500 Wm^{-2} and ambient temperature of 20 ±1 ˚C

As the melting proceeded, the melt fraction increased leading to dominant sensible nature of heat absorption at further beyond to transition temperature resulting in increase PCM temperature and decreased temperature difference between the reference and the two PV-PCM systems. Towards the end of the experiments, most of the PCM had melted and the sensible heating of the PCM dominated shown by sharp increase in the PV-PCM temperatures with a higher gradient shows that PV-PCM_2 maintained a higher temperature difference from the reference throughout the experiment than PV-PCM_1. At the end of the experiment after 6 hours, the temperature difference of PV-PCM_1 from the reference PV dropped to zero however the temperature difference of PV-PCM_2 from the reference PV remained at 4 °C. This showed that the PCM in PV-PCM_2 still had potential to absorb heat and regulate PV temperature for a further period of time. Both the PV-PCM systems have same dimensions and containment materials distinguished solely by the PCM, CP in PV-PCM_1 and $CaCl_2.6H_2O$ in PV-PCM_2. It can be inferred that $CaCl_2.6H_2O$ performed

better than CP at 500 Wm^{-2} achieving higher temperature difference and longer duration of time to maintain the temperature difference.

Figure 5.4 shows the measured V_{oc} for the reference PV and the two PV-PCM systems which showed that the two PV-PCM systems maintained higher V_{oc} than the reference PV.

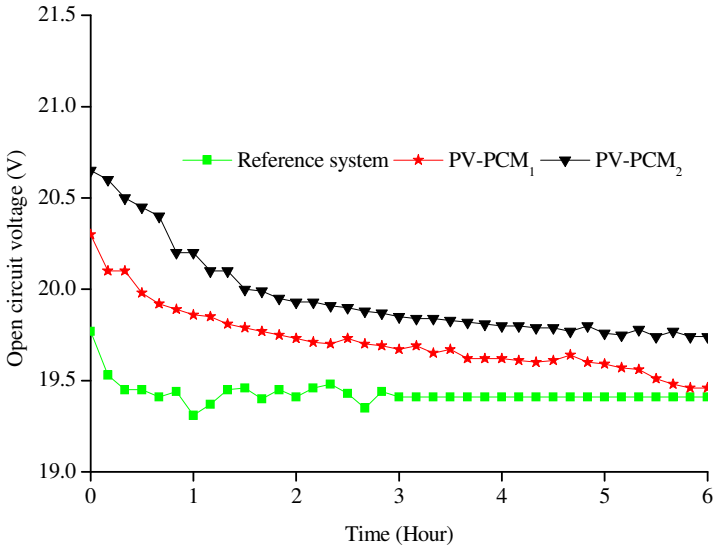

Figure 5.4 Open circuit voltage for indoor experiments at solar radiation intensity of 500 Wm^{-2} and ambient temperature of 20 ±1 ˚C

Higher V_{oc} in the two PV-PCM systems is due the lower temperatures of the systems compared to the reference PV, shown in Figure 5.2, due to heat absorbed by melting PCM contained in the PV-PCM systems. Results found are in agreement with previous studies (Green, 2003; Radziemska, 2003) that found that higher operating temperatures in PV systems caused a drop in PV voltage and power, which can be avoided by maintaining PV at lower temperatures (Krauter, 2004; Tonui and Tripanagnostopoulos, 2007). At start of the experiments, as PV temperatures were lower, V_{oc} was higher for the reference PV and the two PV-PCM systems. As the

temperatures started to increase during the experiments due to incident insolation, the V_{oc} started to decrease. At the end of the experiment the V_{oc} in the PV-PCM$_1$ equalled V_{oc} in the reference PV. However V_{oc} in PV-PCM$_2$ remained higher than the reference PV which is in agreement with the temperatures profiles in Figure 5.2.

Figure 5.5 presents the difference in V_{oc} of the two PV-PCM systems from the reference PV leading to quantification of voltage improvement i.e., prevention of temperature induced voltage drop by maintaining the PV at lower temperatures.

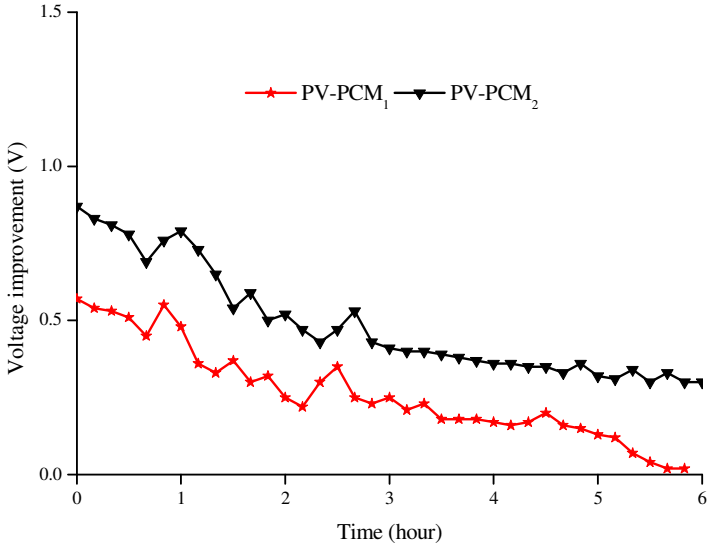

Figure 5.5 Voltage improvement in indoor experiments as a result of temperature regulation by PCM at solar radiation intensity of 500 Wm^{-2} and ambient temperature of 20 ±1 °C

It can be observed that the PV-PCM$_2$ maintained higher voltage improvement than the PV-PCM$_1$ which is in accordance with the temperature difference shown in Figure 5.3 the higher the temperature difference from the reference the higher the voltage improvement and vice versa. At the start of the experiments the voltage improvement

was higher in both PV-PCM systems, 0.6 V for PV-PCM_1 and 0.9 V for PV-PCM_2 which continued to decrease as the experiments proceeded, a similar behaviour as was observed in case of the temperature difference shown in Figure 5.3

5.5.2. Thermal Regulation at Intermediate Insolation

.

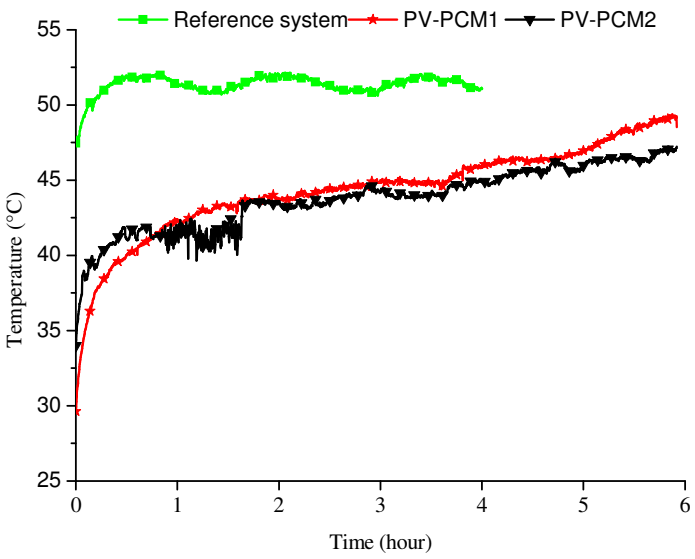

Figure 5.6 Temperature evolution in the indoor experiments for reference PV, PV-PCM_1 and PV-PCM_2 at solar radiation intensity of 750 Wm^{-2} and ambient temperature of 20 ±1 ˚C.

Figure 5.6 shows the temperature rise at the front surface of the reference PV, PV-PCM_1 and PV-PCM_2 when exposed to the solar simulator at 750 Wm^{-2} solar radiation intensity and 20 ±1 C ° ambient temperature. Temperature in the reference PV stabilized at 51 ± 1 °C, temperatures in the PV-PCM_1 and PV-PCM_2 followed the

trend in temperature rise however maintained a lower temperature than the reference PV due to cooling effect produced by latent heat removal by the melting PCM at the back of each PV-PCM system. PV-PCM_1 maintained slightly lower temperature than PV-PCM_2 for the initial 1 hour of the experiment, afterwards PV-PCM_2 maintained a lower temperature than PV-PCM_1. Towards the end of the experiment PV-PCM_1 exhibited a higher gradient of temperature rise than the PV-PCM_2 indicating end of melting and predominantly sensible heating of CP contained in PV-PCM_1. PV-PCM_2 exhibited continued temperature rise with a smaller gradient indicating that $CaCl_2.6H_2O$ was still melting and absorbing latent heat.

Figure 5.7 shows the temperature difference between the reference PV and the two PV-PCM systems at 750 Wm^{-2} insolation and 20 ±1 ˚C ambient temperature.

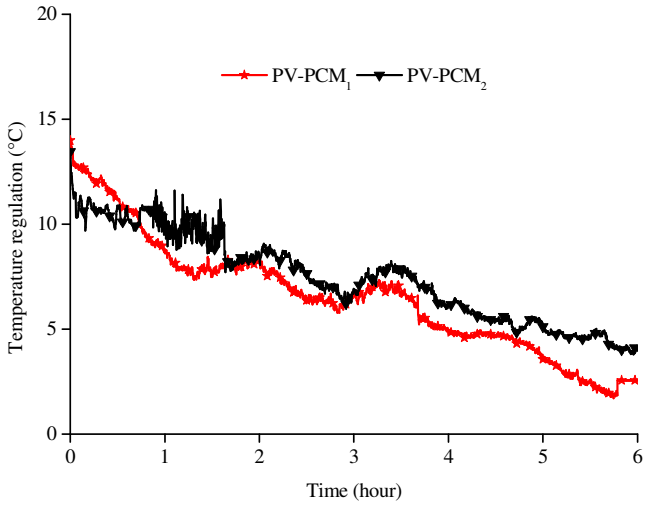

Figure 5.7 Temperature regulation in the indoor experiments for reference PV, PV-PCM_1 and PV-PCM_2 at solar radiation intensity of 750 Wm^{-2} and ambient temperature of 20 ±1 ˚C

It can be observed that both PV-PCM systems showed a higher temperature difference initially, 14 °C for PV-PCM_1 and 12 °C for PV-PCM_2, which continued to decrease until the end of the experiment in 6 hours. For both PV-PCM systems, the temperature difference at 750 Wm^{-2} was higher than the temperature difference at 500 Wm^{-2}. Comparing reference PV temperatures, at 750 Wm^{-2} the reference temperature was 11 °C higher than the reference temperatures at 500 Wm^{-2} which provided PV-PCM systems with possibility to obtain higher temperature difference at higher solar radiation intensities. Figure 5.8 shows V_{oc} of the reference PV and the two PV-PCM systems at 750 Wm^{-2} insolation and 20 ±1 °C ambient temperature.

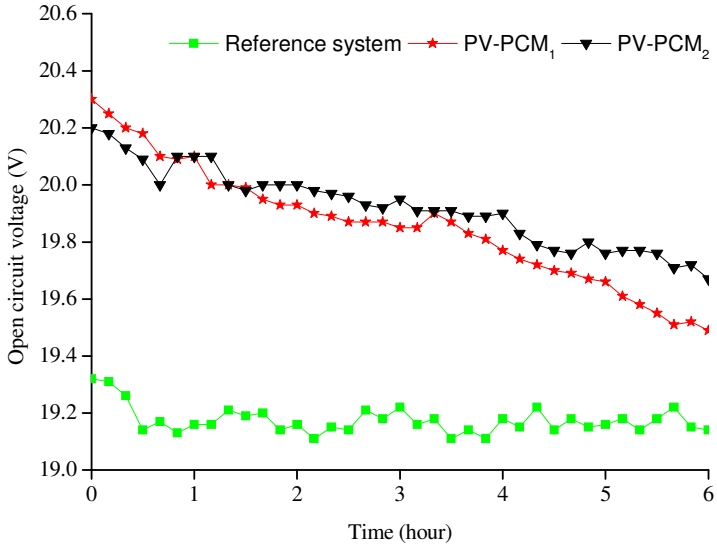

Figure 5.8 Open circuit voltage in indoor experiments at solar radiation intensity of 750 Wm^{-2} and ambient temperature of 20 ±1 °C

It was observed that V_{oc} of the two PV-PCM systems was higher than V_{oc} of the reference PV due to the lower temperature at the PV-PCM systems than the reference PV, similar trend in V_{oc} was observed at 500 Wm^{-2}. V_{oc} in the reference PV remained

around 19.2 V for the duration of the experiment because its temperature remained stable, while V_{oc} in the PV-PCM systems was initially higher and continued to decrease as their temperatures increased during course of the experiments. This again confirms the drop in V_{oc} caused by the increase in PV temperature which can be prevented by keeping the PV at lower temperatures. Figure 5.9 shows the difference in V_{oc} between the reference PV and the PV-PCM systems at 750 Wm^{-2} solar radiation intensity and 20 ±1 °C ambient temperature.

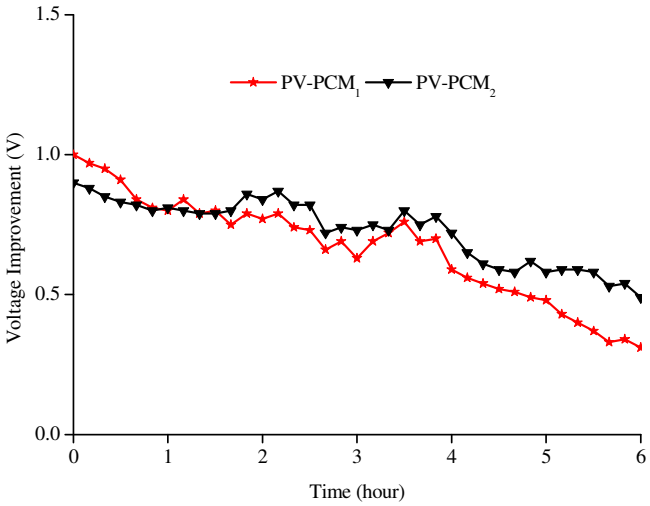

Figure 5.9 Voltage improvement in indoor experiments as a result of temperature regulation at solar radiation intensity of 750 Wm^{-2} and ambient temperature of 20 ± 1 ˚C

PV-PCM_1 had a higher V_{oc} difference from the reference PV for the initial 1 hour of the experiments, afterwards V_{oc} of PV-PCM_2 remained higher. In last hour of the experiments, V_{oc} difference of PV-PCM_1 from the reference started to drop with a larger gradient than that of PV-PCM_2 indicating that the PCM in PV-PCM_1 completed melting while PCM in PV-PCM_2 continued to melt and absorb latent heat, a similar behaviour as was observed for the temperature difference in Figure 5.7.

5.5.3. Thermal Regulation at High Insolation

Figure 5.10 shows the temperature rise at the front surface of the reference PV, PV-PCM_1 and PV-PCM_2 when exposed to the solar simulator at 1000 Wm^{-2} solar radiation intensity and 20 ±1 C ° ambient temperature.

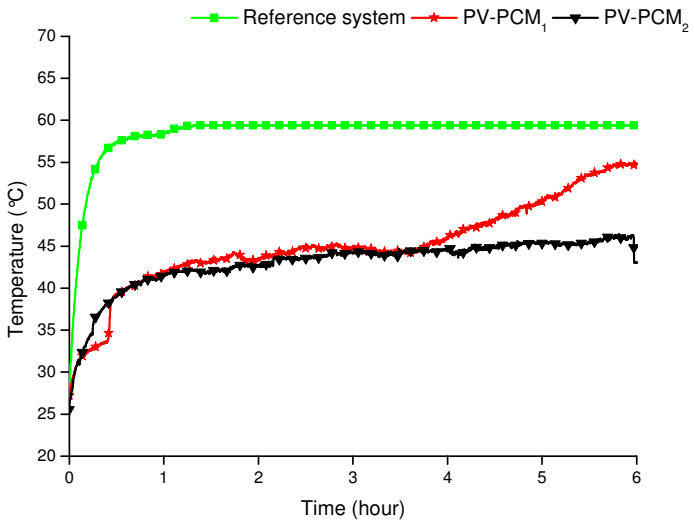

Figure 5.10 Temperature evolution in indoor experiments for reference PV, PV-PCM_1 and PV-PCM_2 at solar radiation intensity of 1000 Wm^{-2} and ambient temperature of 20 ±1 ˚C

Temperature in the reference PV stabilized at 60 °C while temperatures in PV-PCM_1 and PV-PCM_2 remained lower than the reference temperature due to cooling effect produced by latent heat removal by the melting PCM. Both PV-PCM systems maintained similar temperatures evolution upto 45 ˚C for the initial 3.5 hours of the experiments with PV-PCM_1 having slightly higher temperature than PV-PCM_2. After 3.5 hours the temperature in PV-PCM_1 started to increase at a much higher rate

indicating the predominant sensible heating of CP contained in PV-PCM_1 however temperature in PV-PCM_2 continued to increase with the previous rate indicating the predominant latent heating of the $CaCl_2.6H_2O$ contained in the PV-PCM_2. It clearly indicates that $CaCl_2.6H_2O$ possesses higher heat absorption and temperature regulation potential for longer duration than CP.

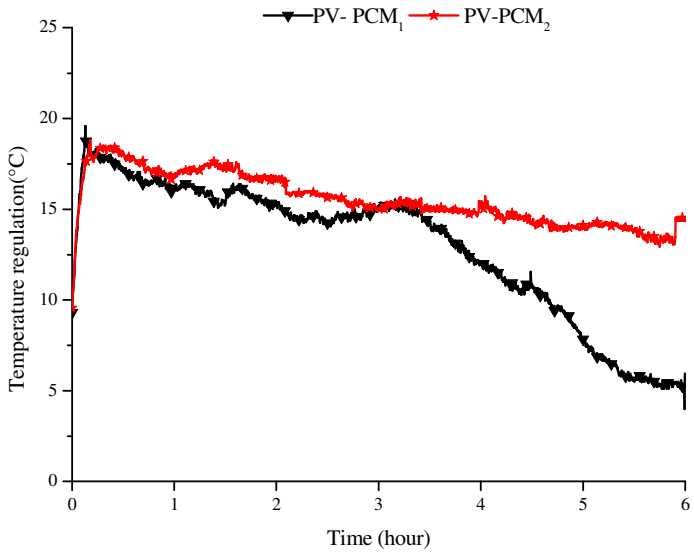

Figure 5.11 Temperature regulation for indoor experiments of the reference PV, PV-PCM_1 and PV-PCM_2 at solar radiation intensity of 1000 Wm^{-2} and ambient temperature of 20 ±1 ˚C

Figure 5.11 shows the temperature difference between the reference PV and the two PV-PCM systems at 1000 Wm^{-2} insolation and 20±1°C ambient temperature. It was observed that both PV-PCM systems showed a higher temperature difference initially, 18 °C for PV-PCM_1 and 19°C for PV-PCM_2 which continued to decrease at a lower rate until 3.5 hours for both the PV-PCM systems. After 3.5 hours, the temperature difference in PV-PCM_1 started decreasing at a much higher rate indicating

predominantly sensible heating of PCM. The temperature difference for the PV-PCM_2 however continued to decrease with smaller gradient indicating predominant latent heating of the PCM. After 6 hours at the end of experiments, the temperature difference of PV-PCM_1 from reference PV dropped to 5 °C while the temperature difference of PV-PCM_2 remained at 13 °C indicating higher heat absorption potential of $CaCl_2.6H_2O$ in PV-PCM_2 than CP in PV-PCM_1. Comparing temperature differences in both PV-PCM systems from reference PV at all the insolations discussed, temperature difference was the highest at 1000 Wm^{-2}. Since the reference PV temperature was also highest at 1000 Wm^{-2} than the reference PV temperatures at 500 Wm^{-2} and 750 Wm^{-2} which indicates that PV-PCM systems are more effective at higher solar radiation intensities and PV temperatures.

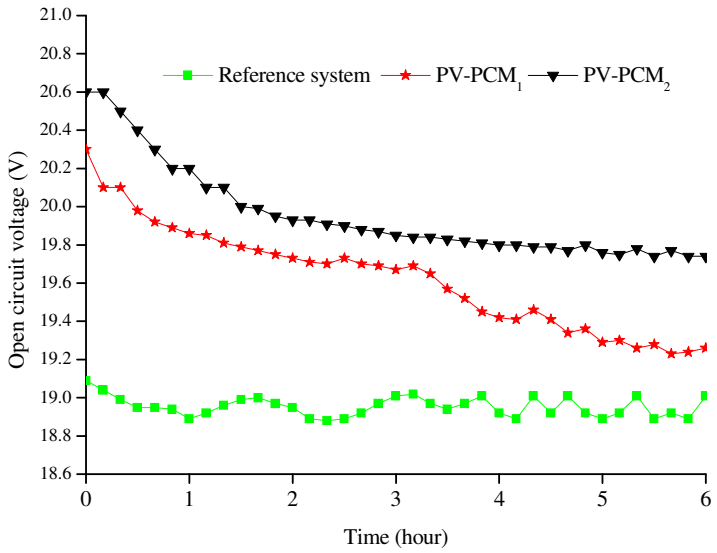

Figure 5.12 Open circuit voltage in indoor experiments at solar radiation intensity of 1000 Wm^{-2} and ambient temperature of 20 ± 1 °C

Figure 5-12 shows the V_{oc} for the reference PV and the two PV-PCM systems at 1000 Wm^{-2} solar radiation intensity and 20 ±1 °C ambient temperature. V_{oc} of the PV-PCM systems was higher than V_{oc} of the reference PV due to the lower temperature at the PV-PCM systems than the reference PV similar to what was observed in Figure 5.4 and Figure 5.8. V_{oc} in the reference PV remained around 19 ± 1 V for the whole duration of the experiment because its temperature remained stable while the V_{oc} in the PV-PCM systems continued to decrease as their temperatures continued to increase during the course of the experiments. Similar to the trend in temperature rise, the voltage drop was similar for both PV-PCM systems for initial 3.5 hours, after that V_{oc} in PV-PCM_1 dropped with larger gradient than V_{oc} in PV-PCM_2. Figure 5.13 shows V_{oc} improvement for the reference PV and the PV-PCM systems at 1000 Wm^{-2} solar radiation intensity and 20 ±1 °C ambient temperature.

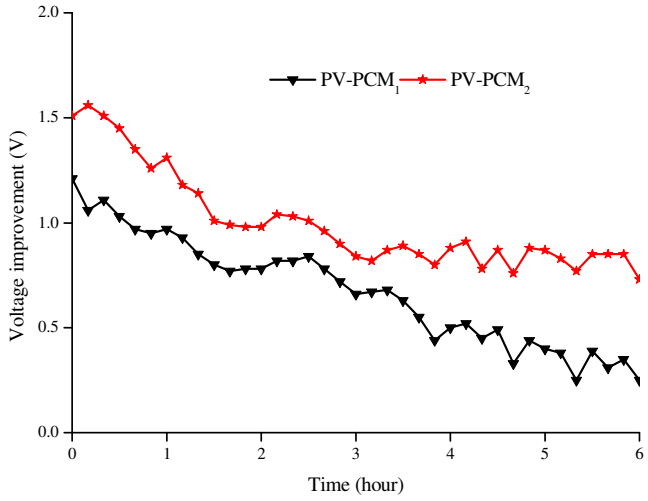

Figure 5.13 Open circuit voltage improvement in indoor experiments at solar radiation intensity of 1000 Wm^{-2} and ambient temperature of 20 ± 1 ˚C

It is observed that PV-PCM_2 maintained a higher voltage improvement than PV-PCM_1 for the duration of experiments with initial V_{oc} improvements of 1.2 V and 1.5 V for PV-PCM_1 and PV-PCM_2 respectively. After 3.5 hours a larger difference between V_{oc} improvement of PV-PCM_1 and PV-PCM_2 was observed Comparing V_{oc} improvements at all the three insolations discussed it is observed that V_{oc} improvements were the highest at 1000 Wm^{-2} than V_{oc} improvements at 500 Wm^{-2} and 750 Wm^{-2} similar to what was observed for temperature reduction.

Experiments conducted at solar radiation intensities of 500 Wm^{-2}, 750 Wm^{-2} and 1000 Wm^{-2} prove consistently through measured data of temperature rise, temperature reduction, V_{oc} output and V_{oc} improvements that the use of PCM in the PV-PCM systems maintained lower temperatures and achieved higher V_{oc}.

5.5.4. Average Temperature Reduction and Voltage Improvement

Temperature reduction and V_{oc} improvement did not stay constant over the duration of the experiments i.e., higher temperature reduction and V_{oc} improvement was observed at the start of the experiments, which decreased as the temperatures in the PV-PCM systems increased towards the end of the experiments in all cases. Higher initial temperature reduction and V_{oc} improvement were caused by latent heat absorption by the PCM in direct contact with PV back at constant temperature. If this situation i.e., pure isothermal latent heat absorption is stabilized for longer durations, maximum temperature regulation and associated power savings (P_s) can be achieved. However as the experiment proceeds sensible heat absorption by melted PCM and latent heat absorption by melting PCM occurs. This causes a rise in PV-PCM temperature and its

temperature difference from the reference PV starts decreasing down the peak. Although the peak temperature reduction could not be maintained through out the experiment however they are important benchmarks to give insight into how higher temperature reductions can be achieved provided the PCM melts without sensible heating.

However the peak V_{oc} improvement and temperature reduction are not realistic indicators to quantify relative performance of the PV-PCM systems because they last for short time. Therefore average temperature reduction and V_{oc} improvement is a more realistic approach to quantify the potential of PV-PCM systems to regulate temperature and prevent temperature induced power drop in PV devices.

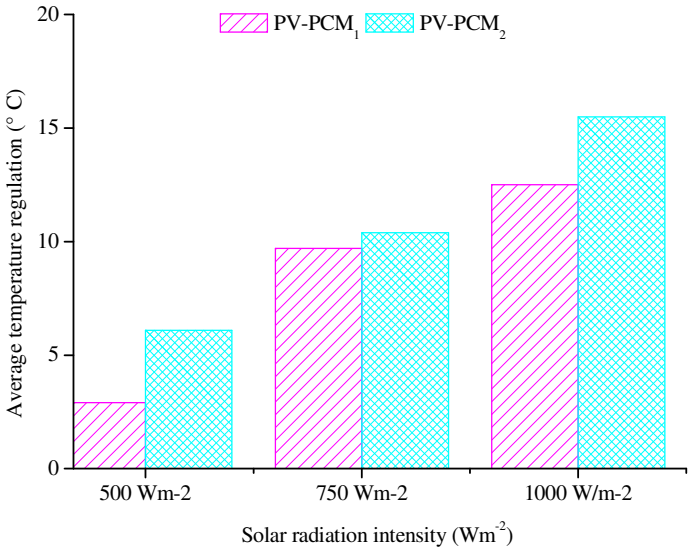

Figure 5.14 Comparison of average temperature reduction achieved for 6 hours in PV-PCM_1 and PV-PCM_2 at solar radiation intensities of 500 Wm^{-2}, 750 Wm^{-2} and 1000 Wm^{-2} and ambient temperature of 21 ±1 °C.

Figure 5-14 shows average PV temperature regulation achieved by both PV-PCM systems at solar radiation intensities of 500 Wm^{-2}, 750 Wm^{-2} and 1000 Wm^{-2} and ambient temperature of 20 ±1 ˚C. PV-PCM_2 achieved higher average temperature reduction than PV-PCM_1 at all solar radiation intensities. In the best case, average temperature reduction of 13 °C was achieved for PV-PCM_1 and 15 °C for PV-PCM_2 at 1000 Wm^{-2}. Higher temperature reduction was observed at higher solar radiation intensities and reference PV temperatures. This is due to maximum heat absorption by PCM during solid-liquid phase change at higher PV temperature. It can be concluded that these PCMs are more suitable for hot climates where higher PV temperatures are more likely to be achieved even at lower solar radiation intensities. In cooler climates although the PCM produce temperature regulation, however because the temperatures at PV surface remain very low which results in very low temperature regulation and the associated improvement in the electrical power, the temperature regulation may be too low to justify economic viability of using PCM.

Average improvement in the V_{oc} was also determined as shown in Figure 5.15, which shows that the voltage improvement also followed the same trend as in temperature reduction shown in Figure 5.14. It was observed that the PV-PCM_2 maintained higher average V_{oc} improvement than the PV-PCM_1 at all insolations, the lowest being 1.4 % obtained at 500 Wm^{-2} by PV-PCM_1 and the highest being 5.5 % obtained at 1000 Wm^{-2} by PV-PCM_2.

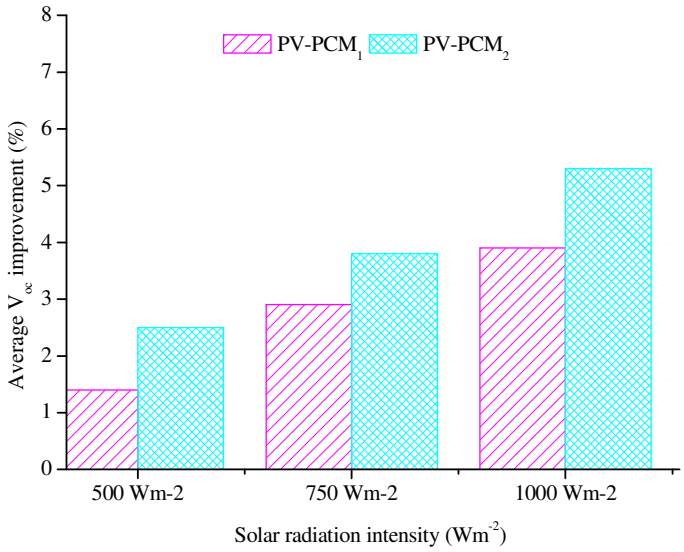

Figure 5.15 Average open circuit voltage improvement compared with the reference PV for 6 hours at solar radiation intensities of 500 Wm^{-2}, 750 Wm^{-2} and 1000 Wm^{-2} and ambient temperature of 20 ± 1 ˚C for PV-PCM_1 and PV-PCM_2

5.5.5. Average Measured Power Saving by Cooling of PV

The term measured power saving points to the fact that the power saving is based on measured electrical parameters of V_{oc} and I_{sc} and calculated value of fill factor *(FF)* from the PV characteristic curve. Use of PCM in this integrated PV-PCM system reduced PV operating temperature and improved V_{oc} which resulted in the prevention of temperature dependent power drop providing power savings (P_s). Measured P_s for the PCM was determined by comparing Power output (P) from PV with and without PCM.

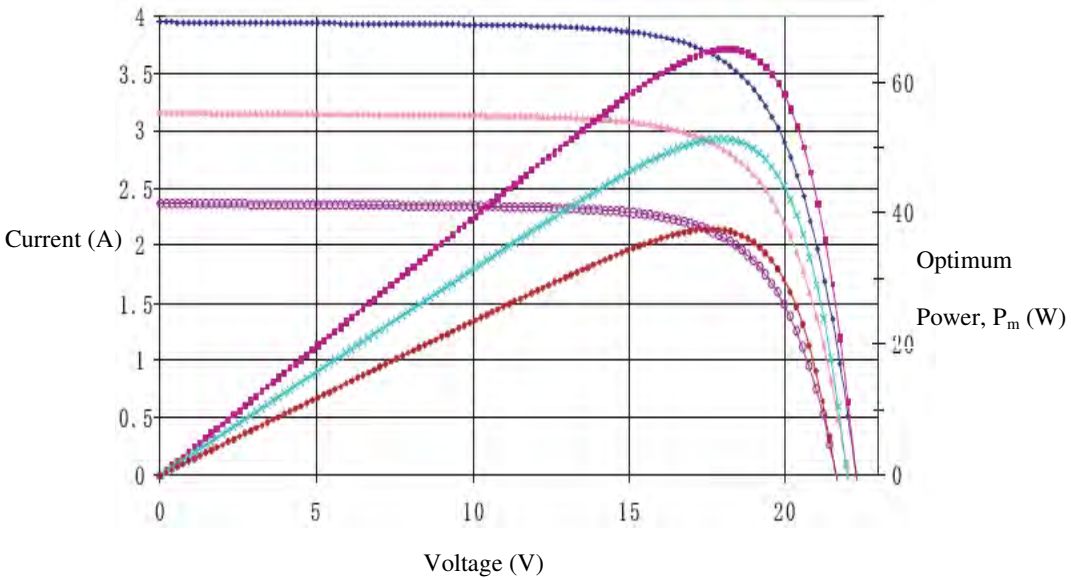

Figure 5.16 Power and *I-V* characteristic of the reference PV panel at 1000 Wm^{-2}, 800 Wm^{-2} and 600 Wm^{-2} at standard test conditions (STC) (Suntech, 2006).

FF was obtained from the *I-V* and power characteristics of the reference PV panel shown in Figure 5.16 by dividing optimum power (P_m) by the product of V_{oc} and I_{sc} at respective solar radiation intensities provided by Figure 5-16 as given by equation 5.1

$$FF = \frac{P_m}{V_{OC} I_{SC}} \tag{5.1}$$

Equation 5.11 and *I-V* curves of the PV provided by Figure 5.16 were used to calculate *FF* at solar radiation intensities of 1000 Wm^{-2}, 800 Wm^{-2} and 600 Wm^{-2}. Which were interpolated to obtain *FF* at 750 Wm^{-2} and 500 Wm^{-2} insolations. *FF* determined by this procedure at 500 Wm^{-2}, 750 Wm^{-2} and 1000 Wm^{-2} assumed a constant PV temperature at 25 °C.

In previous sections, it has been shown that increased solar radiation resulted in increased PV temperature above 25 ˚C e.g. 60 ˚C at 1000 Wm^{-2} illustrated Figure 5.10. *FF* which has been reported to decrease with a temperature dependent coefficient (T_{FF}) of -0.12 %/K (Marshal and Malinovska 2002) to -0.2%/K (Radziemska and Klugmann 2002) for polycrystalline PV as PV temperature rises above 25 ˚C. Replacing standard *FF* at 25 ˚C with *FF* calculated at corresponding temperatures (F_{FT}) Power produced by PV at a temperature T, (P_T) can be calculated as:

$$P_T = F_{FT} x V_{OC} x I_{SC} \qquad (5.2)$$

The F_{FT} can be calculated as:

$$F_{FT} = FF - T_{FF}(T - 25) \qquad (5.3)$$

Substituting equation 5.3 in equation 5. 2, the P_T can be calculated as:

$$P_T = (FF - T_{FF}(T - 25) V_{OC} I_{SC} \qquad (5.4)$$

P_T has been calculated using equation 5.4 for the reference PV, PV-PCM_1 and PV-PCM_2. The difference of P_T between reference PV and the two PV-PCM systems have been determined. This procedure is adopted to quantify the power saving (P_s) achieved by using the PCM by cooling PV. Figure 5.17 summarizes P_s obtained by the PV-PCM systems at solar radiation intensities of 500 Wm^{-2}, 750 Wm^{-2} and 1000 Wm^{-2} and ambient temperature of 20 ± 1 ˚C.

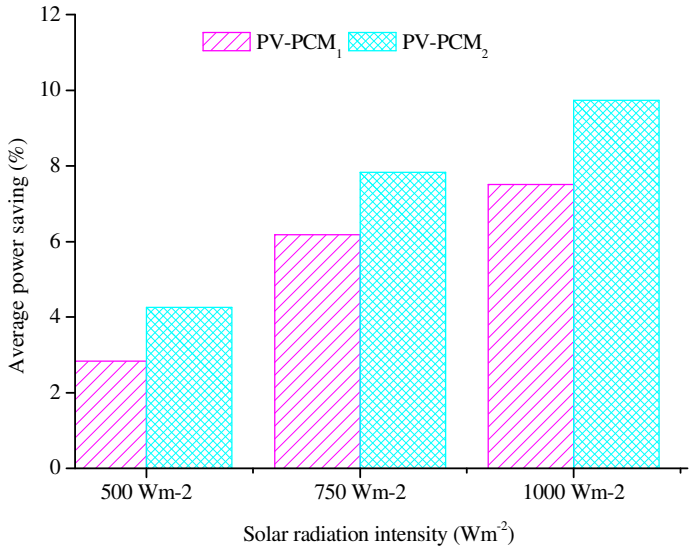

Figure 5.17 Measured average power saving P_s as a percentage of optimum power from PV.

PV-PCM$_2$ achieved higher P_s than PV-PCM$_1$ at all the three solar radiation intensities. P_s increased with increasing solar radiation intensity with a lowest value of 2.8 % achieved by PV-PCM$_1$ at 500 Wm^{-2} and highest value of 9.7 % achieved by PV-PCM$_2$ at 1000 Wm^{-2}.

5.5.6. Average Predicted Power Saving

The term predicted power saving is based on the non electrical measured parameters of temperature and temperature coefficient of power drop obtained from PV manufacturer's data and literature research from which power saving (*Ps*) is predicted. Average predicted power saving P_s was obtained by using the temperature coefficient of power drop (T_c) provided by the manufacturer presented in table 5.1 and

the measured temperature reduction achieved by PV-PCM$_1$ and PV-PCM$_2$ using equation 5.5.

NOCT	48℃ ± 2℃	
Current temperature coefficient	%/K	0.06 ± 0.01
Voltage temperature coefficient	mV/K	-(78 ±10)
Power temperature coefficient	%/K	-(0.5 ±0.05)

Table 5.1 Temperature dependent coefficients of voltage, current and power drop provide by PV catalogue data at standard test conditions (STC) (Suntech, 2006).

$$P_S = T_P(T_{PV} - T_{PV-PCM}) \qquad (5.5)$$

T_{PV} and $T_{PV\text{-}PCM}$ denote temperature of the reference PV and PV-PCM respectively. Predicted P_s was obtained from equation 5.5 shown in figure 5.18.

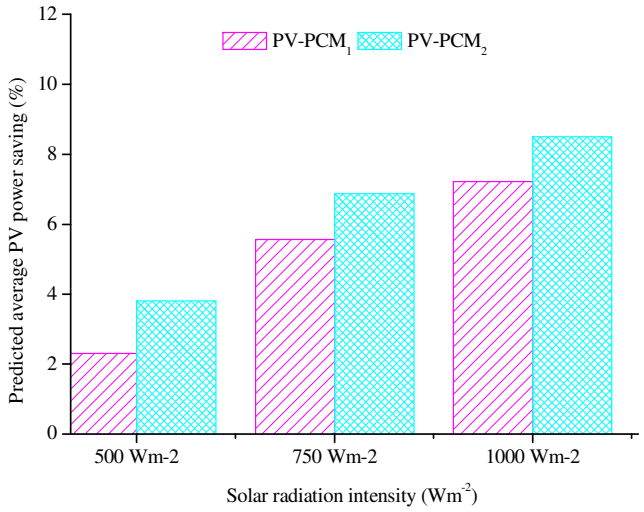

Figure 5.18 Predicted PV power saving obtained by multiplying average temperature regulation by temperature coefficient of power drop.

Comparison of measured and predicted P_s in Figure 5.19 shows that measured and predicted P_s are in good agreement at low temperatures and insolation but deviate for PV-PCM_2 at higher temperatures and solar radiation intensities. This shows that the temperature coefficient of power drop provided from manufacturer is not a true reflection of the actual power drop at higher temperatures and insolation intensities.

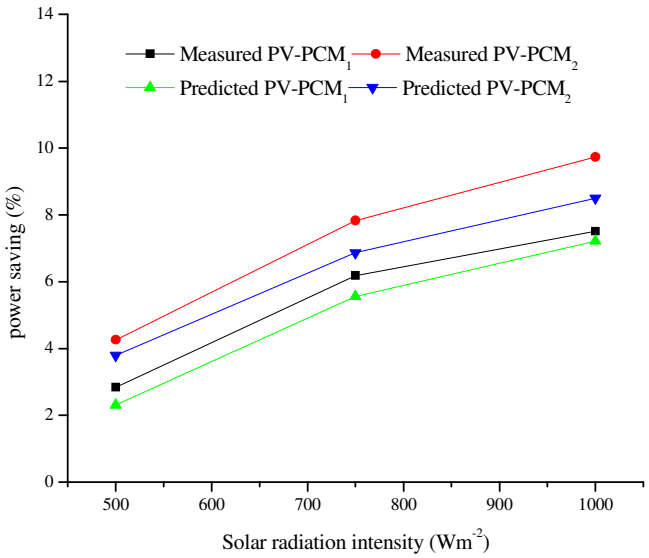

Figure 5.19 Comparison of measured and predicted power saving using PCM integrated into PV.

The calculated value of *FF* changes slightly due to change in solar radiation i.e., from 75.8 % at 1000 Wm^{-2} to 74.7 % at 600 Wm^{-2} when effect of temperature on *FF* is not considered. However considering temperature dependence of *FF* by using the temperature coefficient of fill factor (T_{FF}) of -0.2%/K, the *FF* drops from 75.8 % to 68.8 % when PV temperature increased from 25 ˚C to 60 ˚C at solar radiation

intensity of 1000 Wm^{-2}. The results obtained *FF*, power output (*P*) and power savings (P_s) due to PV cooling are presented in table 5.2.

		Reference PV			PV-PCM_1			PV-PCM_2		
		Insolation			Insolation			Insolation		
		500 Wm^{-2}	750 Wm^{-2}	1000 Wm^{-2}	500 Wm^{-2}	750 Wm^{-2}	1000 Wm^{-2}	500 Wm^{-2}	750 Wm^{-2}	1000 Wm^{-2}
Fill Factor	Standard	0.747	0.7515	0.758	0.747	0.755	0.758	0.747	0.752	0.758
	Considering temperature	0.717	0.6985	0.688	0.724	0.722	0.717	0.732	0.724	0.722
Power (W)	Standard	18.83	30.88	42.23	19.15	31.86	43.58	19.23	32.04	44.16
	Corresponding conditions	18.08	28.70	38.33	18.60	30.48	41.22	18.80	30.86	42.06
Power savings, Ps (W)	Power saving using *FF*	0	0	0	2.84	6.19	7.52	3.98	7.54	9.73
	Power saving using T_C	0	0	0	2.1	5.06	7.22	3.3	6.37	8.5

Table 5.2 Summary of Results for fill factor (*FF*), Power (*P*) and Power savings (*Ps*).

5.6 Conclusions

Results obtained from indoor experiments, at solar radiation intensities of 500 Wm^{-2}, 750 Wm^{-2} and 1000 Wm^{-2} and ambient temperature of 20 ± 1 ˚C indicate that both PV-PCM systems perform comparable however PV-PCM_2 achieved slightly higher temperature regulation, resulting V_{oc} improvement and associated $P_{s..}$ Measured and predicted P_s were found in agreement apart from at higher solar radiation intensities indicating that the temperature coefficients provided by the manufacturer may only be useful at lower temperatures and insolations. Finally, the best-case measured average temperature reduction of 15 ˚C and P_s of 9.7 % for 6 hours was achieved with PV-PCM_2 at 1000 Wm^{-2} and 20 ±1 ˚C which were found in agreement with the predicted values.

5.7 References

Delta-T (2010). "DL2e data logger product information, Delta-T Devices 2010".

Green, A.M. (2003). "General temperature dependence of solar cell performance and implications for device modelling" Progress in Photovoltaics: Research and Applications 11(5): 333-340.

Huang, M. J., Eames, P. C. and Norton, B. (2004). "Thermal regulation of building-integrated photovoltaics using phase change materials" International Journal of Heat and Mass Transfer 47(12-13): 2715-2733.

Huang, M. J., Eames, P. C. and Norton, B. (2006). "Phase change materials for limiting temperature rise in building integrated photovoltaics" Solar Energy 80(9): 1121-1130.

Kipp and Zonnen (2003). "Product Information - CM6B 2003, Kipp and Zonnen Gebrauchsanleitung".

Krauter, S (2004). "Increased electrical yield via water flow over the front of photovoltaic panels" Solar Energy Materials and Solar Cells 82(1-2): 131-137.

Marshal, J. M. and Malinovska, D. D. (2002). "Photovoltaics and Photvovoltaic Materials-Properties, Technology and Applications " Proceedings of the NATO Advanced Study Institute on Photovoltaics and Photovoltaic Materials-Properties, Technology and Applications, Sozopol, Bulgaria, 9-12 September 2001 Volume 80

Radziemska, E. (2003). "The effect of temperature on the power drop in crystalline silicon solar cells" Renewable Energy 28(1): 1-12.

Radziemska, E. and Klugmann, E. (2002). "Thermally affected parameters of the current-voltage characteristics of silicon photocell" Energy Conversion and Management 43(14): 1889-1900.

Suntechnics (2006). "Solar Modules STP065-12S/b, Suntechnics Power Co.Ltd."

Tonui, J. K. and Tripanagnostopoulos, Y. (2007). "Air-cooled PV/T solar collectors with low cost performance improvements" Solar Energy 81(4): 498-511.

Zacharopoulus, A, Mondol, J. D, Smyth, M., Hyde, T. and O'Brien, V. (2009). "State-of-the-art solar simulator with dimming control and flexible mounting" Proceedings of ISES solar world congress 2009, Renewable Energy Shaping our Future: 855-863.

6 OUTDOOR LARGE SCALE EXPERIMENTS IN THE CLIMATES OF IRELAND AND PAKISTAN

6.1. Aim of the Experiments

Results from indoor large scale experiments in the PV-PCM_1 and PV-PCM_2 showed agreement with those achieved from small scale indoor experiments; it was desired to investigate the performance of the PV-PCM systems in real outdoor operating conditions. The aim of these experiments is to compare the behaviour of the PV-PCM systems in outdoor realistic uncontrolled conditions with the indoors controlled test conditions to determine how effective the PV-PCM systems are in 'real' conditions. In addition the PV-PCM systems were characterized in two different climates i.e., high latitude cool climate of Dublin, Ireland and low latitude hot climate of Vehari, Pakistan to compare their performance.

6.2. Methodology

- Experiments were conducted with the same experimental set up and PV-PCM systems as were used in indoor large-scale experiments.

- Experiments were conducted outdoors on the roof of the Focas Institute, Dublin Institute of Technology Dublin, Ireland (53.33 N, 6.24 W) from 28-08-2009 to 12-09-2009 with reference PV, PV-PCM_1 and PV-PCM_2

- Experiments were conducted outdoors on roof of Jam house, Vehari, Pakistan (30.03 N, 72.25 E) from 30-10-2009 to 13-11-2009 with reference PV, PV-PCM_1 and PV-PCM_2

- Temperature evolution was measured on the reference PV, PV-PCM_1 and PV-PCM_2 and the difference of the temperatures of PV-PCM_1 and PV-PCM_2 from the reference was determined to quantify the effect of using PCM on the temperature regulation of the PV.

- V_{oc} and I_{sc} were measured for all systems and the difference of V_{oc} and I_{sc} between reference and the two PV-PCM systems were calculated to determine the effect of PV temperature reduction achieved by PCM on the electrical performance of the PV.

- *FF* was determined from the power and *I-V* curves for the PV at STC and these were interpolated to get the *FF* at real outdoor operating condition of the PV

- *FF* thus obtained were used with measured V_{oc} and I_{sc} to determine electrical power (*P*) produced by reference PV and the two PV-PCM systems to evaluate the effect of the PV temperature reduction on the gain of PV power

- Temperature coefficient of power (T_p) provided by the PV manufacturer's catalogue was used to predict the power saving, P_s obtained by reduced PV operating temperature achieved using the two PV-PCM systems.

- Predicted P_s obtained using T_p with measured temperature reduction and the measured P_s obtained using *FF* and measured V_{oc} and I_{sc} were compared to validate the experimental results with the manufacturer's data.

6.3. Experimental Setup

Experimental set up, sample preparation and the measurement procedures were the same as for indoor large scale experiments explained in chapter 5. The only difference was the source of insolation, instead of the solar simulator; PV and PV-PCM systems were placed outdoors and exposed to sun at the latitudes of Dublin, Ireland (53.33 N, 6.24 W) and Vehari, Pakistan (30.03 N, 72.25 E).

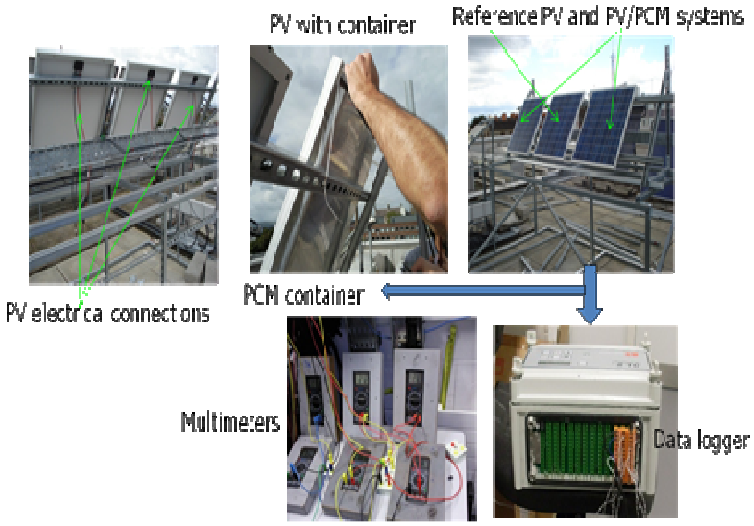

Figure 6.1 Outdoor experimental setup consisting of a reference PV, PV-PCM_1 and PV-PCM_2 installed on the roof of Focas Institute, Dublin Institute of Technology, Dublin, Ireland.

Figure 6.1 shows the experimental setup consisting of the reference PV panels without PCM, PV-PCM_1 and PV-PCM_2 installed outdoors on roof of Focas Institute. The temperatures and V_{oc} and I_{sc} were measured with delta-T 2e data logger and the multimeters shown in Figure 6.1.

6.4. Experimental Procedure

Three PV panels were characterized outdoors in Dublin for three days with solar radiation values ranging from 400 Wm^{-2} to 950 Wm^{-2} over the duration of experiment from 09:00 to 18:00 hours prior to their integration into PV-PCM systems: The V_{oc} and I_{sc} were measured for all three panels to quantify any inconsistencies in the panels which confirmed measured deviation below 1 % which can be described by the accuracy of the measuring instruments.

The reference PV and the two PV-PCM systems were deployed outdoors facing south in Dublin, Ireland at the latitude (53.33 N, 6.24 W) and the experiments were conducted from 28.08.2009 to 12.09.2009 from 09:00 to 18:00. In the same way the reference PV and the two PV-PCM systems were deployed outdoors facing south in Vehari, Pakistan at latitude (30.03 N, 72.25 E) and the experiments were conducted from 30.10.2009 to 13.11.2009 from 09:00 to 18:00. The ambient temperatures, wind speed, solar radiation intensities, temperatures at front and back surfaces, V_{oc} and I_{sc} for the reference PV and the two PV-PCM systems were measured.

6.5. Results and Interpretation

The temperatures, V_{oc} and I_{sc} were measured for the reference PV, PV-PCM_1 and the PV-PCM_2. The difference in the temperatures and the improvement in V_{oc} and I_{sc} from the reference were determined for the PV-PCM_1 and PV-PCM_2 which quantified the effect of using PCM on the temperature and the electrical output of the PV. Based on

the temperature reduction and V_{oc} and I_{sc} improvement, the predicted P was calculated with two different methods, which will be illustrated in the following sections.

6.5.1. Temperature Evolution

Although experiments were conducted from 30-08-2009 to 12-09-2009 for Dublin, Ireland and from 30-10-2009 to 13-11-2009 for Vehari, Pakistan, the weather conditions were not stable on all days. On certain days the solar radiation intensity and the ambient temperatures were not high enough due to overcast weather conditions in Ireland and fog conditions in Pakistan which restricted temperatures at the PV surface to such low values that the PCM could not melt properly. For other days the ambient temperatures and the solar radiation were high enough to raise the PV temperature above the PCM melting point which allowed heat absorption and thus melting of PCM to occur. Higher solar radiation intensity, higher ambient temperature and lower wind speed were available for few days which provided higher reference temperatures at PV surface allowing higher temperature regulation and associated P_s by applying PCM making their use justifiable. Due to this experimental constraint, the solar radiation, ambient temperature, PV panel temperatures, PV-PCM temperatures, thermal regulation by PCM and the associated V_{oc}, I_{sc} and P_s data are given for one day, the best case at each location which provided peak solar radiation intensity of 990 Wm^{-2} and 950 Wm^{-2} , peak ambient temperature of 24 ˚C and 34 ˚C , wind speed of 3.1 ms^{-1} and 0.9 ms^{-1} and combined convective and radiative coefficient of heat transfer of 9.1 $Wm^{-2}K^{-1}$ and 17 $Wm^{-2}K^{-1}$ for Dublin, Ireland and Vehari, Pakistan, respectively.

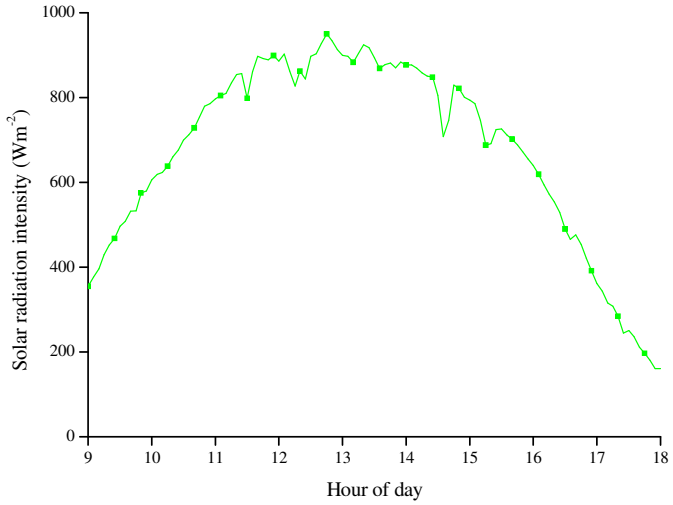

Figure 6.2 Solar radiation intensity measured in Dublin (53.33 N, 6.25 W) Ireland on 12-09-2009.

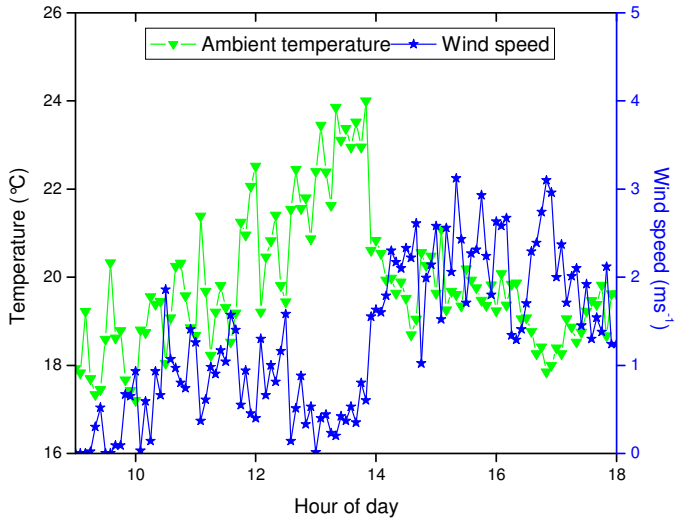

Figure 6.3 Ambient temperature and wind speed measured in Dublin (53.33 N, 6.25 W) Ireland on 12-09-2009.

Figure 6.2 shows that solar radiation intensity ranged from 380 Wm^{-2} at 9:00 to 200 $W\text{-}m^{-2}$ at 18:00 with a peak at 990 Wm^{-2} at 13:20. Figure 6.3 shows that the data measured showed that the ambient temperature remained between 18 °C and 24 °C, the wind speed remained between 0.25 and 3 $m\text{-}s^{-1}$. The best case data with higher solar radiation intensities (990 Wm^{-2}) peak and ambient temperatures (24 ˚C peak) was obtained at 12-09-2009. The stable conditions resulted in higher temperatures at the reference PV front surface. This made more heat available at PV enabling higher heat harnessing by the PCM at the back of PV resulting more temperature reduction. The temperature reduction caused a V_{oc} gain leading to improved PV power and P_s, in PV-PCM_1 and PV-PCM_2 compared to the reference PV.The aim of these experiments is to investigate into the behavior of the PV-PCM systems in climates with higher ambient temperatures.

Figure 6.4 shows the average temperature evolution on the front surface of the reference PV, PV-PCM_1 and PV-PCM_2 measured on September 12th 2009 in Dublin. Temperature at the PV front surface increased rapidly from 22 °C (at 09:00) to 40 °C in 2 hours and 5 minutes (at 11:05) and remained above 40 °C for 4 hours and 15 minutes (up to 15:20) with a peak temperature of 49 °C at 13:20. The peak temperature corresponds to the ambient temperature of 24 °C and solar radiation of 990 Wm^{-2} at a low wind speed of 0.25 $m\text{-}s^{-1}$. Temperature of the reference PV remained around the peak for an hour (between 13:00 to 14:00) followed by a rapid drop to 37 °C in 1.5 hours. This rapid temperature drop was caused by the increase in wind speed from 0.25 ms^{-1} to 2.9 ms^{-1} shown in Figure 6.3; however during the same

duration the solar radiation intensity continued to decrease with a smooth gradient (figure 6.2). This shows the impact of wind speed on the PV temperature.

As shown in figure 6.4 PV-PCM$_1$ and PV-PCM$_2$ followed the same trend in temperature rise as the reference PV temperature however the PV-PCM systems maintained lower temperatures than the reference PV throughout the experiment. After 14:00 the temperature of the reference PV dropped rapidly due to combined effect of (i) decreased incoming heat caused by decreasing solar radiation intensity and (ii) increased heat loss to ambient due to rapid increase in wind speed. The temperature in the PV-PCM systems showed less of a decrease, primarily due to the stored latent heat and thermal mass of the PCM in the PV-PCM systems, which releases stored heat with a small temperature changes.

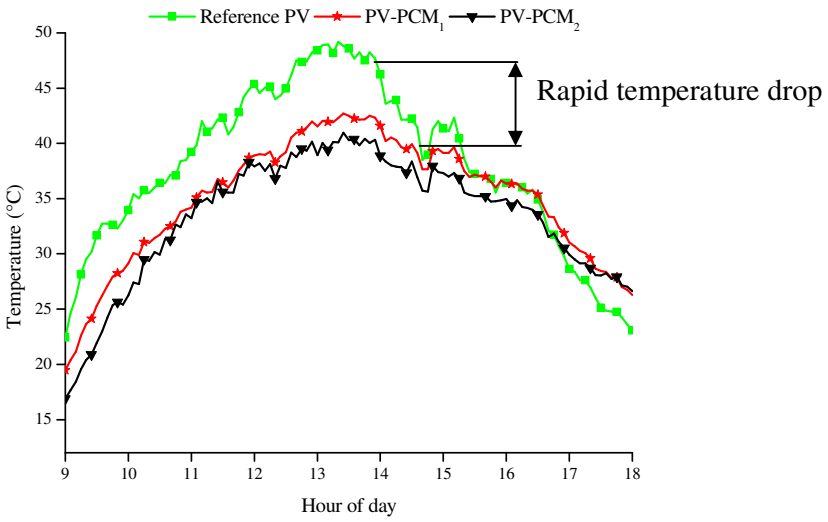

Figure 6.4 Average temperature at front surface of reference PV, PV-PCM$_1$ and PV-PCM$_2$ measured on 12-09-2009 for Dublin, Ireland (53.33 N, 6.25 W).

Figures 6.5, figure 6.6, and figure 6.7 show the solar radiation intensity, wind speed and temperature evolution of the reference PV and the PV-PCM systems containing PCM_1 and PCM_2 measured on 30-10-2009 in Vehari, Pakistan (30.03 N, 72.25 E).

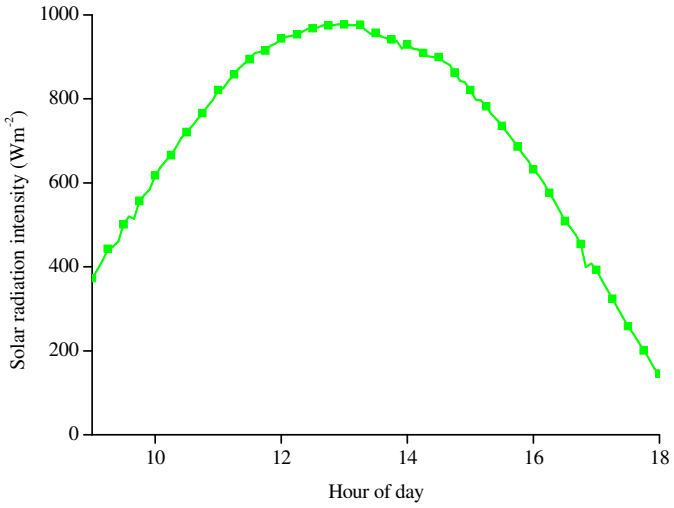

Figure 6.5 Solar radiation intensity measured on 30-10-2009 on roof of Jam house, Vehari (30.03 N, 72.25 E), Pakistan.

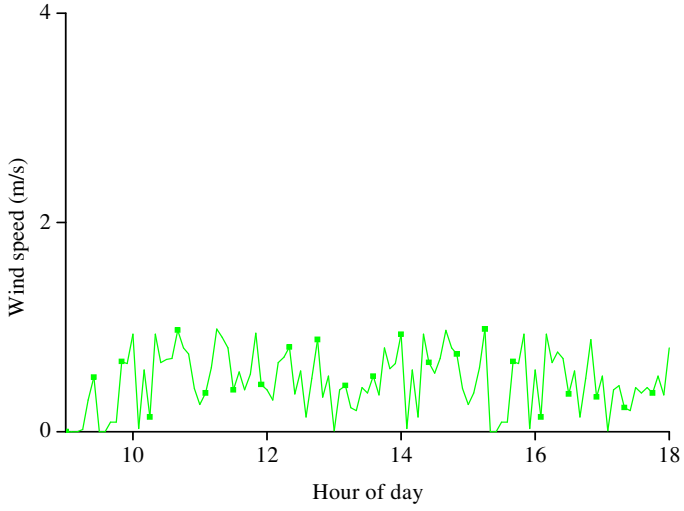

Figure 6.6: The wind speed data measured on 30-10-2009 for Vehari (30.03 N, 72.25 E), Pakistan.

Figure 6.5 shows that the solar radiation intensity started at from 390 Wm^{-2} at 9:00, reached a peak at 950 Wm^{-2} at 13:40 and dropped to below 200 Wm^{-2} till 18:00. The wind speed shown in figure 6.6 remained always between 0 ms^{-1} to 1 ms^{-1} from 9:00 till 18:00. The ambient temperature increased from 16 °C to 34 °C (figure 6.7) at peak around 14:20.

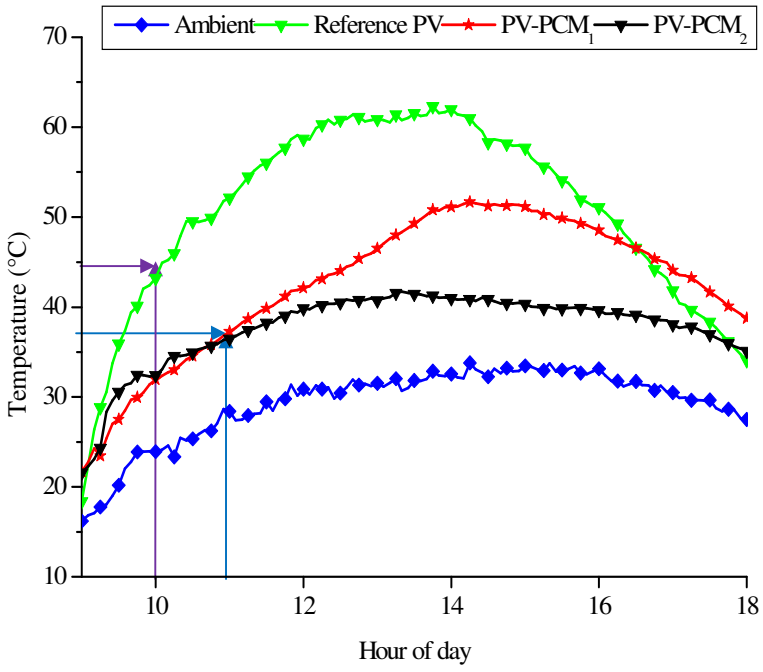

Figure 6.7 Average temperature at front surface of reference PV, the PV-PCM_1 and the PV-PCM_2 measured on 30-10-2009 for Vehari (30.03 N, 72.25 E), Pakistan.

Figure 6.7 shows that PV-PCM_1 and PV- PCM_2 followed the trend of temperature evolution as of the reference PV with smaller temperature difference at start of the experiment for 25 minutes however they started deviating from reference afterwards due to heat absorption by melting PCM at the back of the PV. The temperature at the

front surface of the reference PV increased from 18 °C to 50 °C in 2 hours reaching a peak of 63 °C at 13:45. The temperature remained at or above 50 °C for 6 hours until 17:00 when it dropped to 38 °C in the last hour of the experiment till 18:00. After 13:45, the temperature started to decrease in the reference PV with a stable gradient (higher than that of PV-PCM_1 and PV-PCM_2) indicating smooth cooling of the PV as the solar radiation started to decrease.

The temperature decrease in the PV-PCM systems was very slow which shows the heat retention of the PV-PCM system due to latent heat and thermal mass of the PCM. This also illustrates an important finding that in hot climates, higher ambient temperatures in the evenings result in lesser convective heat loss to ambient. This mechanism encourages higher heat retention of the system. Higher heat retention is required if the heat stored is to be exploited later for domestic water heating. High heat retention however discourages nocturnal solidification of the PCM which may affect its readiness and thermal regulation performance for the next day. In such cases coolant flow into the PCM to maximise heat extraction may be required. A further study needs to be conducted in this direction to make such systems energy efficient in hot climates by finding mechanisms to extract stored energy in PCM.

6.5.2. Temperature Reduction

Temperature difference of the two PV-PCM systems from the reference PV is shown in the Figure 6.8 for Dublin, Ireland. Figure 6.8 shows that PV-PCM_2 maintained a higher temperature reduction than the PV-PCM_1 for the duration of the experiment. Peak temperature reduction of 10 °C was achieved for PV-PCM_2 compared to 7 °C

for PV-PCM$_1$. The higher temperature reduction achieved in PV-PCM$_2$ is due to $CaCl_2.6H_2O$, the PCM in PV-PCM$_2$ that has higher heat of fusion, thermal conductivity and density than CP, the PCM in PV-PCM$_1$.

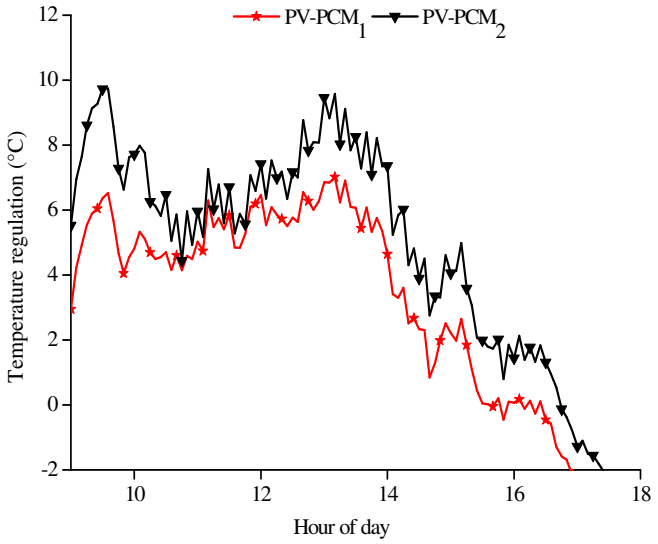

Figure 6.8 Temperature regulation – temperature difference between the reference PV and the PV-PCM systems measured on 12-09-2009 for Dublin, Ireland (53.33 N, 6.25 W).

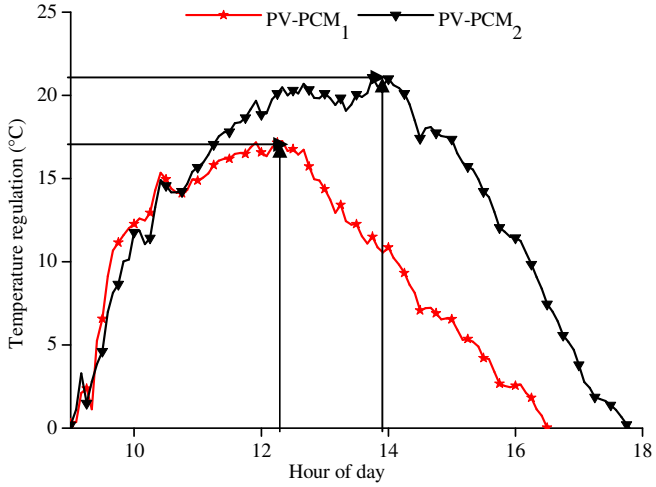

Figure 6.9 Temperature Regulation measured on 30-10-2009 for Vehari (30.03 N, 72.25 E), Pakistan

PCM_2 possessed higher heat of fusion that resulted in large amount of heat removal from the PV, higher thermal conductivity that resulted in more efficient heat removal from the PV, and higher density that resulted in higher thermal mass of PV-PCM_2.

Temperature difference between the reference PV and the PV-PCM systems is shown in Figure 6.9 measured on 30-10-2009 for Vehari (30.03 N, 72.25 E), Pakistan. Figure 6.9 shows that at the start of the experiment, the temperature difference was lower. The temperature difference increased as the incoming solar radiation and the ambient temperature increased to a peak of 17 °C at 12:20 for PV-PCM_1 and a peak of 21.5 °C at 13:55 for PV-PCM_2. It is observed that PV-PCM_2 maintained a higher temperature difference than PV-PCM_1 for the duration of the experiment. PV-PCM_2 maintained a temperature difference from the reference of over 20 °C for two hours between 12:20 to 14:20 which illustrates its potential to achieve high temperature reduction for longer durations. PV-PCM_1 maintained a temperature difference of 15 °C for 2 hours 20 minutes from 10:40 to 13:00. The temperature difference started decreasing after the peak with similar gradient for both PCMs however temperature in PV-PCM_1 equalled reference PV temperature i.e. zero temperature difference at 16:30 while temperature in PV-PCM_2 equalled the reference temperature at 17:50, just before the end of the experiment, which shows higher heat retention in PV-PCM_2 than PV-PCM_1.

6.5.3. Open Circuit Voltage

Figure 6.10 presents the measured V_{oc} for the reference PV and PV-PCM systems measured on 12-09-2009 for Dublin, Ireland.

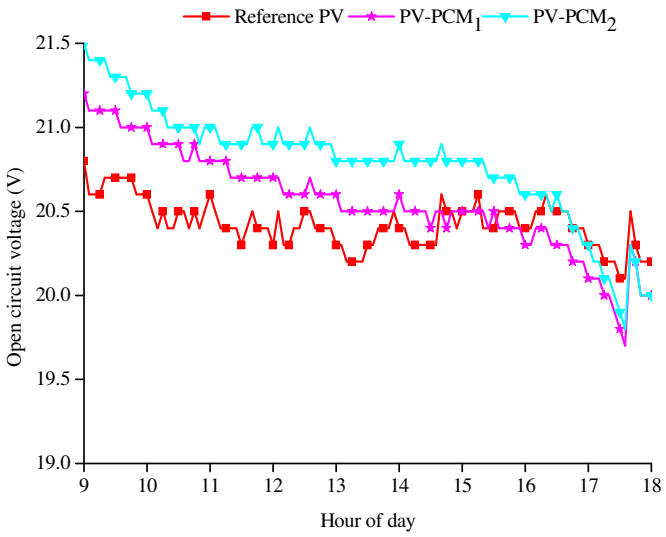

Figure 6.10 Open circuit voltage for the reference PV and the PV-PCM systems measured on 12-09-2009 for Dublin (53.33 N, 6.25 W)

V_{oc} was highest for all systems at the start of the experiment at 9:00 but continued to decrease during the course of the experiment. V_{oc} is reported to increase with the increase in solar radiation intensity (Dvorsky *et al.,* 2009), therefore V_{oc} should be at a minimum at start of the experiment and reach a maximum at 13:45 when the solar radiation intensity is maximum. However, increasing solar radiation also increases the temperature of the PV which has been reported to decrease V_{oc} and PV power (Radziemska and Klugmann, 2002; Nassar and Salem, 2007).

It can be observed that at start of the experiment V_{oc} is at a maximum corresponding to the minimum PV temperature although the solar radiation intensity is at minimum. It is partly due to low PV temperature which encourages higher voltage gain. It can be observed that the two PV-PCM systems maintained higher V_{oc} than the reference PV due to lower temperatures in PV-PCM systems than the reference PV. PV-PCM$_2$

maintained a higher V_{oc} than the PV-PCM$_1$ for the duration of the experiment due to the lower temperature.

Figure 6.11 shows the open circuit voltage for the reference PV and the two PV-PCM systems 30-10-2009 in Vehari.

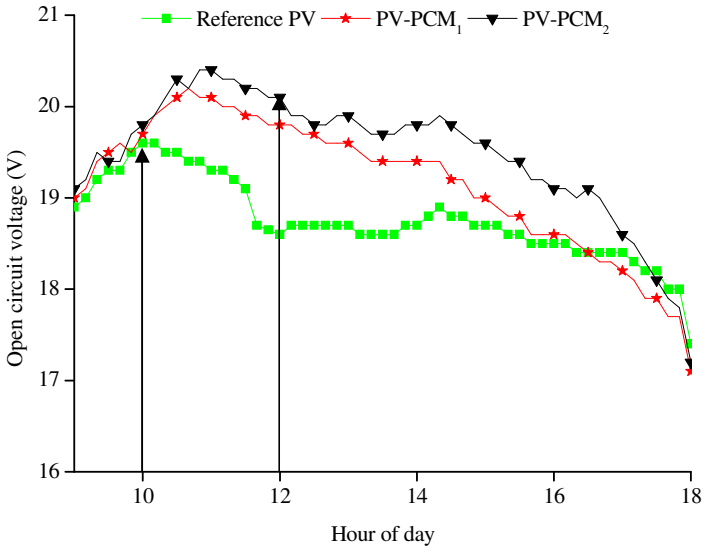

Figure 6.11 Open circuit voltage for reference PV and PV-PCM systems measured on 30-10 2009 for Vehari, Pakistan (30.03 N, 72.25 E)

At the start of the experiment from 9:00 to 10:00, the V_{oc} started to increase for the reference PV and the PV-PCM systems. The increase in V_{oc} was due to the increase in solar radiation. However this increase in solar radiation caused an increase in temperature of the PV. Increase in the solar radiation intensity tends to increases the V_{oc} however the associated increase in the temperature of the PV tends to decrease the

V_{oc} in the PV. Both the phenomena occurred together in the PV as the solar radiation increased when the sun stared coming into the plane of the panel.

Up to 10:00 the increase in the V_{oc} due to increasing solar radiation dominated the decrease in the V_{oc} due to the associated temperature rise resulting a net increase in V_{oc}. Although the solar radiation intensity continued to increase beyond 10:00 tending to increase V_{oc} in the reference PV however the temperature in the PV has increased up to 44 °C which tended to decrease the V_{oc}. This temperature was high enough that the associated temperature dependent decrease in the V_{oc} dominated the insolation induced increase in V_{oc} with a net effect of decreased V_{oc} in the reference PV. On the contrary, for the PV-PCM systems, the V_{oc} continued increasing beyond 10:00 as the temperature in the PV-PCM system remained below the temperature of reference PV. This shows that the cooling in PV-PCM systems caused by heat absorption of the melting PCM prevented the temperature dependent V_{oc} drop yielding a net effect of increased V_{oc} in the PV-PCM systems.

However after 11:00 the temperature in the PV-PCM systems became higher enough that the temperature dependent V_{oc} drop dominated the insolation induced V_{oc} gain with a net effect of decreased V_{oc} in both PV-PCM systems. From figures 6.11 it can be seen that net decrease in the V_{oc} of PV-PCM systems occurred corresponding to 37 °C (figure 6.) while in the reference PV, the net decrease in V_{oc} occurred corresponding to 44 °C (figure 6.7) which seems a disagreement between the reference PV and the two PV-PCM systems.

The temperature distribution on the reference PV was quite uniform which indicates that all the cells in the reference PV were at similar temperatures and their corresponding V_{oc} output was similar. However in the PV-PCM systems the

temperature was not uniform over the surface due to temperature distribution (described in detail in section 6.5.5) which meant that different cells were at different temperatures. It is possible that while the average temperature was 37 °C on PV-PCM surface, the highest temperature on a cell at the top surface may have reached 44 °C where the temperature dependent V_{oc} drop dominated the insolation induced V_{oc} gain yielding a net decrease in $V_{oc.}$ It should be noted that though average temperatures were considered in both cases (i.e., reference PV and in PV-PCM system), in reference PV the average temperature and maximum temperature were similiar due to uniform temperature distribution while in PV-PCM system (due to thermal gradient) the average temperature in PV-PCM system may be quite lower than maximum temperature.

Towards the end of the experiment after 16:00 the V_{oc} in the PV-PCM systems started to decrease with a greater gradient than the V_{oc} in the reference PV. This can be explained by the temperatures in the reference PV and the two PV-PCM systems, it was observed in figure 6.9 that the reference PV started to rapidly decrease in temperature due to lower thermal mass while the PV-PCM systems maintained a slower temperature reduction due to higher thermal mass. This caused the temperature in the reference PV to drop below the temperature in the PV-PCM systems which caused a higher prevention of V_{oc} drop in the reference PV than in the two PV-PCM systems. V_{oc} in PV-PCM$_1$ and PV-PCM$_2$ dropped below the V_{oc} in the reference PV at 16:20 and 17:45 respectively similar to the temperature difference in Figure 6.9.

6.5.4. Improvement in Open Circuit Voltage

Figure 6.12 shows the difference in V_{oc} of the PV-PCM systems from the reference PV in Dublin. It can be observed that the PV-PCM$_2$ maintained higher V_{oc} difference than PV-PCM$_1$ similar to the temperature difference. V_{oc} difference was found to be highest at the start of the experiment at 09:00 and at the time when solar radiation intensity was highest at 13:40 similar to what was observed for temperature difference.

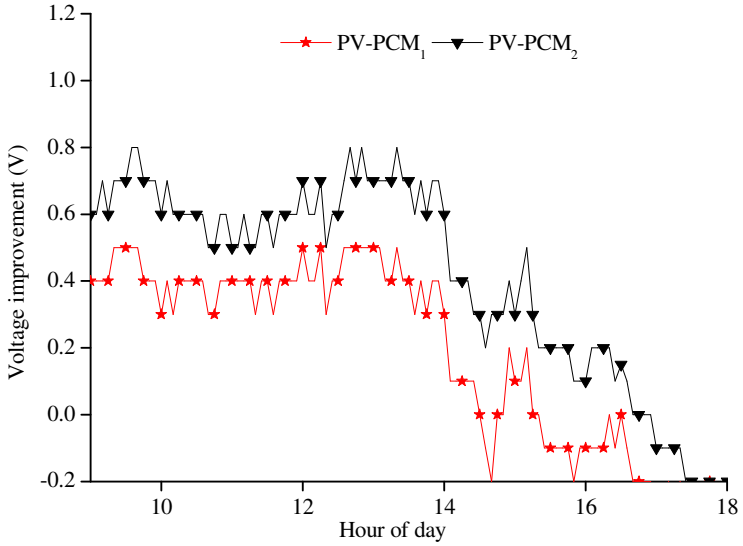

Figure 6.12 Voltage improvement - Difference of V_{oc} between reference PV and PV-PCM systems measured on 12-09-2009 for Dublin (53.33 N, 6.25 W)

It confirms that higher temperature regulation resulted in higher V_{oc} improvement. The peak V_{oc} improvement was of 0.5 V for PV-PCM$_1$ and 0.8 V for PV-PCM$_2$ obtained at 13:40. The temperature coefficient of voltage provided by the PV panel manufacturer was 0.078 ± 0.01 VK^{-1} (Suntech, 2006). Measured peak temperature

regulation was 7 °C for PV-PCM$_1$ and 10 °C for PV-PCM$_2$. Alternatively the predicted peak V_{oc} improvement was obtained by multiplying peak temperature regulation and the temperature coefficient which gave predicted V_{oc} to be 0.47- 0.61 V compared to measured value of 0.5 V for PV-PCM$_1$. Similarly the predicted V_{oc} improvement was found to be 0.68 -0.88 V compared to measured value of 0.8 V for PV-PCM$_2$. It shows that the measured and predicted V_{oc} improvements are in good agreement for both PV-PCM systems. Figure 6.13 shows the improvement in V_{oc} between the reference PV and the two PV-PCM systems for Vehari (30.03 N, 72.25 E), Pakistan measured on 30-10 2009.

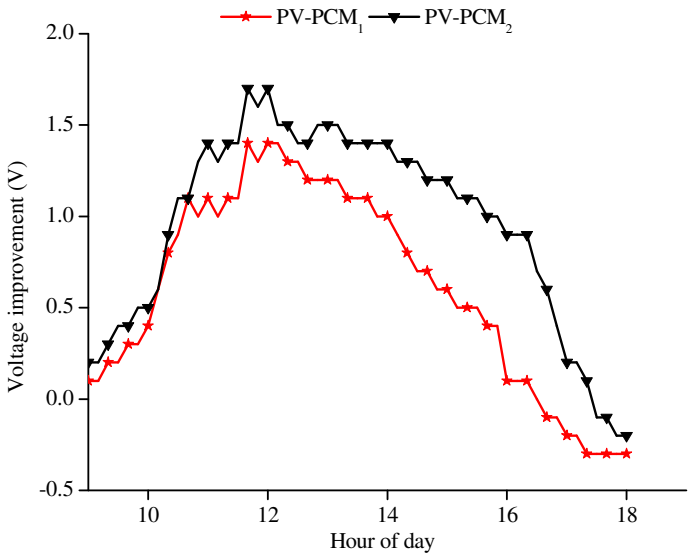

Figure 6.13 Voltage improvement: the difference of voltage between the reference and the two PV-PCM systems measured on 30-10 2009 for Vehari, Pakistan (30.03 N, 72.25 E)

PV-PCM_2 maintained a higher V_{oc} improvement compared to PV-PCM_1 for the duration of the experiment. V_{oc} improvement showed a similar trend as the temperature reduction in Figure 6.9. In the start of the experiment the V_{oc} improvements were similar for both PV-PCM systems when the temperature was lower. As the temperature increased, V_{oc} improvement for PV-PCM_2 showed a remarkable difference from that of PV-PCM_1. This indicates that at higher temperatures $CaCl_2.6H_2O$ in PV-PCM_2, performed much better than CP in PV-PCM_1. Peak V_{oc} measured improvements were 1.35 V and 1.75 V for PV-PCM_1 and PV-PCM_2 respectively.

Measured temperature regulation was 17 °C for PV-PCM_1 and 21.5 °C for PV-PCM_2. Alternatively predicted V_{oc} improvement were calculated by multiplying the temperature coefficient of voltage by the temperature reduction of each PV-PCM system. The V_{oc} predicted improvement was found in the range of 1.16-1.49 V for PV-PCM_1 compared to measured value of 1.4 V. The V_{oc} improvement for PV-PCM_2 was found 1.43-1.85 V compared to measured value of 1.75 V. In both PV-PCM systems the measured and the predicted values of V_{oc} improvements were in close agreement which shows accuracy of the measured data.

6.5.5. Temperature Distribution Over PV surface

Measured temperature was found to be much higher at the top of the front surface compared to the temperature at the bottom of the surface for both PV-PCM systems, showing temperature distribution. Temperature distribution was lower at the start of the experiment when the temperature of the PV was low and only a small amount of PCM had melted. As the temperature increased at the PV front surface, the amount of melted PCM increased and continued moving upward due to natural convection; this buoyancy driven flow of the melted PCM resulted in higher temperatures at the top surface and lower temperatures at the bottom surface of the PV-PCM systems.

The disadvantage of this upward movement of the melted PCM due to natural convection was that a certain amount of incoming heat was carried away by the melted PCM to the top surface into already melted PCM as sensible heat. This resulted in incoming heat being used as sensible heat, heating the melted PCM and raising its temperature instead of being used as latent heat to melt the solid PCM which would inhibit sensible heating and result in lower temperatures in the PV-PCM system. Thus in-homogenous temperature distribution slowed down PCM melting and resulted in increased PV-PCM temperature and limited PCM thermal regulation.

Temperature was measured at 9 thermocouple locations on the front surface of the PV-PCM systems. The temperature difference between thermocouple location with the highest temperature at top surface of PV-PCM system and the thermocouple location with the lowest temperature at bottom surface of the PV-PCM system was taken to quantify temperature distribution. Figure 6.14 shows measured top-bottom temperature difference as an indicator of temperature distribution measured for both

PV-PCM systems for Dublin, Ireland and Vehari, Pakistan. The figure shows that the temperature distribution was higher in Pakistan compared to that in Ireland for both PCM with PV-PCM_2 due primarily to lower convective heat loss coefficient from PV surface in Pakistan (9.1 $Wm^{-2}K^{-1}$) than in Ireland (17 $Wm^{-2}K^{-1}$), however was considerable at both the locations.

Increased temperature difference on the PV surface causes different cells to operate at different temperatures. The temperature rise decreases voltage from the PV cells, thus cells in the same PV panels would produce different voltages and currents. Since power output from PV corresponds to the minimum cell voltage, reduced voltage at certain cell reduces net power output from the PV panel referred to as power mismatch losses (Ramabadran, 2009). The power drop due to unequal temperature distribution needs further investigation to quantify the effect of this phenomenon on the net power output of PV.

The evenly distributed temperature would enable cells to produce same power to minimise power loss due to mismatch. Although the PV-PCM system already consisted of high thermal conductivity metallic fins installed vertically to enhance heat transfer and decrease the temperature distribution, the temperature distribution can further be decreased by optimising fins structure, arrangement and spacing. Different honey comb structures can be incorporated in the PCM matrix to achieve still increased thermal conductivity and reduced temperature distribution over the PV surface due primarily to natural convection.

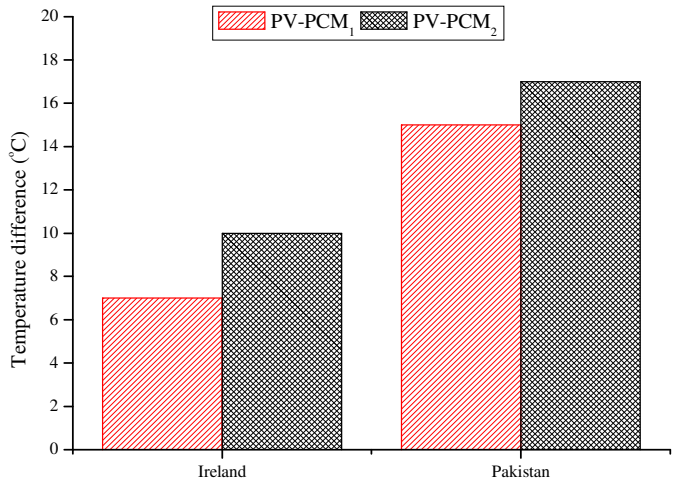

Figure 6.14 Peak measured temperature difference between top and bottom thermocouple locations for both PV-PCM systems in Dublin (53.33 N, 6.25 W), Ireland and Vehari (30.03 N, 72.25 E), Pakistan

6.5.6. Measured and Predicted PV Power Saving

The reduced PV temperature achieved by applying PCM prevented the temperature dependent V_{oc} drop which were measured and are presented in previous sections for Dublin, Ireland and Vehari, Pakistan for both PV-PCM systems. At both geographical locations, PV-PCM$_2$ obtained the higher temperature regulation and V_{oc} improvement than PV-PCM$_1$. Since the use of PCM showed savings on V_{oc}, it is important to determine the impact of temperature reduction on the P_s. P_s are predicted by multiplying temperature coefficient of power (T_p) (provided by the manufacturer, -0.5 % K^{-1} (Suntechics 2008) and T_p reported in the literature, -0.65 %K^{-1}) by the peak and daily averaged temperature reductions measured for both PV-PCM systems presented in Figure 6.15.

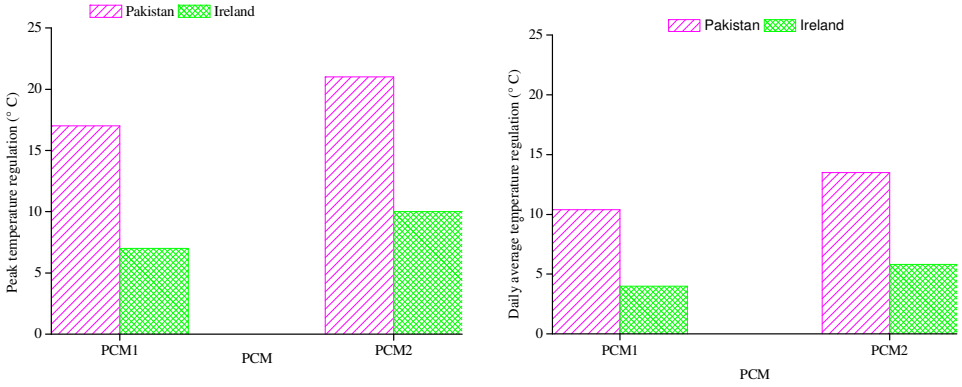

Figure 6.15 Measured peak and daily averaged temperature regulations for the PV-PCM systems in Dublin (53.33 N, 6.25 W), Ireland and Vehari (30.03 N, 72.25 E), Pakistan

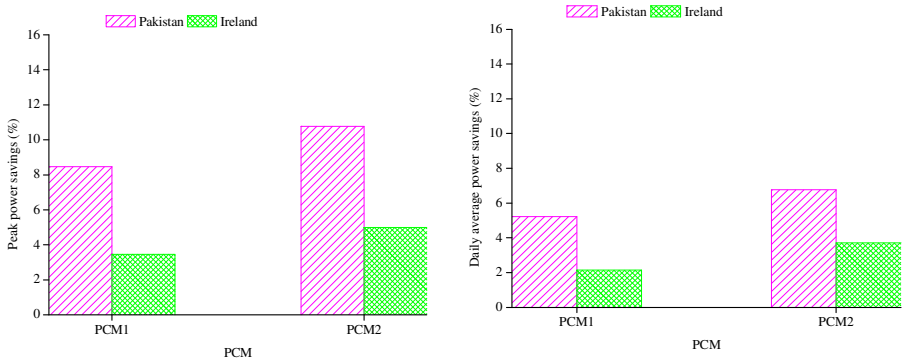

Figure 6.16 Predicted Power saving obtained by using the temperature coefficient of power drop from the manufacturer (-0.5 $\%K^{-1}$) with the measured temperature reduction for PV-PCM_1 and PV-PCM2 in Dublin (53.33 N, 6.25 W), Ireland and Vehari (30.03 N, 72.25 E), Pakistan.

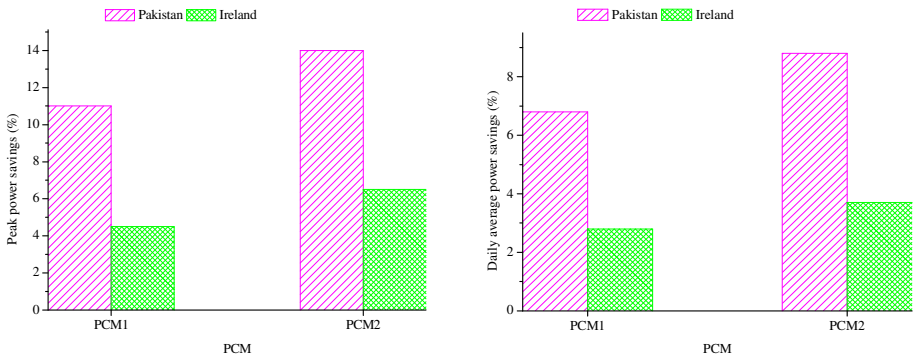

Figure 6.17 Predicted Power saving obtained by using the temperature coefficient of power drop from the literature (-0.65 % K^{-1}) with the measured temperature reduction for PV-PCM_1 and PV-PCM_2 in Dublin (53.33 N, 6.25 W), Ireland and Vehari (30.03 N, 72.25 E), Pakistan.

Figure 6.16 and 6.17 show that a lower peak and daily averaged predicted P_s was obtained for both PV-PCM systems in Ireland than in Pakistan. PV-PCM_2 maintained a higher peak and daily averaged P_s than PV-PCM_1 at both the geographical locations. Peak and daily average P_s of 10.8 % and 6.8 % respectively were obtained using T_p from manufacturer (-0.5 % K^{-1}) and peak and daily average P_s of 14 % and 8.8 % respectively were obtained using T_p from literature (-0.65 % K^{-1}) in Pakistan with PV-PCM_2 .

Measured data of V_{oc} and I_{sc} from the reference PV and the PV-PCM systems were used to determine the measured peak and daily averaged P_s by multiplying product of V_{oc} I_{sc} by FF. FF for the reference PV and the PV-PCM systems were determined by extrapolating from the PV characteristic curve to the required operating conditions in Dublin and Vehari and applying the methodology described in chapter 5. P_s obtained from V_{oc}, I_{sc} and FF is termed as measured P_s because it is based on extrapolation of measured electrical outputs of V_{oc} and I_{sc} from the experiments.

In Dublin, the measured peak and average V_{oc} (Peak V_{oc} corresponds to the value of V_{oc} at which the highest V_{oc} improvement was achieved by using PCM) were 20.1 V and 20.41 V for reference PV, 20.81 V and 20.52 V for PV-PCM_1 and 20.95 V and 20.81 V respectively for PV-PCM_2. Peak and average daily I_{sc} were 3.74 A and 2.82 A for the reference PV, 3.70 A and 2.77 A for PV-PCM_1, 3.68 A and 2.78 A for PV-PCM_2.

In Vehari The measured peak and average V_{oc} were 18.32 V and 18.72 V for reference PV, 19.71 V and 19.42 V for PV-PCM_1 and 20.15 V and 19.92 V respectively for PV-PCM_2. The peak and average daily I_{sc} were 3.42 A and 2.45 A for the reference PV, 3.35 A and 2.41 A for PV-PCM_1, 3.33 A and 2.39 A for PV-PCM_2.

Peak and average *FF* corresponding to the peak and average solar radiation intensities were first calculated at characterization temperature of 25 °C neglecting temperature influence on *FF*, denoted by FF_{st} applying the methodology described in chapter 5. Then the temperature influence on *FF* was incorporated with a coefficient, T_{FF} taken as -0.2 $\%K^{-1}$ drop in *FF* with increasing temperature above 25 °C and *FF* at real operating temperatures (FF_T) was calculated for the reference PV and the two PV-PCM systems. *FF* calculated were used with the peak and average daily V_{oc} and I_{sc} to determine the corresponding peak and daily average power produced (*P*) at particular temperatures and solar radiation intensities for the reference PV and the PV-PCM systems. Peak and daily average *P* from the PV-PCM systems were compared with peak and daily average *P* from the reference PV to determine the peak and daily P_s for the PV-PCM systems. P_s was determined for both the locations, Dublin Ireland and Vehari, Pakistan.

FF at peak and average solar radiation intensities neglecting temperature effect (FF_{st}), *FF* at peak and average solar radiation intensities considering temperatures effect (FF_T), peak and daily average *P* for the reference PV and the PV-PCM systems and the peak and daily average P_s for the PV-PCM systems are shown in Table 6.1.

The peak and daily average P_s were recorded as 4 % and 1 % respectively for PV-PCM_1 and 5.1 % and 1.8 % respectively for PV-PCM_2 in Dublin, Ireland. In Pakistan, the peak and average daily P_s were recorded as 11.3 % and 4.4 % respectively with PV-PCM_1 and 13 % and 7.7 % respectively with PV-PCM_2. It clearly shows that the integration of PCM into PV for their temperature regulation is particularly effective in high temperature climates such as in Vehari, Pakistan, than in low temperature climates, Dublin, Ireland in this study.

Key results of temperature regulation and P_s obtained from indoor experiments and outdoor experiments in Vehari, Pakistan and Dublin, Ireland using PV-PCM_1 and PV-PCM_2 are compared in table 6.2 which show reasonably closer values of temperature regulation and P_s in indoor experiments to outdoor experiments in Vehari, Pakistan.

		Reference PV		PV-PCM_1		PV-PCM_2	
		Dublin	Vehari	Dublin	Vehari	Dublin	Vehari
Insolation ,Wm^{-2}	Average	674	660	674	660	674	660
Fill Factor, FF	Average FF_{st}	74.82	74.78	74.82	74.78	74.82	74.78
	Average FF_T	72.22	69.64	72.82	71.26	73.22	72.24
V_{oc} (V)	Average	20.41	18.72	20.52	19.42	20.81	19.92
I_{sc}(Amp)	Average	2.82	2.45	2.77	2.41	2.78	2.39
Power (W)	Peak	53.3	42.52	55.46	47.34	55.99	48.04
	Average	41.57	31.94	41.71	33.35	42.3	34.39
P_S (%)	Peak	---	---	4	11.3	5.1	13
	Average	---	---	1	4.4	1.8	7.7

.

Table 6.1: Summary of the results for Dublin (53.33 N, 6.25 W), Ireland and Vehari (30.03 N, 72.25 E), Pakistan

		Indoor Experiments			Outdoors Ireland			Outdoors Pakistan		
		Reference PV	PV-PCM_1	PV-PCM_2	Reference	PV-PCM_1	PV-PCM_2	Reference	PV-PCM_1	PV-PCM_2
T (°C)	Ambient	20±1	21±1	20±1	18-24	18-24	18-24	16-34	16-34	16-34
	Surface	60	42	41	49	42	39	63	46	41.5
	Regulation	--	18	19	--	7	10	--	17	21.5
Insolation (Wm^{-2})		1000	1000	1000	990	990	990	950	950	950
Measured P (W)		38.33	41.22	42.06	53.3	55.46	55.99	42.52	47.34	48.04
Measured P_s (%)		---	7.52	9.73	----	4	5.1	---	11.3	13

Table 6.2 : Comparison of results for indoors and outdoors in Dublin (53.33 N, 6.25 W), Ireland and Vehari (30.03 N, 72.25 E), Pakistan.

6.6. Conclusions

PCM, $CaCl_2.6H_2O$ achieved higher PV temperature regulation and resulted in higher P_s than CP at both locations outdoors. In the best case $CaCl_2.6H_2O$ achieved a 1.7 % higher P_s than CP in Vehari, Pakistan. The temperature regulation and resulting P_s is affected adversely by temperature distribution in PCM between top and bottom surface which reached up to 17 °C using PCM $CaCl_2.6H_2O$ in Pakistan. Although the temperature regulation and P_s was higher for $CaCl_2.6H_2O$, yet the adverse effect of temperature distribution was also higher for $CaCl_2.6H_2O$ compared to CP. A maximum PV temperature regulation of 21.5 °C was achieved with $CaCl_2.6H_2O$ in Vehari, Pakistan yielding a peak measured and predicted P_s of 13 % and 14 % respectively. P_s predicted using T_p provided by the manufacturer was always less than P_s calculated through measured values of V_{oc} and I_{sc} with FF while considering temperature dependence of FF. Both PCM evaluated showed promising potential for the desired application, with higher potential in low latitude hot climate of Pakistan compared to high latitude cool climate of Ireland.

6.7. References

Dvorsky, E., Hejtmankova, P., Scerba, E. and Skorpil, J. (2009). "Modelling of PV Systems". Proceedings of ISES World Congress 2007 (Vol. I – Vol. V): 1454-1458.

Nassar, Y. F. and Salem, A. A. (2007). "The reliability of the photovoltaic utilization in southern cities of Libya" Desalination 209(1-3): 86-90.

Radziemska, E. (2003). "The effect of temperature on the power drop in crystalline silicon solar cells" Renewable Energy 28(1): 1-12.

Radziemska, E. and Klugmann, E. (2002). "Thermally affected parameters of the current-voltage characteristics of silicon photocell" Energy Conversion and Management 43(14): 1889-1900.

Ramabadran, R. (2009) "Effect of Shading on Series and Parallel Connected Solar PV Modules" Applied Modern Sciences 3(10): 32-41

Suntechics (2008). "Product Manual, Suntechnich STP065-12/Sb PV Panel ".

7 ENERGY AND ECONOMIC ANALYSIS OF PV-PCM SYSTEMS

7.1 Introduction

Crystalline silicon photovoltaic (PV) cells have currently a 90 % share of the PV market (Bagnall, 2008). As global silicon PV module manufacturing capacity has increased, average manufacturing costs have decreased from US$6 W_p^{-1} in 1992 to US$2.75 W_p^{-1} in 2005 (Margolis *et al.,* 2006), with the rate of reduction being greatest in the period 1992-2000 (Margolis *et al.,* 2006). The reduction in average costs slowed significantly after 2000 when the cost per W_p was already as low as 2.75W_p^{-1}$ equivalent to €2.03 W_p^{-1}. A recent study has shown that actual costs of installed PV are $ 6.5 W^{-1} in USA (Sciencedaily, 2010) equivalent to € 4.8 W^{-1} (XE, 2010). In the next 20 years, total costs p W_p^{-1} of "1st generation" silicon PV technologies are predicted to fall by less than 30% (Bagnall, 2008). This indicates that PV production costs are not expected to decrease enough in the near future to make them cost competitive compared to available conventional energy technologies. The current research seeks to maintain high PV efficiency and increase the operating life by maintaining PV at a low temperature. Making use of the heat available at the PV system may also enable it to reach financial viability. Energy efficiency analysis of PV systems is conducted to evaluate their potential for improved electrical and thermal efficiency. Finally the additional costs incurred in PV-PCM system and the resulting benefits are discussed in this chapter.

7.2 Energy Analysis of a PV-T System

The PV-PCM system in the current research is considered as a new type of a photovoltaic-thermal systems employing latent heat storage. The energy efficiency of a (PV-T) system can be defined as a ratio of total thermal (available on PV as heat) and electrical energy produced to the total solar energy falling on the PV surface given by equation 7.1 (Joshi *et al.,* 2009).

$$\eta_e = \frac{V_{oc} I_{sc} + Q_A}{G\ A_{PV}} \tag{7.1}$$

Where η_e is the energy efficiency of PV system, A_{PV} is the area of the PV exposed to solar radiation and Q_A is the heat lost from the PV to ambient given by equation 7.2

$$Q_A = h_{ca} A_{PV} (T_{PV} - T_{amb}) \tag{7.2}$$

Where T_{amb} and T_{PV} are the ambient and PV temperatures, respectively, A_{PV} is the heat transfer area of the PV and h_{ca} is the combined convective and radiative heat loss coefficient given by equation 7.3 (Tiwari, 2002, Tiwari and Sodha, 2006)

$$h_{ca} = 5.7 + 3.8 v_w \tag{7.3}$$

Where v_w is the wind speed taken from figure 6.3 for Dublin, Ireland and figure 6.6 for Vehari, Pakistan on 12-09-2009 and 30-10-2009, respectively. The maximum heat transfer coefficients (h_{ca}) calculated for Ireland and Pakistan using Equation 7.3 and v_w data from figures 6.3 (3 ms^{-1}) and 6.6 (0.9 ms^{-1}) respectively are 17 $Wm^{-2}K^{-1}$ and 9.12 $Wm^{-2}K^{-1}$, respectively which shows that h_{ca} for Ireland is almost twice that for Pakistan which is in agreement with the general trend of temperature recorded at both

location on PV surface which show that at the same solar radiation intensity, the PV surface temperature in Pakistan was always higher than that in Ireland due primarily to less heat lost from the PV surface in Pakistan. Substituting equations 7.2 and 7.3 into equation 7.1, η_e can be obtained as given in equation 7.4

$$\eta_e = \frac{V_{oc} I_{sc} + (5.7 + 3.8 v_w)(T_{PV} - T_{amb})}{G A_{PV}} \qquad (7.4)$$

Using equation 7.4, η_e of the PV systems were calculated for two different locations of Dublin, Ireland and Vehari, Pakistan and are presented in table 7.1. For Dublin, the weather data of ambient temperature, wind speed and solar radiation required for equation 7.4 was taken from figures 6.2, figure 6.3 and figure 6.4 respectively while V_{oc} and I_{sc} was taken from table 6.1. For Vehari, Pakistan the weather data of solar radiation, wind speed and ambient temperature required for equation 7.4 was taken from figure 6.5, figure 6.6 and figure 6.7, respectively while V_{oc} and I_{sc} were taken from table 6.1.

	Ireland	Pakistan
Electrical energy , $V_{oc} I_{sc}$ (MJ)	1.85	1.49
Combined convective and radiative heat loss coefficient, h_{ca} ($Wm^{-2}K^{-1}$)	9.1	17
Heat lost , Q_A (MJ)	3.03	2.19
Solar energy , GA_{PV} (MJ)	11.01	11.50
Energy efficiency of PV-PCM (%)	44.6	32

Table 7.1 Results obtained for energy efficiency of PV measured from 09:00 to 18:00 for Dublin, Ireland on 12-09-2009 and Vehari, Pakistan on 30-10-2009.

The average η_e values for the duration of experiment (9:00 to 18:00) were 44.6 % for Dublin and 32 % for Vehari, Pakistan and are summarised in Table 7.1. The η_e values obtained (32 % and 44.6 %) are in good agreement with previously reported values ranging from 33 % to 45 % obtained for weather conditions of New Delhi using the same method (Joshi, *et al.,* 2009).

7.3 Cost Analysis of the PV-PCM systems

Total cost associated with the PV-PCM systems is derived using three different costs i.e. (i) cost of the PCM (ii) cost of the containment materials (iii) manufacturing cost of the container. Each of the cost is then further divided into the cost of materials when purchased in kilograms for the experiment and the cost of the materials for large scale mass production when purchased in tonnes of the materials. Cost of the materials was €30 kg^{-1} for PCM_1 and €22 kg^{-1} for PCM_2 respectively when purchased in smaller quantities (Sigma Aldrich, 2008). The cost is projected to reduce to €2.5 kg^{-1} for PCM_1 and €1.9 kg^{-1} for PCM_2 when purchased in tonnes (ISIS, 2010). 12 kg of PCM_1 and 19 kg of PCM_2 were consumed to make the PV-PCM_1 and PV-PCM_2 respectively. So the total cost of the PCM incurred was €360 and €418 from local suppliers which is projected to reduce to €30 and €36 for PCM_1 and PCM_2 respectively.

The amount of aluminium alloy used was 13 kg to fabricate each PV-PCM system. The cost of the aluminium was €3.8 kg^{-1} when purchased from Pakistan and €5.6 kg^{-1} when purchased from Ireland for fabrication of the single PV-PCM system. The cost of aluminium is €1.71 kg^{-1} (Commodity, 2010) for Asian market and €2.5 kg^{-1} (LME, 2010) for European market when purchased in tonnes. Total cost of aluminium is €74

when purchased for single PV-PCM system which drops to €32.5 when purchased for mass production of PV-PCM systems in Ireland. The cost of aluminium is €49.4 when purchased in smaller quantities to fabricate PV-PCM system and €22.2 when purchased for mass production of such PV-PCM systems in Pakistan. Cost of fabrication was € 300 for Ireland and €40 for Pakistan for each PV-PCM system. If the production cost of mass produced systems decreases by a factor of 10 which is normal (KSB, 2010) then the manufacturing cost are expected to be €4 for Pakistan and €30 for Ireland. The costs are presented in table 7.2.

			Single fabricated PV-PCM system		Mass produced PV-PCM system	
			$PV\text{-}PCM_1$	$PV\text{-}PCM_2$	$PV\text{-}PCM_1$	$PV\text{-}PCM_2$
Cost (€)	Ireland	PCM	360	418	30	36
		Aluminium	74	74	32	32
		Manufacturing	300	300	30	30
		Net cost	734	792	92	98
	Pakistan	PCM	360	418	30	36
		Aluminium	49	49	22	22
		Manufacturing	4	4	4	4
		Net Cost	413	471	56	62

Table 7.2 Summary of manufacturing and material costs incurred to produce the proposed PV-PCM systems in Ireland and Pakistan.

In the most simple cost analysis cost incurred on the PV-PCM systems to regulate PV temperature is compared with the benefit obtained through improved PV electrical output due to temperature regulation. It can be observed that the cost incurred in Ireland on the production of PV-PCM systems was €734 for $PV\text{-}PCM_1$ and €792 for $PV\text{-}PCM_2$ produced as single system which is expected to drop to €92 for $PV\text{-}PCM_1$ and €98 for $PV\text{-}PCM_2$ when mass produced. Similarly the cost incurred in Pakistan on the production of PV-PCM systems was €413 for $PV\text{-}PCM_1$ and €471 for $PV\text{-}PCM_2$ produced as single system and is expected to drop to €56 for $PV\text{-}PCM_1$ and

€62 for PV-PCM_2 when mass produced. Since the rated power of PV is 65 W_p so the additional cost incurred due to integration of PCM into PV for mass produced PV-PCM systems in Ireland is €1.41 W_p^{-1} for PV-PCM_1 and €1.50 W_p^{-1} for PV-PCM_2. Similarly the cost involved in mass produced PV-PCM systems in Pakistan is €0.86 W_p^{-1} for PV-PCM_1 and €0.95W_p^{-1} for PV-PCM_2.

7.4 Benefit of the proposed PV-PCM systems

- Peak electrical energy gain due to temperature regulation by PV-PCM_1 in Dublin was found to be 2.16 W. The cost to produce same amount of electricity through installing extra PV would be obtained by multiplying cost per watt of PV (i.e., € 4.81 W^{-1}) to the extra electricity produced (i.e., 2.16 W) which gives the financial benefit of 10.39 € of the PV-PCM system. However the cost incurred to mass produce such PV-PCM_1 in Ireland systems was 92 € which shows that PV-PCM_1 costs 8.8 times the benefit in Ireland.
- Peak electrical energy gain due to temperature regulation by PV-PCM_2 in Dublin was found to be 2.69 W. The cost to produce same amount of electricity through installing extra PV would be obtained by multiplying cost per watt of PV (i.e., € 4.81 W^{-1}) to the extra electricity produced (i.e., 2.69 W) which gives the financial benefit of 12.94 € of the PV-PCM system. However the cost incurred to mass produce PV-PCM_2 in Ireland was € 98, which shows that PV-PCM_2 costs 7.5 times the benefit in Ireland.
- Peak electrical energy gain due to temperature regulation by PV-PCM_1 in Vehari was found to be 4.82 W. The cost to produce same amount of electricity through installing extra PV would be obtained by multiplying cost per watt of PV (i.e., € 4.81 W^{-1}) to the extra electricity produced (i.e., 4.82 W) which gives the financial

benefit of 23.18 € of the PV-PCM system. However the cost incurred to mass produce PV-PCM_1 in Pakistan was € 56 which shows that PV-PCM_1 costs 2.4 times the benefit in Pakistan .

- Electrical energy gain due to temperature regulation by PV-PCM_2 in Vehari was found to be 5.52 W. The cost to produce same amount of electricity through installing extra PV would be obtained by multiplying cost per watt of PV (i.e., € 4.81 W^{-1}) to the extra electricity produced (i.e., 5.52 W) which gives the financial benefit of 26.55 € of the PV-PCM system. The cost incurred to mass produce PV-PCM_2 in Pakistan was € 62 which shows that PV-PCM_2 costs 2.3 times the benefit in Pakistan.

7.5 Conclusions

The energy and economic analysis of the PV-PCM systems was performed. For PV the η_e, was 44.6 % for Dublin, Ireland and 32 % for Vehari Pakistan that is in good agreement with reported values for the similar work in literature. It was observed that in both Ireland and Pakistan, the financial benefit of electrical energy saved by temperature regulation through PV-PCM systems was lesser than the cost incurred to mass produce such systems at the corresponding locations confirming that at this stage the PV-PCM systems are not cost effective. Cost of the systems is from 7-8 times of the benefit in Ireland while about 2 times of the benefit in Pakistan which encourages the possibility of future research to improve performance of such systems in context of warmer climates like Pakistan. Additionally in the current analysis the benefit of exploiting thermal energy stored in PCM, increased PV life due to reduced operating temperature, environmental incentives due to carbon savings, State

incentives for green energy production and increased power density for building integrated photovoltaics were not considered which will further bridge the gap in cost and benefit to make PV-PCM systems cost competitive.

7.6 References

Bagnall, M.D. (2008) "Photovoltaic technologies". Energy Policy, 36, 12, 4390-6.

Commodity online (2010) www.commodityonline.com/commodities/metals/1.html Last visited 01-04-2010

Hepbasli, A., (2008) "A key review on exergetic analysis and assessment of renewable energy resources for a sustainable future". Renewable and Sustainable Energy Reviews. 12(3): p. 593-661

ICIS pricing (2010) www.icispricing.com (last visited 01-04-2010)

Joshi, A.S, Dincer, I. and Reddy, B.V. (2009) "Thermodynamic assessment of photovoltaic systems". Solar Energy 83 P. 1139–1149

KSB Pakistan (2010) www.ksb.com.pk/products.htm. Personal communication 31-03-2010

LME. (2010). London Metal Exchange. www.lme.com Last 02-04-2010

Margolis, R., Mitchell, R., Zweibel, K. (2006) "Lessons Learned from the Photovoltaic Manufacturing Technology/PV Manufacturing R&D and Thin-Film PV Partnership Projects". National Renewable Energy Laboratory

SigmaAldrich (2008). www.sigmaaldrich.com Last accessed 15-03-2010.

Sciencedaily (2010). www.sciencedaily.com/releases/2009/10/091021144249.htm Last visited 02-04-2010

Tiwari, A. and M.S, Sodha, (2006) "Performance evaluation of solar PV/T system: An experimental validation". Solar Energy, 2006. 80(7): p. 751-759.

Tiwari, G.N., 2002. Solar Energy: Fundamentals, Design, Modelling and Applications. Narosa Publishing House, New Delhi and CRC Press, Washington.

WAPDA (2010). Water and Power Development Authority, Pakistan, 2010. Personal communication.

XE. (2010). www.xe.com last visited 02-04-2010.

8 FUTURE PROSPECTS AND CONCLUSIONS

8.1 Future Prospects of the Research

8.1.1 Building Integration of PV-PCM Systems

The next step in this research can be to integrate the PV-PCM system into a building façade or roof and determine the heat gains, temperature regulation and PV power gain due to the system integration. The performance of BIPV systems strongly depends on the climate of geographical location where they are installed. It is strongly recommended that such systems should be installed at selected locations with substantially different latitudes and climatic conditions to measure their operating temperatures, temperature effects on electrical and thermal performance, effectiveness of cooling through use of variety of PCM to generate enough data for validation and establishing general correlations between climatic conditions and PV and PV-PCM performance. A successful integration and performance evaluation of the integrated system with respect to thermal and electrical performance evaluation/improvement will be very important research contribution which is very limited at present.

8.1.2 Heat Extraction from PV-PCM System

It has been shown that PCM integrated into PV stores a large amount of thermal energy available from PV as latent heat. Utilizing the stored energy brings additional benefit of these systems which can be maximised by future research:

- A heat extraction methodology can be devised that will enable improve heat exchange from the PV-PCM into heat transfer media. The study may focus on the cost, effective life and competitive heat exchanger materials. The measures can help to reduce temperature distribution in PCM by efficient heat extraction to improve PV power quality.
- Selection of appropriate heat transfer fluid, qualifying for little to no additional investment and operating cost, higher heat gains, possibility of utilizing heat using water for domestic water heating or air for space heating can be investigated. It has been shown in literature (Wilson, 2009) that water can be passed through such system using the normal hydraulic head available at home water supply systems which will save on pumping power need and extra capital cost. An arrangement of high thermal conductivity metallic cylindrical pipes equally distributed into the PCM matrix can be a start point.
- Optimisation of coolant flow rates will also be important for efficient and optimised heat removal from PCM and would reduce pumping or fan power if any of them arises. The study may involve modelling of heat transfer within the system between PCM and the coolant for design and flow rate optimization.

- The timings of heat extraction from PCM may easily be overlooked nevertheless it can be potentially important depending on site of the installed systems. Timing to start heat extraction may vary with the seasonal variation at the same site or geographical variation between sites during the same season. At high thermal loads in warmer climates the PCM may melt completely in shorter time duration and will thermally insulate PV from back tending to overheat the PV provided the heat is not extracted in timely fashion. Initially starting heat extraction at the (i) end of the day and (ii) mid of the day can be considered. End of the day heat extraction may more suit to cooler climates where PV can absorb heat for longer time durations. Mid of the day heat extraction may be necessary in hot climates where the temperatures are high enough to melt PCM in initial few hours of exposure.

8.1.3 Thermal Conductivity Improvement of the PV-PCM System

It is observed that thermal conductivities of the PCM and PV-PCM container play an important role in thermal regulation performance of the PV-PCM systems. Very low thermal conductivities of the PCM reduces heat transfer rate from PV into PCM and encourages natural convection in the PCM generating temperature gradient within PCM resulting in higher PV operating temperatures. Following measures can be taken to enhance thermal conductivity of the PV-PCM system

- Manipulation of fin design and investigation into different fin arrangements by numerical modelling and validation with experimental measurements.

- Addition of thermal conductivity enhancers (i.e., metallic nanopowders and carbon nanotubes) into the PCM and make uniform distribution (Lee *et al.*, 2005; Collins and Phaedon, 2000)

8.1.4 Optimization of PV-PCM System for Different Climates

Modelling of BIPV systems for different geographical locations with available weather data can be very important contribution to understand the electrical performance, additional benefits and potential challenges for competitive and reliable operation of such systems world wide. Simulation models can be developed using commercial packages such as TRNSYS and RET taking meteorological data to predict performance of BIPV systems at diverse weather conditions which will help provide rational for cooling need of the BIPV systems. At the second stage performance improvement of BIPV can be predicted with integrated PV-PCM systems. The model will help optimise PV-PCM system integrated into BIPV for thermal as well electrical gain for different climates avoiding increased effort and investment for experimental measurements and will guide investigation of suitable PCMs for different climatic conditions.

8.1.5 Corrosion Studies

It has been reported that some PCM show higher tendency to corrode PCM container materials than others. Comparison of different PCMs for their corrosion to the container materials is important to predict PCM container life-time and well as effectiveness of PCM materials for long time performance compatibility. The

corrosion studies will help understand the possible ways and materials to protect PCM containers from corrosion, comprehensive studies relating corrosion protection measures and their effectiveness and limitations have not been reported as yet to Author's knowledge.

8.1.6 Search for New PCM

Investigation into different PCM with suitable thermophysical properties, long time operation reliability, cost competitiveness and availability to suit different climates for PV cooling and enhanced performance is an open area of research. Research with an aim of discovering new materials, learning from cooling potential, techniques, limitation and challenges reported for cooling performance of PCM applied in electronics, building fabrics and food preservation can provide very important inputs for future research. Characterization of new materials, improvement in their properties and measures to functionally grade them can generate a list of optimum PCM for different geographical locations.

8.2 Conclusions

Aim of the current research is to experimentally investigate the PV cooling technique introduced by Huang *et al*., 2004, 2006 extending its use to (i) identify and thermophysically characterize new PCMs for their suitability for PV cooling applications (ii) experimentally evaluate the new PCMs indoors with different PV-PCM system configurations at various solar radiation intensities to adopt PV-PCM systems for different weather conditions (iii) integrate the optimum PCM into large scale PV panel size system with optimum PV-PCM configurations, measure PV temperature regulation through use of PCM and quantify the increased electrical output brought about by PV cooling indoors (iv) evaluate the PV cooling and increased electrical output through use of the novel PV-PCM system outdoors by extensive experimentation in two different climates i.e. (i) high latitude cool climate and (ii) low latitude hot climate.

Different PV types, their efficiencies and effect of temperature on their performance have been reviewed**.** It is proven that temperature has a strong impact on the electrical output as well as long-term operation reliability of almost all PV types. Different active and passive cooling techniques have been reviewed. Almost all of the conventional PV cooling techniques are limited by (i) high initial costs, (ii) operation and maintenance costs, (iii) low heat removal and (iii) inability to produce cooling at higher temperature summer environments.

The thermophysical properties of PCM were reviewed to determine suitable PCM for PV temperature regulation. Consequently five different PCM, RT20, SP22, $CaCl_2.6H_2O$, CL

and CP from three major classes of PCM, (i.e., paraffin waxes, salt hydrates and fatty acids) were selected with melting points around 25±4 °C and heats of fusion between 125-212 $kJkg^{-1}$. Initial characterization of PCM using DSC verified thermophysical properties of PCM. DSC could accommodate only 5-15 mg of the PCM mass, further characterization was deemed necessary with larger PCM masses. THM offered the possibility to place 25 g sample material and showed characterization comparable to DSC. Characterization with both DSC and THM showed good agreement with the results reported in literature. It was found that RT20 melts and solidifies over a wider temperature range and has high volumetric expansion (14%) during melting however it is non corrosive to most of the containment material which favours its use for PV temperature regulation being contained in metallic containers. $CaCl_2.6H_2O$ possessed the highest heat of fusion (i.e., 213 Jg^{-1}), highest thermal conductivity (i.e., 1.09 $Wm^{-1}°C^{-1}$) and melts and solidifies over a small temperature range. It shows an undesired strong corrosion to most of the container materials, a higher undercooling of 11 °C below its freezing point rendering difficulty in solidification and dehydration during thermal cycles if not contained in hermetically sealed containers. CL and CP melt and solidify over relatively narrow temperature ranges and possess higher heats of fusions (i.e., 168 Jg^{-1} and 191 Jg^{-1}, respectively) however CP and CL have very low thermal conductivities (0.14 $Wm^{-1}°C^{-1}$) which impedes heat transfer. SP22 has higher thermal conductivity (0.6 $Wm^{-1}°C^{-1}$) than CP, CL and RT20 however it has the lowest heat of fusion (122 Jg^{-1}) of all PCM, shows undercooling of 8 °C below its freezing temperatures which renders difficulty in solidification

Further indoor experiments on the cell size PV-PCM system enabled to determine actual thermal regulation of PV. Extensive indoor experiments conducted at 500 Wm^{-2}, 750 Wm^{-2} and 1000 Wm^{-2} solar radiation intensities enabled to understand the effect of (i) PV-PCM container material, (ii) melting point of PCM (iii) thermal mass of PCM (iv) heat of fusion of PCM (v) thermal conductivities of PCM and PV-PCM system on thermal regulation enhancement of PV. It was observed that the thermal regulation performance of a PCM depends on the thermal mass of PCM, melting point of PCM, heat of fusion of PCM and thermal conductivity of both (i) PCM and (ii) PV-PCM container material. Comparing PV-PCM systems, the aluminium based system A was found to be the optimum while CP and $CaCl_2.6H_2O$ were found to be the best PCMs. Better thermal regulation was produced at lower insolation by CP and at higher insolation by $CaCl_2.6H_2O$. In the best case both CP and $CaCl_2.6H_2O$ maintained a maximum of 18 °C temperature reduction at PV front surface for 30 minutes, while $CaCl_2.6H_2O$ maintained a 10 °C temperature reduction for 5 hours at 1000 Wm^{-2} insolation in system A. Indicative *Ra* numbers were calculated for all PCMs at three insolations which ranged between 10^3 - 10^7 which shows that the natural convection is present in the PV-PCM system and also the fluid flow is laminar. The experimental results were validated with an emissivity based P1 (Fluent, 2005 a) radiation model for incoming solar radiations and an enthalpy based two dimensional heat transfer model applying Boussinesq approximation for density variation in the fluid to solve phase change. PV without PCM was validated systems at all the three solar radiation intensities while PV-PCM system was validated at 1000 Wm^{-2} insolation using RT20 as PCM which showed good agreement with measurement results. Simulation results confirmed the presence of natural convection by

distribution of melt fraction along the vertical direction, with melted PCM moving to the top surface due to buoyancy and solid PCM moving downwards under gravity.

The best PCM (i.e., $CaCl_2.6H_2O$ and CP) and PV-PCM from small scale indoor experiments (i.e., system A) were characterized, at a larger PV panel scale (70 cm x 60 cm x 5 cm) consisting of PV panel, PV-PCM container fitted with metallic fins with PCM filled in. Indoor experiments with a large scale solar simulator producing solar radiation intensities of 500 Wm^{-2}, 750 Wm^{-2} and 1000 Wm^{-2} enabled to quantify the PV thermal regulation produced by each of the two PCM, CP and $CaCl_2.6H_2O$. Increase in V_{oc} was observed with decreasing PV temperature. It was observed that PV-PCM containing $CaCl_2.6H_2O$ produced highest PV thermal regulation and associated improvement in V_{oc} than the PV-PCM containing CP at all solar radiation intensities. In the best case temperature regulation of 13 °C and 15 °C was achieved with PV-PCM_1 and PV-PCM_2 respectively for 6 hours at 1000 Wm^{-2} solar radiation intensity. This PV thermal regulation increased PV power by 7.52 % and 9.7 % with PV-PCM_1 and PV-PCM_2 respectively.

Good results in indoor characterization encouraged outdoor characterization to be conducted in high latitude cool climates of Dublin, (53.33 N, 6.24 W) Ireland and low latitude warm climate of Vehari, (30.03 N, 72.25 E), Pakistan respectively applying the same experimental setup and measurement procedures. Similar indoor large-scale characterization, temperature reduction and associated PV power improvements were observed outdoors. In Dublin a peak PV temperature regulation of 7 °C with PV-PCM_1 and 10 °C with PV-PCM_2 was achieved yielding a predicted power improvement of 4.6 % with PV-PCM_1 and 6.5 % with PV-PCM_2 (using T_{cp} of 0.65 % $°C^{-1}$). In Vehari a peak

PV temperature regulation of 17 °C with PV-PCM_1 and 21.5 °C with PV-PCM_2 was recorded which produced predicted power improvement of 11 % with PV-PCM_1 and 14 % with PV-PCM_2. It was observed that both PV-PCM systems produced higher PV temperature regulation and greater associated power increase in the warm climate of Vehari than in the cool climate of Dublin. A simplified cost and benefit analysis showed that the PV-PCM systems cost more than the electrical saving due to cooling of PV, however the difference between cost and benefit is much lower in climates of Pakistan than in climates of Ireland.

Although the temperature regulation and power improvement was higher for $CaCl_2.6H_2O$, yet the adverse effect of temperature distribution (temperature difference between top and bottom of PV-PCM system) was also higher for $CaCl_2.6H_2O$ compared to CP causing power loss due to voltage mismatch. It is expected that with improved heat transfer, exploiting stored thermal energy, better design and comprehensive cost analysis, these systems can become cost competitive.

8.3 References

Collins, P.G. and Phaedon, A. (2000). "Nanotubes for Electronics". Scientific American, pp 67-69.

Lee, T.M., Chiou, K.C., Tseng, F.P. and Huang C.C. “High Thermal Efficiency Carbon Nanotube-Resin Matrix for Thermal Interface Materials”. Electronic Components and Technology Conference (2005), pp 55-59.

Wilson, E. (2009). "Theoretical and operational thermal performance of a wet crystalline silicon PV module under Jamaican conditions" Renewable Energy 34(6): 1655-1660.

Appendix

Appendix A- Solar Simulator

Product Name: Griven GR-262 Inse 1200 Followspot 1200W
Product Model: INSE1200
Manufacturer: **GRIVEN**

Griven GR-262 Inse 1200 Followspot 1200W

Followspot for 1200 MSR discharge lamp, zoom optical system: high light output and perfect focusing. Complete with two cooling fans, safety micro-switch, iris diaphragm, built-in ballast, on/off switch and supply cable.

The lamp is sold separately.

Technical features

- LAMP SOURCE

Type: MSR
Wattage (W): 1200
Base: G22
Lamp life (h): 750
Lumens: 110.000

- COLOURS

Color (MIX): Optional colour changer group

- PROJECTION

Zoom: 7-12
Iris:

Dimmer: Optional
Effects: Optional 4-way shutter

- HOUSING

Cooling: FV

- SIZE (mm)

Height: 420
Width: 350
Depth: 1010

- - WEIGHT (kg)

Main fixture: 30

- POWER

Input (V): 230
HZ: 50-60
AMP: 12

Appendix B-Pyranometer

Kipp & Zonen

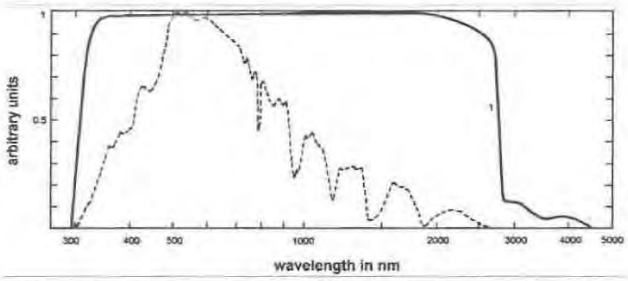

Abbildung 3 *1. Relative spektrale Durchlässigkeit zweier Pyranometer Dome. (Vier Oberflächenreflektionen und ein Indexwechsel mit Wellenlänge sind berücksichtigt)*
2. Spektrale Verteilung der Solarstrahlung auf Meereshöhe, Sonne im Zenit (Luftmasse 1).

1.2.3 Richtungsfehler

Das Richtungsverhalten ist individuell und abhängig von der Reinheit des Materiales des Glasdomes und der Winkelcharakteristik des Schwarzkörpers. Abbildung 4 zeigt ein typisches Polardiagramm des kombinierten Kosinus- und Azimuth-Verhaltens (= Richtungsverhalten). Um mit Hilfe dieses Diagramms Korrekturen zur direkten Solarstrahlung vornehmen zu können, müssen der Sonnenstand und das Verhältnis der Direktstrahlung zur Globalstrahlung bekannt sein.

2. TECHNISCHE DATEN

2.1 SPEZIFIKATIONEN

2.1.1 Technische Daten der Einzelversion CM 6B

Leistung

Spektralbereich:	305-2800 nm (50% Punkte) 335-2200 nm (95% Punkte)
Sensitivität:	zwischen 9 und 15 µV/Wm^{-2}
Impedanz:	70 -100 Ohm
Ansprechzeit:	< 18s (95%) < 24s (99%)
Nichtlinearität:	< ± 1.2% (< 1000 W/m^2)
Temperaturabhängigkeit der Sensitivität:	< ± 2% (-10 ^{0}C to +40 ^{0}C)
Richtungsfehler:	< ± 20 W/m^2 (Strahl 1000 W/m^2)
Neigungsfehler:	< ± 1% (Strahl 1000 W/m^2)
Nulloffset durch Far Infrared (ventiliert mit CV2)	< 15 W/m^2 at 200 W/m^2 Netto-Thermalstrahlung
Nulloffset durch Temperatur-schwankungen	< 4 W/m^2 bei 5 K/h Schwankung
Betriebstemperatur	-40 ^{0}C to +80 ^{0}C
Sichtfeld:	180° 2π sr
Strahlungsaufnahme:	0 - 1400 W/m^2 (max. 2000 W/m^2)

Kipp & Zonen

Sensitivitätsabweichung:	< ± 1% pro Jahr
Spektrale Trennschärfe	± 2% (0,35 µm bis 1,5 µm)

Das genannte Richtungsverhalten enthält folgende relative Fehler:

Kosinusverhalten:	max. ± 1% Abweichung vom Ideal bei 60 ° Sonnenzenitwinkel in jeglicher Azimuthrichtung max. ± 3% Abweichung vom Ideal bei 80 ° Sonnenzenitwinkel in jeglicher Azimuthrichtung

Konstruktion

Farbe Sensorelement:	Kohlschwarz
Glasdom:	Schott K5 optisches Glas, 2mm dick, 30mm und 50mm äußerer Durchmesser
Trocknungsmittel:	Silika-Gel
Libelle:	Sensitivität 0.5° (Luftblase zur Hälfte außerhalb des Ringes, Deckung mit Sensorsockel) Oberfläche des Sensorelementes und Sensorsockel sind deckungsgleich innerhalb 0,1°
Materialien:	seewasserfestes Aluminiumgehäuse und Nivellierschrauben, eloxiert. Rostfreie Stahlschrauben, korrosionsfrei montiert Weißer Plastiksonnenschirm ASA/PC, Trocknungspatrone PMMA
Gewicht:	850 g
Kabellänge:	10 m
Abmessungen:	B x H 150 x 95 mm. (S. a. Abbildung 5)

Appendix C- ΔT Data logger

DELTA-T DEVICES

DL2e DATA LOGGER
PRODUCT INFORMATION

The DL2e is a versatile, programmable field data logger, well suited to remote site, industrial and laboratory applications. Easy to operate, the DL2e system offers a wide choice of sensors, logging intervals, data collection and analysis facilities.

- Battery powered, weatherproof, rugged and portable
- Logs DC, AC, Resistance, Counter, Frequency and Status channels
- Simple GSM Modem connections and automatic data collection from remote sites
- Memory for up to 128k readings
- Easy programming with new Ls2Win 32-bit Software

Proven versatility Chosen by thousands of customers worldwide across science and industry, the DL2e is a highly versatile, rugged and portable data logging system that offers impressive performance and ease of use at low cost.

The DL2e is supplied with the Ls2Win software package. This sets up logging sessions, sensor libraries and conversions from raw readings to physical units, and controls the collection of stored data via the DL2e's RS-232 serial interface.

Once set up, the DL2e acquires data independently and automatically.

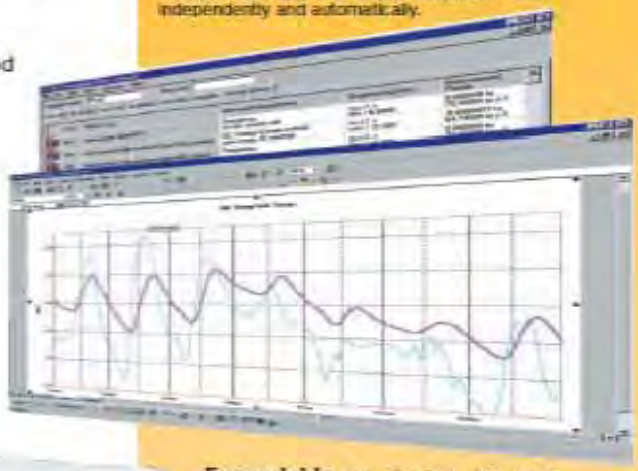

Expandable As standard, the DL2e includes a 15/30 channel DC analogue input card, 4 resident channels (2 digital inputs and 2 relay outputs), and memory for over 64,000 (64k) timed readings. An extra RAM chip extends this to 128k readings. Input cards and extra RAM are easily fitted by the user.

Suitable for most sensors The DL2e measures DC and AC voltage, current, resistance, logic state, pulse train and contact closure inputs, in almost any configuration (see panel on page 2). During programming, each channel can be set up with an individual sensor type and range, a data conversion characteristic, reading frequency from 1 second to 24 hours, and limits above or below which a flag is set or an output relay switched.

Logging sequences may be started at a preset time and date, or by an external event, and can be repeated as many times as desired. The DL2e also provides for sensor excitation and warm-up, control outputs, and malfunction warnings.

DL2e Specifications

Logging

LOGGING INTERVAL AND SPEED
1, 5, 10, 30 seconds, 1, 5, 10, 30 minutes, or 1, 2, 4, 12 or 24 hours, programmable for each channel. Readings can also be reduced to averages, maxima or minima at these intervals. Typically 10 channels per second in total.

INPUT CHANNELS
60 channels maximum, depending on input cards installed, plus 2 resident digital inputs and 2 relay outputs.

Analogue Inputs

STANDARD ANALOGUE CARD, LAC1
Each LAC1 multiplexer card can select analogue inputs from:
Either: 15 channels of differential voltages and/or 3-wire resistances
Or: 30 channels of single-ended (common ground) voltages and/or 2-wire resistances
Directly measures voltages up to ±2V or resistances <1MΩ. Voltages up to ±50V and currents can be measured using precision divider or shunt resistors mounted directly on the input screw terminals, or on an LPR1 or LPR1V card.

4-WIRE CARD, LFW1
Each LFW1 card can handle up to 12 bridge, potentiometric, differential voltage or 2- or 4-wire resistance sensors. 4-wire resistance measurements virtually eliminate cable resistance errors. 4-wire Pt100 platinum resistance thermometers, (e.g. DIN 43760/BS1904 types) are measured over -200 to +850°C. In the -17 to +57°C range of Logger and Pt100 temperature, resolution of 0.01°C and accuracy of ±0.2°C are obtained.

AC/DC INPUT CARD, ACD1
Each ACD1 card provides 15 measurement channels which may be individually configured for AC voltage (true rms), DC voltage (differential), 2- or 3-wire resistance. DC and resistance specifications are the same as for LAC1.

VOLTAGE READINGS

		Full Scale	**Resolution** (12 bits + sign)
4 ranges, user-selected or autoranged:	Range 1:	±4mV	1µV
	Range 2:	±32mV	8µV
	Range 3:	±262mV	64µV
	Range 4:	±2.097V	0.5mV

DC Accuracy (typical figures in brackets)

Logger temperature	**15 to 25°C**	**-20 to +60°C**
Full scale error	±0.07% (0.04%)	±0.2% (0.1%)
Long term stability	±0.25% (0.02%) over 1 year	
Differential offset	±10µV (3µV) ±0.02%	±12µV ±0.02%
Noise	(0.2µV rms)	
Input impedance	100MΩ approx.	
Common Mode Range	±2V or ±1.05V if "+" input is closer to logger 0V than "-" input	
Common Mode Rejection Ratio	(140dB), on voltage range 1	

AC Accuracy

Input level (mV ac rms)	**Sinusoidal signals** 45-60 Hz, -20 to +60°C	**Sinusoidal signals** 65-1000 Hz	**Non-sinusoidal signals** Crest factor 1.0 to 1.7
0 to 10	Reads zero in this range	Reads zero in this range	Reads zero in this range
10 to 50	±3mV	±0.6% reading	maximum additional error ±1.0% reading
50 to 100	±0.6% reading ±0.25mV		
100 to 2000	±0.6% reading		

RESISTANCE READINGS
Autoranging 12-bit voltage readings with programmable 2, 20, 200 or 2000µA excitation, giving 1MΩ full scale, or better than 0.01Ω resolution on lowest range

Accuracy
As voltage readings, with additional errors:

Logger temperature	**15 to 25°C**	**-20 to +60°C**
2µA excitation	±0.3% reading	±0.6% reading (to +50°C)
other excitation currents	±0.05% reading	±0.1% reading
2-wire LAC1, ACD1	±5Ω typical	±5Ω typical

INPUT PROTECTION
Analogue inputs withstand ±15V continuously, and much higher voltages in brief pulses (500V 1.2/50µs). For additional protection, see LPR1V below

ATTENUATOR CARD, LPR1
For use with Standard Analogue Card LAC1 only. Provides socketed positions for mounting signal conditioning resistors to 30 channels. Resistor positions may be left vacant or resistors fitted in shunt or divider configuration, for measuring currents up to 0.1A or voltages up to ±50V respectively

INPUT PROTECTION CARD, LPR1V
Connects transient-absorbing varistors to 30 Standard Analogue Card inputs, or 12 4-wire card inputs, for input protection to 2kV 1.2/50µs. Also provides socketed resistor positions for signal conditioning, but only when used with LAC1 (as LPR1 above). Can cause significant inaccuracies when measuring resistances >100kΩ

Digital Inputs and Outputs

DIGITAL INPUTS
All loggers have 2 resident 16-bit counter channels that continuously monitor logic levels or switch closures, logging digital status, counts or frequency (up to 100Hz), or for triggering special logging sequences

COUNTER CARD, DLC1
Each DLC1 card provides up to 15 extra 16-bit counter or frequency channels. Maximum frequency: 500Hz for switch closures, 500kHz for 5V logic level signals. Every channel can record up to 65472 counts over the logging interval.

RELAY OUTPUTS
2 SPDT relays for powering up sensors, or for providing alarms or malfunction warnings. 1A, 24V rating.

Other Specifications

PROCESSING OF RAW READINGS
The DL2e converts readings into engineering units using look-up tables or a linear conversion y = mx + c. User expandable sensor library includes Delta-T sensors (pages 15-18), Platinum Resistance Thermometers, Thermistors (Fenwal 2K, 2K252, 10K and 100K types), and Thermocouples (types J, K and T). Cold junction temperature is measured at isothermal terminals.

DISPLAY
A 2-line LCD shows instantaneous output from any sensor (in engineering units if appropriate), time, battery and memory condition, and status messages, without disturbing logging.

MEMORY
Highly reliable CMOS RAM, double battery-backed. Expandable from 64k readings (standard) to 128k. Automatic RAM check.

DATA FORMAT
ASCII, easily loaded into many spreadsheets and other packages, e.g. Excel, Lotus 1-2-3. Transmitted readings are date/time stamped, and labelled in engineering units with errors flagged. Data files created by the LS2e software are comma separated.

INTERFACE
RS-232 serial, up to 9600 baud. Up to 10000 readings transferred per minute without disturbing logging.

POWER
6 internal AA alkaline cells typically provide power for 500k readings, or 24 hours' operation using the keypad/LCD or RS-232 interface, or 12 months' quiescent operation. An external 7-15V DC supply can be used, with the alkaline batteries providing a back-up. The internal lithium cell will retain data for 2 months in the event of a power supply failure.

ENVIRONMENTAL
Operating temperature: -20 to +60°C. IP65 weatherproof main case with desiccant and humidity indicator.

EMC CONFORMITY
Tested to comply with EN 50081-1 and EN-50082-1 (1992) harmonised emissions and immunity standards

SIZE/WEIGHT
280 x 220 x 140mm / 2.7kg.

Delta-T Devices Ltd
128 Low Road, Burwell, Cambridge, CB5 0EJ, England
Tel: +44 (0)1638 742922 Fax: +44 (0)1638 743155
Email: sales@delta-t.co.uk Web: www.delta-t.co.uk

DOC REF: DLPT-06-05